Spin Imbalanced Quasi-Two-Dimensional Fermi Gases

by

Willie C. Ong

Department of Physics
Duke University

Date: _____

Approved:

_____
John E. Thomas, Supervisor

_____
Robert P. Behringer

_____
Shailesh Chandrasekharan

_____
Jian-Guo Liu

_____
Werner Tornow

Dissertation submitted in partial fulfillment of the requirements for the degree of
Doctor of Philosophy in the Department of Physics
in the Graduate School of Duke University
2015

Abstract

Spin Imbalanced Quasi-Two-Dimensional Fermi Gases

by

Willie C. Ong

Department of Physics
Duke University

Date: _____

Approved:

_____
John E. Thomas, Supervisor

_____
Robert P. Behringer

_____
Shailesh Chandrasekharan

_____
Jian-Guo Liu

_____
Werner Tornow

An abstract of a dissertation submitted in partial fulfillment of the requirements for the degree of Doctor of Philosophy in the Department of Physics in the Graduate School of Duke University
2015

Abstract

Spin-imbalanced Fermi gases serve as a testbed for fundamental notions and are efficient table-top emulators of a variety of quantum matter ranging from neutron stars, the quark-gluon plasma, to high critical temperature superconductors. A macroscopic quantum phenomenon which occurs in spin-imbalanced Fermi gases is that of phase separation; in three dimensions, a spin-balanced, fully-paired superfluid core is surrounded by an imbalanced normal-fluid shell, followed by a fully polarized shell. In one dimension, the behavior is reversed; a balanced phase appears outside a spin-imbalanced core. This thesis details the first density profile measurements and studies on spin-imbalanced quasi-2D Fermi gases, accomplished with high-resolution, rapid sequential spin-imaging. The measured cloud radii and central densities are in disagreement with mean-field Bardeen-Cooper-Schrieffer theory for a 2D system. Data for normal-fluid mixtures are well fit by a simple 2D polaron model of the free energy. Not predicted by the model is an observed phase transition to a spin-balanced central core above a critical polarisation.

For Daddy, Mummy, Wilfred

Contents

List of Tables

List of Figures

Acknowledgements

History has its means of finding you, more so this time than any other. My career as a graduate student at Duke University and North Carolina State University has been enriched by chance encounters with great souls whose wisdom, generosity, kindness, and friendship I am not sure I deserved. For all that my graduate experience was not, I am thankful for all that it was. Although this list is neither comprehensive nor complete, it pretty much is the group that shaped the last few years of my life.

I express my heartfelt gratitude first and foremost to my advisor, Dr. John Thomas for taking me on as a student. I thank him for allowing me considerable flexibility and latitude for intellectual exploration. He is an outstanding scientist equally adept at Fermi problems as machining tools for lasers. Physics is way simpler over a glass of chianti. Perhaps the one other person this thesis would have been impossible without would be Ilya. To him I owe everything I know about laboratory know-how, from optics to electronics, high field supplies to data acquisition, plumbing and machining. And translated Russian sayings. Never mind that everything had to sit along one-straight-line. The first member of JETLAB who taught me how to work with a dye laser (or a laser for that matter) and allowed me access to one was a lab buddy, Chenglin (Charles) Cao. He remains a great friend to this day. Following Charles' graduation for Northern pastures, Nithya and Arun were the other internationals who made life as a graduate student much more bearable. I have since dedicated Independence day in their honor to lab battery-change day. I

thank Chingyun Cheng for organising group celebrations in my absence; with her at the helm, Riddick 212 is in great hands!

Then there was the rocket scientist I named after all dashi broths, Ethan Elliot. Without him, the high field magnet supplies would not have been where they are right now. Gym matters aside, he was the lab's turn-to source for dealing with all things fluid: perfect or disastrous... Remember the floods? Jessie Petricka was the postdoc with a knack for sniffing out electronic faults. To him, I owe some lab know-how in my early days as a graduate student, and an appreciation for molecules. Jessie was, and I have every reason to believe that he still is, an outstanding teacher in the lab. The other postdoc in the neighboring lab, James Joseph was a treasure trove of knowledge for all matters Mathematica. Being the only remaining reason for my decision to join the group, his very presence was an inspiration. I thank him for extending a helping hand during rough times in the lab.

Beyond the labs, I remember Georgios Laskaris who was my go-to source for all things related to nuclear physics. He was a most passionate and forceful physicist whom I am proud to have known. I thank him for the generosity of his time, wisdom, and expertise. Incidentally, most of my closer friends were members of the Behringer group. Jie Ren provided much help in a Nonlinear Dynamics course. Somayeh Fahardi and Tang Junyao remain great friends until this day.

I thank the staff at Duke for making my time as a student a memorable one. Donna Ruger served as a Duke Mom to a generation of Physics grads, I wish her a happy retirement! Nancy Morgans provided a listening ear and was instrumental in making this thesis a reality. Donna Elliott was everyone's source for finances and administrative matters in general. I thank Richard Nappi for instruction and guidance at the student machine shop, and Ken McKenzie for his tireless efforts in improving the undergraduate physics labs.

At North Carolina State University, Rebecca Savage was the most amazing ad-

ministrative superwoman. From card access to facility membership, she was the department's any-time resource. Her dedication, resourcefulness, and willingness to help is beyond compare. For bringing much cheer to us graduate students, and making us feel at home my thanks and appreciation go out to Rhonda Bennett as well.

I thank the members of my thesis committee, Professors Bob Behringer, Shailesh Chandrasekharan, Jian-Guo Liu, and Werner Tornow for taking the time off their schedules to monitor my progress over the years, serving on my defense committee and for providing feedback on this thesis. I would further like to thank Professors Richard Palmer, Ayana Arce, and Calvin Howell for offering their time and effort at some point during this endeavor.

Of course there's Jayampathi Kangara and Lorin Baird, the newest additions to our lab. Their dedication and energy bring back fond memories of a dual someplace in time, one of entropy, and another of viscosity. If I had to do a thesis all over again, I might just rejoin them !

1

Introduction

1.1 Fermi gases for quantum emulation

The successful realization of degenerate atomic Fermi gases in three dimensional geometries has led to a burgeoning subfield of quantum simulation. In tandem with rapid advances in string theory, high energy physics, condensed matter physics, and quantum information science, to list a few areas, atomic Fermi gases [5, 6] have emerged as tunable table-top neutral analogs to Fermi systems in bridging temperature scales approximately 19 orders of magnitude apart with an unprecedented level of control. Thanks to magnetically tunable collisional (Feshbach) interactions, a relatively impurity-free setting, and direct means of observing quantum phase transitions, atomic Fermi gases are a neat tool to aid our understanding of emergent properties of interacting many-particle systems and realizing complex Hamiltonians otherwise inaccessible in conventional settings.

Despite remarkable strides however, long-standing questions and challenges remain for which atomic Fermi gases may provide new insights. In high-transition temperature iron-based superconductors [7, 8] and layered organic compounds [9, 10] for

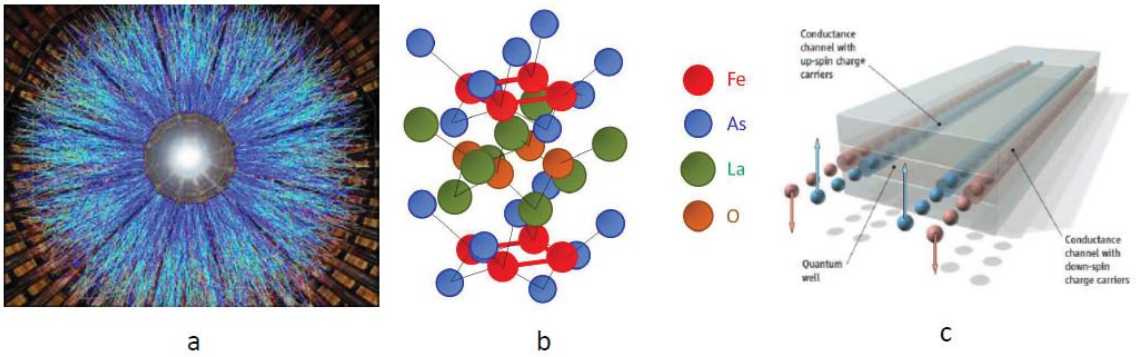

FIGURE 1.1: Fermi gases have emerged as efficient emulators of quantum matter over a variety of energy scales ranging from (a) the Quark-Gluon Plasma to layered high critical temperature cuprate and organic superconductors. In particular, quasi-two dimensional Fermi gases serve as simple model systems for understanding the principles of organization and simulating a variety of technologically relevant quantum materials such as (b) the iron pnictides and (c) quantum well matter [2].

example, electrons are confined in a quasi-2D geometry, creating complex, strongly interacting many-body systems for which the phase diagrams are not well understood [11]. Moreover, the quest for Fermi systems with even stronger correlations and unique quantum phases, spurred in part by technology's race to compactify, urges one in search of the underlying principles of organization for matter in reduced dimensions. In a Fermi gas, the dimensionality is set by the ratio of the axial confinement to the radial chemical potential; where the axial confinement far exceeds the radial chemical potential, the gas is kinematically 2D. When the axial confinement is comparable to the chemical potential, one obtains a quasi-2D gas. Further relaxation of the axial trap frequency leads to a 3D configuration.

Kinematically 2D gases pose fundamental questions in their own right, being in the marginal dimension where particle scattering can be strongly energy dependent, and quantum fluctuations [12] are large enough to destroy long-range order at any finite temperature. Here, the thermodynamic properties of strongly interacting systems are well described by the behavior of few-body clusters. In two dimensions, no true long range order exists [13, 14], but in place a meta-stable state marked by the

proliferation of vortex-anti-vortex pairs occurs. For Fermi gases in the limit of a 2D geometry, the binding energy about $p-$wave Feshbach resonances exhibits a doubly-exponential relation, dubbed a super-Efimov state [15]. The breathing modes of a quantum gas in 2D are known to reveal underlying hidden symmetries [16]. Furthermore, the tightly-confined Fermi gas has been proposed as a prime candidate in the ongoing search for alternative tabletop amplitude modes [17].

Quasi-2D quantum materials exhibit a host of behavior different from that of their three-dimensional counterparts. Ranging from layered high critical temperature superconductors, heterostructures and semimetals, superlattices and dichalcogenides, to tightly confined quantum well systems, surface states and helium-films, each material system is host to a class of phenomena unique and distinct from its counterpart [18]. From the perspective of dimensionality, such systems are intermediate between two and three dimensions; while being manifestly three dimensional in structure, their prominent layering has prompted an understanding from a two-dimensional basis [19, 20]. In composition, an overwhelmingly large proportion of these materials are non-homogeneous, exhibiting competing phases such as superconductivity and magnetism, normally thought not to coexist in conventional solid-state systems. One is invariably led to ask if there might be common themes underlying the variety of complex matter. If so, the need for a system as a basic reference and realistic simulation naturally arises.

Taken together, the spin-imbalanced quasi-two-dimensional Fermi gas serves as a testbed for a unique regime of parameter space to study fundamental notions in and for the effective simulation of a class of quantum materials. At the sweep of a radio-frequency pulse, the relative populations of two spin species are tailored at will to comb the entire polarization spectrum as the magnetic field varies the interaction strength. The basic underlying mechanism for superconductivity, pairing of fermions, can be disrupted by an unequal number of pairing species when the Fermi surfaces

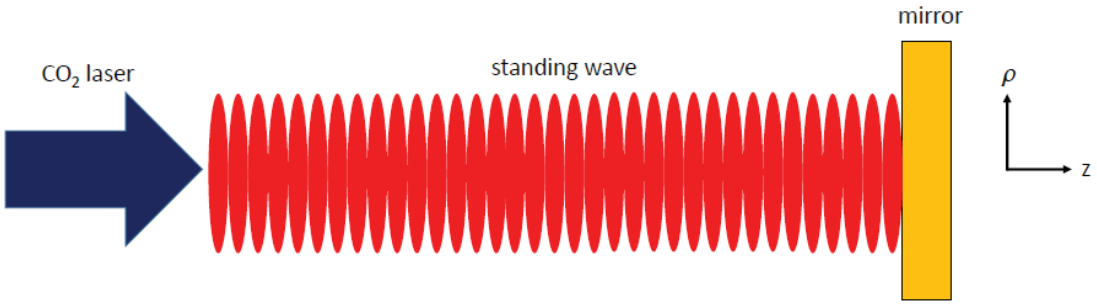

FIGURE 1.2: To set up a standing wave optical dipole trap, a polarized incoming carbon dioxide laser beam is retro-reflected on itself with a low-loss, enhanced reflectivity Copper mirror from II-VI incorporated.

of two spin components are mismatched, leading to exotic superconducting states in which pairs acquire finite momenta. Such spin-imbalanced Fermi mixtures can also contain polarons, quasiparticles formed by mobile impurities in a fermionic bath. The quantum statistics of the gas makes it a basic model for understanding the concepts of pairing, superconductivity, superfluidity, quantum magnetism, and their interplay in reduced dimensions. In undertaking the studies described in this thesis, we had hoped to develop a simple guide to aid in the predictive design of a class of next-generation quantum materials. Before proceeding further, we now turn to the issue of a quasi-2D Fermi gas as opposed to a two-dimensional one to highlight the regime of phase space we operate in.

1.2 Quasi-2D and 2D Fermi Gases

To implement a quasi-2D geometry for a Fermi gas employed in our experiments, we set up a standing wave optical dipole trap composed of an incoming carbon dioxide laser (CO_2) beam ($\lambda = 10.6\,\mu$m) and its retroreflection as shown in Figure 1.2.

The three energy scales of a quasi-2D Fermi gas are the transverse Fermi energy, $E_F = \hbar\omega_\perp\sqrt{2N}$, set by the number of atoms N (approximately 800 atoms per pancake site) and the radial trap frequency, $\omega_\perp$, the two-body binding energy, E_b,

and the trap spacing in the tightly confined axial direction $h\nu_z$. The length scales corresponding to the energy scales are respectively, the cloud Fermi radius in the radial direction, $\sigma_F = 15\,\mu$m , set by $E_F = 2m\omega_r^2\sigma_F^2$, the scattering length, a_{2D} set by $E_b = \hbar^2/ma_{2D}^2$, and the oscillator length l_z set by $l_z = \sqrt{\frac{\hbar}{m\omega_z}} = 0.5\,\mu$m in our experiments. Since the oscillator length is small compared to the 5.3 μm spacing between the antinodes of the standing wave trap, we neglect inter-site tunneling.

The ratio of the transverse Fermi energy relative to the axial energy spacing governs the dimensionality of the gas. A kinematically 2D gas is one where the axial trap spacing far exceeds the transverse Fermi energy, and all the atoms are in the axial ground state. In 3D, the tranverse $E_F \gg h\nu_z$. A quasi-2D Fermi gas, on the other hand, is one where the Fermi energy is comparable to or somewhat larger than the axial trap spacing. These scenarios are illustrated in Figure 1.3. The transverse Fermi energy determines the number of particles per axial state and can be calculated from normalization. At this point, we emphasize that for the experiments conducted in this thesis, where $E_{F\perp} = 1.5h\nu_z$, approximately 90 percent of the atoms are in the axial ground state with the remaining atoms in the first axial excited state at zero temperature. Since the interparticle spacing $l_\perp \propto n_\perp^{-1/2}$ is less than the dimer size, many-body effects feature prominently, even in the strongly interacting regime, where $E_b = 0.24h\nu_z$. In the quasi-2D gas configuration achieved in our labs, one can tune to the 3D Feshbach resonance and have the scattering mean free path comparable to the interparticle spacing, allowing atoms within the dimers to scatter off each other.

As depicted in Figure 1.3, the dimensionality of a single layer is determined by the ratio of the transverse Fermi energy E_F to the energy level spacing $h\nu_z$ in the tightly-confined z-direction. The system is two-dimensional if $E_F/h\nu_z \ll 1$ or three dimensional if $E_F/h\nu_z \gg 1$. This thesis describes experiments conducted

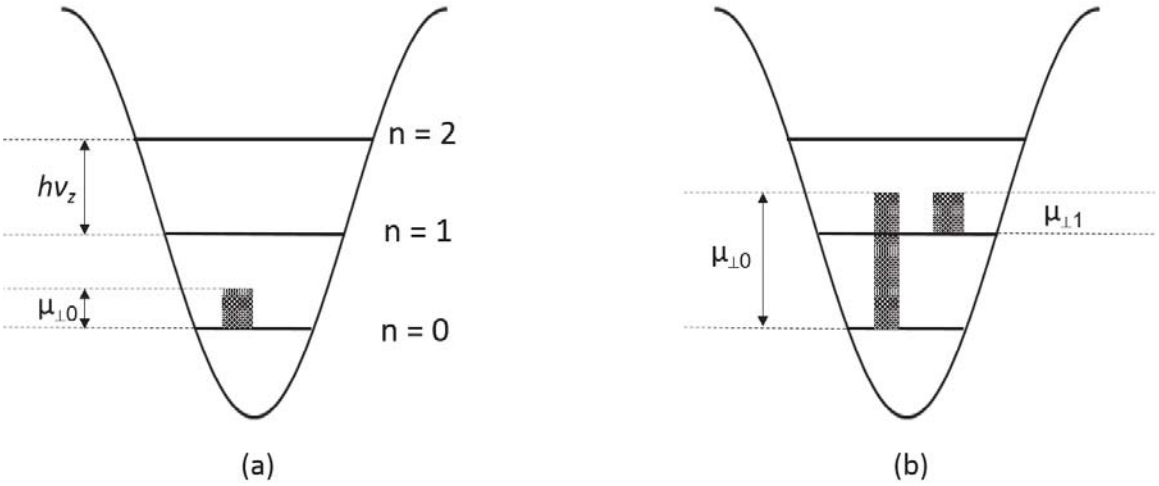

FIGURE 1.3: Distinction between a kinematically (a) 2D and (b) quasi-2D Fermi gas. In (a), the two-dimensional Fermi energy of the gas lies within the harmonic oscillator spacing, $\mu_{\perp 0} < h\nu_z$, atoms occupy only the ground state. For a quasi-2D Fermi gas as in (b), where $E_{F\perp} \geqslant h\nu_z$, more than one axial state is occupied. In the case illustrated, the chemical potential per axial state is given by $\mu_i = \mu_0 - \hbar\omega_z$. Accordingly, the number of particles per axial state is determined by number normalization, as described in Chapter Two.

in the intermediate regime where $E_F/h\nu_z \simeq 1$, where the critical temperature for pairing and superfluidity was predicted to be enhanced by relaxing the transverse confinement and perturbing away from a true 2D system. Moreover, control of the relative spin population permits precision studies of the phase diagram for these quasi-2D gases, which has been a topic of intense theoretical study [21, 22, 23, 24, 25**?** , 26].

1.3 Phase separation in spin-imbalanced Fermi gases

A macroscopic quantum phenomenon, which occurs in spin-imbalanced Fermi gases is that of phase separation; studies on spin imbalanced 3D Fermi gases [27, 28] reveal a three shell structure described by an elegant polaron model: a spin-balanced, fully-paired superfluid core is surrounded by an imbalanced normal-fluid shell, followed by a fully polarized shell. In analogy to a BCS superconductor under an applied

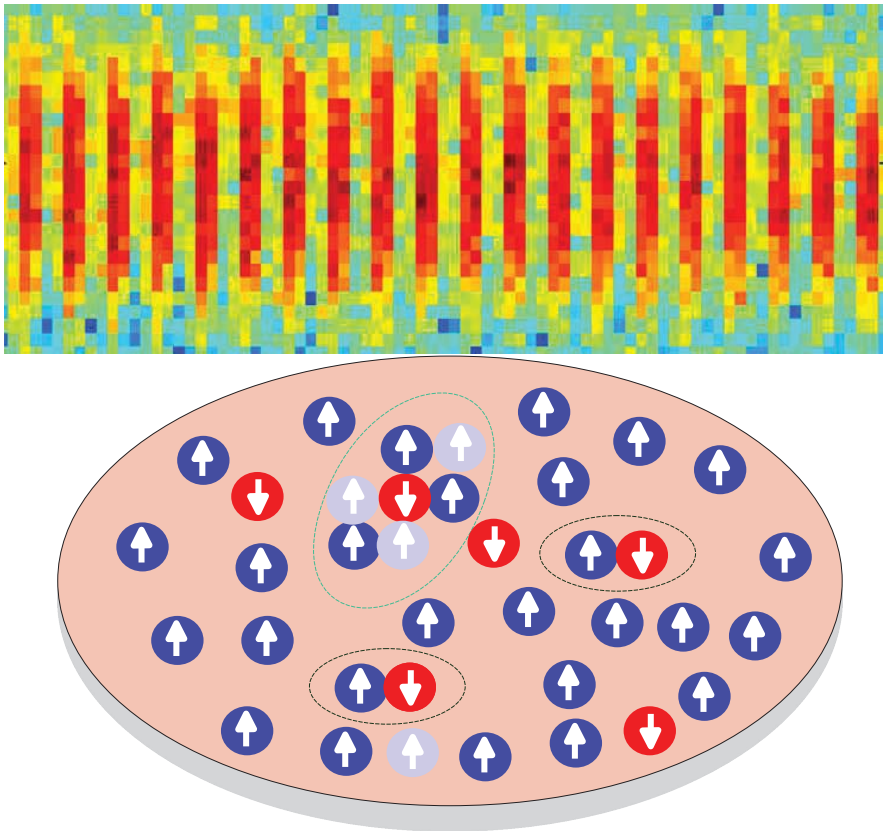

FIGURE 1.4: Top: High-resolution sideport image of layered pancake-shaped atom clouds, separated by 5.3 μm in a carbon dioxide laser standing-wave trap. Bottom: In each pancake, confinement causes majority spins (blue-up arrow) and minority spins (red-down arrow) to pair, producing bound dimers. Polarons form when minority atoms scatter in the Fermi sea of the majority atoms and become surrounded by a cloud of particle-hole pairs (dark-blue-light-blue). Tightly bound dimers also scatter, forming dressed dimers.

Zeeman magnetic field, associating the two pairing hyperfine states with up and down projections of the pseudo-spin 1/2, the density difference $\delta n = n_\uparrow - n_\downarrow$ between the two atomic states is isomorphic to an imposed magnetization $m \equiv \delta n$ with the chemical potential difference $\delta\mu = \mu_\uparrow - \mu_\downarrow$ corresponding to a pure Zeeman field $h \equiv \delta\mu/2$. In contrast to a normal Fermi liquid that exhibits Pauli paramagnetism, a conventional homogeneous BCS state at zero temperature remains unmagnetized until it is destroyed at a critical Zeeman field in a first-order transition to an unpaired

magnetized normal state [29].

In the extreme limit of spin imbalance, one obtains a single particle immersed in a quantum many-body system, the particle “”swims” shrouded by a cloud of excitations of its new environment [30]. Dubbed a polaron, this composite object has the same features as the initial particle, but with modified physical properties. To further test the robustness of pairing in light of polarisation, and the energetic stability of the intermediate phase, one of the groups [31] realised the Fermi polaron scenario by immersing a spin-down atom into a sea of spin-up atoms, and measured the influence of the Fermi sea on the energy of the impurity.

In a study on an array of one-dimensional tubes [32], the behavior of phase separation is dramatically reversed; a balanced phase appears outside a spin-imbalanced core, in agreement with a mean-field (Bethe ansatz) model. The 1D spin-imbalanced attractively interacting Fermi gas was described by the Gaudin-Yang model, and a Thomas-Fermi approximation with variable chemical potential was used to calculate density profiles. In both 1D and 3D cases, efforts are still ongoing for a direct observation of the elusive Fulde-Ferrell-Larkin-Ovchinnikov (FFLO) phase [33, 34].

A natural question that arises is then how the phase diagram of a quasi-two-dimensional cloud, containing a spin-imbalanced Fermi gas, differs from those measured in one and three dimensions. Does phase separation occur? If so, what separates? Unlike a 3D gas in free space, a two-dimensional (2D) gas naturally contains confinement-induced bound dimers. The binding energy of these dimers, $E_b \geqslant 0$, sets the natural scale for scattering interactions in 2D systems [35, 36, 37]. 2D polarons [38] also may be important for a quasi-2D Fermi gas [39]. The phase diagram for imbalanced mixtures in this regime is therefore likely to be very rich [40, 41, 42], involving the interplay and phase separation of several components including dimer gases, polaron gases, and spin-imbalanced normal fluids, as shown in Figure 1.4. Exotic components with spatially modulated superfluids (FFLO states) and vortex-

anti-vortex pairs (Berezinskii-Kosterlitz-Thouless [43, 44] states) also have been predicted for 2D and quasi-2D Fermi gases.

As depicted in Figure 1.3, the dimensionality of a single layer is determined by the ratio of the transverse Fermi energy E_F to the energy level spacing $h\nu_z$ in the tightly-confined z-direction. The system is two-dimensional if $E_F/h\nu_z \ll 1$ or three dimensional if $E_F/h\nu_z \gg 1$. This thesis describes experiments conducted in the intermediate regime where $E_F/h\nu_z \simeq 1$, where the critical temperature for pairing and superfluidity was predicted to be enhanced by relaxing the transverse confinement and perturbing away from a true 2D system. Moreover, control of the relative spin population permits precision studies of the phase diagram for these quasi-2D gases, which has been a topic of intense theoretical study.

1.4 Manipulating the internal states of ^{6}Li

The alkali metal employed in our laboratories for atom cooling and trapping experiments is an isotope of lithium, ^{6}Li. An atom of ^{6}Li is composed of 3 protons, 3 neutrons, and 3 electrons, yielding an overall charge neutral atom. The nuclear ground state has nuclear spin $I = 1$, while the electronic ground state consists of 2 electrons in the 1s orbital and a third, unpaired electron in the 2s orbital. The total angular momentum quantum number F arises from the sum of nuclear, orbital, and electron spins. In the electronic ground state, ($I = 1$, $L = 0$, and $S = 1/2$), angular momentum addition yields two possible values for the total angular momentum, F=3/2 and F=1/2.

1.4.1 Hyperfine states of ^{6}Li

The fine structure of ^{6}Li arises from the magnetic dipole interaction between the electronic spin angular momentum, $\mathbf{S}$, and the orbital angular momentum, $\mathbf{L}$, resulting in a total angular momentum of $\mathbf{J} = \mathbf{L} + \mathbf{S}$. This interaction results in a splitting

of the 2P excited state and two from the ground state transitions into D_1 and D_2 lines indicated in Figure 1.5. In Russell-Saunders notation, the lines correspond to the $2^2S_{1/2} \rightarrow 2^2P_{1/2}$ and $2^2S_{1/2} \rightarrow 2^2P_{3/2}$ transitions, respectively.

Hyperfine splitting of the ground and excited states arises from the interaction between the valence electron and the magnetic and quadrupole moments of the non-spherically symmetric nucleus. The Hamiltonian of the hyperfine interaction includes both the nuclear magnetic dipole and nuclear electric quadrupole interactions. In the absence of a magnetic field, the total angular momentum $F = I + S$ is conserved and the F=1/2 manifold of the ground state is two-fold degenerate, with spin projections $m_F = \pm 1/2$, while the F=3/2 manifold of the ground state is four-fold degenerate, with spin projections $m_F = \pm 3/2$, $m_F = \pm 1/2$.

1.4.2 Zeeman splitting in an external B-field

The application of an external magnetic field lifts this degeneracy, resulting in six distinct eigenstates given by the solution to the Breit-Rabi equation

$$H_{int} = \frac{a_{hf}}{\hbar^2}\mathbf{S}\cdot\mathbf{I} + \frac{\mu_B}{\hbar}\left(g_J^{gnd}\mathbf{S} + g_I\mathbf{I}\right)\cdot\mathbf{B}, \tag{1.1}$$

where a_{hf}/h=152.137 MHz is the magnetic dipole constant and g_J^{gnd}=2.002 is the total electronic g-factor for the ^{6}Li ground state, g_I=-0.000448 is the total nuclear g-factor, μ_B is the Bohr magneton, and B is the external applied magnetic field.

Using the basis kets $|m_S\, m_I\rangle$, with m_S and m_I denoting the electronic spin projection and nuclear spin projection respectively, the eigenstates of equation (1.1) are:

$$|1\rangle = \sin\Theta_+ \left|\frac{1}{2}\quad 0\right\rangle - \cos\Theta_+ \left|-\frac{1}{2}\quad 1\right\rangle \tag{1.2}$$

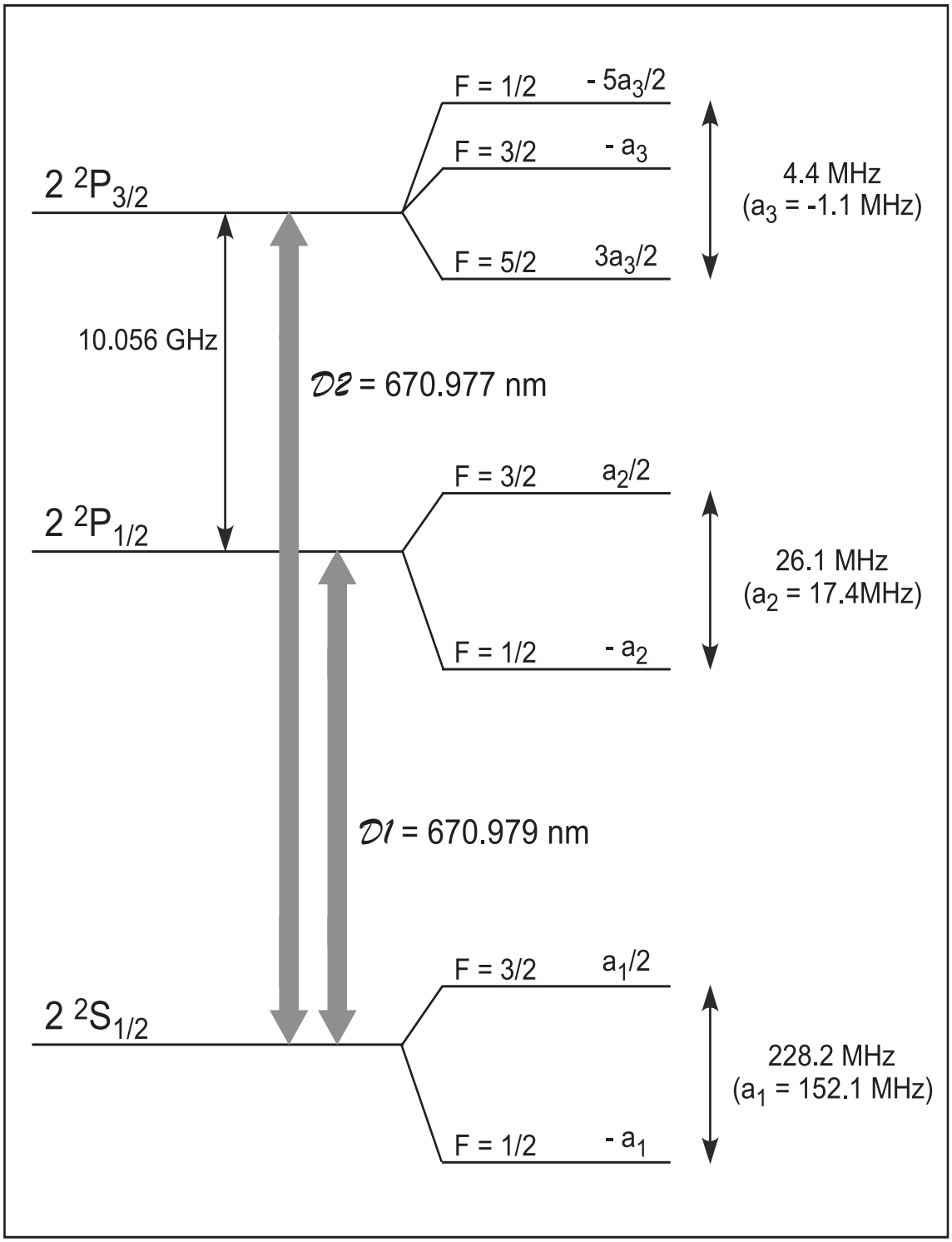

FIGURE 1.5: Fine structure and hyperfine structure of ^{6}Li. The intraatomic interactions responsible for the splittings are explained in the main text.

$$|2\rangle = \sin\Theta_- \left|\frac{1}{2} \quad -1\right\rangle - \cos\Theta_- \left|-\frac{1}{2} \quad 0\right\rangle \tag{1.3}$$

$$|3\rangle = \sin\Theta_- \left|-\frac{1}{2} \quad -1\right\rangle \tag{1.4}$$

$$|4\rangle = \cos\Theta_- \left|\frac{1}{2} \quad -1\right\rangle + \sin\Theta_- \left|-\frac{1}{2} \quad 0\right\rangle \tag{1.5}$$

$$|5\rangle = \cos\Theta_+ \left|\frac{1}{2} \quad 0\right\rangle + \sin\Theta_+ \left|-\frac{1}{2} \quad 1\right\rangle \tag{1.6}$$

$$|6\rangle = \cos\Theta_+ \left|\frac{1}{2} \quad 1\right\rangle \tag{1.7}$$

where the coefficients $\sin\Theta_\pm$ and $\cos\Theta_\pm$ are magnetic field dependent and obey the relations

$$\sin\Theta_\pm = \frac{1}{\sqrt{1 + (Z^\pm + R^\pm)^2/2}} \tag{1.8}$$

$$\cos\Theta_\pm = \sqrt{1 - \sin^2\Theta_\pm} \tag{1.9}$$

$$Z^\pm = \frac{\mu_B B}{a_{hf}}(g_J^{gnd} - g_I) \pm \frac{1}{2} \tag{1.10}$$

$$R^\pm = \sqrt{(Z^\pm)^2 + 2} \tag{1.11}$$

The energy eigenvalues E_n associated with the eigenstates n are

$$E_1 = -\frac{1}{4}\left(a_{hf} - 2g_I\mu_B B + 2a_{hf}R^+\right) \tag{1.12}$$

$$E_2 = -\frac{1}{4}\left(a_{hf} + 2g_I\mu_B B + 2a_{hf}R^-\right) \tag{1.13}$$

$$E_3 = \frac{a_{hf}}{2} - \frac{\mu_B B}{2}\left(2g_I + g_J^{gnd}\right) \tag{1.14}$$

$$E_4 = \frac{1}{4}\left(-a_{hf} - 2g_I\mu_B B + 2a_{hf}R^-\right) \tag{1.15}$$

$$E_5 = \frac{1}{4}\left(-a_{hf} + 2g_I\mu_B B + 2a_{hf}R^+\right) \tag{1.16}$$

$$E_6 = \frac{a_{hf}}{2} + \frac{\mu_B B}{2}\left(2g_I + g_J^{gnd}\right) \tag{1.17}$$

The hyperfine energy eigenvalues of the ^{6}Li ground state are plotted in frequency units versus applied magnetic field in Gauss in Figure 1.6. As the magnetic field increases, the original degenerate states split into six different states, with approximately linear hyperfine energy shifts of -1.4 MHz / G for the three lowest states. The energy differences between energy levels correspond to resonant radiofrequency transitions which we could drive for the purposes of magnetic field calibration as well as a microscopic probe of pairing interactions.

In a two-component Fermi gas, the $|1\rangle$ state has total angular momentum spin projection $m_F = \frac{1}{2}$ and the $|2\rangle$ state has $m_F = -\frac{1}{2}$. By considering equations (1.10) and (1.11), we see that $\cos\Theta_\pm$ becomes very close to unity at magnetic fields higher than 300 G. Hence, when we discuss a two-component mixture of the three lowest hyperfine states at high magnetic fields, typically greater than 700 G, we are considering a mixture of atoms which is very nearly electron-spin polarized, interacting via a triplet electronic potential.

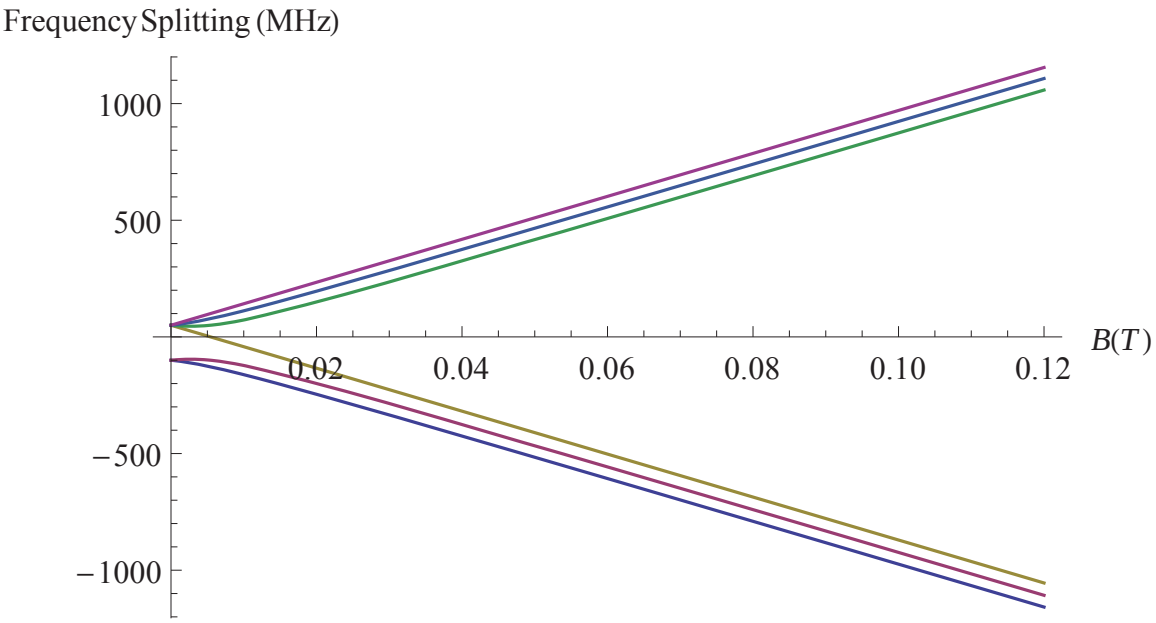

FIGURE 1.6: Zeeman splitting of the hyperfine energy eigenvalues of the ^{6}Li ground state in frequency units versus applied magnetic field in 10^4 Gauss. Eigenstates are labelled in order of increasing energy.

In the ground state of ^{6}Li, the total angular momentum spin projection $m_F = m_S + m_I$ is conserved for $s-$wave collisions. Close to zero magnetic field, a collision between atoms in the $|1\rangle$ and $|4\rangle$ states releases a total energy of approximately $h\times$ 228 MHz, or 10 mK. However, since the starting temperatures for our experiments are approximately 100 nK after evaporative cooling, an approximately $|1\rangle$-$|2\rangle$ mixture is an energetically stable combination of states, where the higher states are not occupied.

1.5 Magnetically tunable interactions in Fermi Gases

A handy and crucial experimental knob employed in a large number of atomic physics experiments is that of a Feshbach resonance. At the sweep of a magnetic field, the energy of a closed, diatomic molecular bound state can be Zeeman tuned relative to the open-channel atomic continuum, providing an unprecedented level of interaction con-

Table 1.1: Feshbach resonances of ^{6}Li. The first column indicates the incoming scattering channel, the second column lists the partial wave, l. This is followed by the resonance B-field location, the width Δ, the background scattering length a_{bg}, and the differential magnetic moment $\delta\mu$ in units of the Bohr magneton μ_0 [1].

Scattering Channel	l	**B (G)**	$\Delta(G)$	a_{bg}/a_0	$\delta\mu/\mu_B$
(1-2)	s	832.2	-300	-1405	2.0
(1-3)	s	690.4	-122.3	-1727	2.0
(2-3)	s	811.2	-222.3	-1490	2.0
(1-2)	s	543.25	0.1	60	2.0
(1-1)	p	159.14	na	na	2.0
(1-2)	p	185.09	na	na	2.0
(2-2)	p	214.94	na	na	2.0

trol, limited only by magnetic field range and stability [45]. In the context of Fermi gases in a three-dimensional geometry, this had led to several studies scanning the fermionic pairing spectrum between the Fermi-surface momentum pairing regime of weakly interacting Cooper pairs to the coordinate space pairing regime of condensed diatomic molecules, both within our group and elsewhere. The atomic species used in our labs, ^{6}Li, has s- and p-wave Feshbach resonances; Table I provides values of the resonance locations, resonance widths, and background scattering lengths for reference. Due to the fermionic nature of ^{6} Li, even-state ($l = 0, 2, 4, ...$) scattering occurs only between non-identical hyperfine states. The experiments described in this thesis are conducted about the broad s-wave Feshbach resonance centered at 832.2 G [46], to which we now turn our attention.

The lithium atoms in the different hyperfine spin states of $|1\rangle$ and $|2\rangle$ interact via either a singlet or triplet molecular potential for s-wave scattering. Antisymmetry of the overall fermion (two-atom) wavefunction implies one of two cases: (i) a symmetric spatial wavefunction and anti-symmetric spin wavefunction or (ii) an antisymmetric spatial wavefunction and a symmetric spin wavefunction. A symmetric

spatial wavefunction allows for a finite electron density between paired atoms, effectively shielding the nuclei of the component atoms from repulsive forces. This results in the singlet potential being much deeper than the triplet potential. As shown in Figure 1.6, the application of an external magnetic field allows the energy of colliding atoms, unbound in the triplet state, to be tuned to degeneracy with a bound state in the singlet potential. The triplet potential is usually termed the "open channel" while the singlet potential is the "closed channel". The difference, $\delta\mu$, between the magnetic moments of the separated atoms and that of the bare bound state results in a magnetically tunable energy detuning of the form

$$\hbar\Delta E = \delta\mu(B - B_c) \tag{1.18}$$

where $\hbar\Delta E$ is zero at a magnetic field equal to B_c.

The broad Feshbach resonance can be calculated from parameters of the singlet and triplet potentials, which are determined by radio-frequency spectroscopy of weakly bound ^{6}Li molecules. The Feshbach resonance is parametrized as a function of magnetic field by [47]

$$a_s(B) = a_{bg}\left(1 + \frac{\Delta}{B - B_0}\right)(1 + \alpha\,(B - B_0)) \tag{1.19}$$

where $a_{bg} = -1405\,a_0$, is the off-resonant background scattering length associated with the last-bound ($\nu = 38$) vibrational level of the open channel and a_0 is the Bohr radius. The scattering length diverges ($a \to \pm\infty$) at the resonance field $B_0 = 832.149\,G$ [47], with a resonance width of $\Delta = 300$ G. The first-order correction parameter is $\alpha = 0.00040\ \mathrm{G}^{-1}$. More recently, precision studies on spin segregation in our group have narrowed the zero crossing of the scattering length to be 527.5 ± 0.2 G [48]. Near the Feshbach resonance, the scattering length a_s is much larger than the average interparticle spacing, l, between ^{6}Li atoms at our trap densities. Thus, the

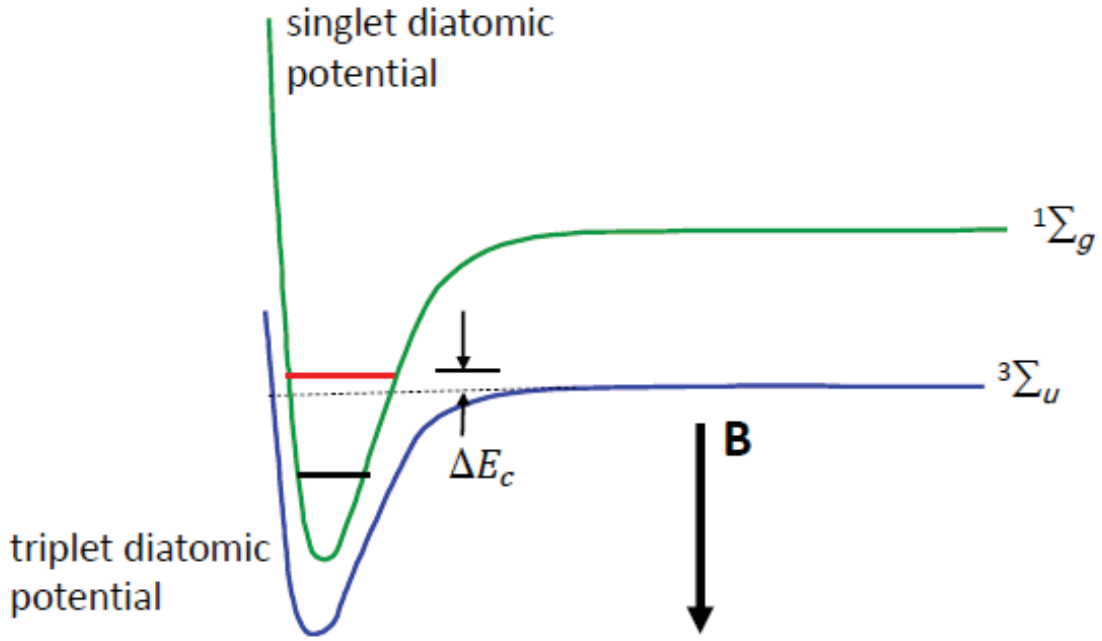

FIGURE 1.7: Pictorial representation of a Feshbach resonance. Application of an external magnetic field Zeeman tunes the triplet potential (blue curve) relative to the singlet potential (green curve). On resonance, the topmost $\nu = 38$ bound molecular state of the singlet potential (shown as a red line) is degenerate with the energy of two colliding atoms in the singlet channel.

diverging scattering length and potential range, R_0, satisfy

$$a_s \longrightarrow \infty >> l >> R_0 \longrightarrow 0 \tag{1.20}$$

This condition ensures that the local macroscopic behavior of such systems at resonance $B = B_0$ only depends on the local density and temperature.

1.6 Thesis outline

This thesis presents investigations on a spin-imbalanced quasi-two dimensional Fermi gas of ^{6}Li, where the ratio of the ideal gas transverse Fermi energy $E_{F\perp}$ to the energy level spacing $h\nu_z$ of the tightly confining potential is held nominally constant, with $E_{F\perp} \simeq 1.5h\nu_z$. In this regime, the system is not strictly 2D, but is far from 3D, as

at most the first few oscillator states are relevant for many-body predictions.

In this chapter, we have provided a brief introduction to the rapidly evolving field of Fermi gases, and their application in quantum simulation. This was followed by a general discussion of spin-imbalanced Fermi gases, and an introduction to the alkali metal employed for our experiments, ^{6}Li, its electronic ground state and hyperfine levels that arise in an external magnetic field, and the Feshbach resonances of the atomic species. We introduced the length and energy scales that provide the distinction between a kinematically two-dimensional gas, and the quasi-two-dimensional regime we work in, where the Fermi energy of the gas is comparable to the axial energy level spacing.

Chapter 2 covers the basic properties of the non-interacting Fermi gas in two and three dimensions, in particular the local and global thermodynamic quantities, which set the scales for our measurements. We present a temperature calibration for spin-imbalanced samples.

In Chapter 3, we proceed to investigate the physics of bound states, and two-body and many-body physics in a two-dimensional gas. In particular, we discuss the binding energy of 2D dimers, and provide some predictions of 2D Bardeen-Cooper-Schrieffer (BCS) theory. A previous radio-frequency spectroscopy experiment conducted by our group [39] which highlighted the inadequacies of mean-field theory will be described, followed by a comparison of results with the noninteracting Fermi gas in 2D and 2D BCS theory. This will be followed by a non-interacting 2D-polaron picture which neatly explains the spectral shifts in the radio-frequency spectra.

The reader interested in experimental details of the experiment, notably the optical set-up for the production of a Fermi gas, high-resolution imaging, rapid sequential pulse sequencing, the preparation of a spin-imbalanced mixture, magnetic field calibration will find more detail in Chapter 4. Inspired by the success of the polaron picture of the rf spectra for a quasi-2D Fermi gas in Chapter 3, we develop the ther-

modynamics of the polaron model in Chapter 5; from a simple two-fluid model, we derive theoretical radii, and densities for both spin-imbalanced and spin-balanced 2D Fermi gases. This will be followed by a detailed comparison of the 2D polaron model to data obtained for a range of magnetic fields in Chapter 6; the failure of the 2D polaron model, in particular the observed transition to a spin-balanced core above a critical polarisation is presented as well.

We then conclude this thesis in Chapter 7 with a summary and an outlook for future work.

2

Ideal 2D and 3D Fermi Gases

A great deal of the concepts employed in studying the thermodynamics of strongly interacting Fermi gases relies on our knowledge of non-interacting gases. In a cold atom experiment, both extremes of interaction are easily accessible with the sweep of a magnetic field. The first part of this chapter describes from first principles the thermodynamics of ideal 3D and 2D Fermi gases in a harmonic trap. These serve as a point of reference in spectroscopic and thermodynamic studies where measured column densities are fit to theoretical profiles to extract the atom number and mean square cloud size in thermal and quantum degenerate regimes. Moreover, since the polaron description we adopt to describe a quasi-2D Fermi gas is essentially a system of two ideal interpenetrating two-dimensional gases with a polaron energy density term to account for interparticle scattering, an understanding of thermodynamic contributions from ideal gases is relevant.

In this chapter, we will derive expressions for the density of states of harmonically trapped two- and three- dimensional [49] gases, which then allows us to obtain simple expressions for the number of atoms and the Fermi energy. To highlight an application of the thermodynamic concepts introduced, we present an approximate

temperature measurement scheme for interacting gases relying on non-interacting Fermi gas results at the end of the chapter. We use this method to calibrate the temperature of our strongly interacting quasi-2D Fermi gases for the experiments described in Chapters 5 and 6.

Throughout this treatment, we assume that the local density approximation (LDA) is valid, i.e., that the trapping potential varies smoothly and slowly enough and that a small volume of the trapped atom cloud contains enough atoms for it to be approximated by a locally homogeneous Fermi system. It should be noted that while these approximations will break down at the edges of the clouds, much of our experimental work supports the validity of the LDA for our trap conditions.

2.1 Local thermodynamic quantities of an ideal 3D Fermi gas

We recall that the Fermi occupation number for an orbital with energy ϵ is given by the Fermi-Dirac distribution

$$f(\epsilon, \mu, T) = \frac{1}{1 + \exp\left(\frac{\epsilon - \mu}{k_B T}\right)}, \tag{2.1}$$

where ϵ is the energy of an orbital, μ is the chemical potential, k_B is Boltzmann's constant and T is the temperature. An interacting Fermi gas is altered relative to a classical gas at the same temperature due to the Pauli exclusion principle, inherent in equation (2.1). Consider N identical fermions of mass m in a general anisotropic trap, with a single-particle Hamiltonian

$$H(\mathbf{r}, p) = \frac{1}{2M}\left[p_x^2 + p_y^2 + p_z^2\right] + \frac{M\omega_x^2}{2}x^2 + \frac{M\omega_y^2}{2}y^2 + \frac{M\omega_z^2}{2}z^2 \tag{2.2}$$

where ω_x, ω_y are the trap frequencies in the radial direction and ω_z is the trap frequency in the axial direction.

2.1.1 Ideal 3D Fermi Gas at Zero Temperature

As the density profile of the trapped Fermi gas can be considered as a continuous distribution, we begin by deriving an expression for the density of states for a harmonically trapped gas. The discrete energy eigenvalues for a three-dimensional harmonic oscillator are given by

$$\epsilon = \hbar \left[\omega_x \left(n_x + \frac{1}{2} \right) + \omega_y \left(n_y + \frac{1}{2} \right) + \omega_z \left(n_z + \frac{1}{2} \right) \right]. \tag{2.3}$$

Here, the n_i take on nonnegative integer values, and the ω_i denote trap frequencies in the $i = x, y, z$ directions . If we suppress the zero-point energy factors of $1/2$ in (2.3), we have

$$\epsilon = \hbar \left(\omega_x n_x + \omega_y n_y + \omega_z n_z \right). \tag{2.4}$$

The total number of states is given by the three-dimensional volume Ω in eigenenergy space

$$\Omega = \frac{1}{3} \times n_z^{max} \times \left(\frac{1}{2} n_x^{max} \times n_y^{max} \right), \tag{2.5}$$

with the n_i^{max} factors representing the values where $n_j^{max} = n_k^{max} = 0$ and vice-versa. From (2.4), we see that

$$n_i^{max} = \frac{\epsilon}{\hbar \omega_i}. \tag{2.6}$$

Substituting (2.29) into (2.5) we obtain

$$V_{DOS} = \frac{\epsilon^3}{6(\hbar \bar{\omega})^3}, \tag{2.7}$$

where the geometric mean of the trap oscillation frequencies is given by $\bar{\omega} = (\omega_x \omega_y \omega_z)^{1/3}$. Taking the derivative of (2.7) with respect to energy yields the three-dimensional density-of-states for a harmonic trap

$$g(\epsilon) = \frac{\epsilon^2}{2(\hbar\bar{\omega})^3}. \tag{2.8}$$

We proceed to determine the atom number and Fermi energy. Denoting by $N_\uparrow$ the total number of particles per spin state in a two-component Fermi gas, we obtain by number normalization

$$N_\uparrow = \int_0^\infty g(\epsilon) f(\epsilon) d\epsilon, \tag{2.9}$$

which leads, in a three-dimensional harmonic trap, to

$$N_\uparrow = \frac{1}{2(\hbar\bar{\omega})^3} \int_0^\infty \frac{\epsilon^2 d\epsilon}{\exp\left(\frac{\epsilon-\mu}{k_B T}\right) + 1}. \tag{2.10}$$

At zero temperature, the Fermi occupation number becomes unity for all energy levels below the Fermi energy ϵ_F and 0 for all energy levels above the Fermi energy. Equation (2.10) then simplifies to

$$N_\uparrow = \frac{1}{2(\hbar\bar{\omega})^3} \int_0^{\epsilon_F} \epsilon^2 d\epsilon = \frac{\epsilon_F^3}{6(\hbar\omega_\perp)^3}. \tag{2.11}$$

Upon rearrangement, the Fermi energy for a noninteracting Fermi gas in a 3D harmonic trap with $N_\uparrow$ particles per spin state is seen to be

$$\epsilon_F = (6N_\uparrow)^{1/3} \hbar\bar{\omega}, \tag{2.12}$$

with a corresponding Fermi temperature

$$T_F = \frac{\epsilon_F}{k_B} = \frac{(6N_\uparrow)^{1/3} \hbar\bar{\omega}}{k_B}. \tag{2.13}$$

The Thomas-Fermi radius of a three-dimensional ideal trapped gas, R_{TF}

$$R_{TF} = \sqrt{\frac{2E_F}{M\omega_r^2}} = (48N_\uparrow)^{1/6}\bar{\sigma}, \tag{2.14}$$

where $\bar{\sigma} = (\hbar/M\omega_r)^{1/2}$ is the radial width of the Gaussian ground state of the trap.

To determine the average energy per particle for a harmonically confined Fermi gas, we note that

$$E(T) = \int_0^\infty \epsilon g(\epsilon) f(\epsilon) d\epsilon. \tag{2.15}$$

Using (2.8) in (2.38) for the density of states in three dimensions,

$$E(T) = \frac{1}{2(\hbar\bar{\omega})^3} \int_0^\infty \frac{\epsilon^3 d\epsilon}{\exp\left(\frac{\epsilon-\mu}{k_B T}\right) + 1}. \tag{2.16}$$

Similar to our derivation of equation (2.39) for a gas at zero temperature,

$$E(0) = \frac{\epsilon_F^4}{8(\hbar\bar{\omega})^3}. \tag{2.17}$$

Hence, the energy per particle is seen to be

$$\frac{E(0)}{N_\uparrow} = \frac{3}{4}\epsilon_F. \tag{2.18}$$

2.1.2 3D Spatial Distribution at Zero Temperature

In the local density approximation, the total number of states, dN , is given by the box normalization condition

$$dN_\uparrow = \frac{dV}{(2\pi)^3} d^3\mathbf{k}. \tag{2.19}$$

Taking an integral over momentum space on both sides of equation (2.19) up to the Fermi wavevector

$$\Delta N_\uparrow = \frac{\Delta V}{(2\pi)^3}\int_0^{k_F} 4\pi k^2 dk. \tag{2.20}$$

The local density is thus seen to be

$$n_\uparrow = \frac{\Delta N_\uparrow}{\Delta V} = \frac{k_F^3}{6\pi^2}. \tag{2.21}$$

Rearranging equation (2.44) gives the local Fermi wavevector

$$k_F = \left(6\pi^2 n\right)^{1/3}, \tag{2.22}$$

where we recall that the local Fermi energy is given by $\epsilon_F(r) = \frac{\hbar^2 k_F(r)^2}{2m}$. By energy conservation,

$$\epsilon_F(\mathbf{r}) = \epsilon_F(0) - U(\mathbf{r}) = \epsilon_F(0)\left[1 - \frac{U(\mathbf{r})}{\epsilon_F(0)}\right]. \tag{2.23}$$

Equating the trap potential $\frac{1}{2}m\omega_i^2\sigma_i^2$ to the Fermi energy at the trap center, $\epsilon_F(0)$, we obtain $\sigma_i^2 = \frac{2\epsilon_F(0)}{m\omega_i^2}$. The local Fermi energy can then be written as

$$\frac{\hbar^2 k_F^2}{2m} = \epsilon_F(0)\left[1 - \frac{\tilde{r}^2}{\sigma^2}\right]. \tag{2.24}$$

where $\tilde{r}^2 = \sqrt{x^2 + y^2}$. Thus, it can be seen that the local density n is

$$n = \frac{1}{6\pi^2}\left(\frac{2m\epsilon_F(0)}{\hbar^2}\right)^{3/2}\left(1 - \frac{\tilde{r}^2}{\sigma^2}\right)^{3/2}. \tag{2.25}$$

2.2 Local thermodynamic quantities of an ideal 2D Fermi gas

In the experimentally relevant scenario of a tightly-confining standing wave dipole trap, where $\omega_z \gg \omega_x, \omega_y$, the axial degrees of freedom are frozen out, all atoms

are in the ground axial state and particle motion is restricted to the radial plane. A convenient two-dimensional basis results if one neglects the axial (z) degree of freedom in equation (2.2).

The energy eigenvalues for a two-dimensional harmonic oscillator with trap oscillation frequencies ω_i, for $i = x, y$ are given by

$$\epsilon = \hbar \left[\omega_x \left(n_x + \frac{1}{2} \right) + \omega_y \left(n_y + \frac{1}{2} \right) \right]. \tag{2.26}$$

Here, the n_i take on nonnegative integer values. If we suppress the zero point energy factors of 1/2 in (2.26), we have

$$\epsilon = \hbar \left(\omega_x n_x + \omega_y n_y \right). \tag{2.27}$$

The total number of states is given by the area Ω in eigenenergy space, where

$$\Omega = \frac{1}{2} \times n_x^{max} \times n_y^{max}, \tag{2.28}$$

with n_x^{max} as the coordinate value where $n_y^{max} = 0$ and vice-versa. From (2.27), we see that

$$n_x^{max} = \frac{\epsilon}{\hbar \omega_x} \; ; \; n_y^{max} = \frac{\epsilon}{\hbar \omega_y}. \tag{2.29}$$

Substituting (2.29) into (2.28) we obtain

$$\Omega_{DOS} = \frac{\epsilon^2}{2(\hbar \omega_\perp)^2}. \tag{2.30}$$

We note that $\omega_\perp = \sqrt{\omega_x \omega_y}$. Taking the derivative of (2.31) with respect to energy yields the two-dimensional density-of-states for a harmonic trap

$$g(\epsilon) = \frac{\epsilon}{(\hbar \omega_\perp)^2}. \tag{2.31}$$

2.2.1 Ideal 2D Fermi Gas at Zero Temperature

Denoting by N the total number of particles per spin state in a two-component Fermi gas, we obtain by number normalization

$$N_\uparrow = \int_0^\infty g(\epsilon) f(\epsilon) d\epsilon, \tag{2.32}$$

which leads, in a two-dimensional harmonic trap, to

$$N_\uparrow = \frac{1}{(\hbar\omega_\perp)^2} \int_0^\infty \frac{\epsilon d\epsilon}{\exp\left(\frac{\epsilon-\mu}{k_B T}\right) + 1}. \tag{2.33}$$

At zero temperature, the Fermi occupation number becomes unity for all energy levels below the Fermi energy ϵ_F and 0 for all energy levels above the Fermi energy. Equation (2.33) then simplifies to

$$N_\uparrow = \frac{1}{(\hbar\omega_\perp)^2} \int_0^{\epsilon_F} \epsilon d\epsilon = \frac{\epsilon_F^2}{2(\hbar\omega_\perp)^2}. \tag{2.34}$$

Upon rearrangement, the Fermi energy for a noninteracting Fermi gas in a 2D harmonic trap with N particles per spin state is seen to be

$$E_F = \hbar\omega_\perp \sqrt{2N_\uparrow}, \tag{2.35}$$

with a corresponding Fermi temperature

$$T_F = \frac{E_F}{k_B} = \frac{\hbar\omega_\perp \sqrt{2N}}{k_B}. \tag{2.36}$$

The excursion of a particle with total energy E_F in the trap potential sets the characteristic size of the ideal trapped gas, which we denote by the Thomas-Fermi radius, R_{TF}, where $\frac{1}{2} M\omega_\perp^2 R_{TF}^2 = E_F$ implies

$$R_{TF} = \sqrt{\frac{2E_F}{M\omega_r^2}} = (8N)^{1/4}\sigma_r, \tag{2.37}$$

where $\sigma_r = (\hbar/M\omega_r)^{1/2}$ is the radial width of the Gaussian ground state of the trap. For large N, the width of the degenerate Fermi cloud is much greater than the quantum length σ_r, and the Fermi energy is much greater than the level spacing of the trap due to the Pauli repulsion between fermions.

To determine the average energy per particle for a harmonically confined Fermi gas, we note that

$$E(T) = \int_0^\infty \epsilon g(\epsilon) f(\epsilon) d\epsilon. \tag{2.38}$$

Using (2.33) in (2.38) for the density of states in two dimensions,

$$E(T) = \frac{1}{(\hbar\omega_\perp)^2} \int_0^\infty \frac{\epsilon^2 d\epsilon}{\exp\left(\frac{\epsilon-\mu}{k_B T}\right) + 1}. \tag{2.39}$$

Similar to our derivation of equation (2.39) for a gas at zero temperature,

$$E(0) = \frac{E_F^3}{3(\hbar\omega_\perp)^2}. \tag{2.40}$$

Hence, the energy per particle is seen to be

$$\frac{E(0)}{N_\uparrow} = \frac{2}{3} E_F. \tag{2.41}$$

To provide the reader with a sense of temperature and length scales involved, we note that for the experiments, with approximately 800 atoms per trap at a temperature of $T/T_F < 0.21$ and with harmonic oscillation frequencies $\omega_\perp = 2\pi \times 440$ Hz and $\omega_z = 2\pi \times 9.0$ kHz , we obtain an axial energy level trap spacing of $h\nu_z = 0.43\,\mu$K , a Fermi energy of $0.85\,\mu$K, and a Thomas-Fermi radius of $R_{TF} = 17.5\,\mu$m.

2.2.2 2D Spatial Distribution at Zero Temperature

At zero temperature in a two-dimensional trap, we may define a "local" Fermi wavenumber $k_f(r)$ by

$$\frac{\hbar^2 k_F^2}{2M} + V(r) = E_F, \tag{2.42}$$

where $V(r)$ is the trap potential. The number of quantum states in an area $L^2 d^2\mathbf{k}$ of phase space is

$$dN = \frac{L^2 d^2\mathbf{k}}{(2\pi)^2}. \tag{2.43}$$

Integrating both sides of this equation results in the local density $n_\perp(r) = \frac{N}{L^2}$

$$n(r) = \frac{\int_0^{k_F(r)} 2\pi k dk}{(2\pi)^2} = \frac{k_F^2(r)}{4\pi}. \tag{2.44}$$

Using the LDA, equation (2.42) takes the form

$$\epsilon_F(r) + U(r) = \epsilon_F(0), \tag{2.45}$$

where the local chemical potential $\epsilon_F(r) = \frac{\hbar^2 k_F^2(r)}{2M}$ leads to

$$\epsilon_F(r) = \frac{2\pi\hbar^2}{m} n_\perp(r). \tag{2.46}$$

In equation (2.45), $U(r) = \frac{1}{2}mw_x^2 + \frac{1}{2}mw_y^2$ the trap potential and $\epsilon_F(0)$ the chemical potential at the center of the trap. On rearranging terms in equation (2.45), one obtains

$$\epsilon_F(r) = \epsilon_F(0)\left[1 - \frac{U(r)}{\epsilon_F(0)}\right], \tag{2.47}$$

or alternatively,

$$\frac{\hbar^2 k_F^2}{2m} = \epsilon_F(0)\left[1 - \frac{x^2}{\sigma_x^2} - \frac{y^2}{\sigma_y^2}\right], \tag{2.48}$$

where $\sigma_i = \sqrt{\frac{2\epsilon_F(0)}{m\omega_i^2}}$. Using the substitutions $\omega_x x = \bar{w}\tilde{x}$ and $\omega_y y = \bar{w}\tilde{y}$ with $\bar{\omega} = (\omega_x\omega_y)^{1/2}$, we see that $\bar{\omega}^2\tilde{\bar{r}}^2 = \omega_x^2 x^2 + \omega_y^2 y^2$. Equation (2.48) can thus be written as

$$\frac{\hbar^2 k_F^2}{2m} = \epsilon_F(0)\left[1 - \frac{\tilde{r}^2}{\sigma^2}\right]. \tag{2.49}$$

A further substitution for n leads to

$$n(\tilde{r}) = \frac{m}{2\pi\hbar^2}\epsilon_F(0)\left(1 - \frac{\tilde{r}^2}{\sigma^2}\right), \tag{2.50}$$

with $n_\perp(0) = \frac{m}{2\pi\hbar^2}\epsilon_F(0)$. An expression we shall encounter several times in later chapters is the local Fermi energy, given by

$$\epsilon_F(\rho) = 2\pi\hbar^2/m \times n_\perp(\rho). \tag{2.51}$$

Note that in equation (2.50), n(r) vanishes where $r > R_F$ with ρ being the radius

$$\rho = (x^2 + y^2)^{\frac{1}{2}}. \tag{2.52}$$

From number normalisation, taking the integral of the density radially gives the total number of atoms N, i.e. ,

$$\int_0^{R_{TF}} 2\pi\tilde{r}d\tilde{r}n_\perp(\tilde{r}) = N. \tag{2.53}$$

Plugging equation (2.50) into equation (2.53) yields

$$\frac{m\epsilon_F(0)}{\hbar^2}\frac{R_{TF}^2}{2}\left[1 - \frac{R_{TF}^2}{2\sigma_r^2}\right] = N, \tag{2.54}$$

which we identify to be similar to equation (2.35). Hence, we see that

$$\epsilon_F(0) = E_F = \hbar\omega_\perp\sqrt{2N_\uparrow}. \tag{2.55}$$

2.3 Temperature Calibration of a Quasi-2D Fermi Gas

Having explored the basic thermodynamic concepts, we now apply our knowledge to obtain an estimate for the temperature of the clouds. In essence, we compare the measured one-dimensional column density profiles with that obtained in the local density approximation for an ideal Fermi gas. To account for the anharmonicity of the shallow optical trap used in the experiments, we assume a Gaussian trapping potential of the form

$$U(\rho) = U_0 \left(1 - e^{-\frac{m\omega_\perp^2 \rho^2}{2U_0}}\right), \tag{2.56}$$

where U is the trap depth and ω is the transverse harmonic oscillation frequency for an atom of mass m. For large U_0, $U(\rho) \rightarrow \frac{1}{2}m\omega_\perp^2\rho^2$.

The two-dimensional density at radius ρ is readily obtained by integrating the ideal Fermi gas occupation number with the density of transverse kinetic energy states per unit area

$$\frac{\Delta N}{L^2} = \int_0^\infty \frac{2\pi k dk}{(2\pi)^2} f(p) p dp. \tag{2.57}$$

with $k = p/\hbar$. For each axial state n,

$$n_{2D}^n(\rho) = \int_0^\infty \frac{2\pi p dp}{(2\pi\hbar)^2} \frac{\Theta\left[U_0 - \frac{p^2}{2m} - U(\rho)\right]}{e^{\frac{1}{k_B T}\left[\frac{p^2}{2m} + U(\rho) - \mu_n\right]} + 1}. \tag{2.58}$$

where $\Theta[U_0 - \frac{p^2}{2m} - U(\rho)]$ ensures that the total $E < U_0$ relative to the bottom of the trap. The chemical potential for axial state n relative to the ground state, μ_n is

$$\mu_n = \mu_0 - (E_n - E_0) = \mu_0 - n\hbar\omega_z. \tag{2.59}$$

Since the kinetic energy $q = \frac{p^2}{2m}$, we see that $dq = \frac{pdp}{m}$ or alternatively $pdp = mdq$. For trapped atoms, the integral extends from zero kinetic energy up to maximum $q = \frac{p^2}{2m} = U_0 - U(\rho)$. Substitution in equation (2.58) results in

$$n_{2D}^n(\rho) = \frac{m}{2\pi\hbar^2}\int_0^\infty dq \frac{\Theta\left[U_0 - U(\rho) - q\right]}{e^{\frac{1}{k_B T}[q+U(\rho)-\mu_n]}+1}. \tag{2.60}$$

We note that as the ideal gas Fermi energy is larger than the axial energy level spacing, an evaluation of the integral leads to the spatial profile for each occupied axial state, n,

$$n_{2D}^n(\rho) = \frac{mk_BT}{2\pi\hbar^2}\ln\left[\frac{1+e^{\frac{\mu_n - U(\rho)}{k_BT}}}{1+e^{\frac{\mu_n - U(0)}{k_BT}}}\right]. \tag{2.61}$$

In the low temperature limit $T \to 0$, the expression $1 + e^{\frac{\mu_n - U_0}{k_BT}} \to 1$ and for the axial states of interest, with $U \gg \mu_n$, $\ln\left[1 + e^{\frac{\mu_n - U}{k_BT}}\right] \to 0$. Hence, the two-dimensional density profile in equation (2.61) reduces to a Thomas-Fermi profile given by

$$n_{2D}^{(n)}(\rho) = \frac{m}{2\pi\hbar^2}\left[\mu_n - U(\rho)\right]\Theta\left[\mu_n - U(\rho)\right]. \tag{2.62}$$

For an ideal single component Fermi gas with N atoms, we normalize energy scales to the Fermi energy $E_F = \hbar\omega_\perp\sqrt{2N}$ and length scales to the corresponding Fermi radius, $R = R_{TF} = (8N)^{1/4}(\hbar/m\omega_\perp)^{1/2}$, resulting in $\tilde{T} = k_BT/E_F$ and $\tilde{U} = U/E_F$. Similarly, the chemical potential for each axial state is $\tilde{\mu}_n = \tilde{\mu}_0 - n\hbar\omega_z/E_F$, where the global chemical potential $\tilde{\mu}_n = \tilde{\mu}_0 - n\hbar\omega_z/E_F$ is referred to the ground state energy. Equation (2.61) then becomes

$$\frac{n_{2D}^n(\rho)}{N} = \frac{2}{\pi}\frac{1}{R^2}\tilde{T}\ln\left[\frac{1+e^{\frac{\tilde{\mu}_n - U(\tilde{\rho})}{\tilde{T}}}}{1+e^{\frac{\tilde{\mu}_n - U(0)}{\tilde{T}}}}\right]. \tag{2.63}$$

For a zero temperature single component Fermi gas in the axial ground state of a harmonic trap, equation (2.61) reduces to

$$\frac{n_{2D}(\rho)}{N}|_{T=0} = \frac{2}{\pi}\frac{1}{R_{TF}^2}\left(1-\frac{\rho^2}{R_{TF}^2}\right)\Theta\left[R_{TF}-\rho\right]. \tag{2.64}$$

In equation (2.64), we note that the normalisation factors of $2/\pi R_{TF}^2$ is dimensionally consistent with the number per unit area for the two-dimensional density. As a check, we note that by normalisation

$$\int_0^{R_{TF}} 2\pi\rho d\rho n_{2D}(\rho) = 1. \tag{2.65}$$

Performing an integration over both sides of equation (2.64) with the change of variables $u = \rho^2/R_{TF}^2$ leads to

$$4\int_0^1 \frac{du}{2}(1-u), \tag{2.66}$$

which we readily verify to be 1.

While we have described two-dimensional densities so far, it is the column densities which are obtained through high resolution imaging; an imaging beam incident on an atomic cloud projects out information along the direction it is incident from (y), generating an image in the x-z plane. The column density provides information along the radial direction. This is clearly shown in Figure 2.1. As a straightforward application, we see that the integral of the 2D zero-temperature Thomas-Fermi density profile in equation (2.62) from 0 to ∞ yields

$$n_c(x)|_{T=0} = \frac{N}{R_{TF}}\left(1-\frac{x^2}{R^2}\right)^{3/2}\Theta\left[R_{TF}-|x|\right], \tag{2.67}$$

with the normalization factor of $1/R_{TF}$ dimensionally consistent with the number per unit length for the one-dimensional column density.

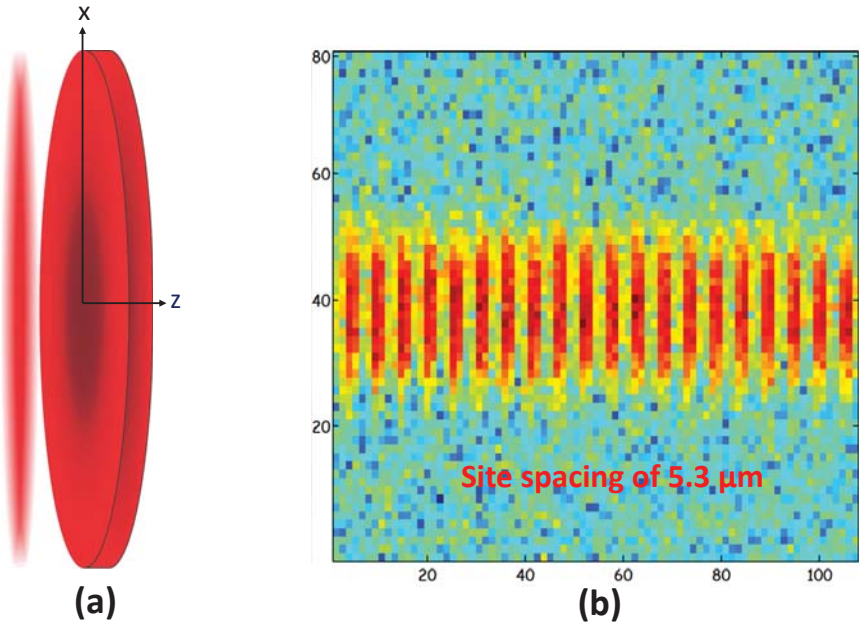

FIGURE 2.1: In the spatial configuration for high-resolution absorption imaging adopted (a) a pulse of light propagating along the y-direction projects out the x-z plane. A typical absorption image obtained, with the individual pancakes spaced 5.3 μm apart, is shown in (b). Since the axial (z) direction is tightly confining, the column density gives information in the radial direction.

To compute column density profiles in general, we first determine the chemical potential as a function of T/T_F by normalization

$$N = \sum_n N_n, \tag{2.68}$$

where

$$N_n = \int_0^\infty 2\pi\rho\, d\rho\, n_{2D}^{(n)}(\rho). \tag{2.69}$$

In units of the central density $n_0 = \frac{m}{2\pi\hbar^2}E_F = \frac{2N}{\pi R_{TF}^2}$, equation (2.69) can be written as

$$N_n = 2\pi R_{TF}^2 n_0 \int_0^\infty d\tilde{\rho}\tilde{\rho}\tilde{n}_{2D}^{(n)}(\tilde{\rho}), \tag{2.70}$$

where $\tilde{\rho} = \rho/R_{TF}$. We note that the prefactor $2\pi n_0 R_{TF}^2 = \frac{2E_F^2}{m\omega_\perp^2} = 4N$ using $n_{2D}^{(n)} =$

Table 2.1: Fraction of particles per axial state, assuming an occupation of three axial states at T/T_F of 0.21. For this calculation, we used a trap depth of 3.88 E_F, and an axial level spacing of 0.505 E_F. The Mathematica program used to calculate axial populations is provided for reference in Appendix A.

Axial State n	**Fraction of particles**
0	0.781
1	0.192
2	0.027

$n_0\tilde{n}_{2D}^{(n)}$. The fraction of particles in axial state n is then simply determined from the equation

$$\frac{N_n}{N} = 4\int_0^\infty d\tilde{\rho}\tilde{\rho}\tilde{n}_{2D}^n(\tilde{\rho},\tilde{T}). \tag{2.71}$$

Table 2.1 shows the computed fraction of particles for T/T_F of 0.21, assuming an occupation of three axial states. In our experiments, with approximately 800 particles per site, one obtains a Fermi energy of 0.85 μK, a trap potential depth of 3.3 μK, and an axial trap spacing of 0.43 μK. In terms of the Fermi energy, the trap depth is 3.88 E_F, while the axial trap spacing works out to be 0.505 E_F.

The corresponding one-dimensional column densities can then be obtained by integration of the two-dimensional densities

$$n_c^{(n)}(x) = 2\int_0^\infty dy n_{2D}^{(n)}(\sqrt{x^2+y^2}), \tag{2.72}$$

which in units of the Thomas-Fermi radius, R_{TF} ,yields

$$n_c^{(n)}(x) = R_{TF}n_0\,2\int_0^\infty d\tilde{y}\tilde{n}_{2D}^n(\sqrt{\tilde{x}^2+\tilde{y}^2}), \tag{2.73}$$

where we note that the prefactor $n_0R_{TF} = \frac{m}{2\pi\hbar^2}\frac{2E_F^2}{m\omega_\perp^2} = \frac{2N}{\pi R_{TF}}$. Hence, the atom

number-normalized one-dimensional column density is

$$n_c^{(n)}(x) = \frac{4N}{\pi R_{TF}} \int_{-\infty}^{\infty} d\tilde{y} \tilde{n}_{2D}^{(n)}(\sqrt{\tilde{x}^2 + \tilde{y}^2}). \tag{2.74}$$

Upon normalizing to N and the Thomas-Fermi radius R_{TF}, where R_{TF} we arrive at the total number of atoms per axial state of $N^{(n)} = \int_{-\infty}^{\infty} dx\, n_c^{(n)}(x)$.

The normalised one-dimensional column density is defined by

$$n_c^{(n)}(x) = \frac{N}{R_{TF}} \tilde{n}_c^n(\tilde{x}). \tag{2.75}$$

In practice, we fit experimentally measured profiles to theoretical one-dimensional column densities to extract the temperature. At magnetic fields employed in the experiments where the two-body scattering lengths are non-zero, we account for deviations from ideal gas behavior by scaling to the radius, R.

As N_2/N_1 is increased, the cloud deviates from ideal gas behavior. To estimate T/T_F, we employ a technique developed previously for a resonantly interacting Fermi gas in 3D [50]. We define an effective reduced temperature $\tilde{T} = k_B T/(m\omega_\perp^2 R^2/2)$, corresponding to the radius R obtained for a fit to a zero temperature profile. Similarly, in $\tilde{\mu}_n$ and in $\tilde{U}$, we use $E_F \to m\omega_\perp^2 R^2/2$ in the equation above (column density profile 2D). This method ensures that the spatial profile remains normalized to unity and yields a Maxwell-Boltzmann profile at high temperature, independent of R, and a zero temperature Thomas-Fermi profile of radius R at low T. We estimate R by initially fitting a zero temperature profile to estimate the cutoff radius and then fit $\tilde{T}$ to match the measured spatial profiles which deviate from zero T shape in the wings.

Figure 2.2 shows the column density profiles at finite temperatures of T/T_F of 0.14 and T/T_F of 0.21, first assuming all particles are in the ground axial state. For

comparison, a plot of a zero temperature single component gas in the ground axial state of a harmonic trap, equation (2.67) is shown. A crucial point of note is that finite temperature plots differ from zero-temperature Thomas-Fermi profiles primarily in the wings. Hence, a fit to the wings of the column density profiles is crucial for an accurate temperature measurement. Technically, this was achievable only upon the successful implementation of a high resolution imaging setup with an excellent signal-to-noise ratio, discussed further in Chapter 4. A Mathematica program to calculate finite temperature profiles is provided in Appendix A, where we explicitly consider the contributions of three axial states, and obtain the column density profiles at T/T_F of 0.14, 0.18, and 0.21. This appendix also provides expressions to determine the chemical potential as a function of temperature, as well as the relative population for each axial state.

Figure 2.3 shows some finite temperature column density profiles (in black dots) obtained for the tightly bound limit of $E_F/E_b = 2.1$, and the 3D Feshbach resonance limit at $E_F/E_b = 6.6$, for typical data from our experimental runs described later in Chapters 5 and 6. Shown together are calculated fits assuming three occupied axial states from our Mathematica program in Appendix A. The dotted curves shown are the ground axial state contributions to the column densities. Excellent fits to the data were obtained with calculated profiles, particularly in the wings. In the tightly bound limit and a low polarization of $N_2/N_1 = 0.1$, an upper bound on the temperature of $T/T_F = 0.21$ was obtained.

To compare the temperatures of clouds at different interaction strengths, we note that $T/T_F = \tilde{T}(R^2/R_{TF}^2)$ which defines the temperature T relative to the ideal gas Fermi temperature $T_F = E_F/k_B$ with E_F evaluated for the total majority atom number N_1. In our fits, we use $\tilde{T}$ as the fit parameter. The graphs in the middle and on the right of Figure 2.3 depict the scenario for polarizations of $N_2/N_1 = 0.5$, and $N_2/N_1 = 1$ for the interaction strength of $E_F/E_b = 6.6$, respectively.

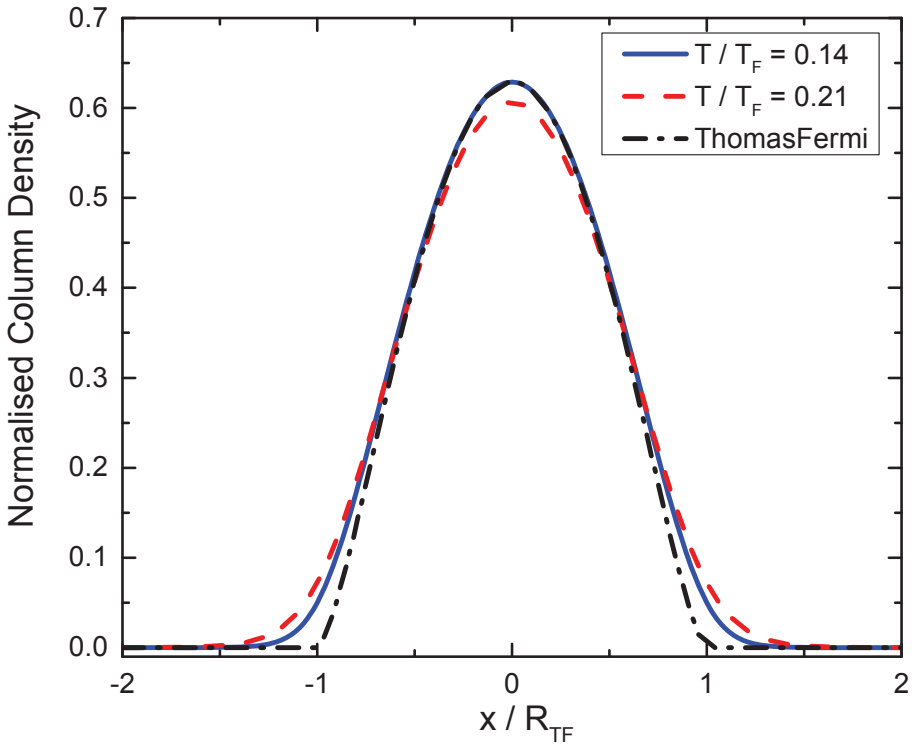

FIGURE 2.2: Finite temperature column density profiles in units of N_1/R_{TF1} for T/T_F of 0.14 (solid blue curve) and T/T_F of 0.21 (red dotted curve). At higher temperatures, the density profile drops in peak amplitude and broadens in the wings. The profiles shown were obtained by assuming that all the particles were in the ground axial state (n=0) at a trap depth U_0 of $3.88E_F$ and a trap axial spacing $h\nu_z$ of 0.51 E_F. Shown for comparison is a Thomas-Fermi profile with the same amplitude (black dash-dotted curve).

At the relatively lower polarization of $N_2/N_1 = 0.5$, we find the data to be well fit by a density profile with a temperature of $T/T_F = 0.18$, whereas for the spin-balanced sample of $N_2/N_1 = 1$, the data is well fit by a density profile with a temperature of $T/T_F = 0.14$. The lower sample temperature for spin-balanced gases is to be expected, an increased frequency of collisions between unlike particles leads to efficient evaporation.

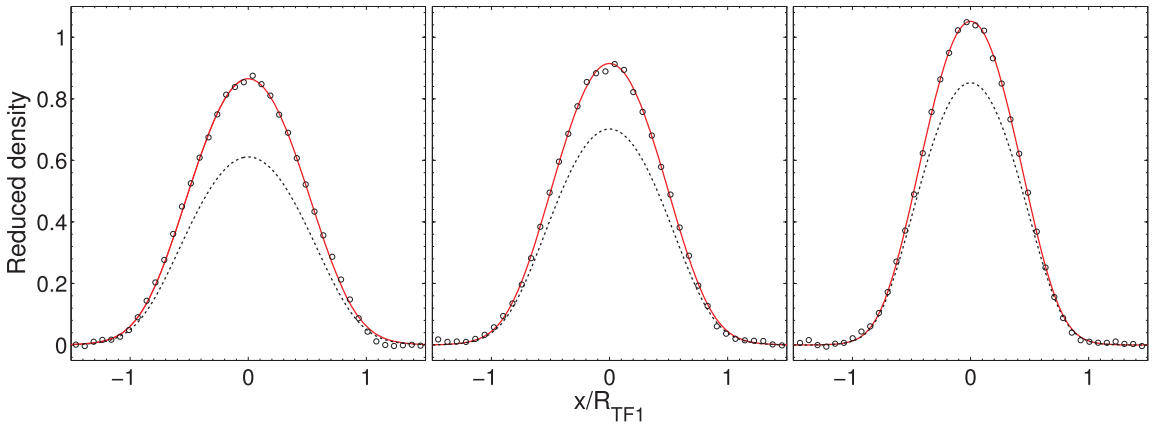

FIGURE 2.3: Finite temperature column density profiles in units of N_1/R_{TF1}. Dots: data; Red solid curves: fit including lowest three axial states; Dotted curves: ground axial state contribution. Left: $N_2/N_1 = 0.1$, $E_F/E_b = 2.1$, $T/T_F = 0.21$; Middle: $N_2/N_1 = 0.5$, $E_F/E_b = 6.6$, $T/T_F = 0.18$; Right: $N_2/N_1 = 1$, $E_F/E_b = 6.6$, $T/T_F = 0.14$

3

Two-Body and Many-Body Physics of quasi-2D Fermi Gases

In this chapter, we consider the effects of atomic interactions in reduced dimensions. In one and two dimensions, an attractive interaction always allows for a two-body bound state. For dimensions higher than one, few-body bound states can impact the statistics of the many-body quasiparticle excitations. For example, in three dimensional Fermi gases, the two-body bound state is fundamental to the understanding of the BCS-BEC crossover [51]. In 1D, one can have a Luttinger liquid of trimers. In the limit of a 2D geometry, where the Efimov effect is absent, both trimers and tetramers have been predicted [52]. Moreover, a doubly-exponential relationship in the binding energy, dubbed the super-Efimov effect, is expected to occur near p-wave Feshbach resonances of identical fermions [15]. Tight harmonic confinement along one direction strongly modifies the scattering properties of atoms, and stabilizes bound dimers.

The binding energy of atom pairs sets the length scale for scattering interactions in reduced dimensions. We begin with a consideration of bound states in one-dimension for a δ-function potential before describing two-body scattering prop-

erties in two dimensions, and the dimer bound states that exist in this regime. The predictions of two-dimensional many-body Bardeen-Cooper-Schrieffer (BCS) theory will be summarized [19, 53, 40]. However, in a prior radio-frequency spectroscopy experiment conducted by our group [39], the predictions from BCS theory and dimer theory were inconsistent with data obtained at unitarity.

The real space picture encountered in our experiments is one where the interparticle spacing is smaller than the dimer size; hence at 832 G, one encounters at the outset a many-body scenario where particles scatter within the dimers. Motivated by prior work [31, 54] in three dimensions, we then consider the limiting case of a single-impurity atom interacting via a short-range potential with a bath of an ideal atomic Fermi gas. This problem of a dressed impurity, called a Fermi polaron, in analogy with electrons dressed by the bosonic phonon bath in a crystal, turns out to be particularly prominent in theoretical predictions of the thermodynamics and quantum phase transitions of quasi-2D Fermi gases [38, 52]. A simple way of estimating the polaron energy and effective mass in two dimensions can be found in [55]. An elegant analytic approximation for the polaron energy found in this reference will be used in our derivation of 2D density profiles in Chapter 6. We derive the bound state energies for a two-dimensional polaron and compare them against rf spectra to find that they fit very well towards the end of this chapter.

3.1 Bound States in 1D

To prove that bound states exist in the one-dimensional case for an arbitrary attractive potential, we consider the δ-function potential

$$V(x) = -\alpha\delta(x), \tag{3.1}$$

where $\alpha > 0$. The Schrödinger equation reads

$$-\frac{\hbar^2}{2m}\frac{d^2\psi}{dx^2} - \alpha\delta(x)\psi = E\psi. \tag{3.2}$$

In the region $x < 0$, $V(x) = 0$, so

$$\frac{d^2\psi}{dx^2} = -\frac{2mE}{\hbar^2}\psi = \kappa^2\psi, \tag{3.3}$$

where

$$\kappa \equiv \frac{\sqrt{-2mE}}{\hbar}. \tag{3.4}$$

Since E is negative, κ is real and positive. The general solution is

$$\psi(x) = Ae^{-\kappa x} + Be^{\kappa x}. \tag{3.5}$$

When $x \to -\infty$, we see the unphysical case $Ae^{-\kappa x} \to \infty$, thus we set A = 0 and obtain

$$\psi(x) = Be^{\kappa x}, (x < 0). \tag{3.6}$$

Similarly, when $x > 0$, $V(x) = 0$ and the general solution is of the form $F\exp(-\kappa x) + G\exp(\kappa x)$. In this case, the second term, $G\exp(\kappa x) \to \infty$. Hence, we obtain

$$\psi(x) = Fe^{-\kappa x}, (x > 0). \tag{3.7}$$

Using the continuity of ψ and its spatial derivative, we arrive at the conclusion that $F = B$, so

$$\psi(x) = Be^{\kappa x}, (x \leqslant 0) \qquad \psi(x) = Be^{-\kappa x}, (x \geqslant 0) \tag{3.8}$$

where

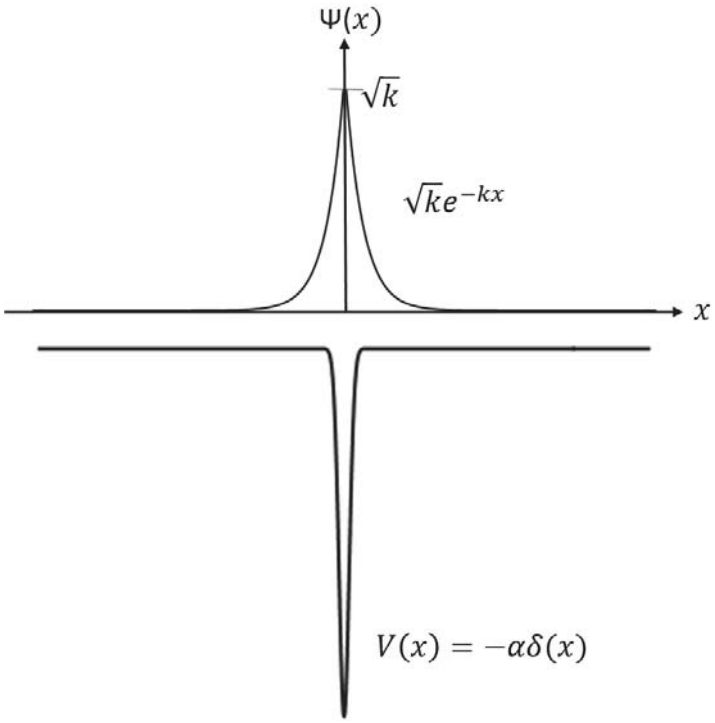

FIGURE 3.1: A one dimensional Dirac-delta potential results in a bound state wave-function as shown. Regardless of the magnitude of α , the delta function potential has exactly one bound state.

$$\kappa = \frac{m\alpha}{\hbar^2} \tag{3.9}$$

with the allowed bound state energy

$$E = -\frac{\hbar^2\kappa^2}{2m} = -\frac{m\alpha^2}{2\hbar^2}. \tag{3.10}$$

By normalisation,

$$\int_{-\infty}^{\infty} |\psi(x)|^2 dx = 2|B|^2 \int_0^{\infty} e^{-2\kappa x} dx = \frac{|B|^2}{\kappa} = 1, \tag{3.11}$$

we obtain the value of B

$$B = \sqrt{\kappa} = \frac{\sqrt{m\alpha}}{\hbar}, \tag{3.12}$$

and the corresponding bound state wave function

$$\psi(x) = \frac{\sqrt{m\alpha}}{\hbar} e^{-m\alpha|x|/\hbar^2}. \tag{3.13}$$

Having demonstrated the existence of bound states for arbitrarily weak interactions in 1D, we now turn our attention to the two-dimensional case.

3.2 Two Dimensional Scattering Theory

In two dimensions, bound states always exist [56]. We begin by considering the homogeneous, purely 2D elastic pair scattering problem subject to a short range potential $U(\rho)$, which allows us to define the two dimensional scattering length, a_{2D} [57]. We then extend the results to the case of a trapped gas subject to tight confinement along the axial (z) direction. This allows us to consider the more complicated case of bound state dimers and polarons in a quasi-2D Fermi gas subsequently.

3.2.1 Scattering in a homogeneous plane

In a homogeneous two-dimensional gas, the two-body scattering state can be written as a superposition of an incident plane wave and a scattered circular wave [57]

$$\psi_{\mathbf{k}}(x) = e^{i\mathbf{q}\cdot\rho} - \sqrt{\frac{i}{8\pi}} f(q,\phi) \frac{e^{iq\rho}}{\sqrt{q\rho}}, \tag{3.14}$$

where $\mathbf{q}$ is the relative momentum and $f(q,\phi)$ the dimensionless scattering amplitude for the two-body relative energy $E = \hbar^2 q^2/m$. The scattering amplitude is $s-$ wave dominant if the condition $qR_e \ll 1$ is satisfied, where the range of the interatomic potential R_e for ^{6}Li is approximately 20 Å. In this limit, the scattering amplitude is angle independent. The probability, $\alpha(q)$, for a particle to pass through a circle of radius ρ per unit time is then given by the product of the 2D flux through the circumference of the circle as

$$\alpha(q) = 2\pi\rho\frac{\hbar q}{\mu}|\sqrt{\frac{i}{8\pi}}\frac{f}{\sqrt{q\rho}}|^2 = \frac{\hbar}{2m}|f(q)|^2, \tag{3.15}$$

where $\mu = m/2$ is the reduced mass. The two-dimensional cross section, $\sigma(q)$, is

$$\sigma(q) = \frac{\alpha(q)}{\hbar q/\mu} = \frac{|f(q)|^2}{4q}. \tag{3.16}$$

To obtain the $s-$ wave scattering amplitude, we solve the Schrödinger equation for the $s-$ wave of the relative motion of the colliding atoms at energy $\epsilon = \hbar^2 q^2/m$

$$\left[-\frac{\hbar^2}{m}\Delta_\rho + U(\rho)\right]\psi_s(q,\rho) = \frac{\hbar^2 q^2}{m}\psi_s(q,\rho). \tag{3.17}$$

Neglecting the interatomic interactions at large distances, one obtains

$$\psi_s(q,\rho) \propto J_0(q\rho) - \frac{if(q)}{4}H_0(q\rho). \tag{3.18}$$

Noting that the motion is free for $R_e \ll \rho \ll 1/q$, and $\psi_s \propto \ln\left(\frac{\rho}{d}\right)$ in this region, with d being a potential-dependent constant, we arrive at the low-energy $s-$ wave scattering amplitude

$$f(q) = \frac{2\pi}{\ln(1/qd_*) + i\pi/2}, \tag{3.19}$$

where $d_* = d/2\exp(C)$, and $C = 0.577$ is Euler's constant.

This can alternatively be written as

$$f(q) = \frac{4}{-\cot\delta_0(q) + i} \to \frac{4\pi}{2\ln(1/qa_{2D}) + i\pi}, \tag{3.20}$$

where a_{2D} is the 2D scattering length.

3.2.2 2D Scattering in a trap

We now extend our treatment from the previous section to the experimental scenario of a quasi-2D gas realised under tight confinement in the axial (z-) direction. In three-dimensional free space, bound states occur only for $a > 0$. In a trap, confinement-induced two-body bound states occur for arbitrary (positive or negative) scattering lengths at normalized energies $\epsilon_b = E_b/\hbar\omega_z$ given by the transcendental equation [58]

$$\frac{l_z}{a} = \int_0^\infty \frac{du}{\sqrt{4\pi u^3}} \left[1 - \left(\frac{2u}{1 - e^{-2u}} \right)^{\frac{1}{2}} e^{-\epsilon_b u} \right], \tag{3.21}$$

where E_b is the two-body binding energy. This is a result we will derive in the next section from first principles. For small binding energies, $\epsilon_b \leqslant 1$, an analytic form for the bound state energies results

$$E_b = \hbar\omega_z \cdot \frac{0.905}{\pi} \exp\left(-\sqrt{2\pi} l_z/|a| \right). \tag{3.22}$$

In this limit, it can be seen from equations (3.20) and (3.21) that the 2D scattering length is related to the 3D scattering length, a and the confinement scale $l_z = [\hbar/(m\omega_z)]^{1/2}$ by

$$a_{2D}(a) = l_z \frac{\pi}{0.905} \exp\left(-\sqrt{\frac{\pi}{2}} \frac{l_z}{a} \right). \tag{3.23}$$

Since a_{2D} is always positive, regardless of the sign of a , a two-particle bound state always exists for arbitrary sign and interaction strength, parametrized by l_z/a or equivalently E_F/E_b. Using equation (3.23) in equation (3.19), we see that the effective low energy scattering amplitude for a strongly confined 2D gas is given by

$$f(k) = \frac{4\pi}{\sqrt{2\pi} l_z/a + \ln(0.905/(\pi k^2 l_z^2)) + i\pi}. \tag{3.24}$$

Under weak confinement, $l_z \gg a$ such that the logarithm and imaginary terms

in the denominator of equation (3.24) can be neglected, the resulting scattering amplitude

$$f(k) \simeq \sqrt{8\pi}\,\frac{a}{l_z} \tag{3.25}$$

is energy-independent.

3.3 2D Confinement induced dimers

In this section, we determine the spatial wavefunctions and the pair binding energies of dimers in a trapped 2D gas [59]. The Hamiltonian for a harmonically-trapped two atom system in a three-dimensional harmonic trap can be written as the sum of kinetic and potential energy

$$\begin{aligned} H^{(0)} &= \frac{\mathbf{p}_1^2}{2m} + \frac{\mathbf{p}_2^2}{2m} + \frac{1}{2}m\omega_x^2 x_1^2 + \frac{1}{2}m\omega_x^2 x_2^2 + \\ &\quad \frac{1}{2}m\omega_y^2 y_1^2 + \frac{1}{2}m\omega_y^2 y_2^2 + \frac{1}{2}m\omega_z^2 z_1^2 + \frac{1}{2}m\omega_z^2 z_2^2. \end{aligned} \tag{3.26}$$

The form of the Hamiltonian allows a separation into the center-of-mass motion and relative motion,

$$\begin{aligned} H^{(0)} &= \left(\frac{\mathbf{P}^2}{2M} + \frac{1}{2}M\omega_x^2 X^2 + \frac{1}{2}M\omega_y^2 Y^2 + \frac{1}{2}M\omega_z^2 Z^2\right) + \\ &\quad \left(\frac{\mathbf{p}^2}{2\mu} + \frac{1}{2}\mu\omega_x^2 x^2 + \frac{1}{2}\mu\omega_y^2 y^2 + \frac{1}{2}\mu\omega_z^2 z^2\right), \end{aligned} \tag{3.27}$$

where $Z = \frac{z_1+z_2}{2}$, $z = z_1 - z_2$ and similarly for the x and y directions. As with usual convention, we denote the total mass by $M = 2m$ and the reduced mass by $\mu = m/2$.

To determine the binding energies experimentally, we conduct radio-frequency

spectroscopy experiments, where the center-of-mass motion is unchanged. Considering only the relative motion portion of equation (3.27), we obtain

$$H_0 = \frac{\mathbf{p}^2}{2\mu} + \frac{1}{2}\mu\omega_x^2 x^2 + \frac{1}{2}\mu\omega_y^2 y^2 + \frac{1}{2}\mu\omega_z^2 z^2. \tag{3.28}$$

Since the range of the two-body interaction is small compared to the interparticle spacing as well as to the harmonic oscillator confinement scale $l_z \equiv \sqrt{\hbar/(m\omega_z)}$, the short-range s-wave interaction is written using the $s-$ wave pseudopotential [60]

$$V(\mathbf{r})\psi(\mathbf{r}) = \frac{4\pi\hbar^2 a}{m}\delta(\mathbf{r})\frac{\partial}{\partial r}[r\psi(\mathbf{r})], \tag{3.29}$$

where $\mathbf{r} = \mathbf{r_1} - \mathbf{r_2}$ is the distance between the atoms, m is the mass of a single atom, and a is the magnetically tunable zero-energy s-wave scattering length. The total Hamiltonian for the relative motion of two-atom system is

$$H_{\mathbf{r}} = H_0 + V(\mathbf{r}). \tag{3.30}$$

The bound state is most easily determined using a Green's function solution to the time-dependent Schrödinger equation, which reads:

$$[H_0 + V(\mathbf{r})]\psi(\mathbf{r}, t) = i\hbar\frac{\partial}{\partial t}\psi(\mathbf{r}, t) \tag{3.31}$$

or

$$\left[H_0 - i\hbar\frac{\partial}{\partial t}\right]\psi(\mathbf{r}, t) = -V(\mathbf{r})\psi(\mathbf{r}, t). \tag{3.32}$$

The time-dependent Green's function obeys

$$\left[H_0 - i\hbar\frac{\partial}{\partial t}\right]G\left(\mathbf{r}, \mathbf{r}', t - t'\right) = \delta(t - t')\delta(\mathbf{r} - \mathbf{r}'). \tag{3.33}$$

The solution to equation (3.32) is

$$\psi(\mathbf{r},t) = \psi^{(0)}(\mathbf{r},t) - \int_{-\infty}^{\infty} dt' \int d^3\mathbf{r}' G(\mathbf{r},\mathbf{r}',t-t')V(\mathbf{r}')\psi(\mathbf{r}',t'). \tag{3.34}$$

Here, $\left[H_0 - i\hbar\frac{\partial}{\partial t}\right]\psi^{(0)}(\mathbf{r},t) = 0$, and the Green's function reads

$$G(\mathbf{r},\mathbf{r}',t-t') = \frac{i}{\hbar}\theta(t-t')\sum_n e^{-\frac{i}{\hbar}E_n(t-t')}\phi_n(\mathbf{r})\phi_n^*(\mathbf{r}'). \tag{3.35}$$

An important property we will utilise in equation (3.35) to obtain the appropriate form of the Green's function is the symmetry under exchange of coordinates $\mathbf{r} \leftrightarrow \mathbf{r}'$. We write the Green's function as

$$G(\mathbf{r},\mathbf{r}',\tau) \equiv \frac{i}{\hbar}\theta(\tau)g(\mathbf{r},\mathbf{r}',\tau), \tag{3.36}$$

with the time translation operator in position representation, g, given by

$$g(\mathbf{r},\mathbf{r}',\tau) = e^{-\frac{i}{\hbar}H_0(\mathbf{r})\tau}\delta(\mathbf{r}-\mathbf{r}'). \tag{3.37}$$

In the above equations $\tau = t - t'$. Applying the Heisenberg operator, defined by

$$\mathbf{r}_H(\tau) = e^{\frac{i}{\hbar}H_0(\mathbf{r})\tau}\mathbf{r}e^{-\frac{i}{\hbar}H_0(\mathbf{r})\tau} \tag{3.38}$$

to operate on $g(\mathbf{r},\mathbf{r}',\tau)$, we are able to solve for $\mathbf{r}_H(\tau)$. We find the derivative of $\mathbf{r}_H(\tau)$ with respect to τ

$$\dot{\mathbf{r}}_H(\tau) = e^{\frac{i}{\hbar}H_0(\mathbf{r})\tau}\frac{\mathbf{p}}{\mu}e^{-\frac{i}{\hbar}H_0(\mathbf{r})\tau}. \tag{3.39}$$

Consequently, the second derivative in the z-direction reads

$$\ddot{\mathbf{z}}_H(\tau) = e^{\frac{i}{\hbar}H_0(\mathbf{r})\tau}\frac{i}{\hbar}\left[\frac{1}{2}\mu\omega_z^2 z^2, \frac{p_z}{\mu}\right]e^{-\frac{i}{\hbar}H_0(\mathbf{r})\tau} = -\omega_z^2\mathbf{z}_H(\tau). \tag{3.40}$$

Using the initial conditions $\mathbf{z}_H(0) = z$ and $\dot{\mathbf{z}}_H(0) = \frac{p_z}{\mu}$, we arrive at

$$\mathbf{z}_H(\tau) = zcos(\omega_z\tau) + \frac{p_z}{\mu\omega_z}sin(\omega_z\tau) \tag{3.41}$$

and similarly for the x and y directions.

Using

$$\mathbf{r}_H(-\tau)g(\mathbf{r},\mathbf{r}',\tau) = \mathbf{r}'g(\mathbf{r},\mathbf{r}',\tau), \tag{3.42}$$

and $\theta_i = \omega_i\tau$; $i = x, y, z$, and $g = g_x(x,x')g_y(y,y')g_z(z,z')$, we obtain for the z direction

$$\left(\cos\theta_z z - \frac{\sin\theta_z}{\mu\omega_z}\frac{\hbar}{i}\frac{\partial}{\partial z}\right) g_z(z,z',\tau) = z' g_z(z,z',\tau). \tag{3.43}$$

Thus, we arrive at

$$g_z(z,z',\tau) = C_z e^{\frac{i}{\hbar}\frac{\mu\omega_z}{sin\theta_z}\left(cos\theta_z\frac{z^2}{2} - zz'\right)}, \tag{3.44}$$

where C_z is a constant. Due to symmetry, $g_x(x,x',\tau)$ and $g_y(y,y',\tau)$ take the same forms. Thus, the Green's function can be written as

$$\begin{aligned} G(\mathbf{r},\mathbf{r}',t-t') &= \frac{i}{\hbar}\theta(t-t')\left[\left(\frac{\mu}{2\pi i\hbar}\right)^3 \frac{\omega_x\omega_y\omega_z}{\sin\theta_x\sin\theta_y\sin\theta_z}\right]^{\frac{1}{2}} \\ &\cdot e^{\frac{i\mu\omega_x}{\hbar\sin\theta_x}\left[\cos\theta_x\frac{x^2+x'^2}{2} - xx'\right]} \\ &\cdot e^{\frac{i\mu\omega_y}{\hbar\sin\theta_y}\left[\cos\theta_y\frac{y^2+y'^2}{2} - yy'\right]} \\ &\cdot e^{\frac{i\mu\omega_z}{\hbar\sin\theta_z}\left[\cos\theta_z\frac{z^2+z'^2}{2} - zz'\right]}. \end{aligned} \tag{3.45}$$

3.3.1 Bound state and Scattering State wave functions

In this subsection, we apply the Green's functions obtained in the previous section to obtain the bound and scattering eigenstates and the dimer binding energies. Based on the solution to the Schrödinger equation, we have

$$\psi_E(\mathbf{r},t) = e^{-\frac{i}{\hbar}Et}\psi_E(\mathbf{r}) \tag{3.46}$$

$$\psi_E^{(0)}(\mathbf{r},t) = e^{-\frac{i}{\hbar}Et}\psi_E^{(0)}(\mathbf{r}). \tag{3.47}$$

We thus obtain the eigenstate directly from the time-dependent Green's function as

$$\psi_E(\mathbf{r}) = \psi_E^{(0)}(\mathbf{r}) - \int_{-\infty}^{\infty} dt' \int d^3\mathbf{r}' G\left(\mathbf{r},\mathbf{r}',t-t'\right) V(\mathbf{r}') e^{\frac{i}{\hbar}E(t-t')}\psi_E(\mathbf{r}'). \tag{3.48}$$

For a scattering state,

$$\psi_{E_s}(\mathbf{r}) = \psi_E^{(0)}(\mathbf{r}) - \int d^3\mathbf{r}' G_E(\mathbf{r},\mathbf{r}') V(\mathbf{r}')\psi_E(\mathbf{r}'), \tag{3.49}$$

where $\psi_E^{(0)}$ is an input plane wave in free space, and $G_E(\mathbf{r},\mathbf{r'})$ is a stationary Green's function for an eigenstate. For a bound state,

$$\psi_{E_b}(\mathbf{r}) = -\int d^3\mathbf{r}' G_E(\mathbf{r},\mathbf{r}') V(\mathbf{r}')\psi_E(\mathbf{r}'). \tag{3.50}$$

Using the pseudo-potential form for V(r), we write the bound state as

$$\begin{aligned}\psi_{E_b}(\mathbf{r}) &= -\frac{4\pi\hbar^2 a}{m} G_{E_b}(\mathbf{r},0)\frac{\partial}{\partial r'}[\mathbf{r}'\psi_E(\mathbf{r}')]|_{r'\to 0} \\ &= -\frac{4\pi\hbar^2 a}{m} G_{E_b}(\mathbf{r},0)u_E^{'}(0) \\ &= AG_{E_b}(\mathbf{r},0). \end{aligned} \tag{3.51}$$

where A is a constant, G_{E_b} is the bound state Green's function, $\psi_E(\mathbf{r}) \equiv \frac{u_E(r)}{r}$ and $\psi_E^{(0)}(\mathbf{r}) \equiv \frac{u_E(r)}{r}$. Hence, the wavefunction of the corresponding bound state is known once we have determined $G_{E_b}(\mathbf{r})$ and E_b. Applying the derivative $\frac{\partial}{\partial r}[r...]|_{r\to 0}$ we obtain

$$\begin{aligned} 1 &= -\frac{4\pi\hbar^2 a}{m}\frac{\partial}{\partial r}[rG_{E_b(\mathbf{r},0)}]|_{r\to 0} \\ &= -\frac{4\pi\hbar^2 a}{m}[G_{E_b(\mathbf{r},0)} - G_0(\mathbf{r})]|_{r\to 0} \end{aligned} \tag{3.52}$$

Here, $G_0(\mathbf{r})$ is the part of G_{E_b} that is $\propto \frac{1}{r}$, where $\frac{\partial}{\partial r}[rG_0(r)] = 0$ and $G_E - G_0$ is then regular at $r = 0$. To find the form of $G_0(\mathbf{r})$, we note from equation (3.45) that $G_{E_b}(\mathbf{r}, \mathbf{r}' \to 0)$ is

$$\begin{aligned} G_{E_b(\mathbf{r},0)} &= \frac{i}{\hbar}\left(\frac{m}{4\pi i\hbar}\right)^{3/2}\int_0^\infty d\tau e^{\frac{i}{\hbar}E\tau}\left(\frac{\omega_x\omega_y\omega_z}{\sin\theta_x\sin\theta_y\sin\theta_z}\right)^{1/2} \\ &\cdot e^{\frac{im\omega_x}{\hbar\sin\theta_x}\cos\theta_x\frac{x^2}{4}}\cdot e^{\frac{im\omega_y}{\hbar\sin\theta_y}\cos\theta_y\frac{y^2}{4}}\cdot e^{\frac{im\omega_z}{\hbar\sin\theta_z}\cos\theta_z\frac{z^2}{4}}. \end{aligned} \tag{3.53}$$

Using the substitutions $\xi \equiv \omega_z\tau$, $l_i^2 = \frac{\hbar}{m\omega_i}$, $\beta_i = \frac{\omega_i}{\omega_z}$, with $i = x, y, z$, and $E_0 = \frac{\hbar\omega_x}{2} + \frac{\hbar\omega_y}{2} + \frac{\hbar\omega_z}{2}$ and $E - E_0 = -E_b$, where the binding energy is $E_b = \epsilon_b\hbar\omega_z > 0$, we see that

$$
\begin{aligned}
G_{E_b}(\mathbf{r},0) &= \frac{1}{4\pi\hbar\omega_z l_x l_y l_z}\int_0^\infty \frac{id\xi}{\sqrt{4\pi}} e^{-i\epsilon_b\xi}\left(\frac{2}{1-e^{-2i\xi\beta_z}}\right)^{\frac{1}{2}} e^{i\cot(\xi\beta_z)\left(\frac{z}{2l_z}\right)^2} \\
&\quad\cdot\left(\frac{2}{1-e^{-2i\xi\beta_x}}\right)^{\frac{1}{2}} e^{i\cot(\xi\beta_x)\left(\frac{x}{2l_x}\right)^2} \\
&\quad\cdot\left(\frac{2}{1-e^{-2i\xi\beta_y}}\right)^{\frac{1}{2}} e^{i\cot(\xi\beta_y)\left(\frac{y}{2l_y}\right)^2}. \qquad (3.54)
\end{aligned}
$$

With a change of variables $\xi \to -iu$, we obtain

$$
\begin{aligned}
G_{E_b}(\mathbf{r},0) &= \frac{1}{4\pi\hbar\omega_z l_z^3}\int_0^\infty \frac{du}{\sqrt{4\pi}} e^{-\epsilon_b u}\left(\frac{2\beta_z}{1-e^{-2u\beta_z}}\right)^{\frac{1}{2}} e^{-\coth(u\beta_z)\left(\frac{z}{2l_z}\right)^2} \\
&\quad\cdot\left(\frac{2\beta_x}{1-e^{-2u\beta_x}}\right)^{\frac{1}{2}} e^{-\coth(u\beta_x)\left(\frac{x}{2l_x}\right)^2} \\
&\quad\cdot\left(\frac{2\beta_y}{1-e^{-2u\beta_y}}\right)^{\frac{1}{2}} e^{-\coth(u\beta_y)\left(\frac{y}{2l_y}\right)^2}, \qquad (3.55)
\end{aligned}
$$

$$
G_{E_b}(\mathbf{r}) = \frac{1}{4\pi\hbar\omega_z}\frac{1}{l_z^3}\int_0^\infty \frac{du}{\sqrt{4\pi u^3}} e^{-\epsilon_b u - \frac{r^2}{4ul_z^2}}. \qquad (3.56)
$$

If we let $s^2 = \frac{r^2}{4ul_z^2}$, we get

$$
\begin{aligned}
G_{E_b}(\mathbf{r}) &= \frac{m}{4\pi\hbar^2 r}\frac{2}{\sqrt{\pi}}\int_0^\infty ds\, e^{-s^2-\left(\frac{-r\sqrt{\epsilon_b/l_z^2}}{2}\right)^2\frac{1}{s^2}} \\
&= \frac{m}{4\pi\hbar^2 r} e^{-r\sqrt{\epsilon_b/l_z^2}}. \qquad (3.57)
\end{aligned}
$$

The three-dimensional molecular binding energy E_b is approximately $\hbar^2/ma^2$ when $l_z \gg a$, where the small dimer barely experiences the effects of the harmonic trap. Hence, $\frac{\epsilon_b}{l_z^2} = \frac{E_b}{\hbar\omega_z l_z^2} = \frac{1}{a^2}$. We thus obtain

$$G_{E_b}(\mathbf{r}) = \frac{m}{4\pi\hbar^2 r} e^{-r/a}. \tag{3.58}$$

For $r \ll a$, we obtain

$$G_{E_b}(\mathbf{r}) = G_0(\mathbf{r}) = \frac{m}{4\pi\hbar^2 r}, \tag{3.59}$$

which is the free-particle Green's function for small r. Thus, equation (3.56) turns into G_0's equation as well when $r \ll a \ll l_z$. Hence, we write

$$G_0(\mathbf{r}) \to \frac{m}{4\pi\hbar^2 l_z} \int_0^\infty \frac{du}{\sqrt{4\pi u^3}}, \tag{3.60}$$

$$G_{E_b}(\mathbf{r}) = \frac{m}{4\pi\hbar^2} \frac{1}{l_z} \int_0^\infty \frac{du e^{-\epsilon_b u}}{\sqrt{4\pi u^3}} \prod_j \left(\frac{2\beta_j u}{1 - e^{-2\beta_j u}} \right)^{1/2} e^{-\coth(\beta_j u)(x_j/2l_j)^2}. \tag{3.61}$$

As $\mathbf{r} \to 0$, the last factor of G_{E_b} becomes 1, we then have from equation (3.52)

$$\frac{l_z}{a} = \int_0^\infty \frac{du}{\sqrt{4\pi u^3}} \left[1 - \prod_j \left(\frac{2\beta_j u}{1 - e^{-2\beta_j u}} \right)^{1/2} e^{-\epsilon_b u} \right], \tag{3.62}$$

where $\beta_j = \frac{\omega_j}{\omega_z}$. This self-consistent equation can be used to calculate $E_b = \epsilon_b \hbar\omega_z$. The dimer binding energy is significantly increased for nonzero transverse confinement [39]. When l_z/a is large, $a \ll l_z, \frac{\hbar^2}{ma^2} \gg h\nu_z$, the dimer is tightly bound and its size is small compared to the harmonic oscillator length scale l_z, thus the shape of the trap does not affect the interaction between the two atoms very much. For weakly bound dimers, the trap plays a significant role in dimer statistics. At resonance, where $l_z/a \to 0$ for $\nu_\perp/\nu_z = 0$, we obtain $E_b = 0.245\, h\nu_z$, while for $\nu_\perp/\nu_z = 1/25$, we obtain $E_b = 0.290\, h\nu_z$. At 842 G in the shallowest trap, the binding energy of the 1-3 dimer is increased from 0.15 kHz without transverse confinement to 0.78 kHz with

transverse confinement. Further values of the two-body binding energy, calculated from equation (3.62) are provided in Table 3.1.

A plot of $\epsilon_b = E_b/(h\nu_z)$ as a function of l_z/a is shown in Figure 3.2 for a transverse confinement of $\nu_\perp = \nu_z/22$, the trap condition for experiments reported in Chapters 5 and 6.

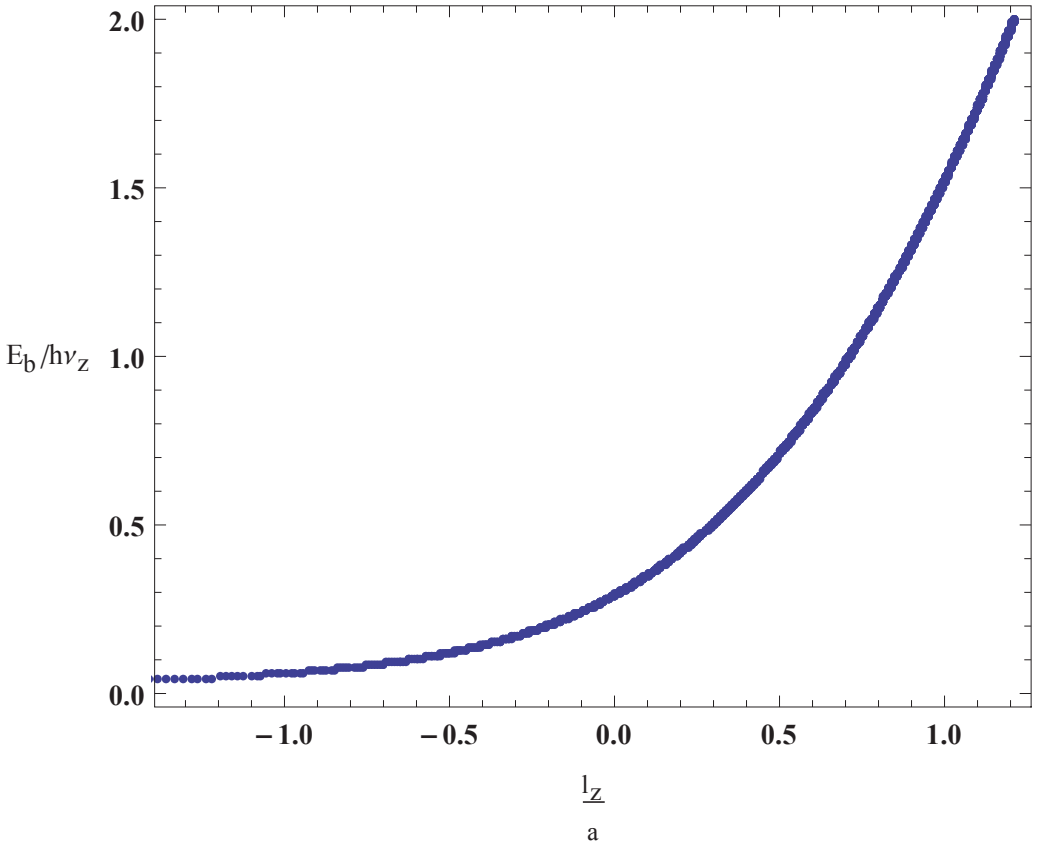

FIGURE 3.2: Plot of $\epsilon_b = E_b/(h\nu_z)$ as a function of l_z/a generated from equation (3.62), for a transverse confinement of $\nu_\perp = \nu_z/22$

.

3.3.2 Bound and Scattering State Wavefunctions

To calculate the bound state and scattering state wave functions, we first note that in our setup, $\omega_\perp/\omega_z = 1/25$. We make the simplest approximation and take $\omega_\perp/\omega_z = 0$, i.e., $\beta_x, \beta_y \to 0$ while $\beta_z = 1$.

Table 3.1: Shown are 1-2 and 1-3 dimer binding energies calculated based on equation (3.62) for $\nu_\perp$ of 0 and $\nu_z/25$. Values in columns labelled E_{b0} are for the case with no transverse confinement; values in columns labelled E_b have the confinement included.

B(G)	ν_z	E_{b0}^{13} (kHz)	E_b^{13} (kHz)	E_{b0}^{12} (kHz)	E_b^{12} (kHz)
718.5	26.0	1.95	2.91	144.2	145.3
768.2	24.5	0.45	1.21	36.82	37.8
832.2	24.5	0.17	0.81	6.29	7.25
841.7	24.5	0.15	0.78	4.96	5.91

Thus, in equation (3.60), $\frac{2\beta_x u}{1-e^{-2\beta_x u}\to 1}$, $\coth(\beta_x u)\frac{x^2}{4l_x^2} \to \frac{x^2}{\beta_x u 4l_x^2} = \left(\frac{x}{2l_z}\right)^2 \frac{1}{u}$, and similarly for the y-direction. In the z-direction, $\frac{2\beta_z u}{1-e^{-2\beta_z u}} \to \frac{2u}{1-e^{-2u}}$. Hence,

$$G_{E_b}(\mathbf{r}) = \frac{m}{4\pi\hbar^2}\frac{1}{l_z}\int_0^\infty \frac{du\, e^{\epsilon_b u}}{\sqrt{4\pi u^3}}\left(\frac{2u}{1-e^{-2u}}\right)^{1/2} e^{-\coth u(z/2l_z)^2} e^{-\left(\frac{\rho}{2l_z}\right)^2\frac{1}{u}}. \tag{3.63}$$

Here $\rho = \sqrt{x^2+y^2}$. The bound state energy should be lower than the harmonic ground state, but close to it when the binding energy is small. The ground state axial wave function is $\phi_0(z) = \phi_0(0)e^{-\left(\frac{z}{2l_z}\right)^2}$ with $\phi_0(0) = \frac{1}{(2\pi l_z^2)^{1/4}}$. For small ϵ_b, we assume that the primary component of the bound state wave function is the projection onto $\phi_0(z)$

$$\begin{aligned} I_{E_b}(\rho) &= \int_{-\infty}^{\infty} dz G_E(\mathbf{r})\phi_0(z) \\ &= \phi_0(0)\frac{m}{4\pi\hbar^2}\frac{1}{l_z}\int_0^\infty \frac{du e^{-\epsilon_b u}}{\sqrt{4\pi u^3}} e^{-\left(\frac{\rho}{2l_z}\right)^2\frac{1}{u}} I_z(u), \end{aligned} \tag{3.64}$$

with

$$
\begin{aligned}
I_z(u) &= \int_{-\infty}^{\infty} dz e^{-\left(\frac{z}{2l_z}\right)^2(1+\coth u)} \left(\frac{2u}{1-e^{-2u}}\right)^{1/2} \\
&= \sqrt{\frac{\pi(2l_z)^2}{1+\coth u}} \left(\frac{2u}{1-e^{-2u}}\right)^{1/2} = \sqrt{4\pi} l_z u^{1/2}. \qquad (3.65)
\end{aligned}
$$

Then, we obtain

$$
\begin{aligned}
I_{E_b}(\rho) &= \phi_0(0) \frac{m}{4\pi\hbar^2} \int_0^{\infty} \frac{du}{u} e^{-\epsilon_b u - \frac{1}{u}\left(\frac{\rho}{2l_z}\right)^2} \\
&= \phi_0(0) \frac{m}{4\pi\hbar^2} 2K_0 \left(\frac{\rho\sqrt{\epsilon_b}}{l_z}\right), \qquad (3.66)
\end{aligned}
$$

where K_0 is a modified Bessel function. This is the projection of $G_E(\mathbf{r})$ onto $\phi_0(z)$. The bound state wave function can thus be written as

$$
\psi_{E_b}(\mathbf{r}) = A\phi_0(z) K_0 \left(\frac{\sqrt{\epsilon_b}\rho}{l_z}\right), \qquad (3.67)
$$

with A the normalisation coefficient. Integrating equation (3.67), we have

$$
\int_{-\infty}^{\infty} dz \int_0^{\infty} 2\pi\rho d\rho |A|^2 \phi_0^2(z) K_0^2 \left(\frac{\sqrt{\epsilon_b}\rho}{l_z}\right) = 1, \qquad (3.68)
$$

and thus $A = \frac{\sqrt{\epsilon_b}}{l_z\sqrt{\pi}}$. Defining $\kappa = \sqrt{\epsilon_b}/l_z$ the bound state wavefunction can be written as

$$
\psi_{E_b}(z,\rho) = \frac{\kappa}{\sqrt{\pi}} \phi_0(z) K_0(\kappa\rho). \qquad (3.69)
$$

Components from higher axial states have been ignored since the binding energy is small compared with $\hbar\omega_z$.

The scattering state is obtained by noting from equation (3.50) that

$$\psi_{E_s}(\mathbf{r}) = \psi^0_{E_s}(\mathbf{r}) - \frac{4\pi\hbar^2 a}{m} G_{E_s}(\mathbf{r}, 0) \frac{\partial}{\partial r'}[r'\psi_{E_s}(\mathbf{r}')]|_{r'\to 0}, \tag{3.70}$$

where the scattering state energy $E_s = E - E_0 = \epsilon\hbar\omega_z$, with $\epsilon > 0$. We assume that scattering occurs only in the ground state, and let $E_s = \frac{\hbar^2 k_\perp^2}{m}$, the relative kinetic energy in the transverse direction. Using the same trick as we did for the bound state, we obtain

$$u'_{E_s}(0) = u'^{(0)}_{E_s}(0) - \frac{4\pi\hbar^2 a}{m} \frac{\partial}{\partial r}[rG_{E_s}(\mathbf{r})]|_{r\to 0} u'_{E_s}(0). \tag{3.71}$$

Here $u_{E_s} = r\psi_{E_s}$ and is regular at the origin. So,

$$u'_{E_s}(0) = \frac{u'^{(0)}_{E_s}(0)}{1 + \frac{4\pi\hbar^2 a}{m} \frac{\partial}{\partial r}[rG_{E_s}(\mathbf{r})]|_{r\to 0}}. \tag{3.72}$$

We use the relation $1 = -\frac{4\pi\hbar^2 a}{m} \frac{\partial}{\partial r}[rG_{E_b}(\mathbf{r}, 0)]|_{r\to 0}$ from equation (3.52) in equation (3.72),

$$u'_{E_s}(0) = \frac{m}{4\pi\hbar^2 a} \frac{u'^{(0)}_{E_s}(0)}{-\frac{\partial}{\partial r}[rG_{E_b(\mathbf{r})}]|_{r\to 0} + \frac{\partial}{\partial r}[rG_{E_s(\mathbf{r})}]|_{r\to 0}}. \tag{3.73}$$

Subtraction in the denominator cancels out the irregular parts $\propto \frac{1}{r}$ in both Green's functions. The remaining parts are regular when $r \to 0$. So, we can write $\frac{\partial}{\partial r}[r(G_{E_s} - G_{E_b})]|_{r\to 0} = (G_{E_s} - G_{E_b})|_{r\to 0}$ and obtain

$$u'_{E_s}(0) = \frac{m}{4\pi\hbar^2 a} \frac{u'^{(0)}_{E_s}(0)}{[G_{E_s}(\mathbf{r}) - G_{E_b}(\mathbf{r})]|_{r\to 0}}. \tag{3.74}$$

Plugging equation (3.74) back into equation (3.71), and considering $u'^{(0)}_{E_s}(0) = \frac{\partial}{\partial r}[r\psi^{(0)}_{E_s}]|_{r\to 0} = \psi^{(0)}_{E_s}(0)$. We obtain the simple form

$$\psi_{E_s}(\mathbf{r}) = \psi^{(0)}_{E_s}(\mathbf{r}) - \frac{G_{E_s}(\mathbf{r})u^{'(0)}_{E_s}(0)}{[G_{E_s}(\mathbf{r}) - G_{E_b}(\mathbf{r})]|_{r\to 0}}$$

$$= \psi^{(0)}_{E_s}(\mathbf{r}) - \frac{G_{E_s}(\mathbf{r})\psi^{(0)}_{E_s}(0)}{[G_{E_s}(\mathbf{r}) - G_{E_b}(\mathbf{r})]|_{r\to 0}}. \tag{3.75}$$

Projecting the scattering state Green's function G_{E_b} onto $\phi_0(z)$, replacing E_b by E_s and changing $\epsilon_b \to -\epsilon$, we make the same approximations based on $\omega_\perp \ll \omega_z$ and $\beta_x, \beta_y \ll 1$. We arrive at the relations $\frac{2\beta_x}{1-e^{2i\xi\beta_x}\to\frac{1}{i\xi}}$ and $cot(\xi\beta_x)\frac{1}{l_x^2} \to \frac{\xi}{l_z^2}$. Thus, we write $G_{E_s}(\mathbf{r})$ as

$$G_{E_s}(\mathbf{r}) = \frac{m}{4\pi\hbar^2}\frac{1}{l_z}\int_0^\infty \frac{d\xi e^{i\epsilon\xi}}{\sqrt{4\pi\xi^2}}\left(\frac{2}{1-e^{-2i\xi}}\right)^{1/2} e^{icot\xi\left(\frac{z}{2l_z}\right)^2 + \frac{i}{\xi}\left(\frac{\rho^2}{2l_z}\right)}. \tag{3.76}$$

Projecting onto the ground state $\phi_0(z)$, we obtain

$$I_{E_s}(\rho) = \int_{-\infty}^{\infty} dz\phi_0(z)G_{E_s}(\mathbf{r}) = \phi_0(0)\frac{m}{4\pi\hbar^2}\frac{1}{l_z}\int_0^\infty \frac{d\xi e^{-i\epsilon_b\xi}}{\sqrt{4\pi\xi^2}} e^{\left(\frac{\rho}{2l_z}\right)^2\frac{i}{\xi}} I'_z(\xi). \tag{3.77}$$

The l=0 component of an incoming wave in the transverse direction can be written as

$$\psi^{(0)}_{k\perp}(\rho) = \frac{1}{\sqrt{A}}J_0(k_\perp\rho), \tag{3.78}$$

where A is the area and J_0 is a Bessel function. The incoming state, considering only the axial ground state contribution, is

$$\psi^{(0)}_{E_s}(\mathbf{r}) = \phi_0(z)\frac{1}{\sqrt{A}}J_0(k_\perp\rho). \tag{3.79}$$

Since

$$H^{(1)}_0(x) = J_0(x) + iY_0(x), \tag{3.80}$$

and

$$K_0(x) = \frac{i\pi}{2}[J_0(ix) + iY_0(ix)], \tag{3.81}$$

we get

$$\begin{aligned}\psi_{E_s}(\mathbf{r}) &= \phi_0(z)\frac{1}{\sqrt{A}}J_0(k_\perp\rho) \\ &\quad - \frac{\phi_0(z)\phi_0(0)\frac{m}{4\pi\hbar^2}\pi i H_0^{(0)}(k_\perp\rho)\psi^{(0)}_{E>0}(0)}{\phi_0(0)\left[\phi_0(0)\frac{m}{4\pi\hbar^2}\pi i H_0^{(0)}(k_\perp\rho) - \phi_0(0)\frac{m}{4\pi\hbar^2}2K_0\left(\frac{\rho\sqrt{\epsilon_b}}{l_z}\right)\right]|_{\rho\to 0}}.\end{aligned} \tag{3.82}$$

Here, $\psi^{(0)}_{E_s}(0) = \phi_0(0)\frac{1}{\sqrt{A}}J_0(0) = \phi_0(0)\frac{1}{\sqrt{A}}$. Using equations (3.80) and (3.81) in the denominator, we get for $x \to 0$.

$$\psi_{E_s}(\mathbf{r}) = \phi_0(z)\frac{1}{\sqrt{A}}\left[J_0(k_\perp\rho) - \frac{\pi i}{\pi i + \ln\left(\frac{\epsilon_b}{\epsilon_\perp}\right)}H_0^{(1)}(k_\perp\rho)\right] \tag{3.83}$$

for a scattering state of relative kinetic energy $\frac{\hbar^2 k_\perp^2}{m} = \epsilon_\perp\hbar\omega_z$. A comparison to equation (3.18) then yields the two-dimensional scattering amplitude

$$f = \frac{4\pi}{\pi i + \ln\frac{\epsilon_b}{\epsilon_\perp}}. \tag{3.84}$$

3.3.3 Comparison of 2D dimer theory with experiment

In a prior experiment conducted by our group, radio-frequency (rf) spectra were obtained for a 50-50 mixture of the two lowest hyperfine states denoted by 1 and 2, by driving transitions to an initially empty hyperfine state 3, and measuring the depletion of state 2 for different magnetic fields which scan the spectrum of weakly bound Cooper pairs and tightly bound molecular dimers. For this scenario, the two possible outcomes are a (1,2) bound-to-(1,3) bound state or a (1,2) bound-to-(1,3) free state. At 720 G, well below the Feshbach resonance, the 1-2 dimer binding

energy E_b is larger than the local Fermi energy, and the observed spectra exhibit the expected threshold form, arising from the dissociation of 1-2 dimers into 1-3 scattering states, as shown in Figure 3.3 below.

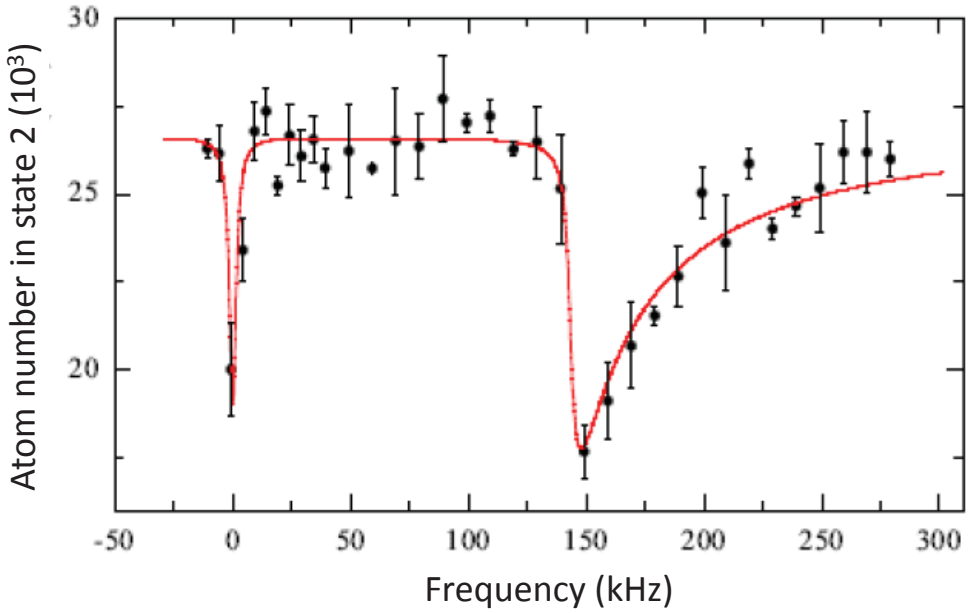

FIGURE 3.3: RF spectra in a 1-2 mixture for a $2 \rightarrow 3$ transition in a quasi-2D Fermi gas near 720 G. The left resonance occurs at the bare atomic resonance and the threshold resonance spectrum on the right is in very good agreement with predictions for molecular dimers.

The contribution to the spectrum from a dimer-to-dimer transition is determined by computing the corresponding fraction ϵ_{bb}. In the weak-binding approximation, including only the axial ground state part of the dimer wave function, we obtain [59]

$$\epsilon_{bb}(q) = \frac{q^2}{4\sinh^2(q/2)}, \tag{3.85}$$

where $q \equiv \ln(\epsilon_b^{13}/\epsilon_b^{12})$ for a $2 \rightarrow 3$ transition in a 1-2 mixture. The measured spectra at 720 G are shown in Figure 3.3. At this magnetic field, the molecular binding energy is much larger than the local Fermi energy. For the trap depth used, the bound-to-free transitions dominate the spectra. Consistent with our calculation in

Table 3.1 earlier in this chapter for the same field, we see that the resonance near 150 kHz is well fit by a threshold function using the calculated 1-2 and 1-3 dimer binding energies for the 12-bound state and 13-scattering states

$$I_{bf}(\nu) = \frac{\epsilon_b^{12}\nu_z}{\nu^2}\frac{q^2\theta\left(\nu-\epsilon_b^{12}\nu_z\right)}{\left[q-\ln\left(\frac{\nu}{\epsilon_b^{12}\nu_z}-1\right)\right]^2+\pi^2}, \tag{3.86}$$

where ν is the radio frequency in Hz, relative to the bare atomic transition frequency and $E_b^{12} = \epsilon_b^{12}h\nu_z$ is the 1-2 dimer binding energy in Hz. We relegate further details, including plots of ϵ_{bb}, and data analysis for intermediate magnetic fields to the Supplementary Material in reference [39] and Chapters 2 and 6 of reference [59].

3.4 BCS theory in Two Dimensions

In this section, we extend our analysis of a two-body bound state above, to include the pairing in the many-body ground state for a two dimensional gas. Our treatment deals with the homogeneous case, and takes into account only two-body interactions for atoms in different hyperfine states. We refer the interested reader to a three dimensional version of BCS theory in references [61], providing in the following paragraph only the key results.

For a 3D Fermi gas, the BCS ground state is given by

$$|\psi_G\rangle = \prod_{\mathbf{k}=\mathbf{k}_1,\ldots,\mathbf{k}_M}\left(u_{\mathbf{k}} + v_{\mathbf{k}}c^*_{\mathbf{k}\uparrow}c^*_{-\mathbf{k}\downarrow}\right)|\phi_0\rangle, \tag{3.87}$$

with M denoting the total number of states. The creation operator $c^*_{\mathbf{k}\uparrow}$ creates a spin up state with momentum $\mathbf{k}$. The annihilation operator $c_{\mathbf{k}\uparrow}$ empties the corresponding state. Here, $u_{\mathbf{k}}$ and $v_{\mathbf{k}}$ are complex constants of the quasiparticle operators which satisfy $|u_{\mathbf{k}}|^2 + |v_{\mathbf{k}}|^2 = 1$. The probability of pair $(\mathbf{k}_\uparrow, -\mathbf{k}_\downarrow)$ occupation is $|v_{\mathbf{k}}|^2$, while the probability that it is unoccupied is $1 - |v_{\mathbf{k}}|^2$. Denoting the bare interaction

strength by U_0, and the pairing gap by Δ_0, the gap equation is given by

$$-\frac{\Delta_0}{U_0} = \frac{1}{V}\sum_{\mathbf{k}} u_k v_k^* \left\{N\left(\hbar\omega_{\mathbf{k}\uparrow}\right) - \left[1 - N\left(\hbar\omega_{\mathbf{k}\downarrow}\right)\right]\right\}, \tag{3.88}$$

and the three-dimensional BCS number equation which determines the chemical potential of the particles in state $|\uparrow\rangle$ is given by

$$n_\uparrow = \frac{1}{V}\sum_{\mathbf{k}} \left\{|u_k|^2 N\left(\hbar\omega_{\mathbf{k}\uparrow}\right) + |v_k|^2\left[1 - N\left(\hbar\omega_{\mathbf{k}\downarrow}\right)\right]\right\}. \tag{3.89}$$

The chemical potential of particles in state $|\downarrow\rangle$ can be similarly determined by substituting $\uparrow$ with $\downarrow$. In equations (3.88) and (3.89),

$$u_k = \frac{1}{\sqrt{2}}\left(1 + \frac{\xi_{\mathbf{k}}}{\sqrt{\xi_k^2 + |\Delta_0|^2}}\right)^{1/2}, \tag{3.90}$$

and

$$v_k^* = -\frac{\Delta_0}{|\Delta_0|}\frac{1}{\sqrt{2}}\left(1 - \frac{\xi_{\mathbf{k}}}{\sqrt{\xi_k^2 + |\Delta_0|^2}}\right)^{1/2}. \tag{3.91}$$

The factor $N\left(\hbar\omega_{\mathbf{k}}\right) = 1/\left(\exp\left[\beta\hbar\omega_{\mathbf{k}}\right] + 1\right)$ is the Fermi distribution for the quasi-particles. At zero temperature, where no excitations occur, $N \to 0$, and the gap equation reduces to

$$-\frac{1}{U_0} = \frac{1}{2V}\sum_{\mathbf{k}'} \frac{1}{\sqrt{\xi_{k'}^2 + |\Delta_0|^2}}. \tag{3.92}$$

Similarly, the number equation reduces to

$$n_\uparrow = n_\downarrow = \frac{1}{V}\sum_{\mathbf{k}'} |v_{k'}|^2. \tag{3.93}$$

Using the form for v_k from equation (3.91) in equation (3.93) yields

$$n_\uparrow = \frac{1}{2V}\sum_{\mathbf{k}'}\left(1 - \frac{\xi_{k'}}{\sqrt{\xi_{k'}^2 + |\Delta_0|^2}}\right). \tag{3.94}$$

The zero-temperature 2D BCS theory results follow by making the substitutions $V \to A$ and $\mathbf{k} \to \mathbf{k}_\perp$. The two-dimensional BCS gap equation is thus given by

$$-\frac{1}{U_0} = \frac{1}{2A}\sum_{\mathbf{k}'_\perp} \frac{1}{\sqrt{\xi^2_{k'_\perp} + |\Delta|^2}}, \tag{3.95}$$

and the number equation by

$$n_\uparrow = n_\downarrow = \frac{1}{2A}\sum_{\mathbf{k}'_\perp} \left(1 - \frac{\xi_{k'_\perp}}{\sqrt{\xi^2_{k'_\perp} + |\Delta|^2}}\right), \tag{3.96}$$

The T-matrix for the relative motion between the two particles as

$$T_{\mathbf{k}'_\perp \mathbf{k}_\perp} = U_{\mathbf{k}'_\perp \mathbf{k}_\perp} + \sum_{\mathbf{k}''_\perp} \frac{U_{\mathbf{k}'_\perp \mathbf{k}''_\perp} T_{\mathbf{k}'_\perp \mathbf{k}''_\perp}}{E_{\mathbf{k}_\perp} - E_{\mathbf{k}''_\perp} + i\epsilon}, \tag{3.97}$$

where the two-body kinetic energy is given by $E_{\mathbf{k}} = 2\epsilon_{\mathbf{k}}$, and the two-body interaction by $U(\mathbf{x}_{\perp 1} - \mathbf{x}_{\perp 2}) = U_0\,\delta(\mathbf{x}_{\perp 1} - \mathbf{x}_{\perp 2})$. The bare interaction is given by $U_0 \equiv g_0 \frac{\hbar^2}{m}$. For future reference, we denote $\mathbf{x}_\perp \equiv \mathbf{x}_{\perp 1} - \mathbf{x}_{\perp 2}$, which conserves center-of-mass momentum. In equation (3.97), we note that

$$U_{\mathbf{k}'_\perp \mathbf{k}''_\perp} \equiv \frac{1}{A}\int d^2\mathbf{x}_\perp e^{i\left(\mathbf{k}''_\perp - \mathbf{k}'_\perp\right)\cdot \mathbf{x}_\perp} U_0 \delta(\mathbf{x}_\perp) = \frac{U_0}{A}. \tag{3.98}$$

If we denote the physical interaction strength by T_{2B}, equation (3.97) can be written as

$$T_{\mathbf{k}'_\perp \mathbf{k}_\perp} \equiv \frac{T_{2B}(\mathbf{k}_\perp)}{A}. \tag{3.99}$$

The bare interaction is then renormalized using

$$\frac{1}{U_0} = \frac{1}{T_{2B}(\mathbf{k}_\perp)} - \frac{1}{2}\frac{1}{A}\sum_{\mathbf{k}'_\perp} \frac{1}{\epsilon_{\mathbf{k}'_\perp} - \epsilon_{\mathbf{k}_\perp}}. \tag{3.100}$$

Substituting for $\frac{1}{U_0}$ from equation (3.95) into equation (3.100) leads to the two-dimensional gap equation

$$-\frac{1}{T_{2B}\left(\mathbf{k}_{\perp}\right)}=\frac{1}{2A}\sum_{\mathbf{k}'_{\perp}}\left(\frac{1}{\sqrt{\xi^2_{k'_{\perp}}+|\Delta|^2}}-\frac{1}{\epsilon_{\mathbf{k}'_{\perp}}-\epsilon_{\mathbf{k}_{\perp}}}\right), \tag{3.101}$$

where the summation over all momentum space in two dimensions

$$\sum_{\mathbf{k}'_{\perp}}\rightarrow\frac{A}{(2\pi)^2}\int_0^{\infty}2\pi k'_{\perp}dk'_{\perp}, \tag{3.102}$$

leads to

$$-\frac{1}{T_{2B}\left(\mathbf{k}_{\perp}\right)}=\frac{1}{4\pi}\int_0^{\infty}dk'_{\perp}k'_{\perp}\left(\frac{1}{\sqrt{\xi^2_{k'_{\perp}}+|\Delta|^2}}-\frac{1}{\epsilon_{\mathbf{k}'_{\perp}}-\epsilon_{\mathbf{k}_{\perp}}}\right), \tag{3.103}$$

with the kinetic energy given by $\epsilon_{k'_{\perp}}=\frac{\hbar^2k'^2_{\perp}}{2m}$ and $d\epsilon_{k'_{\perp}}=\frac{\hbar^2}{m}k'_{\perp}dk'_{\perp}$, we obtain

$$-\frac{4\pi\hbar^2}{mT_{2B}\left(k_{\perp}\right)}=-\pi i+\ln\left(\frac{2\epsilon_{k_{\perp}}}{|\Delta|}\right)-\ln\left[\sqrt{\frac{\mu^2}{|\Delta|^2}+1}-\frac{\mu}{|\Delta|}\right]. \tag{3.104}$$

Equation (3.99) can be found from the 2D scattering amplitude

$$T_{2B}(k_{\perp})=\frac{4\pi\hbar^2}{m}\frac{1}{\pi i+\ln\left[\epsilon_b/(2\epsilon_{\perp})\right]} \tag{3.105}$$

with $\epsilon_{\perp}=2\epsilon_{k_{\perp}}$ and ϵ_b the dimer binding energy. Comparing equation (3.105) with equation (3.104), we end up with the exact result of the 2D BCS gap equation for any μ

$$\epsilon_b=\sqrt{\mu^2+|\Delta|^2}-\mu. \tag{3.106}$$

Since $\epsilon_b\equiv E_b$, where E_b is the binding energy of the dimer pair, we obtain

$$E_b=\sqrt{\mu^2+|\Delta|^2}-\mu. \tag{3.107}$$

From Chapter 2, we learnt that the local density of a Fermi gas is given by

$$n_{\uparrow} = \frac{k_{F\perp}^2}{4\pi}, \tag{3.108}$$

which leads to a local Fermi energy of

$$E_{F\perp} = \frac{\hbar^2 k_{F\perp}^2}{2m} = 2\pi \frac{\hbar^2}{m} n_{\uparrow}. \tag{3.109}$$

Using our results for the local density from the 2D BCS number equation, given by equation (3.96), in equation (3.109), we obtain

$$E_{F\perp} = 2\pi \frac{\hbar^2}{m} \frac{1}{2A} \sum_{\mathbf{k}_{\perp}^{'}} \left(1 - \frac{\xi_{k_{\perp}^{'}}}{\sqrt{\xi_{k_{\perp}^{'}}^2 + |\Delta|^2}} \right). \tag{3.110}$$

Once more, converting summation over momentum vectors $\mathbf{k}_{\perp}^{'}$ to an integral, equation (3.102), we obtain the exact result for the BCS number equation

$$E_{F\perp} = \frac{1}{2} \left[\sqrt{\mu^2 + |\Delta|^2} + \mu \right]. \tag{3.111}$$

Eliminating the $\sqrt{\mu^2 + |\Delta|^2}$ term from equations (3.107) and (3.111) leads to the single atom chemical potential

$$\mu = E_{F\perp} - \frac{E_b}{2}. \tag{3.112}$$

Using the form for μ from equation (3.112) in equation (3.107) leads to the gap equation

$$|\Delta|^2 = 2E_{F\perp} E_b. \tag{3.113}$$

3.4.1 Breakdown of 2D BCS theory in radio-frequency spectral shifts

In a simple BCS approximation to the rf spectrum in two dimensions at zero temperature, the trap-averaged rf transition rate to excite an atom from one populated

in a 50-50 mixture to an unpopulated noninteracting final state is

$$\int_0^\infty d^2x_\perp |\Delta|^2 \theta \left[\hbar\omega + \mu - \sqrt{\mu^2 + |\Delta|^2}\right] /\omega^2, \tag{3.114}$$

where ω is the radio frequency relative to the bare atomic transition frequency, μ is the chemical potential, and Δ is the pairing gap for the initial mixture. Alternatively, this implies

$$\hbar\omega = \sqrt{\mu^2 + |\Delta|^2} - \mu. \tag{3.115}$$

Hence, we obtain by comparing equations (3.107) and (3.115)

$$\hbar\omega = E_b. \tag{3.116}$$

BCS theory therefore predicts a dimer spectrum for tightly bound pairs, where many-body effects are noticeably absent. It should be emphasized that the experimental scenario encountered in our trap conditions is one where the interparticle spacing is smaller than the dimer pair size. Near the Feshbach resonance, the atoms scatter off each other within the dimer, giving rise to polarons, which we describe in a later section.

Before turning to a description for this rich system, we consider some results obtained close to the Feshbach resonance at 832 G. At this magnetic field, the measured radio frequency spectra were consistent with neither dimer transitions nor 2D BCS theory. As shown in Figure 3.3, line shapes were fit to each of the two observed resonances to determine the frequency shift $\Delta\nu$ between them. A threshold line shape is used for the bare atom peak, which is convolved with a narrow Lorentzian profile. A Lorentzian profile with a larger width is used for the second resonance. The results for $\Delta\nu$ do not agree with the predictions for dimer-to-dimer transitions, $h\Delta\nu_{dimer} = E_b^{12} - E_b^{13}$, and cannot be fit by $h\Delta\nu_{dimer} = \lambda_{12}E_b^{12} - \lambda_{13}E_b^{13}$ for any

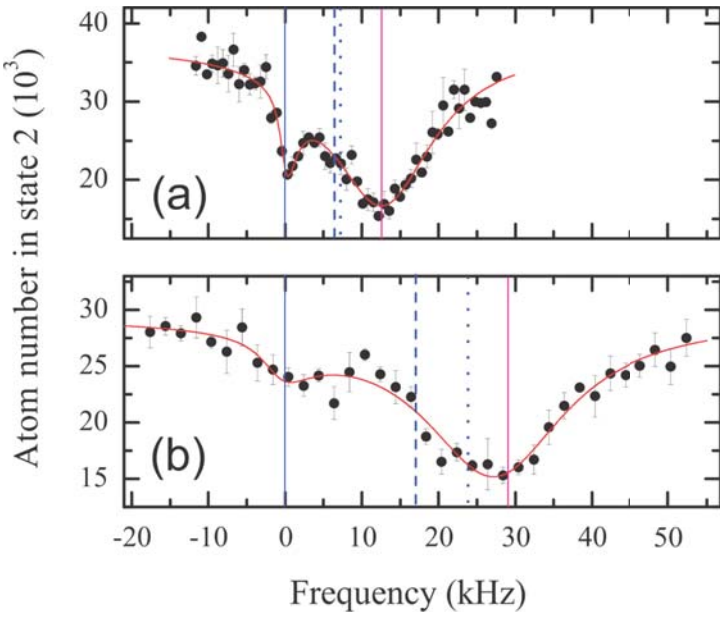

FIGURE 3.4: Radio-frequency spectra for a 12 mixture ($12 \rightarrow 13$ transition) near the Feshbach resonance at 832 G, versus trap depth U_0. The atom number remaining in state 2 is shown versus radio frequency: (a) $U_0 = 21\ \mu$ K, $\nu_z = 24.5$ kHz; (b) $U_0 = 280\ \mu$ K, $\nu_z = 82.5$ kHz. Blue vertical lines show the measured bare atomic resonance position(solid)and the predicted frequencies for confinement-induced dimers: bound to bound transition resonance $h\nu = E_b^{12} - E_b^{13}$ (dashed line) and the threshold for the bound-to-free transition $h\nu = E_b^{12}$ (dotted line). The dashed and dotted lines do not match any features in the spectra. Red vertical lines show the predictions of polaron theory, described in section 3.5, in excellent agreement with the observed resonances in the data.

fixed scale factors λ_{12}, λ_{13}.

However, we now turn our attention to the microscopic description of an impurity scattering off a Fermi sea of majority atoms. Dubbed the Fermi polaron, this description of the Fermi gas provided excellent fits to the rf spectrum [39].

3.5 Polaron description of a quasi-2D Fermi gas

We consider the basic Hamiltonian for a polaron description of a dilute, two-component mixture of fermions interacting via a short range potential $V(r)$. If the range of the potential, R, is small compared to the interparticle spacing $1/k_F$, we can treat the

Table 3.2: Parameters for the radio-frequency spectra: magnetic field B; trap depth U_0; axial frequency ν_z; total number of atoms per pancake trap N_{site}; transverse Fermi energy $E_{F\perp} = h\nu_\perp\sqrt{N_{site}}$; E_b^{12} and E_b^{13} are the dimer binding energies in kHz, for $\nu_\perp/\nu_z = 1/25$ calculated using the methods in the prior section, $\Delta\nu_{dimer} = E_b^{12} - E_b^{13}$, and ϵ_{bb} is the bound dimer to bound dimer transition fraction. Measured frequency shifts between resonances, $\Delta\nu_{meas}$ do not agree with dimer predictions $\Delta\nu_{dimer}$.

B(G)	$U_0(\mu$K)	ν_z (kHz)	N_{site}	$E_{F\perp}(\mu$K)	E_b^{12}	E_b^{13}	$\Delta\nu_{dimer}$ (kHz)	$\Delta\nu_{meas}$ (kHz)	ϵ_{bb}
832	24.4	24.5	1620	1.97	7.25	0.81	6.44	12.3	0.66
832	742	135	1800	11.47	39.1	12.45	26.65	38.8	0.89

potential as a δ-function. The Fourier transform $V(\mathbf{k})$ of the potential is constant, which we denote by U_0. In two dimensions, U_0 is the interaction strength, $U_0 = g_0\frac{\hbar^2}{m}$, where g_0 is dimensionless and U_0/A has the dimensions of energy.

$$H = \sum_{\mathbf{k}_\perp\sigma} \epsilon_{\mathbf{k}_\perp}\hat{\mathbf{c}}^\dagger_{\mathbf{k}_\perp\sigma}\hat{\mathbf{c}}_{\mathbf{k}_\perp\sigma} + \frac{U_0}{A}\sum_{\mathbf{k_1}_\perp\mathbf{k}'_{\mathbf{1}\perp}\mathbf{k_2}_\perp\mathbf{k}'_{\mathbf{2}\perp}} \hat{\mathbf{c}}^\dagger_{k'_{1\perp}\uparrow}\hat{\mathbf{c}}^\dagger_{k'_{2\perp}\downarrow}\hat{\mathbf{c}}_{k_{2\perp}\downarrow}\hat{\mathbf{c}}_{k_{1\perp}\uparrow}\delta_{\mathbf{k}_{1\perp}+\mathbf{k}_{2\perp},\mathbf{k}'_{1\perp}+\mathbf{k}'_{2\perp}}, \quad (3.117)$$

where the first part of the Hamiltonian is the total kinetic energy of the individual atoms and the second term describes collisions of two atoms with initial momentum $\mathbf{k}_{1\perp} + \mathbf{k}_{2\perp}$ and final momentum $\mathbf{k}'_{1\perp} + \mathbf{k}'_{2\perp}$. The labels $\sigma = \uparrow, \downarrow$ denote spin states, A is the quantization area of the 2D system for box normalized states, with $\mathbf{c}^\dagger$ and $\mathbf{c}$ the usual creation and annihilation operators for fermions with momentum $\mathbf{k}_\perp$ and spin σ.

Applying the Chevy ansatz [54], with one impurity spin down atom in a Fermi sea of spin up atoms, we have

$$|E_\downarrow\rangle = \varphi_0|0\rangle_\downarrow|FS\rangle_\uparrow + \sum_{q_\perp<k_{F\perp}<k_\perp} \varphi_{\mathbf{k}_\perp\mathbf{q}_\perp|\mathbf{q}_\perp-\mathbf{k}_\perp\rangle_\downarrow}\hat{\mathbf{c}}^\dagger_{k\perp\uparrow}\hat{\mathbf{c}}_{q\perp\uparrow}|FS\rangle_\uparrow \quad (3.118)$$

In the first term, $|0\rangle_\downarrow$ is a spin $\downarrow$ impurity with zero momentum, and $|FS\rangle_\uparrow$ is a Fermi sea state with 0 momentum. The second term describes a simple interaction

between the impurity and the Fermi sea. The impurity knocks a spin up atom with momentum $q_\perp$ out of the Fermi sea and creates a hole. At the same time, it creates a particle with momentum $\mathbf{k}_\perp$ above the Fermi momentum $\mathbf{k}_{F\perp}$. This particle-hole pair Fermi sea has momentum $\mathbf{P}_{FS\uparrow} = \mathbf{k}_\perp - \mathbf{q}_\perp$ and the impurity has momentum $\mathbf{P}_{\perp\downarrow} = \mathbf{q}_\perp - \mathbf{k}_\perp$ which preserves the net zero momentum of the system zero. We note however, that this is only a good approximation. This state is not the exact eigenstate for a single polaron.

To find the polaron eigenstate $|E_\downarrow\rangle$ with energy $E_\downarrow$, we take the expectation value of H and minimize under variation of parameters φ_0 and $\varphi_{\mathbf{k}_\perp\mathbf{q}_\perp}$ with the constraint of a constant norm

$$\langle E|E\rangle = |\varphi_0|^2 + \sum_{\mathbf{q}_\perp<\mathbf{k_{F\perp}}<\mathbf{K}_\perp} |\varphi_{\mathbf{k}_\perp\mathbf{q}_\perp}|^2 = 1. \tag{3.119}$$

The quantity to minimize is $\langle E_\downarrow|H|E_\downarrow\rangle - E_\downarrow \langle E|E\rangle$. In the 2D scenario, this yields [39]

$$E_\downarrow = \frac{1}{A}\sum_{q\perp<k_{F\perp}} f(E_\downarrow, \mathbf{q}_\perp), \tag{3.120}$$

with

$$f^{-1}(E_\downarrow, \mathbf{q}_\perp) = \frac{1}{U_0} + \frac{1}{A}\sum_{\mathbf{k}_\perp>\mathbf{k}_{F\perp}} \frac{1}{\epsilon_{\mathbf{k}_\perp} - \epsilon_{\mathbf{q}\perp} + \epsilon_{\mathbf{q}\perp-\mathbf{k}\perp} - E}, \tag{3.121}$$

where the bare interaction strength $U_0 = g_0\hbar^2/m$ and g_0 is dimensionless and $\epsilon_{\mathbf{k}\perp} = \frac{\hbar^2}{2m}k_\perp^2$. We renormalize the $1/U_0$ using

$$\frac{1}{U_0} = \frac{1}{T_{2B}(k_{\perp 0})} - \frac{1}{2A}\sum_{\mathbf{k}_\perp} \frac{1}{\epsilon_{\mathbf{k}_\perp} - \epsilon_{\mathbf{k}_{\perp 0}}}. \tag{3.122}$$

Here T_{2B} is the two-dimensional T-matrix element, obtained from our dimer scatter-

ing states

$$T_{2B}(k_{\perp 0}) = \frac{4\pi\hbar^2}{m}\frac{1}{\pi i + \ln(\epsilon_b/\epsilon_{\perp 0})}, \tag{3.123}$$

and $\epsilon_{\perp 0} \equiv 2\frac{\hbar^2}{2m}k_{\perp 0}^2 = 2\epsilon_{\mathbf{k}_{\perp 0}}$ is the relative kinetic energy of a colliding atom pair. We separate the sum of $k_\perp$ of equation (3.122) into two parts $\sum_{\mathbf{k}_\perp} = \sum_{\mathbf{k}_\perp < \mathbf{k}_{F\perp}} + \sum_{\mathbf{k}_\perp > \mathbf{k}_{F\perp}}$. The $\sum_{\mathbf{k}_\perp < \mathbf{k}_{F\perp}}$ part can be written as $\frac{1}{A}\sum_{\mathbf{k}_\perp < \mathbf{k}_{F\perp}} \rightarrow \frac{1}{A}\frac{A}{(2\pi)^2}k_\perp dk_\perp d\phi$,

$$\begin{aligned}
\frac{1}{2A}\sum_{k_\perp < k_{F\perp}} \frac{1}{\epsilon_{k_\perp} - \epsilon_{k_{\perp 0}}} &= \frac{1}{2A}\frac{A}{(2\pi)^2}\int_0^{k_{F_\perp}} \frac{dk_\perp k_\perp (2\pi)}{\frac{\hbar^2}{2m}(k_\perp^2 - k_{\perp 0}^2)} \\
&= \frac{m}{2\pi\hbar^2}\int_0^{k_{F_\perp}} \frac{dk_\perp k_\perp}{k_\perp^2 - k_{\perp 0}^2} \\
&= \frac{m}{4\pi\hbar^2}\ln\left(\frac{k_{F_\perp}^2 - k_{\perp 0}^2}{-k_{\perp 0}^2}\right)
\end{aligned} \tag{3.124}$$

Using equation (3.124) in equation (3.122), we obtain

$$\begin{aligned}
f^{-1}(E, \mathbf{q}_\perp) &= \frac{m}{4\pi\hbar^2}\left[\pi i + \ln\left(\frac{\epsilon_b}{\epsilon_{\perp 0}}\right) - \ln\left(\frac{k_{F_\perp}^2 - k_{\perp 0}^2}{-k_{\perp 0}^2}\right)\right] \\
&\quad \frac{1}{A}\sum_{\mathbf{k}_\perp > \mathbf{k}_{\mathbf{F}\perp}}\left[\frac{1}{\epsilon_{\mathbf{k}_\perp} - \epsilon_{\mathbf{q}_\perp} + \epsilon_{\mathbf{q}_\perp - \mathbf{k}_\perp} - E} - \frac{1}{2(\epsilon_{\mathbf{k}_\perp} - \epsilon_{\mathbf{k}_{\perp 0}})}\right].
\end{aligned} \tag{3.125}$$

After some mathematical manipulation, we end up with

$$f^{-1}(E, \mathbf{q}_\perp) = \frac{m}{4\pi\hbar^2}\left[\ln\left(\frac{\epsilon_b}{2\epsilon_{F\perp}}\right) - \ln\left(1 - \frac{k_{\perp 0}^2}{k_{F_\perp}^2}\right) + I\right], \tag{3.126}$$

where

$$I = \frac{1}{\pi}\int_{k_{F_\perp}}^{\infty} dk_\perp k_\perp \left[\int_0^{2\pi} \frac{d\phi}{k_\perp^2 - q_\perp k_\perp \cos\phi - \frac{m}{\hbar^2}E} - \frac{2\pi}{k_\perp^2 - k_{\perp 0}^2}\right]. \tag{3.127}$$

If we let $k_\perp = xk_{F_\perp}$ and $y = q_\perp/k_{F_\perp}$, we have

$$I = \frac{1}{\pi}\int_1^\infty dxx\left[\int_0^{2\pi}\frac{d\phi}{x^2 - xycos\phi - \frac{E}{2\epsilon_{F_\perp}}} - \frac{2\pi}{x^2 - k_{\perp 0}^2/k_{F\perp}^2}\right]. \tag{3.128}$$

After some algebra, we obtain

$$I = \ln(2) + \ln\left(1 - \frac{k_{\perp 0}^2}{k_{F_\perp}^2}\right) - \ln\left[\sqrt{\left(1-\frac{\epsilon}{2}\right)^2 - y^2} + \left(1 - \frac{\epsilon}{2} - \frac{y^2}{2}\right)\right]. \tag{3.129}$$

Since $y = q_\perp/k_{F_\perp}$, $\epsilon = E/\epsilon_{F_\perp}$, we put I back into f^{-1} and get

$$f^{-1}(E, q_\perp) = \frac{m}{4\pi\hbar^2}\left\{\ln\left(\frac{\epsilon_b}{\epsilon_{F_\perp}}\right) - \ln\left[\sqrt{\left(1-\frac{\epsilon}{2}\right)^2 - y^2} + \left(1 - \frac{\epsilon}{2} - \frac{y^2}{2}\right)\right]\right\}. \tag{3.130}$$

We can see that f^{-1} is independent of $k_{F_\perp}$ as it should be. The polaron binding energy can thus be written as

$$\begin{aligned}
E_\downarrow &= \frac{1}{A}\frac{A}{(2\pi)^2}\int_0^{k_{F_\perp}} dq_\perp 2\pi q_\perp f(E_\downarrow, q_\perp) \\
&= \frac{1}{2\pi}\int_0^{k_{F_\perp}} dq_\perp q_\perp f(E_\downarrow, q_\perp) \\
&= \frac{k_{F_\perp}^2}{2\pi}\int_0^1 dyyf\left(\epsilon = \frac{E_\perp}{\epsilon_{F_\perp}}, y\right) \\
&= \frac{k_{F_\perp}^2}{2\pi}\frac{4\pi\hbar^2}{m}\int_0^1 \frac{dyy}{\ln\left(\frac{\epsilon_b}{\epsilon_{F_\perp}}\right) - \ln\left[\sqrt{\left(1-\frac{\epsilon}{2}\right)^2 - y^2} + \left(1 - \frac{\epsilon}{2} - \frac{y^2}{2}\right)\right]}.
\end{aligned} \tag{3.131}$$

If we set $u = y^2$, we can get a dimensionless expression for the polaron binding energy. Recalling $\epsilon = \frac{E_\downarrow}{E_{F\perp}}$, we get

$$\epsilon \equiv \sum(\epsilon) = -2\int_0^1 \frac{du}{\ln\left(\frac{E_b}{E_{F\perp}}\right) + \ln\left[\sqrt{\left(1-\frac{\epsilon}{2}\right)^2 - u} + \left(1-\frac{\epsilon}{2}-\frac{u}{2}\right)\right]}, \tag{3.132}$$

which determines the polaron energy $E_\downarrow$. We illustrate the polaron binding energy (in units of $(E_{F\perp})$) as a function of the interaction parameter $\ln(E_b/E_{F\perp})$ in Figure 3.5. An analytic form of the polaron binding energy [55],

$$E_p = \frac{-2E_{F\perp}}{\ln\left[1 + 2\frac{E_{F\perp}}{|E_b|}\right]}, \tag{3.133}$$

is used to generate the red dotted line. We use this approximation to study the thermodynamics and generate density profiles for spin-imbalanced quasi-2D Fermi gases in Chapters 5 and 6 of this thesis.

3.5.1 Experimental Fits for Polaron Description of a Quasi-2D Fermi Gas

Returning to figure 3.3, we consider the scenario where polarons and not dimers determine the primary spectral features, so the difference between the initial and final state polaron energies determines the observed frequency shifts. We assume that the coherent part of the spectrum is given by $Z\delta[\hbar\omega - E_p(3,1) + E_p(2,1)]$, where $E_p(i,1)$ is the polaron energy for an impurity atom in state $i = 2,3$ immersed in a bath of state 1. For experiments at 832 G, strong overlap between the initial and final polaron states results in a significant contribution of polaron states to the spectrum.

To calculate the polaron frequency shift, we assume that the peak position is determined by the trap-averaged local Fermi energy E_F, which we take to be proportional to the ideal gas global Fermi energy, $E_F = 0.67E_{F\perp}$, where 0.67 is a fixed fit parameter. As calculated in [39] and equation (3.133), the polaron frequency

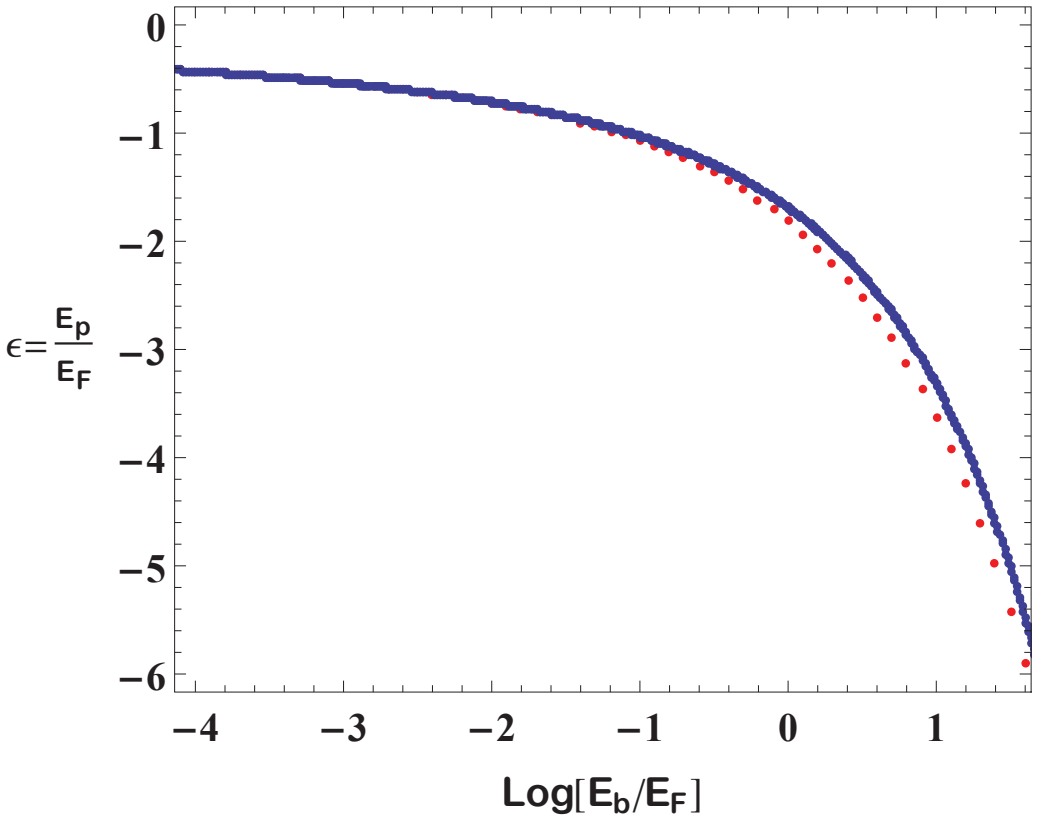

FIGURE 3.5: The polaron binding energy $\epsilon = E_p/(E_{F\perp})$ as a function of the interaction strength parametrized by $ln(E_b/E_{F\perp})$ from equation (3.133), is shown as a blue curve. The red dotted curve shows the case for an approximate form to the polaron energy given by $E_p = \frac{-2E_{F\perp}}{\ln\left[1+2\frac{E_{F\perp}}{|E_b|}\right]}$.

shifts agree very well with the measured frequency shifts at all trap depths.

Table 3.3: Frequency shifts $\Delta\nu$ between the bare atom peak and the second resonance peaks for the radiofrequency spectra shown in Figure 3.3 for 1-2 mixtures near the Feshbach resonance at different trap depths. Trap axial frequencies are given in the ν_z column, while the measured frequency shifts (difference between red and blue vertical solid lines in Figure 3.3) are provided in the $\Delta\nu_{meas}$ column. The polaron frequency shifts are calculated from equation (3.133) assuming a transition from a polaron in state 2 to a polaron in state 3, in a bath of atoms in state 1. Dimer predictions, $\Delta\nu_{dimer}$, as shown in Table 3.2, are provided for comparison.

B(G)	ν_z(kHz)	$\Delta\nu_{meas}$ (kHz)	$\Delta\nu_{polaron}$(kHz)	$\Delta\nu_{dimer}$ (kHz)
832	24.5	12.3	11.6	6.44
832	135	38.8	42.8	26.65

4

Creating and Imaging a quasi-2D Fermi gas

This chapter discusses the technology required to create and image a spin-imbalanced quasi-two dimensional Fermi gas. The reader will be introduced to the atom source, oven and lock system electronics, slower, lasers employed in the experiments, optical setup, MOT and high-field magnet supplies, chopper controller, and automated data-acquisition system. One purpose of this chapter is to provide the reader with a general feel for the layout of the lab, and to introduce some key principles underlying the all-optical trapping, cooling, and imaging of a Fermi gas in a standing wave trap. For the most part, more detailed descriptions of the experimental setup can be found in the theses of previous group members [62, 4, 59]. For example, for details on the vacuum chamber construction and measurements, the reader could refer to the theses of Bason Clancy [3] and Le Luo [4].

The new implementations of this work in the lab, and described in detail in this chapter, are of high resolution, spin-selective absorption imaging, which enabled a density analysis of the individual pancake sites as discussed later in Chapters 6 and 7, and radiofrequency sweeps for the generation of spin-imbalanced mixtures. The placement of two pairs of cylindrical telescopes in the trapping beam path allowed

control of the trapping beam aspect ratio and curvatures. Furthermore, the installation of a current sensor aided in monitoring of magnetic field variations, which came in particularly handy for our radiofrequency spectroscopic investigations.

4.1 Atom and Light Sources

As described in Chapter 2, the source of atoms used in our labs are solid chunks of 95 percent enriched ^{6}Li, purchased from Sigma-Aldrich (P/N 340421). These are placed in an oven with a wick (316 stainless steel mesh, 300 cells per inch) that recirculates liquid lithium from the exit of the nozzle back into the oven. To ensure adequate atom flux into the main chamber, a temperature gradient profile with an active region temperature of approximately 390 degrees Celcius is achieved with a DC power supply, a current controller and coils of heater wires (Omega PN NI80-020-50). The current controller utilises five parallel units of N-channel power MOSFETs (Harris Semiconductor, IRF243).

The thermal velocity of the atoms is too high for them to be captured by the atom traps, necessitating the use of a counter-propagating laser beam in conjunction with a Zeeman slower to decelerate the atoms over a short distance. The slowing process involves Zeeman tuning the energy levels of the atoms to account for the Doppler shift they experience during deceleration. The stream of atoms at the end of the slower are travelling between 30 and 40 meters per second. To further cool the atoms, a combination of magnetic fields and laser beams are used to form a Magneto-Optic Trap (MOT), which we discuss in detail in a later section.

The light used to generate optical beams near the D_2 resonance in ^{6}Li for atom trapping is produced by a Coherent 899-21 dye laser, which is pumped by a Coherent Verdi V-10 diode-pumped solid state laser. The Coherent 899-21 has an autolock active stabilisation system for stable operation at a single frequency with linewidths less than 1 MHz rms. The pump laser outputs up to 10 W of power at 532 nm

and has excellent pointing stability. A typical output pump power for the Verdi is approximately 5.5 W to avoid saturation of the dye. For the dye laser, we utilize 1.17 grams of LD 688 dye dissolved in 1.1 liters of 2-phenoxyethanol, with a peak output power of approximately 900 mW of power in single-mode operation near 671 nm. Over time, degradation of the dye results from repeated pump cycles, necessitating a dye change when the output power drops to approximately 300 mW.

A Coherent DeMaria ElectroOptics Systems Inc. LC100-NV CO_2 laser with a peak output power of 110 Watts at a wavelength of 10.6 μm is used for standing wave trapping beam generation and forced evaporative cooling. Following initial evaporation, a total of 400,000 atoms per spin state are obtained, and after forced evaporation, approximately 50,000 atoms remain. An extensive discussion of the optical layout, noise and trap heating effects, cooling, and electronic control system for this laser has been provided in the thesis of Le Luo; we discuss in here the basic physics of such a trap, some improvements to the beam path, with a focus on the standing wave trap configuration and its characteristics.

4.2 Optical Layout for Dye Laser Beams

The optical layout for the beam generated by the Coherent 899-21 dye laser is shown in Figure 4.1. The light from the dye laser is further subdivided into the locking region beam, slowing beam, MOT and repump beams, and imaging beams.

We point out for now two recurrent beam routing schemes encountered in Figure 4.1: (a) To distribute the power of a laser beam, we employ a half waveplate (HWP) in conjunction with a polarising beam splitting cube (PBS). This configuration splits the beam into two separate beams with perpendicular polarizations. (b) The combination of an acousto-optic modulator (AOM), quarter wave plate (QWP), and a mirror; an AOM diffracts an incoming beam into its multiple orders, the frequency of the beam is chosen by selecting the beam of the appropriate order (usually the

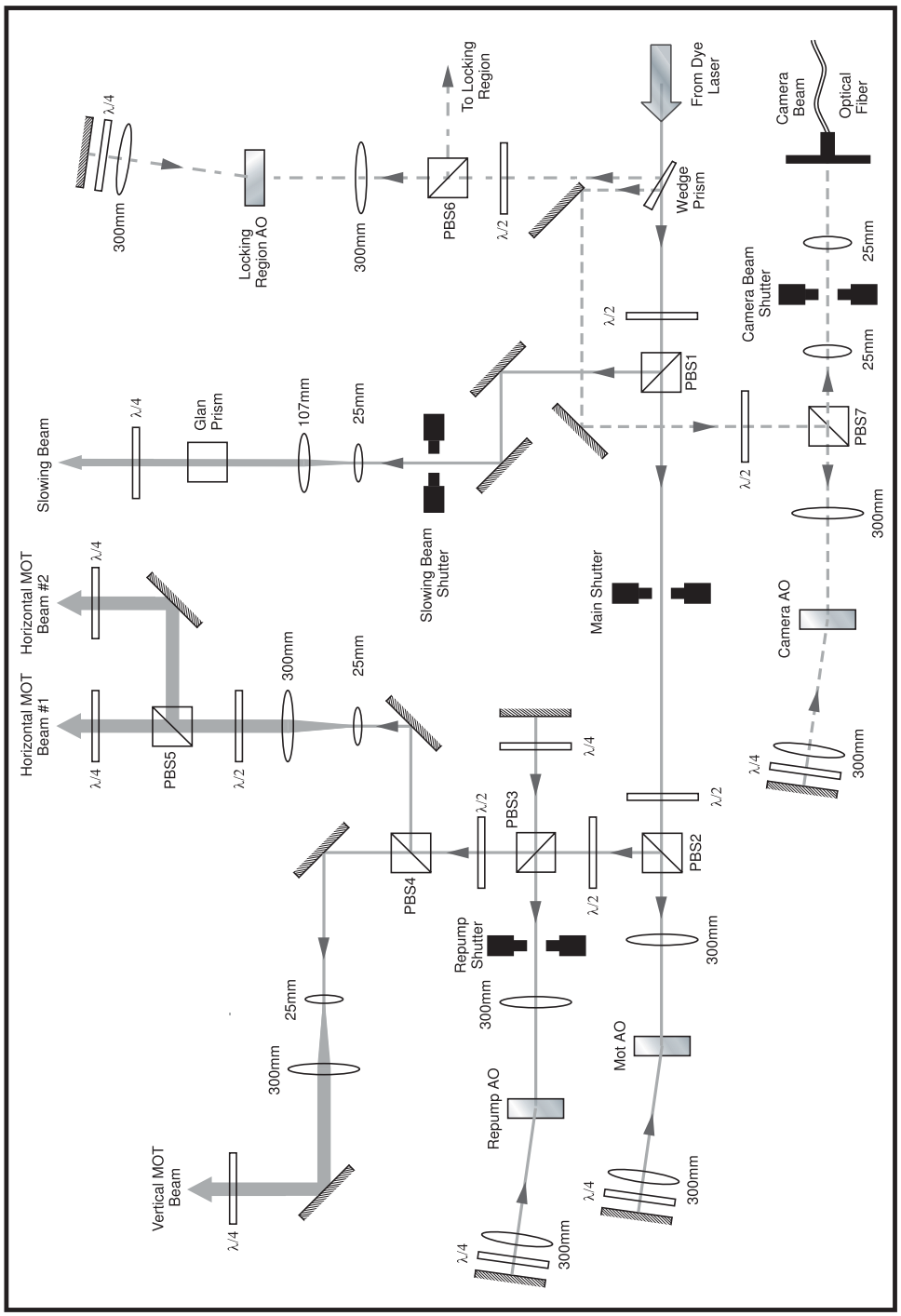

FIGURE 4.1: Optical layout for generating the MOT, slowing, locking region, and camera beams. The solid lines are MOT and slowing beams, the dashed line is the camera beam, which leads to imaging optics that we describe in a later section. The dot-dashed line is the locking region beam. The squares are polarizing beam splitting cubes. The schematic is not to scale [3].

first), and the intensity of the beam is varied by crystal alignment. In both cases, the voltage applied to the crystal sets the nominal frequencies and intensities. A quarter wave plate converts linearly polarized light into circularly polarized light; used together with a mirror, the configuration rotates the polarization of the light by 180 degrees.

The output of the laser is split into two main paths: one for the lock region and imaging beams. The other is composed of the slower, MOT and repump beams. The former path is composed of the reflections off the front and back of a thick glass plate, and contains approximately 4 percent of the total laser power. The latter path is the transmitted beam, which is then directed to a HWP-PBS combination. This combination splits the incident light into the slower and MOT-repump paths. Approximately 100 mW of power is required for the slowing beam, which traverses a telescope configuration to focus the beam at the nozzle of the oven thereby optimizing MOT loading. The output of the laser is locked 200 MHz below resonance for the slower beam, which contains much more power than any sub-beam path with an AOM. A combination of a glan prism and quarter waveplate ensures a nearly perfect circular polarization to address the optical transition in the Zeeman slower.

We now consider in the following subsections some facts on the lock and slower regions, leaving a detailed description of the MOT, repumper, and imaging beams to later sections.

4.2.1 Laser frequency locking

For typical cold atom experiments, the laser frequency should ideally remain stable to within one MHz for several hours. As an added challenge for the experiments described in this work, the laser undergoes two frequency unlock-shift-relock shifts per experimental cycle: once to blow out a spin state prior to forming spin-imbalanced mixtures, and another for the imaging.

To provide a stable lock, approximately 1 - 2 mW of laser power is upshifted by about 200 MHz by a double passed AO and sent into the locking region, which consists of an atomic beam in a vacuum system separate from the main chamber. The DC voltage for AO frequency shift is modulated by a 10 kHz sine wave to provide a reference frequency for a Stanford Research System SR510 lock-in amplifier. The modulation depth is chosen less than 2 percent of the amplitude of the carrier wave to avoid amplitude modulation of the laser power.

A probe beam, upshifted by approximately 200 MHz by a double-passed AOM, passes through a $\lambda/4$ waveplate to produce a circular polarized light beam, which perpendicularly intersects the atomic beam in the locking vacuum chamber. The resulting resonance fluorescence signal is collected by a PMT, which is converted into a voltage signal, before being sent to a lock-in amplifier. The lock-in amplifier outputs a linear error signal, which is used as the error signal for a home-built electronic servo circuit. This circuit also drives the laser reference cavity, which locks the laser frequency to the required frequency corresponding to the maximum fluorescence.

4.2.2 Slower region

Upon exiting from a thermal source, the atoms travel at a speed of about 2 kilometers per second. To slow them down for capture in an atomic trap, we employ a slower, composed of a series of graduated wire coils connected to a Hewlett-Packard 6246B power supply. Built by Bason Clancy and a previous undergraduate in the group, the wire coils are separated by air fins for efficient heat dissipation. The slower beam is first expanded by a telescope before being directed through the vacuum chamber and focused at the nozzle of the oven. Upon exiting the slower, atoms travelling at about 2 kilometers per second upon entering the Zeeman slower can be slowed to approximately 30 meters per second upon exiting the slower, slow enough to be

captured in the next stage of cooling, the work horse for the initial production of cold samples in a variety of atom cooling and trapping experiments: the magneto-optical trap (MOT).

4.3 Creating a Cold Atom Sample

This section begins by exploring the basic physics of a MOT, before going on to describe the trapping beams, implementation requirements, and magnet supplies.

4.3.1 Physics of a MOT

As implied by its name, the trap employs a combination of three-dimensional optical Doppler cooling and spatial magnetic field tuning of optical forces to provide confinement. Figure 4.2 shows a one-dimensional schematic which captures the essential physics of a MOT. For simplicity, we consider atoms in a ground state with total angular momentum $F = 0$, and atoms in the first excited state with total angular momentum $F = 1$. A spherical quadrupole magnetic field splits the degeneracy of the hyperfine states $m_F = -1, 0, 1$, resulting in a linear variation of the energy levels about the center of the trap. In addition to the magnetic field, two counter-propagating red-detuned optical beams with opposite polarizations are applied. The moving atoms absorb photons preferentially from the beam propagating in the opposite direction to their motion, resulting in an overall momentum decrease. As illustrated in Figure 4.2, atoms in the ground state moving to the $z > 0$ region are closer to resonance with the $m_{F'} = -1$ state than the $m_{F'} = 0$ or $m_{F'} = 1$ states. Thus, there is a higher probability for photon absorption from the σ^- beam, and subsequent promotion for ground state atoms to the $m_{F'} = -1$ state.

To estimate the temperature of the MOT, we note that the minimum temperature achievable is set by a balance between the cooling rate and heating rate. We denote the detuning between the laser frequency and atomic resonance frequency in units

of linewidth, $\delta \equiv (\omega - \omega_0)/(\gamma_s/2)$, where $\gamma_s/2$ is the half-width at half-maximum (HWHM) of the Lorentzian factors. The cooling is most effective relative to the heating when $\omega - \omega_0$ is as large as possible. Since

$$\frac{(\omega - \omega_0)}{(\omega - \omega_0)^2 + (\gamma_s/2)^2} = \frac{2}{\gamma_s}\frac{\delta}{\delta^2 + 1}, \tag{4.1}$$

we maximize the δ-dependent factor by differentiation and obtain δ^2=1. Since we want negative detuning, the ideal case is δ=-1, or

$$(\omega - \omega_0)_{opt} = \frac{-\gamma_s}{2}. \tag{4.2}$$

The heating rate can then be shown to be

$$\left(\frac{dE}{dt}\right)_{opt} = \frac{\sigma_0 I}{\hbar\omega} \cdot 2 \cdot \left\{-\frac{\hbar q^2 v_x^2}{\gamma_s} + E_R\right\}. \tag{4.3}$$

At equilibrium, when the average heating rate balances the cooling rate, the mean square velocity must satisfy

$$\frac{\hbar q^2}{\gamma_s}\langle v_x^2\rangle = E_R = \frac{\hbar^2 q^2}{2m}, \tag{4.4}$$

where E_R denotes the recoil energy. Hence, we obtain $(v_x^2)\,(\hbar\gamma_s/2m)$ or

$$\frac{m}{2}\langle v_x^2\rangle = \frac{\hbar\gamma_s}{4} = \frac{k_B T_{Doppler}}{2}, \tag{4.5}$$

where we use the equipartition theorem for the energy in the x-direction. The Doppler limited temperature is then

$$k_B T_{Doppler} = \frac{\hbar\gamma_s}{2}. \tag{4.6}$$

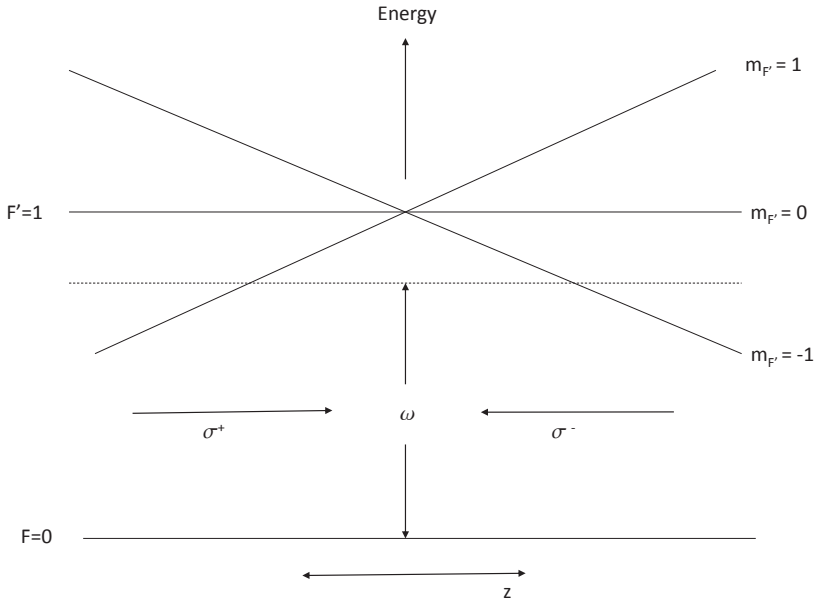

FIGURE 4.2: Schematic of a MOT. An optical beam propagating from left to right has a circular polarization of σ^+ while the counter-propagating beam has a circular polarization of σ^-.

For three-dimensional cooling in the simplest configuration, we use 3 orthogonal sets of counter-propagating beams for cooling, which yields the same limiting temperature in each direction. For ^{6}Li, we have $\gamma_s = 2\pi \times 5.9$ MHz. Using $\hbar\gamma_s = h\gamma_s(Hz)$, we have $T_{Doppler} = 140\mu K$.

For atoms close to the trap center, the net force is inversely proportional to the frequency detuning, with a spatial dependence given by $F = -Kz$. The optimum spring constant, K, is given by

$$K = \frac{\hbar k}{2}\frac{\Delta\mu}{\hbar}\frac{\partial B}{\partial z}, \tag{4.7}$$

with k the wavevector of the laser photon, $\Delta\mu$ the change of the magnetic moment from the lower level to the upper level, and $\frac{\partial B}{\partial z}$ the magnetic field gradient. The maximum size of the MOT is determined by the Zeeman detuning

$$\frac{\Delta\mu}{\hbar}\frac{\partial B}{\partial z}z_{max} = 2\pi\gamma_s. \tag{4.8}$$

Thus, the depth of the MOT is given by

$$U_{max} = \frac{1}{2}K_{opt}z_{max}^2 = \frac{h\gamma_s}{4}kz_{max} = k_B T_{Doppler}\frac{kz_{max}}{2}, \tag{4.9}$$

with $k_B T_{Doppler} = \hbar\gamma_s/2 = 140\mu K$ the limiting temperature for Doppler cooling due to heating arising from spontaneous emission. We estimate the depth of the MOT to be approximately 1 K.

We now proceed to describe the conditions for generating a MOT in the lab.

4.3.2 Generating a MOT

To generate a MOT, an incoming beam first double passes a MOT AO which upshifts the laser frequency by approximately 165 MHz for the optical transition corresponding to the $F = 3/2$ ground state. A HWP-PBS combination directs approximately 25 percent of the incoming power into the repumper AO. Here, the light is further upshifted by approximately 228 MHz to address the transition corresponding to the $F = 1/2$ ground state. Optimal MOT loading is found to occur when the MOT to repump powers are in a 3:1 ratio. The MOT and repumper beams are first recombined before being split once again into three mutually perpendicular beams. Each beam is expanded to approximately 1.5 inches in diameter before being passed through a QWP to generate the requisite polarisation. Upon exiting the vacuum chamber, each beam is passed through a QWP-mirror combination to produce an opposite polarisation to the incoming beam.

Table 4.1: Parameters used for various stages of the MOT. Numbers before brackets denote AO detunings from resonance.

	Loading	**Cooling**	**Pumping**
Detuning	-30 MHz (MOT)	-5 MHz (MOT)	0 (MOT)
	-10 MHz (Repumper)	-5 MHz (Repumper)	Off
Intensity	Full	Decrease	Full
Duration	10 s	5 ms	200 μs
Atom Number	200 x 10^6	N.A.	2 x 10^6

4.3.3 Loading a MOT into an Optical Trap

Prior to starting our experiments, we do our best to ensure that a sufficiently large number of atoms is available in the optical trap. Fulfilling this condition translates to more efficient evaporation, and a better signal-to-noise ratio for imaging. We optimize the transfer of atoms from the MOT to an optical trap in three-steps, termed the loading, cooling, and pumping stages. In the loading stage, we wish to load a maximum number of atoms into the MOT. From equation (4.8), we note that the size of the MOT is proportional to the detuning of the MOT beams, thus we set the detuning beams to be approximately six linewidths below resonance. The next step would be the cooling stage of the MOT, where we seek to compress the volume of the MOT thereby ensuring that only the coldest atoms close to the Doppler limit of 140 μK remain at the bottom of the trap. In the optical pumping stage, the repump beams are completely shut, leaving the MOT beams to pump all atoms into the $F = 1/2$ ground state. The parameters for these stages of a MOT are shown in Table 4.1.

A timing sequence used in this section for daily optimization of the FORT fluorescence, with typical timescales for the three stages of the MOT, is shown in Appendix B. The EXCEL file shows the time points and the duration of each step for the experiment, in units of 10^{-4} s. A total of nine analog channels send user-defined

voltages to the lock region, MOT, rempump, and imaging AOMs, the MOT and high field magnet supplies, and the chopper controller. In addition, there are 24 available digital channels which switch a preset voltage value on or off at various time steps of the experimental sequence.

In addition to the voltage controls described above, we are able to optimize the atom number further by moving the MOT relative to the optical trap. This is done in the horizontal plane with three bias trim coils. A variable resistor with a 2 ohm range in parallel with the bottom MOT magnet coils translates the MOT vertically. Together, these fine controls achieve a perfect overlap of the center of the MOT with the center of the optical trap for maximum loading.

4.4 High Field Magnets

4.4.1 Power Supplies and Current Sensor

The MOT magnet coils are in an anti-Helmholtz configuration and are powered by an Agilent 6651A power supply in constant current mode at 1 V, 12 A. This current produces a magnetic field gradient of 28 G/cm at the center of the trapping region.

The high field magnet coils are run in a Helmholtz configuration and are powered by an Agilent 6691A power supply capable of providing currents as high as 250 A and producing uniform magnetic fields of up to 1300 Gauss. To avoid overheating, interlocks are implemented to monitor the power consumption of the magnets as well as the flow of cooling water. An analog external voltage from 0 to +5 V is used to control the output current of the power supply. When we demand a magnetic field change by sending two different command voltages in sequence, the Agilent power supply has an internal delay, which makes the magnetic field exponentially increase or decrease from the original magnetic field to the final field. The total time for changing magnetic fields is measured to be 0.8 seconds.

In order to optimize loading of the MOT to the FORT, we have found it necessary

to make adjustments to the MOT location particularly following a dye change. To displace the MOT in the horizontal plane, the current through two sets of horizontal trim coils is adjusted with an external power supply. For vertical adjustment of the MOT, a 2-Ohm variable resistor was placed in parallel with the bottom MOT coil to vary the current flow.

To monitor the stability of current flow from the power supply to the magnets, our experiments incorporated an LEM IT 200-S UltraStab current transducer current sensor. A 1 mV variation on the current sensor reading corresponds to a 0.2 G shift in the magnetic field. A typical radio-frequency spectrum consists of 4 runs of 30 randomly sampled data points each, taking approximately 45 seconds per data point, and 90 minutes per complete scan, during which the current sensor reading varies by approximately 370 μV, corresponding to a magnetic field stability of 74 mG.

4.5 Carbon Dioxide Laser Trap

The workhorse trapping laser used in our lab is a Coherent GEM-SELECT 100 carbon dioxide laser which outputs 110 W of power. To allow for higher transverse spatial frequencies to diffract away, creating a better mode prior to entering the AO, the output beam is reflected off two mirrors. This reduces thermal fluctuations of the beam after the AO. The first-order refracted beam from the IntraAction Corporation AGM-4010BG1 AO used to generate the optical trap has an efficiency of 70 percent. This AO is in turn driven by a modified IntraAction GE-4050 RF modulator. The power of the trap at the end of the beam path is user-controlled by appropriately varying the amplitude and frequency (40 MHz and 32 MHz) of the RF waves from the RF modulator. The 32 MHz is used to maintain the temperature of the AO as the power of the 40 MHz is reduced. The temperature compensation allows the beam path to be nominally constant as the trap depth is lowered. To correct for beam ellipticity, two pairs of cylindrical lenses with focal lengths of 50 mm are employed.

The first set of lenses, positioned after the AO, sets the aspect ratio of the beam near the input to the expansion telescope. The second pair of lenses, placed before the expanding telescope, changes the curvature of the optical trap. The optical layout for beam conditioning is shown in Figure 4.3. Typically, we measure an overall efficiency of approximately 50 percent after accounting for losses due to absorption and reflection from lens surfaces, and AO efficiency.

4.5.1 Far off-resonance dipole trap (FORT) physics

We begin this section by investigating the optical dipole forces on an atom. When placed in an external electric field, a neutral atom experiences a net force due to interactions between the static dipole moment of the atoms and the external electric field. In an optical field, an oscillating electric field generates an induced dipole moment given by $\mathbf{d} = \alpha\mathbf{E}$. The optical dipole force arises from the dispersive interaction of the induced atomic dipole moment with the intensity gradient of the light field. The interaction potential of the induced dipole moment in the optical field is given by

$$U = -\frac{1}{2}\overline{\mathbf{d}\cdot\mathbf{E}} = -\frac{1}{2}\alpha\overline{\mathbf{E}^2}, \tag{4.10}$$

where the factor of $\frac{1}{2}$ accounts for the fact that the dipole moment is an induced, not a permanent one. In terms of the intensity of the optical field, this potential can be rewritten as

$$U = -\frac{1}{4}\alpha\varepsilon^2 = -\frac{2\pi}{c}\alpha I(CGS) = -\frac{1}{2\epsilon_0 c}\alpha I(MKS), \tag{4.11}$$

where the time averaging $\mathbf{E}^2$ is $\varepsilon^2/2$. ε is the slowly-varying field amplitude of the optical field and I is the optical intensity.

The polarizability of atoms in the ground state is given by

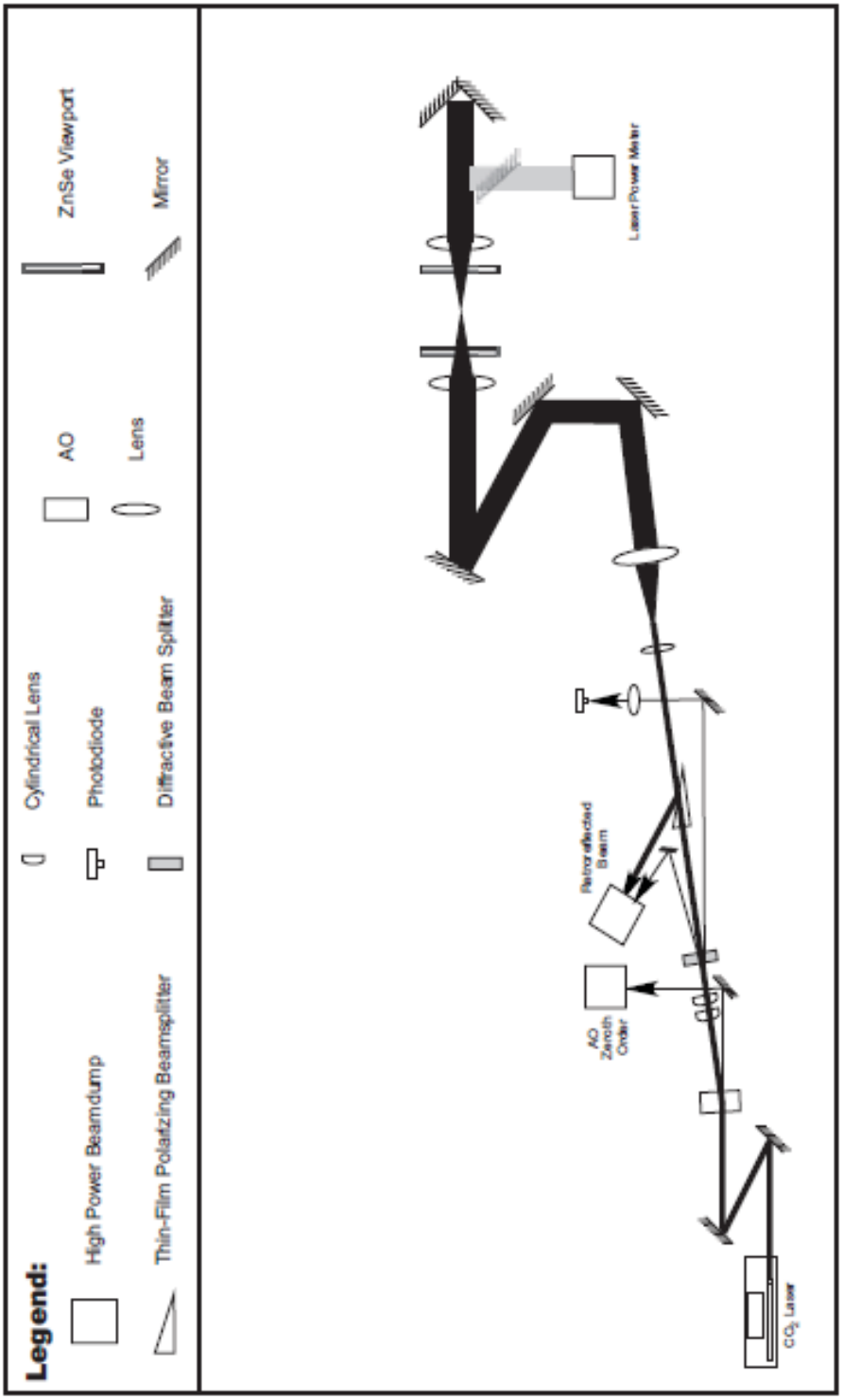

FIGURE 4.3: Carbon dioxide laser beam path [4]. At the end of the beam path, we typically end up with approximately 50 percent of the power at the source. To account for diurnal variations, we optimize the chiller flow rate through the laser power supply and coolant temperature in 0.1 degree steps before parametric trap characterization.

$$\alpha = \frac{1}{\hbar} \sum \mu_{eg}^2 \left[\frac{1}{\omega_{eg} - \omega} + \frac{1}{\omega_{eg} + \omega} \right], \tag{4.12}$$

where μ_{eg} is the electric dipole moment transition matrix element between ground state $|g\rangle$ and excited state $|e\rangle$, and ω_{eg} is the associated transition frequency. In a semi-classical treatment, we estimate the polarizability by integration of the equation of motion for a driven electron bound elastically to the core $\ddot{x} + \Gamma_\omega \dot{x} + \omega_0^2 x = -eE(t)/m_e$, which yields the result

$$\alpha = \frac{e^2}{m_e} \frac{1}{\omega_0^2 - \omega^2 - i\omega\Gamma_\omega}. \tag{4.13}$$

In this equation,

$$\Gamma_\omega = \frac{e^2\omega^2}{6\pi\epsilon_0 m_e c^3} \tag{4.14}$$

is the classical damping rate due to the radiative energy loss. For atoms to be trapped at the focus of the beam, the polarizability α needs to be positive. This implies that the laser frequency be red detuned .

The light intensity of a focused laser beam is almost Gaussian. In cylindrical coordinates, this is given by

$$I(r, z) = \frac{I_0}{1 + (z/z_F)^2} \exp\left(-\frac{2r^2}{a_f^2} \right), \tag{4.15}$$

where λ is the wavelength of the laser beam. I_0 is the maximum beam intensity at the focal point $z = 0$, $z_f = \pi a_f^2/\lambda$ is the Rayleigh range, and a_f is the $1/e^2$ width of the intensity at the focal point. Accordingly, the optical potential also has the same Gaussian shape

$$U_{gauss}(r,z) = -\frac{U_0}{1+(z/z_f)^2}\exp\left(-\frac{2r^2}{a_f^2}\right), \tag{4.16}$$

with $U_0 = \frac{\alpha I_0}{2\epsilon_0 c}$.

In the deepest portion of the optical trap, the Gaussian potential is well approximated by a harmonic one. A Taylor expansion of the Gaussian potential leads to

$$U(r,z) \simeq -U_0 + \frac{U_0}{z_f^2}z^2 + 2\frac{U_0}{a_f^2}r^2 + ... \tag{4.17}$$

Comparing the z^2 and r^2 terms with the harmonic oscillator potential for a particle with mass m, we obtain

$$\frac{U_0}{z_f^2}z^2 \equiv \frac{1}{2}m\omega_z^2 z^2\,,\ 2\frac{U_0}{a_f^2}r^2 \equiv \frac{1}{2}m\omega_r^2 r^2, \tag{4.18}$$

with the radial and axial harmonic frequencies given by

$$\omega_z = \sqrt{\frac{2U_0}{mz_f^2}}\,,\ \omega_r = \sqrt{\frac{4U_0}{ma_f^2}}. \tag{4.19}$$

In an electromagnetic field, an oscillating dipole radiates power given by the equation

$$P = \frac{2\ddot{d}^2}{3c^3} = \frac{1}{3c}^3\omega^4\alpha^2\varepsilon^2, \tag{4.20}$$

where α is the polarizability of atoms, ω is the frequency of the photon, and ε is the amplitude of the optical field. The atom-photon scattering rate R_{sc} is

$$R_{sc} = \frac{P}{\hbar\omega} = \frac{\sigma_s I_0}{\hbar c k}, \tag{4.21}$$

where $\sigma_s = 8\pi\alpha^2 k^4/3$ is the atom-photon scattering cross section. The atomic resonant frequency ω_{eg} is much larger than the carbon dioxide laser frequency. Thus, equation (4.12) gives $\alpha = \alpha_s \equiv 2\mu_{eg}^2/\hbar\omega_{eg}$, which is the static polarizability of a two-level atom. The trap depth and atom-scattering rate of a single-beam trap are given by

$$U_0 = 2\pi\alpha_s I_0/c \tag{4.22}$$

$$R_{sc} = \frac{2\Gamma}{\hbar\omega_0}\left(\frac{\omega}{\omega_0}\right)^3 U_0, \tag{4.23}$$

where $\Gamma = 4\mu_{eg}^2\omega_{eg}^3/3\hbar c^3$ is the spontaneous emission rate (resonance linewidth) for a two-level atom.

4.6 Standing wave dipole trap

As described in Chapter 1 and probably understood by the reader at this point, a quasi-2D Fermi gas is realised in a standing wave trap. An integral part of our standing wave experiments is based on the timed motion of a mechanical chopper, which serves to deflect the beam into an air-cooled Kentek beam dump for single beam experiments and initial forced evaporation. In this configuration, a command voltage of +5V moves the mechanical chopper upwards. Conversely, an applied voltage of -5V moves the chopper downwards. In the cooling stages of a cycle prior to high resolution imaging, a voltage pulse triggers the lifting of the chopper, thus setting up the standing wave trap. Post-imaging, the trapping beam is extinguished, and a reverse voltage causes the chopper to be lowered, ready for the next cycle.

The trap potential for a standing wave set up along the axial z-direction in our experiments can be approximated by

$$U_{sw}(\mathbf{r}) = -U_0 \cos^2(kz) \left[1 - 2 \left(\frac{r}{w_0} \right)^2 - \left(\frac{z}{z_R} \right)^2 \right], \tag{4.24}$$

with U_0 the potential depth, k the wavevector, w_0 the $1/e^2$ beam waist and $z_R = \pi w_0^2/\lambda$ the Rayleigh length. The potential depth is four times as large as the corresponding single-beam potential depth. The axial trapping potential is spatially modulated with a period of $\lambda/2 = 5.3\,\mu$m. Atoms are tightly confined in the antinodes of the resulting standing wave. The resulting extension of our pancake samples, $5.3\,\mu$m is much less than the specified beam waist of 50 μm. Further, the tight beam waist leads to a large Rayleigh length, z_R , of approximately $750\,\mu$m. Hence, the last two terms in equation (4.24) are usually dropped. The curvature of the wavefront and the polarization for the standing wave configurations are maintained from the initial single-beam configuration.

4.6.1 Trap characterization by Parametric Resonance

To measure the oscillation frequency of atoms in the trap, the technique of parametric resonance is employed. In a standing wave dipole trap, there are three resonant frequencies corresponding to the three orthogonal spatial dimensions. For the quasi-2D gas experiments, the frequencies in the radial (x,y) direction are symmetric, whereas the atoms are tightly confined in the axial (z) direction. To determine the resonant frequencies, the trap laser intensity is sinusoidally modulated at a frequency ν, with a small amplitude. At the resonant frequencies of the respective directions, the atoms will be excited and make jumps to higher energy levels. From energetic considerations, such an excitation shows up as an increase in mean square cloud size as a function of drive frequency with negligible loss of atoms following release from the optical trap and a small time-of-flight.

The resulting trap frequencies employed in our experiments have a radial-to-

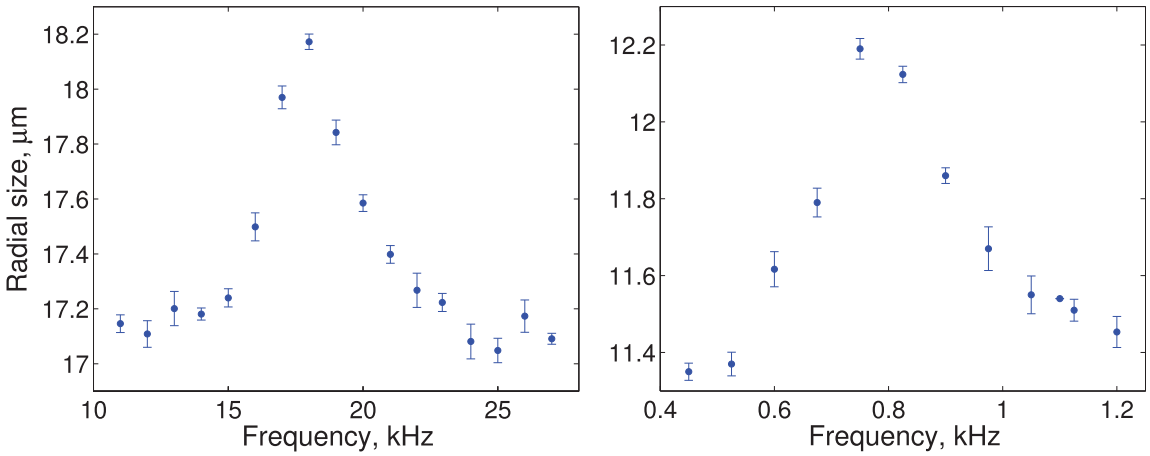

FIGURE 4.4: The technique of parametric resonance is used to estimate trap frequencies. Shown here are measured cloud sizes as a function of drive frequencies for a standing wave at low trap depth (0.5 percent of maximum power). In the figure on the left, we measure the axial trap frequency to be approximately $\omega_z = 2\pi \times 17.5/2 = 2\pi \times 8.75$ kHz. The spectrum shown is obtained following a drive for 0.2 seconds, followed by a 0.5 second equilibration time. Similarly, we see in the figure on the right that the radial trap frequency is approximately $\omega_\perp = 2\pi \times 800/2 = 2\pi \times 400$ Hz. This spectrum is obtained following a 0.5 second drive with three times the amplitude used in (a) and a 0.5 second equilibration time.

axial ratio of approximately 1 : 22, as shown in Figure 4.4. Here, an excitation of a weakly interacting gas at twice the resonant trap frequency leads to an approximate 15 percent increase in cloud size. However, at low trap depths, anharmonic effects lower the measured resonance frequency.

4.7 Radio-frequency Setup for generating spin imbalance

As discussed in Chapter 2, transitions between the hyperfine ground states of ^{6}Li atoms occur in the radio-frequency range. Having an RF antenna installed in the vacuum chamber accomplished three essential objectives: (a) Balancing of spin state populations prior to forced evaporation for efficient cooling. (b) Rapid passage for the formation of ultracold spin-imbalanced samples, and (c) Radio-frequency spectroscopy as a probe of sample microscopic thermodynamics, pairing and superfluidity,

for example. In its current state, the setup is capable of all three implementations within the same automated experimental cycle.

4.7.1 Spin Balancing

The source of the RF signal for spin-balancing is a Hewlett Packard 33120A function generator whose output is routed through a Mini-Circuits 15542 ZAD-1 frequency mixer before being sent to the antenna. In our scheme, a noisy RF pulse centered at a central frequency of 8.75 MHz and peak-to-peak amplitude of 800 mV is frequency-modulated by 1 MHz with a 1 kHz linear ramp for 0.1 seconds. The central frequency is selected to correspond to the calculated frequency splitting of the two lowest hyperfine states at the applied magnetic field of approximately 8 G. A typical spin-balance ratio of approximately 99 percent is achieved by averaging over 10 shots prior to the start of our experiments.

4.7.2 Rapid Passage

To create spin imbalance in a cooled atom sample starting with an initially spin-balanced 1-2 mixture, we apply a radio-frequency sweep to selectively transfer the population of atoms in state 2 to state 3, before blowing out atoms in state 3 with a short optical pulse at a magnetic field which corresponds to a weak interaction between the atoms to avoid three-body recombination losses and heating. The resulting spin-imbalanced 1-2 mixture is then brought to the desired field for further cooling. In practice, we first sweep the magnetic field after forced evaporation at 832 G to the weakly interacting regime at 1200 G. A 5 V signal from the computer card triggers an Agilent 33250A Arbitrary Wavefunction Generator to output a linear ramp with a peak-to-peak voltage of 2 V. This linear sweep is applied to the MOD IN input of an Agilent N9310A frequency generator which outputs a sine wave of central frequency 80.354 MHz with a frequency modulation of 5 kHz. Changing the

amplitude of the linear sweep changes the efficiency of transfer.

For adiabatic passage, the transfer efficiency, T, is given by

$$T \propto e^{-2\pi\left(\frac{\Omega_R^2}{\dot{\omega}}\right)}, \tag{4.25}$$

where Ω_R is the Rabi frequency and $\dot{\omega}$ is the frequency sweep rate. Hence, a slow sweep ensures efficient transfer of atoms from one internal state to another. Conversely, a rapid sweep results in incomplete transfer. Subsequently, we utilize a 7 μs optical pulse to blow out atoms in state 3. This results in a spin-polarized Fermi gas. Prior to reaching the rf antenna, all signals are routed through an Amplifier Research Model 30L amplifier, which provides a specified amplification of 35 dBm.

4.8 High Resolution Absorption Imaging

The imaging method employed in our experiments is that of absorption imaging. Compared to other forms of imaging, such as phase-contrast imaging, our method allows a direct observation of cloud density profiles. In this method, following a short expansion time of approximately 30 μs upon release from the optical trap, a resonant pulse of light strikes the cloud and the resulting shadow image is recorded on a CCD camera. This process is destructive in nature, and results in atoms in the cloud being scattered. As a control light pulse, a second pulse is triggered after these atoms have had time to disperse. Comparing photon counts in this second pulse with photon counts in the first allows one to reconstruct the spatial distribution of the atoms.

To study the thermodynamics of a spin-imbalanced quasi-2D Fermi gas, one requires high resolution images of the individual sites achieved in a standing wave optical dipole trap. Furthermore, to calibrate the temperature of the samples precisely necessitates imaging of the wings of the density profiles. The geometry of the vacuum chamber sets the diffraction limit to approximately 3 μm along the horizontal direction, and 1.8 μm along the vertical direction. Due to further limits imposed

by a magnet holder, as well as space limitations for the magnification optics in the vertical direction, the images obtained in this thesis were from side port imaging. In this scheme, illustrated in Figure 2.1, photons in a beam propagating along the y-direction are absorbed by atoms in the cloud; What is reflected on the image (x-z) plane, therefore, is a shadow image of the atoms.

We now discuss some considerations in high resolution imaging, before investigating the absorption of a probe beam whose frequency is close to resonance in a two-level closed atomic system, and the implementation of high resolution, spin-selective imaging.

4.8.1 Absorption Imaging of Atomic Samples

Absorption imaging of ^{6}Li atoms in a high external magnetic field ($\geqslant$ 300 Gauss) can be thought of as exciting the $^2S_{1/2} \rightarrow ^2 P_{3/2}$ transition. In this thesis, the atomic levels are separated by approximately 80 MHz. Laser light with linear polarization perpendicular to the quantization axis of the magnetic field is used for absorption imaging, and its frequency is adjusted to select the $m_J = -1$ transition.

The resonant optical absorption cross section is a two level system is given by

$$\sigma_{opt} = \frac{4\pi k(\hat{e} \cdot \hat{\mu})^2}{\hbar\gamma_s/2}, \tag{4.26}$$

where $\hat{\mu}$ is the vector of the optical transition element pointing along the quantization direction of the magnetic field, and $\hat{e}$ is the unit vector of the linear momentum of the photon, with k the wavevector of the the photon and $\gamma_s = 4\mu^2 k^3/3\hbar$ the natural linewidth of the transition. In the case of left-circularly polarized imaging light propagating coaxially with the quantization axis of the magnetic field, we define $\hat{e} \cdot \hat{\mu} = \mu$ and we obtain

$$\sigma^{-}_{opt} = \frac{3\lambda^2}{2\pi}. \tag{4.27}$$

In the case of imaging light with $\hat{x}$ linear polarization perpendicular to the quantization axis of the magnetic field, we have $\hat{e}_x = -\hat{e}_+/\sqrt{2} + \hat{e}_+/\sqrt{2}$, where $\hat{e}_+$ correspond to right-circular and left-circular polarized light, respectively. Right circular polarized light is for the $\Delta m_J = 1$ transition, which is well separated from the $\Delta m_J = -1$ transition, so only one component of the light can be absorbed by the atoms. We readily get the optical cross section for the imaging light whose linear polarization is perpendicular to the magnetic field

$$\sigma^*_{opt} = \frac{3\lambda^2}{4\pi}. \tag{4.28}$$

For ^{6}Li atoms, $\sigma^*_{opt} = 0.107\mu m^2$. This optical cross section is a factor of 2 smaller than that of the absorption imaging using left-circularly polarized light, which propagates coaxially along the quantization axis of the magnetic field.

4.8.2 Atom acceleration, cloud density effects

In this section, we consider Beer's Law in the case of a high input intensity, which results in atoms being accelerated and detuned. The energy contained in a beam of light with energy E_0 is characterized by an intensity distribution I_0. Consider an absorber, with cross-sectional area A perpendicular to the beam with a width of dz. The total energy absorbed from the beam in time Δt is

$$\Delta E = -h\nu RN\Delta t, \tag{4.29}$$

where R denotes the number of photons absorbed from the beam per atom per unit time. The total atom number in the absorber, with density n is $N = nAdz$. Substituting for N, we obtain Beer's law for intensities as

$$\frac{dI}{dz} = -h\nu Rn. \tag{4.30}$$

In steady-state, the excited state population n_e is set by the corresponding rates:

$$\dot{n}_e = absorption - stim.emission - spon.emission = 0 \tag{4.31}$$

The first two terms give the number of photons missing from the beam per unit time

$$R = \gamma n_e \tag{4.32}$$

where $\gamma = 2\pi$x 5.87 MHz is the natural linewidth of the ^{6}Li $2s_{1/2} \rightarrow 2p_{3/2}$ transition. The steady state solution of the optical Bloch equations give

$$n_e = \frac{s}{2(1+s)} \tag{4.33}$$

with the saturation parameter s given by

$$s = \frac{I}{I_s}\left(\frac{\gamma^2}{4\delta^2+\gamma^2}\right), \tag{4.34}$$

where the saturation intensity $I_s = \frac{h\pi c\gamma}{3\lambda^3}$ and λ=671 nm. Both detuning and the natural linewidth are written in units of the angular frequency. Defining $s_0 = I/I_s$ and $\Delta = \delta/\gamma$, Beer's law becomes

$$I_s\frac{ds_0}{dz} = -\frac{h\nu\gamma n}{2}\frac{s_0}{1+s_0+4\Delta^2}. \tag{4.35}$$

Substituting I_s, we get

$$ds_0 + (1+4\Delta^2)\frac{ds_0}{s_0} = -\sigma n dz, \tag{4.36}$$

where the absorption cross section $\sigma = \frac{3\lambda^2}{2\pi} = 0.215\ \mu m^2$. If we now write $s_0 \rightarrow s$ such that s_0 corresponds to the input intensity and s to the transmitted intensity, we obtain

$$ds + (1 + 4\Delta^2)\frac{ds}{s} = -\sigma n dz. \tag{4.37}$$

Integrating equation(4.37) leads to

$$(s - s_0) + (1 + 4\Delta^2) ln\frac{s}{s_0} = -\sigma\tilde{n}, \tag{4.38}$$

where s_0 is the saturation parameter on resonance before the absorber, s being the corresponding quantity after the absorber, and the column density represented by $\tilde{n} = \int n dz$. Equation (4.38) can be solved numerically for an input intensity and optical density $OD = \sigma\tilde{n}$

4.8.3 Atom Acceleration due to Input Intensity

Upon multiple absorption-emission cycles, each atom gains momentum k per spontaneous emission event along the laser beam at a rate R that results in a spontaneous force. This force leads to atomic acceleration which Doppler shifts the laser frequency away from resonance. In what follows, we assume a time-dependent Doppler shift, $\delta(t)$ with $\delta(0)= 0$. Writing $\delta(t) = -\vec{k} \cdot \vec{v}(t)$ for an initially resonant pulse, Newton's Second Law reads

$$m\dot{v} = \hbar k \frac{\gamma}{2} \frac{s_0}{1 + s_0 + \left(\frac{2k\nu}{\gamma}\right)^2}. \tag{4.39}$$

Rearranging terms leads to

$$\left(1 + s_0 + \frac{4k^2v^2}{\gamma^2}\right) dv = \hbar k \frac{\gamma}{2} \frac{s_0}{m} dt. \tag{4.40}$$

Assuming the atoms to be at rest initially, i.e. $v|_{t=0} = 0$, the velocity is given by the cubic equation

$$\frac{4k^2}{3\gamma^2}v^3 + (1+s_0)v - \hbar k\frac{\gamma}{2}\frac{s_0}{m}t = 0. \tag{4.41}$$

The corresponding detuning will be given be

$$\frac{4}{3}\Delta^3 + (1+s_0)\Delta + \hbar k^2\frac{s_0}{2m}t = 0. \tag{4.42}$$

Solving these equations numerically, we see that for $s_0 = 5$, the maximum dispacement due to the spontaneous force is about $r = 25\mu m$ as the acceleration is about $10^6\, m/s^2$.

4.8.4 Estimation of optical density

In high resolution absorption imaging of our atoms, we wanted to ensure that the cloud sizes were a few times that of the obtainable resolution; for pancake samples spaced $5.3\,\mu$m apart, we eventually worked with radial cloud sizes larger than $15\,\mu$m. The cloud size is in turn set by the final trap depth; a deep trap gives rise to tighter confinement and consequently a smaller cloud. However, atoms in tighter traps being more closely packed, give rise to high central cloud densities. The problem of atom acceleration discussed in the previous subsection then becomes pronounced, rendering quantities extracted from the images, such as the atom number, inaccurate. To give the reader a sense of the trap depths we work at to overcome these problems, we present our estimation of the optical density in this section.

We begin by assuming atoms to be in the ground state of the quantum harmonic oscillator in the axial direction and harmonically trapped non-interacting zero-temperature 2D Fermi gas in the radial direction. The gas density can then be written, from equation (2.64), as

$$n(\rho, z) = N\sqrt{\frac{m\omega_z}{\pi\hbar}}e^{-\frac{m\omega_z}{\hbar}z^2}\cdot\frac{2}{\pi R_{TF}^2}\left(1-\frac{\rho^2}{R_{TF}^2}\right)\Theta\left[R_{TF}-\rho\right], \tag{4.43}$$

where the Fermi radius $R_{TF} = \sqrt{\frac{2E_F}{m\omega_\perp^2}} = \sqrt{\frac{\hbar}{m\omega_\perp}} \cdot (8N)^{1/4}$. The density is normalized to the atom number N (per spin state). The column density is given by

$$\tilde{n}(x,z) = \int n(x,y,z)dy = N\sqrt{\frac{m\omega_z}{\pi\hbar}}e^{-\frac{m\omega_z z^2}{\hbar}} \cdot \frac{1}{R_{TF}}\left(1-\frac{x^2}{R^2}\right)^{3/2}\Theta\left[R_{TF}-|x|\right]. \tag{4.44}$$

The optical density is then

$$OD = \tilde{n}|_{max}\sigma = \frac{N}{\sqrt{\pi}R_{TF}}\frac{\sigma}{l_z}, \tag{4.45}$$

with the harmonic oscillator length, l_z , denoted as $l_z = \sqrt{\frac{\hbar}{m\omega_z}}$, and $\sigma = 0.215\,\mu m^2$ the absorption cross section. Assuming $\omega_z/\omega_\perp = 25$,

$$l_z \cdot R_{TF} = 5(8N)^{1/4}\frac{\hbar}{m\omega_z}. \tag{4.46}$$

The axial trap frequency scales with the CO_2 laser power as $\omega_z = 2\pi \cdot 17\text{kHz}\,\sqrt{P}$. The total atom number 2N was approximately 1600, and thus

$$OD \sim \frac{100\mu m^2}{l_z\sigma_\perp}. \tag{4.47}$$

We note the scaling relation $OD \sim N^{3/4}\omega_z$. For imaging purposes, we maintain an optical density of approximately 1.

4.9 Practical Implementation of High Resolution Imaging

Having described the theory behind absorption imaging, and provided estimates for the optical density and atom acceleration effects, we proceed to discuss some practical considerations in the implementation of a high resolution imaging setup.

The acousto-optic modulator (AOM) setup was modified from previous group theses to enable dual spin imaging. In addition, we installed a new Pixelfly QE camera capable of taking two sequential shots in a short amount of time. This was crucial for an accurate determination of the sample polarisation for our studies on spin-imbalanced gases.

4.9.1 AOM arrangement for dual spin imaging

To condition the imaging beam for rapid sequential dual spin imaging, we utilised the arrangement for the acousto-optic modulators shown in Figure 4.5. The power of an incoming beam is first divided by a polarising beam splitting cube into a lock beam region and the imaging beam. The imaging beam is then focused by a ThorLabs LB 1676-B lens with a focal length of 100 mm onto an ISOMET Model 1206C acousto-optic modulator (AOM) capable of imparting a frequency shift of 25 MHz each way about a central frequency of 110 MHz. At an operational magnetic field of 832 G, the separation of the two lowest hyperfine states of lithium are approximately 74 MHz apart with a magnetic field tunability of about 1.4 kHz per Gauss. The nominal voltage sent to the AOM parks the frequency shift imparted to the imaging beam at the middle of the 1-2 transition after a double-pass. This provides a symmetric frequency shift to each spin state. Each of the two arms shown contains an LB 1465-B lens with a focal length of 500 mm, and a QWP-mirror combination to condition the first order beam resulting from the imparted voltage shift for the respective spin-state of interest.

4.9.2 Rapid sequential imaging of minority and majority hyperfine states

In our experiments, a compact, high-resolution Pixelfly QE CCD (Charge-Coupled Display) camera employing digital temperature compensation is used. A unique double-shutter feature of the model allows the user to acquire two images in succes-

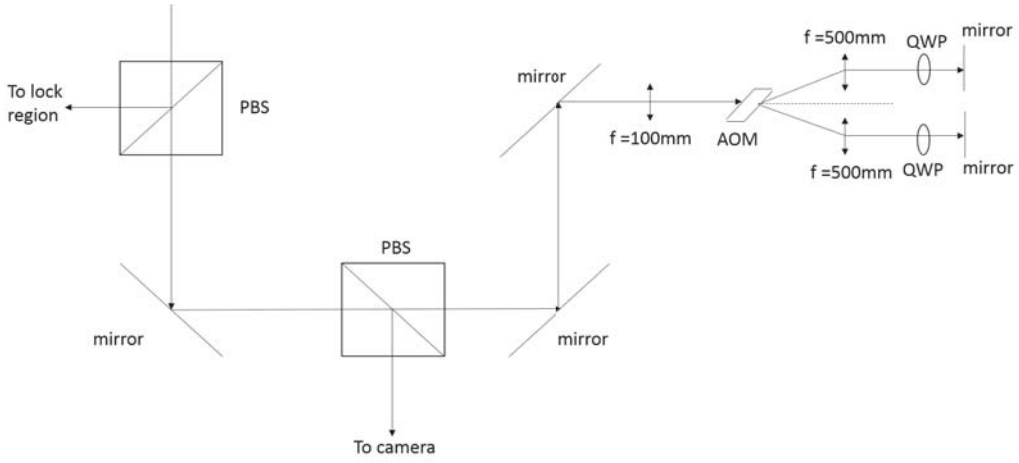

FIGURE 4.5: Optical layout to condition the imaging beam for rapid sequential imaging.

sion. In this setting, there is a 1 μs delay between camera frames.

The voltage pulse sequences required to image a single spin species is illustrated in Figure 4.6. Shown are the unlocking of the dye laser, frequency shifts, shutter open times, and imaging AO voltage pulse durations relative to one another. The camera AO amplitude denotes the times when imaging pulses are sent to the camera.

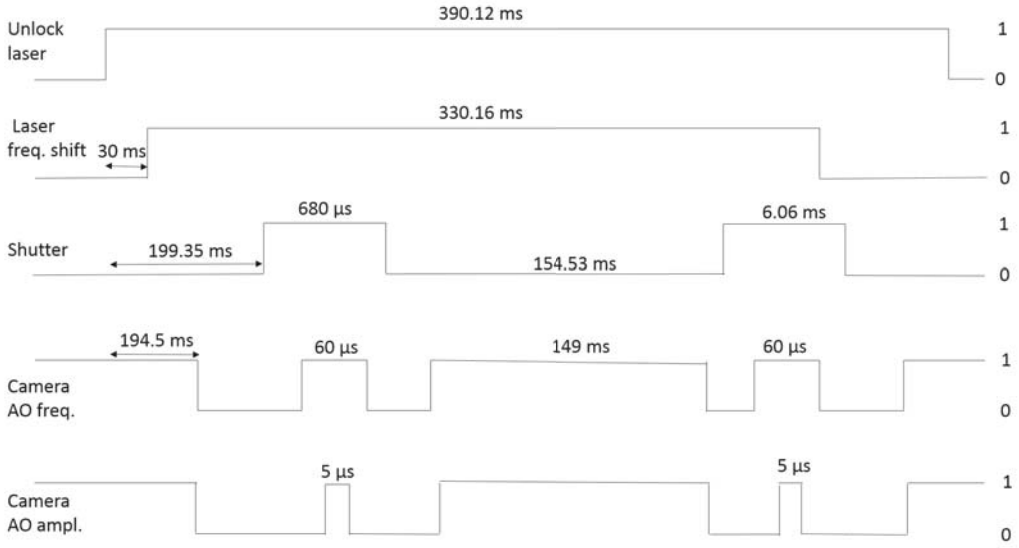

FIGURE 4.6: Voltage pulse sequences for the dye laser, imaging AO, and shutter for imaging a single spin species.

In this figure, the first shot, termed the signal shot, is fired to acquire an image of the atoms. The second shot, termed the reference shot, is acquired after the atoms have dispersed. We subtract the reference shot from the signal shot to obtain cloud density profiles.

For our study of spin-imbalanced Fermi gases, we obtain a total of four images per cycle. To determine the atom number per spin state, and hence the sample polarization accurately, we image the minority population ten microseconds before imaging majority atoms. The subsequent two reference shots are obtained after waiting a few milliseconds for the atoms to disperse. This schematic is shown in Figure 4.11.

4.9.3 High-resolution imaging

In this subsection, we illustrate some considerations in obtaining high-resolution images, which is essentially a competition between the diffraction limit and aberrations. The diffraction limit is set by the geometry of the configuration, $x = f\lambda/d$, where f is the effective focal length of the lens, λ is the wavelength of the imaging beam, 670 nm , and d is the diameter of the aperture. In our case, the diffraction limit is set by the geometry of the vacuum chamber. Although both vertical and horizontal imaging ports were available, with the vertical port giving a better diffraction limit, we settled upon the horizontal port with a diffraction limit of $3.5\,\mu$m, due mainly to mechanical stability and space constraint issues of the imaging optics.

An optical design software such as OSLO or ZEMAX is highly recommended for the lens design enthusiast seeking to understand the aberrations inherent in an optical system. In-built ray tracing capabilities make it convenient to generate diagnostics ranging from ray fan plots to spot diagrams. Our simulations showed that spherical aberrations were the dominant form of aberrations in our optical setup. These are quantified by the root-mean-square spot size of the rays at focus.

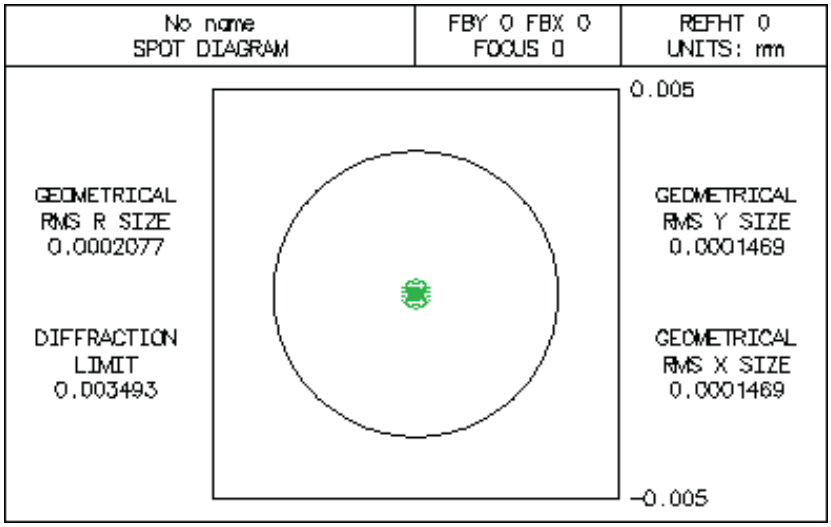

FIGURE 4.7: A spot diagram illustrates the competition between the diffraction limit and spherical aberrations. For a diffraction limited imaging configuration, the rays at the point of focus would fall within the diffraction limit, indicated by the black circle. The case here shows the results of a simulation for our high resolution setup; the geometrical root mean square size is calculated to be $0.2\,\mu$m , clearly within the diffraction limit of $3.5\,\mu$m.

To achieve diffraction-limited resolution in our setup, we used a custom-designed high-resolution objective from JML Optics as the focusing lens at the imaging port. This is followed by a Newport achromat and a x 10 microscope objective for magnification purposes. To obtain an estimate for the minimum beam spot size at focus obtainable with the custom objective, we conducted a simulation in OSLO with the optical path reversed as shown in Figure 4.8. Table 4.2 further shows the specifications of the objective, namely the radii of curvature for the individual surfaces, the spacing between each surface, the aperture size of each surface, and the material each optic is fabricated out of.

To evaluate the feasibility of our optical setup as a whole as shown in Figures 4.9 and 4.10, we used OSLO to generate the spot diagram shown in Figure 4.7. The green dots represent the two dimensional distribution of ray pierces, computed by ray

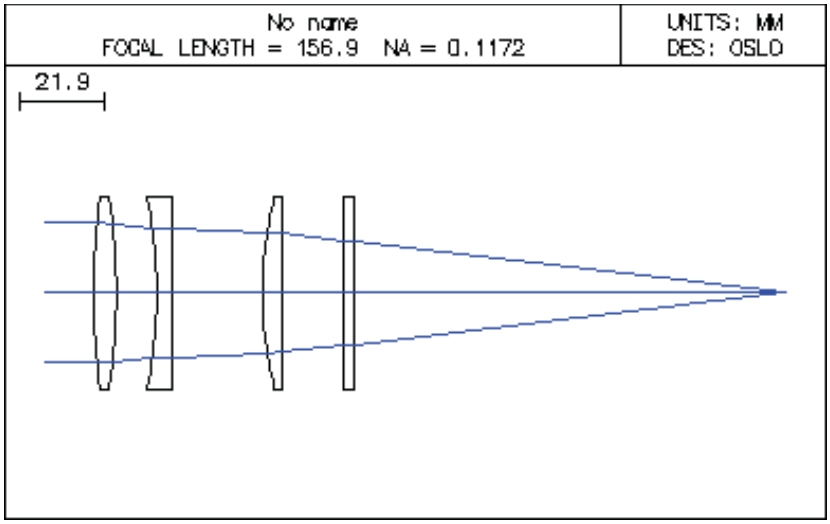

FIGURE 4.8: OSLO simulation of custom three-lens high-resolution objective positioned before a vacuum chamber window. As shown in Figure 4.9, the three lenses are housed in a 50 mm lens mount. Specifications for lens surfaces, air spacings, lens thickness, and glass types are listed in Table 4.2.

Table 4.2: Surface data for OSLO simulation of high-resolution objective employed in experiments. An entrance beam radius of 18.4 mm yields a diffraction-limited spot diagram shown in Figure 4.7.

SRF	**Radius of Curvature (mm)**	**Thickness**	**Aperture Radius**	**Glass**
OBJ	1e20	1e20	1e14	AIR
AST	178.57	6	25.4	N-BK7
2	-178.57	11.268	25.4	AIR
3	-128.77	3.9	25.4	N-BK7
4	1e20	24	25.4	AIR
5	104.24	5.1	25.4	B270
6	1e20	16.33	25.4	AIR
7	1e20	2.67	25.4	S-FSL5
8	1e20	115	13.489935	AIR

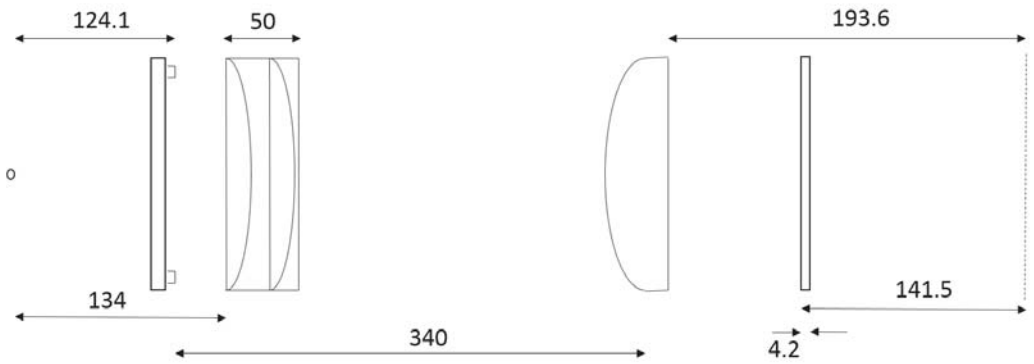

FIGURE 4.9: Schematic view of side-port high-resolution imaging setup. Shown from left to right are atoms, MDC vacuum chamber port, high resolution objective with an effective focal length of 157 mm, an anti-reflection(AR)-coated Newport PAC 087, N-BK7 and SF-5 precision achromatic doublet with an effective focal length of 200 mm, a 4.2 mm thick glass slide on the Pixelfly camera, and the image plane. The imaging beam focuses 130 mm from the edge of the high-resolution objective. Dimensions are listed in mm. Figure not drawn to scale.

tracing equations, in the image plane at focus. The diffraction limit is represented by the black circle. The more compact the spot diagram, the lesser the aberrations. An unaberrated systems would have the spot diagram appear as a single point.

4.9.4 PixelFly camera characteristics

The camera employed in our experiments is a compact, high-resolution digital 12 bit CCD (Charge-Coupled Display) Pixelfly QE camera. The pixel array is 1392 pixels (horizontal) by 1024 pixels (vertical), with a pixel size of 6.45μm. An in-built digital temperature compensation minimizes space requirements. The camera has a specified quantum efficiency of 35 percent in standard operation mode and 50 percent in high sensitivity mode at the operational wavelength of 670 nm. A low readout noise of 7 e^- rms is desirable for imaging purposes. It is connected to our operating system via a high speed serial data link. In addition, the system boasts available exposure times ranging from 5 μs to 65 s.

A key reason for our choice of cameras was the unique double-shutter feature

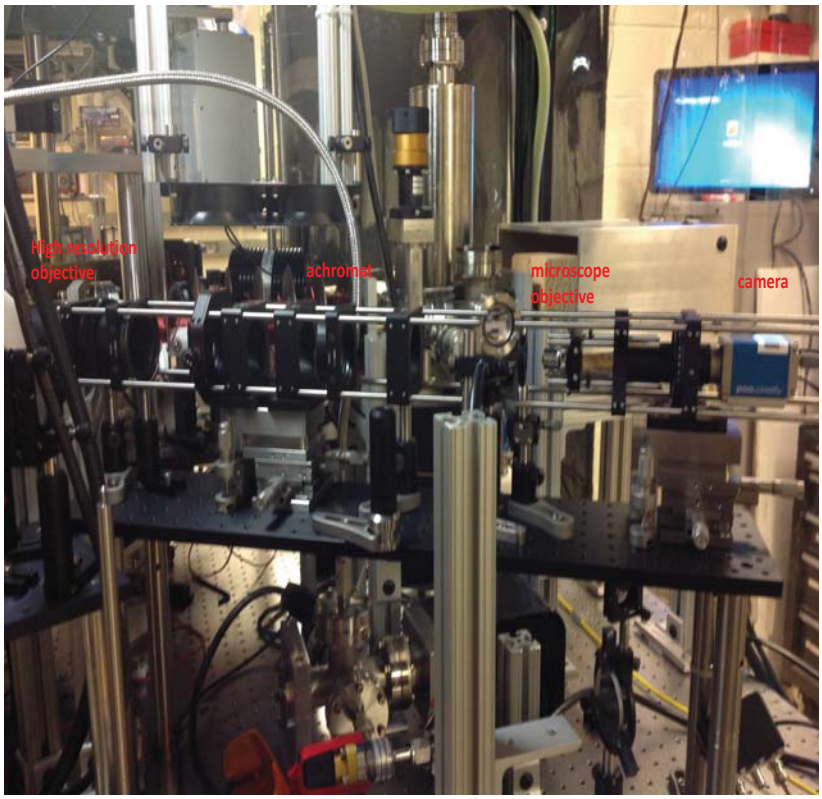

FIGURE 4.10: Photograph of side-port high-resolution imaging setup, showing a custom-designed high-resolution objective placed next to the vacuum chamber, followed by a precision achromat to focus the imaging beam, and a microscope objective before the camera for further magnification. The entire setup is positioned in a cage mount for tilt alignment.

which allows the user to acquire two images with a short interframing time. In this setting, there is a 1 μs delay between the two frames. This is particularly crucial for our experiments, where an accurate determination of the sample polarisation, given by N_2/N_1 where N_2 and N_1 denote the number of minority and majority atoms respectively, is essential. In our experiments, the signal shots for both spin species are each 5 μs in duration. For clarity, an image acquisition sequence illustrating the time points for an external trigger, together with the signal and reference pulses for both spin species is shown in Figure 4.11.

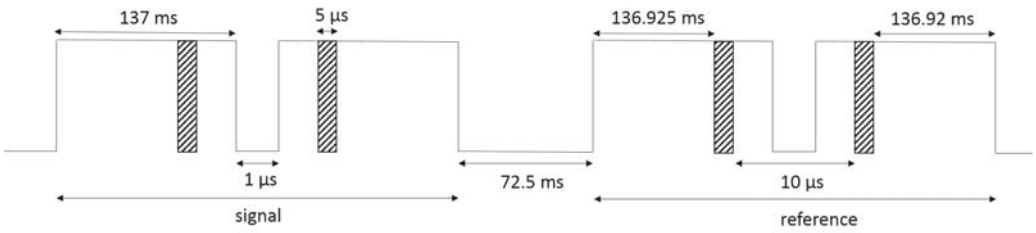

FIGURE 4.11: Rapid sequential imaging light pulse sequence. An external trigger prompts the Pixelfly QE camera to collect light for 137 ms. Imaging pulses of 5μs duration are indicated by striped boxes. The minority species is imaged before the majority species. The camera is triggered a second time 72.5 ms after the signal shots are acquired to obtain reference shots.

4.9.5 Focusing the Camera

To determine the focal point of the cloud, we first note that the camera is mounted on a tri-axis translation stage. The camera is translated along its imaging axis to locate the point where the cloud radius is smallest to within $\pm$ 50 μm. To ascertain if the location in question was the true focus, the camera is intentionally moved out of focus and the frequency of the imaging beam detuned above and below resonance; in one direction perpendicular to the camera (eg. away from the cloud), a blue-detuned imaging beam gives rise to a split cloud while a red-detuned imaging beam gives rise to a dim cloud. In the other direction (eg. closer to the cloud), the converse holds true.

4.9.6 Magnification of Imaging System

The magnification of the imaging system is set by the ratio of the focal length (200 mm) of the Newport PAC 087 achromat to the high-resolution objective (specified to be 157 mm) and the magnification of the microscope objective (4X) just before the camera. These lead to a theoretical magnification of 5.1. The experimental magnification is determined by a controlled displacement of the optical trap, and a subsequent measurement of the corresponding motion of the atom cloud. As a

realistic example for our experimental conditions, if a 50 μm displacement of the optical trap corresponds to a 37 pixel shift of the maximum intensity point, a pixel size of 6.45 μm would imply a magnification of 4.77.

4.9.7 Imaging Beam Size measurement

A large imaging beam introduces additional aberrations due to the additional optical paths traversed by the beam to the plane of focus. A smaller beam with the same power, however, leads to saturation and unwanted atom acceleration effects described in the earlier section. A good measurement of the beam size is thus important in achieving the appropriate balance between the achievable resolution and a reasonable ratio of $I/I_{sat} \simeq 1$. The field radius of a collimated imaging beam is estimated by reducing the size of an iris in the beam path until the power drops by a factor of 1/2. The diameter at which this occurs is twice the $1/e$ field radius.

5

Polaron Thermodynamics of quasi-2D Fermi Gases

Earlier in this thesis, we found that transitions between non-interacting polaronic states provided an adequate form to determine the primary spectral features at unitarity. The difference between the initial and final state polaron energies determined the frequency shifts for a spin-balanced mixture reasonably well. In this chapter, we extend our earlier treatment to compute and determine theoretical density profiles of both spin-imbalanced and spin-balanced trapped gases, which in turn determines the entire thermodynamic landscape at T = 0. Further, we will compare the predictions for spin-balanced mixtures to measured cloud radii and pressure. A discussion of the data and fits for spin imbalanced quasi-2D Fermi gases will be relegated to Chapter 6.

The interested reader might note that for the one-dimensional spin-imbalanced attractively interacting Fermi gas, which is aptly described by the Gaudin-Yang model, the equation of state at finite temperature is obtained by numerically solving a set of thermodynamic Bethe ansatz equations. This was thoroughly investigated in a prior density profile study on 1D tubes [32].

Our general approach is as follows: We begin by writing out the free energy den-

sity for a gas. Taking its derivative with respect to the densities of the respective spin species gives the local chemical potentials. We will see that the normalized chemical potentials are in turn simple functions of the normalized densities, and their ratio, x. The cutoff radii for both spin states are determined by setting the densities to zero; expressions for the densities at the center of the trap can be similarly determined. The iterative steps required to obtain the density profiles will be illustrated as we proceed. We note that this method is generic and works equally well for generating both spin-balanced and spin-imbalanced density quasi-2D Fermi gas profiles with an appropriate modification of the free energy density. A companion tutorial on generating density profiles in Mathematica for a spin-imbalanced gas at a fixed interaction strength with an arbitrary polarisation is provided in Appendix C for the reader's reference.

5.1 Polaron Thermodynamics of a Spin Imbalanced quasi-2D Fermi Gas

In this section, we derive the zero temperature density profiles for a spin-imbalanced quasi-two dimensional Fermi gas for the homogeneous case and trapped case. The treatment follows that in the Supplementary Material of [63]. We ignore the effective mass and do not include a molecular dimer pressure or molecular dimers and dimer-polarons. In our simple polaron picture, an impurity spin species (state 2) is immersed in a majority-spin (state 1) bath, i.e., $N_2 < N_1$ for the total number of atoms per spin state. The free energy density of the homogenous gas can hence be written as the sum of noninteracting gas energy densities for the majority and minority species given by the first two terms on the right hand side of equation (5.1), together with an attractive polaron energy term, $n_2 E_p(2)$

$$f = \mathcal{E} = \frac{1}{2} n_1 \epsilon_{F1} + \frac{1}{2} n_2 \epsilon_{F2} + n_2 E_p(2), \tag{5.1}$$

with the ideal 2D local Fermi energy of the components, ϵ_{Fi} given by

$$\epsilon_{Fi} = \frac{2\pi\hbar^2}{m} n_i \equiv \alpha_\perp n_i. \tag{5.2}$$

Here, $\hbar$ is the Planck constant divided by 2π, m is the particle mass, and n_i is the density (per unit area) of the atomic species, with $i = 1, 2$. It is worth pointing out that the factor of $\frac{1}{2}$ arises from the energy of the ideal two-dimensional Fermi gas. For the 3D problem at resonance, the same method with $\frac{1}{2} \rightarrow \frac{3}{5}$ yields the Fermi liquid equation used in reference [64] for the normal imbalanced mixture, with $m^* = 1$. The two-dimensional polaron energy (per minority particle), which arises from scattering of state 2 atoms off the Fermi sea of state 1 atoms, is denoted by

$$E_p(2) = y_m(q_1)\epsilon_{F1}, \tag{5.3}$$

where $q_1 \equiv \epsilon_{F1}/E_b$ denotes the ratio of the local Fermi energy, ϵ_F, of the majority species to the binding energy, E_b, of 1 -2 dimer pairs in a 2D trap. We note that q_1 is a measure of the interaction strength in two dimensions. Since the local Fermi energy is only atom-number and trap-frequency dependent, it remains relatively constant for gas samples obtained at different magnetic fields. In contrast, the two-body binding energy varies by approximately a factor of 50 (2 kHz vs 100 kHz) for the magnetic fields of interest in ^{6}Li, and is the dominant factor determining the interaction strength in two dimensions. We point out that $E_p(2)$ is negative and proportional to the density of majority atoms, n_1. A detailed description of the 2D polaron model used is found in the supplementary material of reference [39]. We simplify the treatment by neglecting the contribution of higher axial states and adopting an analytic expression for $y_m(q_1)$ due to [55], which interpolates between

polaron behavior in the BCS regime and molecular behavior in the BEC regime,

$$y_m(q_1) = \frac{-2}{\log(1+2q_1)}. \tag{5.4}$$

In the limit where $\epsilon_{F1} \ll E_b$ or correspondingly $q_1 \ll 1$, equation (5.4) yields $E_p(2) \rightarrow -E_b - \epsilon_{F1}$, which is the energy to break a pair and place a majority atom back on the Fermi surface [65].

From the thermodynamic relation $\mu_i = \partial f/\partial n_i$ valid in the grand canonical ensemble, the chemical potentials of each atomic species is found to be

$$\mu_1 = \frac{\partial f}{\partial n_1} = \epsilon_{F1} + y_m^{'}(q)\frac{n_2}{n_1}\epsilon_{F1}, \tag{5.5}$$

$$\mu_2 = \frac{\partial f}{\partial n_2} = \epsilon_{F2} + y_m(q)\epsilon_{F1}, \tag{5.6}$$

where we have defined the local density ratio of the two components as $x = n_2/n_1 = \epsilon_{F2}/\epsilon_{F1}$. Using the proportionality relation $\epsilon_{Fi} = \alpha_\perp n_i$ we obtain the following simplified forms for the chemical potentials:

$$\mu_2 = \epsilon_{F1}\left[x + y_m(q_1)\right], \tag{5.7}$$

$$\mu_1 = \epsilon_{F1}\left\{1 + x\left[y_m(q_1) + y_m^{'}(q_1)\right]\right\}, \tag{5.8}$$

where the second term in equation (5.8), $y_m^{'}(q_1) = dy_m(q_1)/d\log q_1 = q_1 dy_m(q_1)/dq_1$, can be written as

$$y_m^{'}(q_1) \equiv \frac{q_1\left[y_m(q_1)\right]^2}{1+2q_1}. \tag{5.9}$$

In equations (5.7) and (5.8), the first terms $x\epsilon_{F1}$ and ϵ_{F1} are the local Fermi energies for the minority and majority noninteracting gases. As the minority concentration

vanishes, $x \to 0$, we see that $\mu_2 \to E_p(2)$ as expected. The second terms in equations (5.5) and (5.6) denote the modifications to the chemical potential of the atoms arising from interactions with the other spin-component.

To account for the effect of an external harmonic confining potential, the system is taken to be locally uniform within the local density approximation (LDA), with a spatially varying local chemical potential given by

$$\mu_i(\rho) = \mu_{io} - \frac{1}{2} m \omega_\perp^2 \rho^2, \tag{5.10}$$

where $\omega_\perp$ is the radial trap frequency, and ρ is the spatial extent of the cloud in the radial direction. For the experiments described in this thesis with ^{6}Li atoms in a tightly confining ($\omega_z \gg \omega_\perp$) far-off resonance 50 W CO_2-laser standing wave trap at 0.5% trap depth, $\omega_\perp \sim 2\pi \times 440$ Hz and $\omega_z \sim 2\pi \times 9$ kHz. A typical radial cloud size for the samples is $\rho \sim 15\mu$m. The pancake-shaped trapping potential has an aspect ratio of approximately 1:20.

These expressions will come in handy at a later point when we compute density profiles. For now, we turn our attention to the derivation of an equation that provides constraints on the central densities by considering the pressure of the gas sample.

5.1.1 2D Pressure

From thermodynamic considerations, the local 2D pressure, p , is given by

$$p = \mu_1 n_1 + \mu_2 n_2 - f. \tag{5.11}$$

Applying the form for the free energy from equation (5.1) in (5.11) , and equations (5.7) and (5.8) for the chemical potentials yields

$$p = \frac{1}{2} n_1 \epsilon_{F1} + \frac{1}{2} n_2 \epsilon_{F2} + n_1 \epsilon_{F1} x \left(y_m(q_1) + y_m^{'}(q_1) \right). \tag{5.12}$$

A further simplification gives

$$p = \frac{1}{2} n_1 \epsilon_{F1} \left\{ 1 + x^2 + 2x[y_m(q_1) + y_m^{'}(q_1)] \right\}. \tag{5.13}$$

Rearranging equation (5.13), we obtain the local pressure for an ideal two-dimensional Fermi gas

$$\frac{p}{\frac{1}{2} n_1 \epsilon_{F1} (1 + x^2)} = 1 + \frac{2x}{1 + x^2} \left[y_m(q_1) + y_m^{'}(q_1) \right], \tag{5.14}$$

with the second term on the right-hand side denoting modifications from an ideal gas with the same minority and majority densities. In the limiting case when $q_1 \ll 1$, $y_m(q_1 \gg 1) \rightarrow \frac{-E_b}{\epsilon_{F1}} - 1$ and $y_m^{'}(q_1 \gg 1) \rightarrow \frac{-E_b}{\epsilon_{F1}}$, thus equation (5.14) reduces to

$$\frac{p}{\frac{1}{2} n_1 \epsilon_{F1} (1 + x^2)} = 1 - \frac{2x}{1 + x^2}. \tag{5.15}$$

5.1.2 Thermodynamic Quantities in Normalized Units

Before proceeding further, we introduce a few quantities of interest. A parameter for the interaction strength is given by

$$q_0 \equiv \frac{E_F}{E_b}, \tag{5.16}$$

with $E_F \equiv \hbar \omega_\perp \sqrt{2N_1}$ the ideal gas Fermi energy for the majority component at the center of a harmonic trap, and $\omega_\perp \equiv \sqrt{\omega_x \omega_y}$ the transverse oscillation frequency. The ideal 2D gas unit of density is given by

$$n_0 \equiv \frac{E_F}{\alpha_\perp} = \frac{\hbar \omega_\perp}{\alpha_\perp} \sqrt{2N_1} = \frac{2}{\pi} \frac{N_1}{R_{TF1}^2}, \tag{5.17}$$

where $R_{TF1} \equiv \sqrt{2E_F/(m\omega_\perp^2)}$ is the Thomas-Fermi radius for majority component atoms of mass m.

A considerable simplification for numerical simulations results by writing quantities in normalized units; the chemical potentials, densities, and transverse radii are normalized as $\tilde{\mu_i} = \mu_i/E_F$, $\tilde{n_i} = n_i/n_0$, and $\tilde{\rho} = \rho/R_{TF1}$, respectively. Further, we scale the interaction as $q_1 = q_0\tilde{n_1}$. In a harmonic potential, $\mu_i = \mu_{i0} - m\omega_\perp^2\rho^2/2 = \tilde{\mu}_{i0} - \tilde{\rho}^2$ with ρ the transverse radius. Using normalised units, equations (5.7) and (5.8) for the chemical potentials of the spin species then become

$$\tilde{\mu}_1 = \tilde{\mu}_{10} - \tilde{\rho}^2 = \tilde{n}_1 \left\{ 1 + x \left[y_m \left(q_0 \tilde{n}_1 \right) + y_m^{'} \left(q_0 \tilde{n}_1 \right) \right] \right\}, \tag{5.18}$$

$$\tilde{\mu}_2 = \tilde{\mu}_{20} - \tilde{\rho}^2 = \tilde{n}_1 \left[x + y_m \left(q_0 \tilde{n}_1 \right) \right], \tag{5.19}$$

where μ_{i0} is the trap central chemical potential for $i = 1, 2$.

Physically, the density profile for a spin-imbalanced gas can be partitioned into two sections, $0 \leqslant \tilde{\rho} \leqslant \tilde{R}_2$ where the normalized density of the minority spin species is non-zero, i.e. $\tilde{n}_2 \neq 0$, and another spatial region $\tilde{R}_2 \leqslant \tilde{\rho} \leqslant \tilde{R}_1$ where $\tilde{n}_2 = 0$. In the region of space where the minority species is 0, $\tilde{R}_2 \leqslant \tilde{\rho} \leqslant \tilde{R}_1$, the minority density vanishes, leading to the condition $x = 0$. Applying this condition into equation (5.18) yields a Thomas-Fermi profile for the majority in the region $\tilde{R}_2 \leqslant \tilde{\rho} \leqslant \tilde{R}_1$.

$$\tilde{n}_1(\tilde{\rho}) = \tilde{\mu}_{10} - \tilde{\rho}^2. \tag{5.20}$$

Where the majority density vanishes, $\tilde{n}_1 = 0$. This requires the radius of the entire cloud to be

$$\tilde{R}_1 = \sqrt{\tilde{\mu}_{10}}. \tag{5.21}$$

Moreover, for a gas with attractive interactions, $E_p(2) < 0$, thus we expect $\tilde{R}_1$ to be smaller than the Thomas-Fermi radius, i.e., $\tilde{R}_1 \leqslant 1$, which requires $0 \leqslant \tilde{\mu}_{10} \leqslant 1$.

To find the radius at which the minority component vanishes, we set $x = 0$ and

$\tilde{\rho} = \tilde{R}_2$ in equation (5.19). We then obtain the minority radius

$$\tilde{R}_2 = \tilde{\mu}_{20} - \tilde{n}_1(\tilde{R}_2) y_m \left[q_0 \tilde{n}_1 \left(\tilde{R}_2 \right) \right], \tag{5.22}$$

where we obtain $\tilde{n}_1(\tilde{R}_2)$ from equation (5.20) to solve for $\tilde{R}_2$ numerically.

Given the chemical potentials at the trap center μ_{10} , μ_{20}, the cutoff radii $\tilde{R}_1$ and $\tilde{R}_2$ are known. Equations (5.18) and (5.19) can then be solved for $\tilde{n}_1$ and $\tilde{n}_2$ in the region $0 \leqslant \tilde{\rho} < \tilde{R}_2$. With $x\tilde{n}_1(\tilde{\rho}) = \tilde{n}_2(\tilde{\rho})$, equation (5.19) immediately yields

$$\tilde{n}_2(\tilde{\rho}) = \tilde{\mu}_{20} - \tilde{\rho}^2 - \tilde{n}_1(\tilde{\rho}) y_m \left[q_0 \tilde{n}_1 \left(\tilde{\rho} \right) \right], \tag{5.23}$$

where $\tilde{n}_1(\tilde{\rho}) \equiv \tilde{n}_1$ is consistently determined for $0 \leqslant \tilde{\rho} < \tilde{R}_2$ by eliminating $\tilde{n}_2(\tilde{\rho})$ from equation (5.18),

$$\tilde{n}_1 = \frac{(\tilde{\mu}_{10} - \tilde{\rho}^2) - (\tilde{\mu}_{20} - \tilde{\rho}^2) \left[y_m \left(q_0 \tilde{n}_1 \right) + y_m^{'} \left(q_0 \tilde{n}_1 \right) \right]}{1 - y_m \left(q_0 \tilde{n}_1 \right) \left[y_m \left(q_0 \tilde{n}_1 \right) + y_m^{'} \left(q_0 \tilde{n}_1 \right) \right]}. \tag{5.24}$$

5.1.3 Normalisation of 2D Density Profiles

The 2D density profiles are normalized according to $N_i = \int_0^\infty 2\pi\rho d\rho n_i(\rho)$. For the majority, this requires

$$I_1 = 4 \int_0^{\tilde{R}_1} d\tilde{\rho}\tilde{\rho}\tilde{n}_1(\tilde{\rho}) = 1, \tag{5.25}$$

with $\rho = R_{TF1}\tilde{\rho}$ and we have used $n_1 = n_0\tilde{n}_1$ with n_0 given by equation (5.17). For the minority, we require

$$I_2 = 4 \int_0^{\tilde{R}_1} d\tilde{\rho}\tilde{\rho}\tilde{n}_2(\tilde{\rho}) = \frac{N_2}{N_1}. \tag{5.26}$$

5.1.4 Pressure as a Constraint

To obtain density profiles as a function of imbalance ratio, we use equation (5.14) as a constraint for possible values of q_1, by first considering the pressure at the trap center. From the Gibbs-Duhem relation at fixed temperature, $dp = n_1 d\mu_1 + n_2 d\mu_2$. Since $d\mu_1 = -dU_{trap}$, and the pressure vanishes for $U_{trap} \to \infty$, we have

$$p(0) = -\int_{\infty}^{0} \left[n_1(\rho) + n_2(\rho)\right] dU_{trap}. \tag{5.27}$$

In a harmonic trap, $dU_{trap} = m\omega_{\perp}^2 \rho d\rho$ and $U_{trap} \to \infty$ as $\rho \to \infty$, we immediately obtain

$$p(0) = \frac{m\omega_{\perp}^2}{2\pi} \int_0^{\infty} 2\pi\rho d\rho \left[n_1(\rho) + n_2(\rho)\right] = \frac{m\omega_{\perp}^2}{2\pi} \left(N_1 + N_2\right). \tag{5.28}$$

This result is readily generalized for an anharmonic (Gaussian) transverse trapping potential, leading to an additional negative term $\propto \langle \rho^2 \rangle_i$ for each state i=1,2. To constrain the trap central density, $n_1(0)$ versus $x_{\perp}(0) = n_2(0)/n_1(0)$, we divide both sides of equation (5.28) by the quantity αn_0^2,

$$\frac{p(0)}{\alpha n_0^2} = \frac{m\omega_{\perp}^2}{2\pi} \frac{N_1 + N_2}{\alpha \left(\frac{E_{F1}}{\alpha}\right)^2} = \frac{1}{2}\left(1 + \frac{N_2}{N_1}\right). \tag{5.29}$$

Using equation (5.29) in equation (5.13), we arrive at the constraint equation for $\tilde{n}_1(0)$ for a selected value of $x(0)$.

$$\frac{1}{2}\left(1 + \frac{N_2}{N_1}\right) = \frac{1}{2}\tilde{n_1}^2(0) \left\{1 + x^2(0) + 2x(0) \left[y_m(q_0 \tilde{n}_1(0)) + y_m^{'}(q_0 \tilde{n}_1(0))\right]\right\}. \tag{5.30}$$

5.2 Calculating 2D density profiles from Spin Imbalanced Thermodynamics

We now discuss the iterative steps required to extract the 2D density profiles from the described thermodynamics for a spin-imbalanced quasi-2D Fermi gas. At this point,

it is instructive for the reader to refer to Appendix C, which contains a Mathematica program for 2D density profile calculation. In this file, we have selected a starting q_0 of 6.6 and a polarisation N_2/N_1 of 0.5 to solve equation (5.30) numerically for choices of $x(0)$ in steps of 0.05. We use the local density approximation of equation (5.10), and assume a harmonic confining potential. The trap central normalized chemical potentials for the majority and minority species can now be computed by noting that

$$\tilde{\mu}_{20} = \tilde{n}_1(0)\left[x(0) + y_m(q_0\tilde{n}_1(0))\right], \tag{5.31}$$

and

$$\tilde{\mu}_{10} = \tilde{n}_1(0)\left\{1 + x(0)\left[y_m(q_0\tilde{n}_1(0)) + y_m^{'}(q_0\tilde{n}_1(0))\right]\right\}. \tag{5.32}$$

Equations (5.31) and (5.32) provide the normalized chemical potentials for both species in terms of the central density for the majority, the ratio of the trap central chemical potentials $x(0)$, and the approximate analytic form for the polaron interaction, y_m. The value of q is set by the value of the magnetic field employed. From the pressure constraint condition, equation (5.30), for a chosen polarisation N_2/N_1 , an interpolating function of the central density $\tilde{n}_1(0)$ as a function of $0 \leqslant x(0) \leqslant 1$ can be generated and the relevant values used in equations (5.31) and (5.32) to compute the chemical potentials for both majority and minority species at the center of the trap. To evaluate the cutoff radii of the spin species, we employ the normalised equations (5.21) and (5.22) for all values of $0 \leqslant x(0) \leqslant 1$.

At this point, we remind the reader that the normalised density for the majority species at the trap center can be calculated from equation (5.24) by setting $\tilde{\rho} = 0$. At the location, R_2 , where the minority species vanishes, we use equation (5.20) to evaluate the density of the majority species. The density profile of the majority species between $R_2 \leqslant R \leqslant R_1$, where the minority density vanishes, is a Thomas-Fermi one. The density profile of the majority for $0 \leqslant R \leqslant R_2$ is obtained by numerically solving for $\tilde{\rho}$ in terms of $\tilde{n}_1$ in equation (5.18).

However, the appropriate value of the trap central minority to majority density ratio $x(0)$ is the one for which the normalised density of the majority species, given by the sum of the integral equation (5.25) from $0 \leqslant R \leqslant R_2$ and from $R_2 \leqslant R \leqslant R_1$, adds to 1. We evaluate the integral of the densities for the interpolating functions generated in Appendix C.1. We choose $x(0) = 0.5$, and obtain a value for the norm of 1.25. We repeat the entire iteration for the range of values of $x(0)$ to generate a list of values of norm vs $x(0)$. We interpolate with a straight line to find the $x(0)$ that gives a norm of 1. This list is shown in Appendix C.2. For P=0.5 at an interaction strength of $q = 6.6$, we find that $x(0) = 0.738$.

In addition to the density profile of the majority, the density profile of the minority species between $0 \leqslant R \leqslant R_2$ can now be found from equation (5.19). Cloud radii and density profiles for the particular polarisation are then obtained. This method was extended to provide theoretical calculations at arbitrary polarisations (N_2/N_1). In Appendix C.2, we present the results for $q = 6.6$ at various polarisations in steps of 0.1. The calculations are crucial in obtaining the theoretical curves for cloud sizes as a function of polarization, as well as theoretical central density fits further discussed in Chapter 6.

Using this technique, some calculated spatial profiles for the spin-imbalanced (with $N_2/N_1 = 0.5$) 2D Fermi gas are shown in Figures 5.1 to 5.3. For this case, we find both majority and minority central densities greater than 1, $x(0) = n_2(0)/n_1(0) = 0.762$, $R_1 = 0.894\, R_{TF1}$ and $R_2 = 0.592\, R_{TF1}$. In the region $R_2 \leqslant \rho \leqslant R_1$, the majority density profile is of the Thomas-Fermi form. However, for $0 \leqslant \rho \leqslant R_2$, the spatial profiles are strongly modified by attractive interactions between the two components. For comparison, we note that for an ideal noninteracting Fermi gas, the corresponding 2D radius for the majority component is $R_{1ideal} = R_{TF1}$, while the 2D radius for the minority component is $R_{2ideal} = (N_2/N_1)^{1/4} R_{TF1} = 0.841\, R_{TF1}$.

5.2.1 1D Column Densities from 2D Density Profiles

Until this point, we have dealt exclusively with obtaining two-dimensional density profiles from theoretical polaron thermodynamics. However, in an imaging experiment, it is the one-dimensional column densities which we obtain and fit our theories. This subsection explores the relationship between the two quantities.

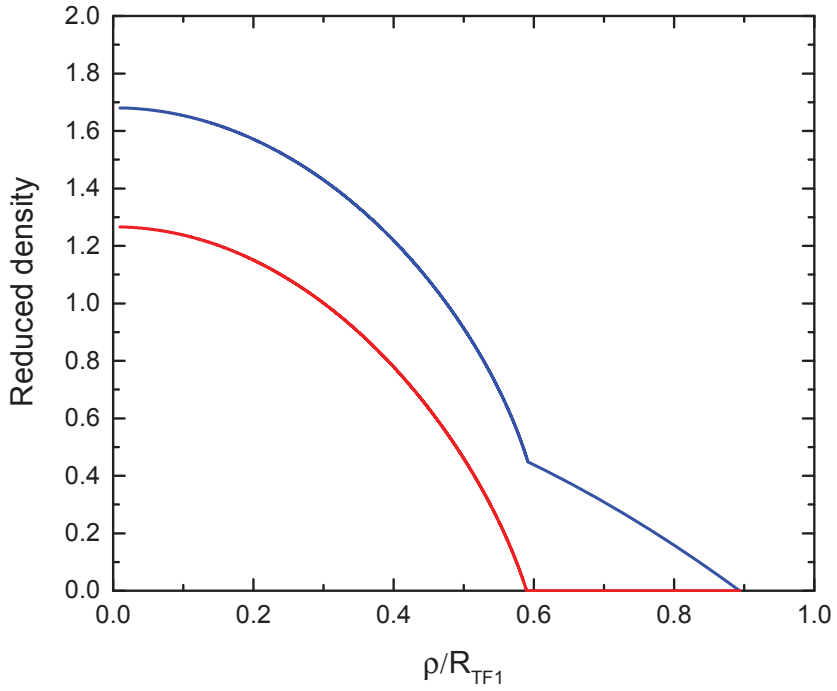

FIGURE 5.1: Calculated 2D density profiles in units of $n_0 = \frac{m}{2\pi\hbar^2}E_F$ for the minority (red lower) and majority (blue upper) for $E_F/E_b = 0.73$ and $N_2/N_1 = 0.5$. The interaction between spin components significantly modifies the spatial profiles.

The one-dimensional column densities, denoted by $n_{ci}(\tilde{x})$, are given in normalized units of N_1/R_{TF1}. These are obtained by integrating the theoretical 2D density profiles in one direction. For the majority, in the interval $-\tilde{R}_1 \leqslant \tilde{x} \leqslant \tilde{R}_1$,

$$\tilde{n}_{c1}(\tilde{x}) = \frac{4}{\pi}\int_0^{\sqrt{\tilde{R}_1^2-\tilde{x}^2}} d\tilde{y}\,\tilde{n}_1\left(\sqrt{\tilde{x}^2+\tilde{y}^2}\right), \tag{5.33}$$

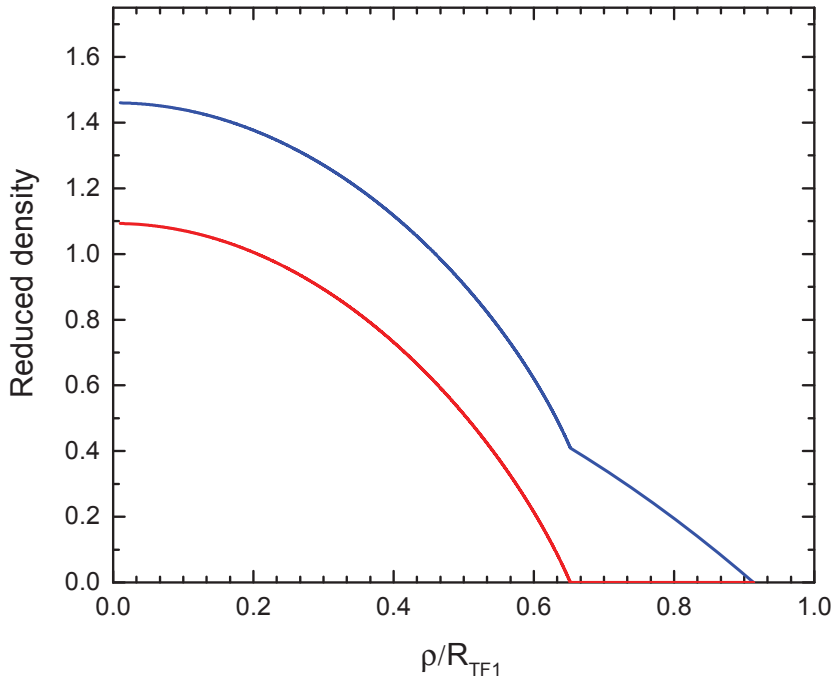

FIGURE 5.2: Calculated 2D density profiles in units of $n_0 = \frac{m}{2\pi\hbar^2}E_F$ for the minority (red lower) and majority (blue upper) for $E_F/E_b = 2.1$ and $N_2/N_1 = 0.5$. The interaction between spin components significantly modifies the spatial profiles.

where the majority column density is normalized to 1. For the minority, which exists in the interval $-\tilde{R}_2 \leqslant \tilde{x} \leqslant \tilde{R}_2$

$$\tilde{n}_{c2}(\tilde{x}) = \frac{4}{\pi}\int_0^{\sqrt{\tilde{R}_2^2-\tilde{x}^2}} d\tilde{y}\,\tilde{n}_2\left(\sqrt{\tilde{x}^2+\tilde{y}^2}\right). \tag{5.34}$$

Here, the minority column density is normalized to N_2/N_1.

5.3 Density Profiles for a Spin Balanced 2D Fermi Gas

In this section, we apply the framework developed in the previous sections to a homogeneous, spin-balanced two-dimensional Fermi gas.

The form for the free energy, similar to equation (5.1) can be written as

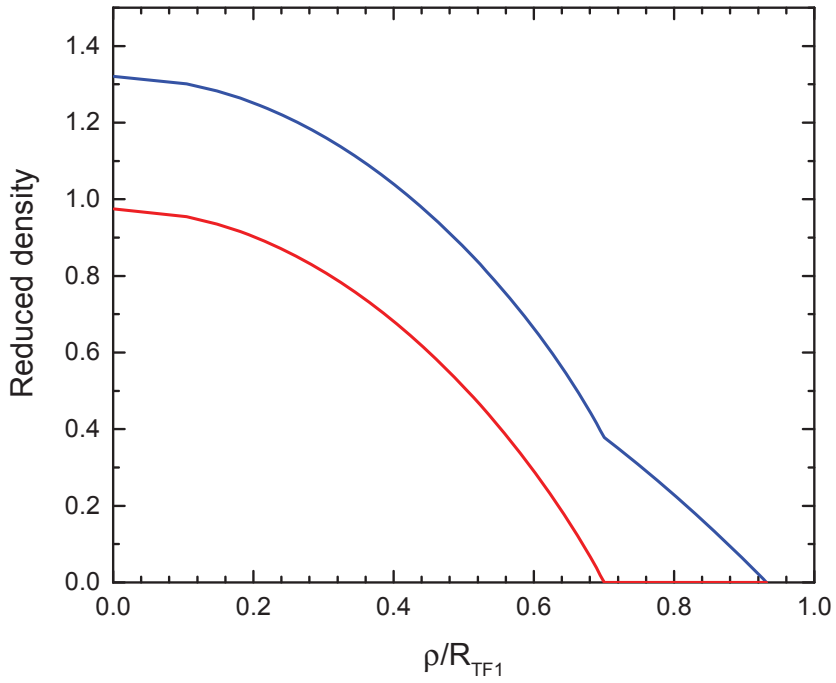

FIGURE 5.3: Calculated 2D density profiles in units of $n_0 = \frac{m}{2\pi\hbar^2}E_F$ for the minority (red lower) and majority (blue upper) for $E_F/E_b = 6.6$ and $N_2/N_1 = 0.5$. Notice that to conserve atom number, as $q = E_F/E_b$ increases, the peak densities decrease while the cutoff radii for the minority species increase.

$$f = \epsilon = \frac{1}{2}n_{1\perp}\epsilon_{F1} + \frac{1}{2}n_{2\perp}\epsilon_{F2} + \frac{1}{2}y_m(q_1)n_2\epsilon_{F1} + \frac{1}{2}y_m(q_2)n_1\epsilon_{F2}, \tag{5.35}$$

where the first two terms represent the Fermi energies of the individual species and the last two terms denote the polaron energy arising from an intermixing of both spins. This differs from the imbalanced case, equation (5.1), by symmetrizing the polaron term. As before, we note the polaron energies to be $E_p(2) = y_m(q_1)\epsilon_{F1}$ and $E_p(1) = y_m(q_2)\epsilon_{F2}$. For the 3D problem at resonance, where $y_m = -0.6$, the same method with $1/2 \to 3/5$ yields the correct pressure for the balanced gas. Substituting $\bar{\mu} \to (\mu_1 + \mu_2)/2$, we recover the result of [54] for the balanced superfluid with a Bertsch parameter $1 + y_m = 0.4$. We note that this form of $y_m(q_i)$ introduced

in equation (5.4) yields the correct chemical potential per single atom in the limit $\epsilon_{F1} \ll E_b$. However, this analytic approximation neglects the non-monotonicity that occurs in the intermediate polaron-to-molecule transition region described in [52].

The chemical potentials are obtained by differentiating equation(5.35) with respect to densities, $\mu_i = \partial f/\partial n_i$, resulting in

$$\mu_2 = \epsilon_{F2} + \frac{1}{2} y_m(q_1)\epsilon_{F1} + \frac{1}{2} y_m(q_2)\frac{n_{1\perp}}{n_{2\perp}}\epsilon_{F2} + \frac{1}{2}\frac{n_1}{n_2} y_m^{'}(q_2)\epsilon_{F2}, \tag{5.36}$$

$$\mu_1 = \epsilon_{F2} + \frac{1}{2} y_m(q_2)\epsilon_{F2} + \frac{1}{2} y_m(q_1)\frac{n_2}{n_1}\epsilon_{F1} + \frac{1}{2}\frac{n_2}{n_1} y_m^{'}(q_1)\epsilon_{F1}. \tag{5.37}$$

Noting that $\epsilon_{F1} = \epsilon_{F2}$ and $n_1 = n_2 = n/2$ for a spin-balanced mixture,

$$\mu_1 = \mu_2 = \epsilon_{F1} + y_m(q_1)\epsilon_{F1} + \frac{1}{2} y_m^{'}(q_1)\epsilon_{F1}. \tag{5.38}$$

Similarly, the free energy density simplifies to

$$f = \frac{n}{2}\epsilon_{F1}\left[1 + y_m(q_1)\right], \tag{5.39}$$

where we have used the same notation as for the previous section, with $\epsilon_{F1} = \alpha n_1$, $q_1 \equiv q_0 \tilde{n}_1$ and $\tilde{n}_1 \equiv n_1/n_0$, where n_0 is the ideal gas unit of density.

To establish a constraint for the density profiles, we write a corresponding form for the local central pressure, $p = n_1\mu_1 + n_2\mu_2 - f$, as

$$\frac{p(0)}{\frac{n}{2}\epsilon_{F\perp}\left(\frac{n}{2}\right)} = 1 + y_m(q_1) + y_m^{'}(q_1), \tag{5.40}$$

which is of the same form as (5.14) with $x_{2\perp}$=1. In the limit where $q \gg 1$,

$$\frac{p(q \gg 1)}{\frac{n}{2}\epsilon_F\left(\frac{n}{2}\right)} \to 0. \tag{5.41}$$

A consistency check gives

$$\mu_1 = \mu_2(q \gg 1) \to -\frac{E_b}{2}, \tag{5.42}$$

thus justifying our choice of 1/2 for the polaron terms in equation (5.35). For $E_b \gg \epsilon_{F1}$, i.e. for $q \to 0$, Taylor expansion of y_m and y'_m leads to $1 + y_m(q) + y'_m(q) \to 0$.

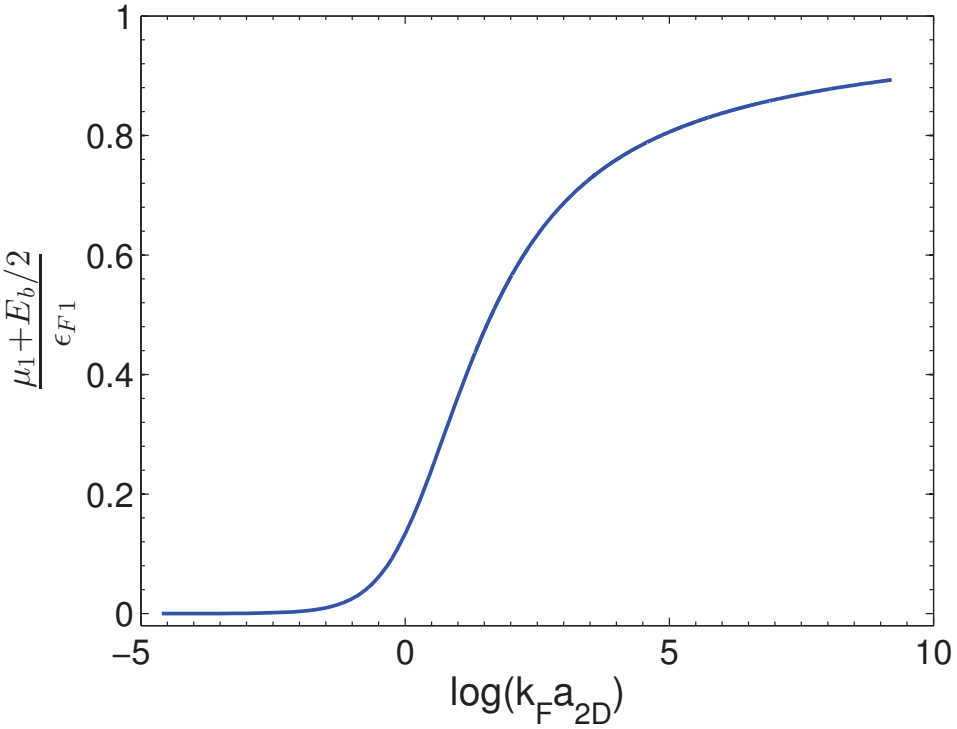

FIGURE 5.4: Chemical potential of a 2-dimensional polaron model used for the balanced mixture, plotted against the interaction parameter $\log[k_F a_{2D}]$. Note that $\mu_1 \to -E_b/2$ for $\epsilon_{F1} \ll E_b$ as it should.

Figure 5.4 shows a plot of the chemical potential from equation (5.38) in units of the local Fermi energy ϵ_{F1} as a function of $\log[k_F a_{2D}]$, where k_F is the local Fermi wavevector, i.e., $k_F^2 = 4\pi n_1$ and $a_{2D} \equiv 2e^{-\gamma_E}\hbar/\sqrt{mE_b}$ is the 2D scattering length as defined in Chapter 3, where $\gamma_E = 0.577$ is Euler's constant.

To obtain the chemical potential and density at the trap center, we first note from the Gibbs-Duhem result, equation (5.28), for $N_1 = N_2$, that $p(0) = m\omega_\perp^2 N_1/\pi$.

Using $x(0) = 1$ for a balanced mixture in the constraint equation (5.24), the central density is immediately determined by numerically solving

$$\tilde{n}_1(0) = \frac{1}{\sqrt{1 + y_m\left[q_0\tilde{n}_1(0)\right] + y_m^{'}\left[q_0\tilde{n}_1(0)\right]}}. \tag{5.43}$$

Normalizing the chemical potential to units of E_F, using the same notation as in the previous section, equation (5.38) becomes

$$\tilde{\mu}_1 = \tilde{n}_1\left[1 + y_m(q_0\tilde{n}_1) + \frac{1}{2}y_m^{'}(q_0\tilde{n}_1)\right]. \tag{5.44}$$

Using eq. (5.43) for $\tilde{n}_1(0)$ then determines $\tilde{\mu}_{10} = \tilde{\mu}_1(0)$. With $\tilde{\mu}_1 = \tilde{\mu}_{10} - \tilde{\rho}^2$, the density profile is then determined for the given $q_0 = E_F/E_b$ using

$$\tilde{\mu}_{10} - \tilde{\rho}^2 = \tilde{n}_1(\tilde{\rho})\left[1 + y_m(q_0\tilde{n}_1) + \frac{1}{2}y_m^{'}(q_0\tilde{n}_1)\right]. \tag{5.45}$$

In the limiting case of $\tilde{n}_1 \to 0$ in equation (5.45), Taylor expansion of y_m and $y_m^{'}$ shows that the right-hand side approaches $-1/(2q_0)$, i.e., $-E_b/(2E_F)$, which is half the dimer binding energy, as expected for the chemical potential of a single atom. With $\tilde{\rho}_{max} = \tilde{R}_1$, the cloud radius in units of R_{TF1} is then given by

$$\tilde{R}_1 = \sqrt{\tilde{\mu}_1(0) + \frac{1}{2q_0}}. \tag{5.46}$$

We note that the density is self-consistently normalized, i.e., it obeys the normalisation equation (5.25) as it should.

5.4 Calculating 2D Density Profiles in Mathematica

For clarity, the steps used to generate spin-balanced 2D density profiles are shown in Appendix D for a Fermi gas with an interaction strength of $q = 2.19$. The definitions

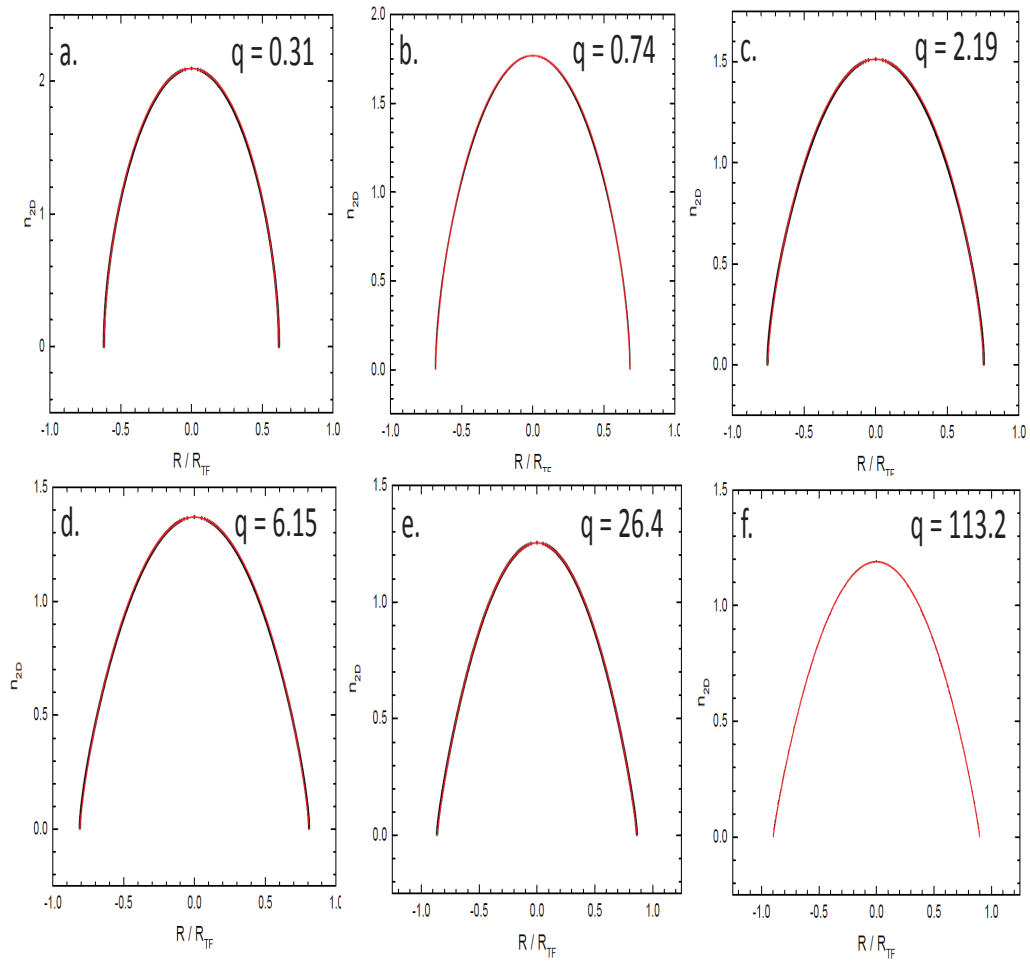

FIGURE 5.5: Calculated 2D density profiles for spin-balanced quasi-2D Fermi gases. As in the prior section, we define the interaction parameter $q = E_F/E_b$ (a) q = 0.31, B = 750 G, (b) q = 0.74, B = 775 G, (c) q=2.19, B = 800 G, (d) q = 6.6, B = 832 G, (e) q = 26.4, B = 880 G, (f) q = 113.2, B = 1200 G. Black dots: Points calculated by iteratively solving equation (5.45) with the same technique described in section 5.2. Red lines: Fits to extract the exponent n in equation (5.49).

for the polaron energy term, $y(q)$, and its derivative, $y'(q)$, are the same as used in the previous section on spin-imbalanced gases. From equation (5.43), we can compute the density at the trap center. This then allows us to evaluate the corresponding chemical potential from equation (5.44). The cloud radius follows from equation (5.46). The density profile is then evaluated from equation (5.45). The calculated 2D spatial density profiles for a spin-balanced 2D Fermi gas with q values of 0.31,

0.74, 2.19, 6.6, 26.4, and 113.2 are shown in Figure 5.5.

5.5 Column Density of Spin-Balanced 2D Fermi Gases

The column density for the spin balanced mixture is calculated by integrating the 2D spatial profiles obtained from equation (5.45). In a harmonic trap, the predicted column density $n_{1D}(x)$ is very well fit by

$$n_{1D}(x) = n_{1D0}\left(1 - \frac{x^2}{R^2}\right)^n \Theta\left[R - |x|\right], \tag{5.47}$$

where Θ is a Heaviside function, n_{1D0} is the peak column density, and n is an exponent, determined from the fit. Normalizing the x-integral of equation (5.47) to the number of atoms in one spin state yields

$$R = \frac{N_1}{n_{1D0}\sqrt{\pi}} \frac{\Gamma(n+3/2)}{\Gamma(n+1)}, \tag{5.48}$$

which determines R from the measured atom number and peak column density.

To find the peak column density we fit the data within 70 percent of the apparent Thomas-Fermi radius. Thus, we avoid fitting the wings of the column density, which suffer from relatively high noise. For comparison, we also fit the measured profiles with the ideal Thomas-Fermi distribution to obtain directly the cut-off radii shown as the black circles in Figure 5.6.

The corresponding 2D profile takes the form

$$n_{2D}(\rho) = n_{2D0}\left(1 - \frac{\rho^2}{R^2}\right)^{n-1/2} \Theta[R - \rho], \tag{5.49}$$

where $\rho = \sqrt{x^2 + y^2}$. Normalization of equation (5.49) to the measured number N_1 and elimination of R using equation (5.48) relates n_{2D0} to n_{1D0},

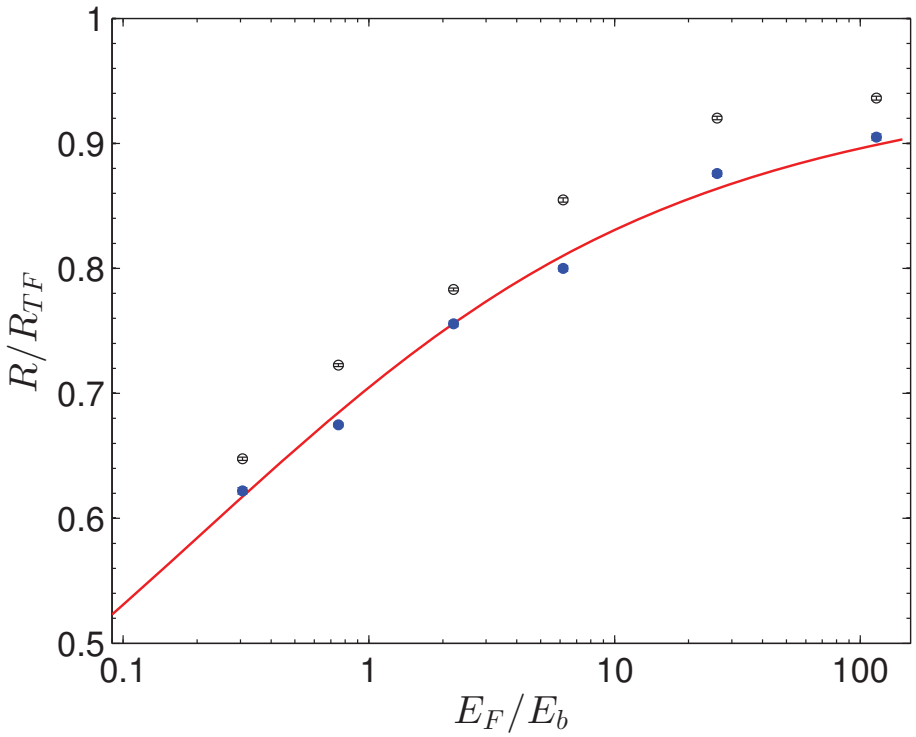

FIGURE 5.6: Radius of the 2D balanced mixture. Blue solid dots: Radius determined from equation (5.48) using the measured central column density and total number N_1. Open black circles: Cut-off radii using ideal gas Thomas-Fermi fits; Red solid curve: Polaron model for the balanced mixture versus interaction parameter $q = E_F/E_b$, where $E_F = \hbar\omega_\perp\sqrt{2N_1}$.

$$\tilde{n}_{2D0} = \frac{\pi}{2}\frac{[\Gamma(n+1)]^2}{\Gamma(n+1/2)\Gamma(n+3/2)}\tilde{n}_{1D0}^2. \tag{5.50}$$

The density profiles of equations (5.47) and (5.49) fit the spatial profiles predicted by the polaron model very well. For an ideal Fermi gas, we would have $n = 3/2$ for the 1D fit. For the polaron model, we find n decreases as $q_0 = E_F/E_b$ decreases, from $n = 1.5$ at $q_0 = 100$, where the gas is nearly ideal, down to $n = 1.03$ at $q_0 = 0.05$, where E_b/E_F is large. Over this range, the first factor in equation (5.50) only varies from 1.39 to 1.34, and therefore is insensitive to n. Using the predicted power law exponents, equation (5.50) then relates $\tilde{n}_{2D0}$ to the measured $\tilde{n}_{1D0}$.

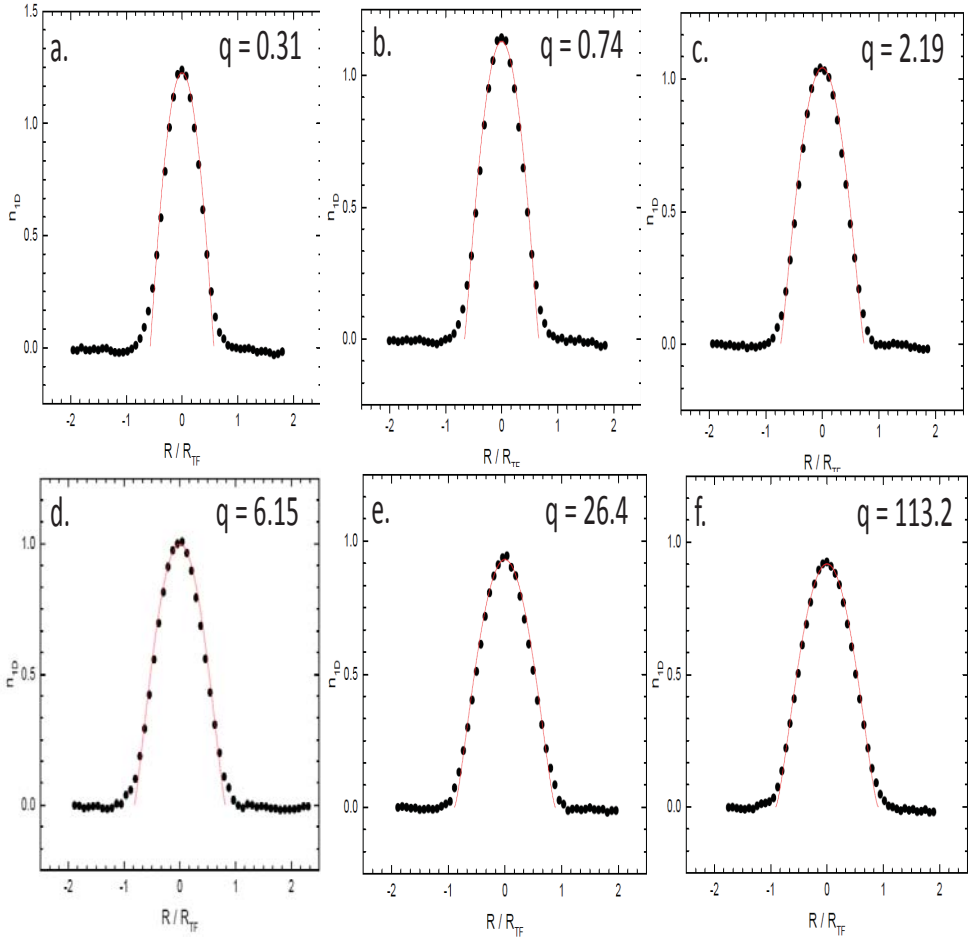

FIGURE 5.7: Column density fits to a quasi-2D Fermi gas for (a) q = 0.31, B = 750 G, (b) q = 0.74, B = 775 G, (c) q=2.19, B = 800 G, (d) q = 6.15, B = 832 G, (e) q = 26.4, B = 880 G, (f) q = 113.2, B = 1200 G. Black dots: Data from experiments. Red lines: Thomas-Fermi fits, with n_0 obtained by fitting data within 70 percent of the peak value to minimize the effects of noise in the wings.

5.6 Experiments on Spin-Balanced Fermi Gases

To obtain column density profiles for spin-balanced quasi-two-dimensional Fermi gases, a 50-50 mixture of the two lowest hyperfine states of ^{6}Li is confined in a single-beam CO_2 laser trap and initially cooled by forced evaporation near the Feshbach resonance at 832 G. The bias magnetic field is then swept to the region of interest before further cooling in a standing wave to an energy close to the ground state.

Table 5.1: Table of values for magnetic fields, interaction parameter $q = E_F/E_b$ values, and fit parameters to equations and used in Figure 5.6.

B-field (G)	**q**	n_0	**n**	R/R_{TF}	R/R_{TF} **fit**
750	0.31	1.226	1.09	0.627	0.650
775	0.74	1.129	1.14	0.690	0.731
802	2.19	1.042	1.22	0.763	0.786
834	6.15	0.999	1.29	0.809	0.860
880	26.4	0.931	1.37	0.886	0.926
1200	113.2	0.918	1.42	0.908	0.933

The correspondence of magnetic field to interaction strength, q-values, is shown in Table 5.1. Rapid, dual-spin high resolution imaging, described in Chapter 4 is used to obtain the spatial profile of the gas from the first image, and the second image is used to extract the atom number for the spin-balanced samples. Reversing the roles of the first and second image made no significant difference to the data. The experimental data is shown in Figure 5.6 on cloud sizes and in Figure 5.7 on column density profiles, obtained from averaging over eight samples at each magnetic field.

5.7 Pressure at Trap Center

Throughout this chapter, we have used the pressure as a constraint for the central density in calculating density profiles from polaron thermodynamics. In this section, we illustrate how the pressure at the trap center is extracted from density profile measurements of a spin-balanced gas at various values of q. The Gibbs-Duhem relation, equation (5.28), leads to a constant value for the pressure at the trap center for a harmonic trap, $p(0) = m\omega_\perp^2 N_1/\pi$. Thus, the reduced pressure for balanced gas is determined from 2D central density

$$\tilde{p}(0) = \frac{p(0)}{p_{ideal}} = \frac{1}{\tilde{n}_1^2(0)}, \tag{5.51}$$

where $p_{ideal} = \epsilon_{F1}(n_1 + n_2)/2 = n_1\epsilon_{F1}$, and $\tilde{n}_1(0)$ is the 2D central density in ideal gas units n_0. We determine $\tilde{n}_1(0) = \tilde{n}_{2D0}$ from the measured column density at the trap center. The measurements are compared with the polaron model predictions,

$$\tilde{p}(0) = 1 + y_m[q_0\tilde{n}_1(0)] + y_m^{'}[q_0\tilde{n}_1(0)]. \tag{5.52}$$

Figure 5.8 shows the polaron prediction(solid curve) for the pressure of the balanced gas as a function of E_F/E_b, which agrees very well with the measurements. For comparison, using BCS theory for a true 2D gas, we have $\epsilon_{F1} = \mu_1 + E_b/2$. Then, the Gibbs-Duhem relation ensures that the pressure at the trap center is just $\epsilon_{F1}^2(0)/\alpha = n_1(0)\epsilon_{F1}(0)$, which yields a reduced pressure $\tilde{p} = 1$ for all E_F/E_b (dotted line), in contrast to the measurements.

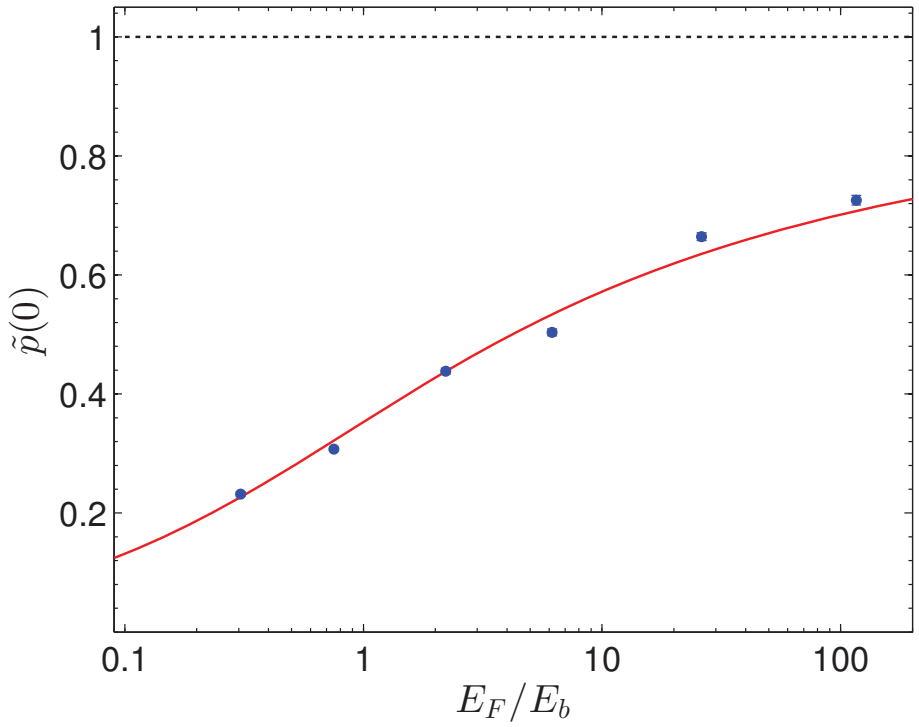

FIGURE 5.8: Reduced 2D pressure at the trap center versus E_F/E_b for the balanced gas. Dots: Experiment; Solid red curve: Prediction based on the polaron model for the balanced gas; Dashed line: prediction of 2D BCS theory.

6

Measurements with Spin Imbalanced Quasi-2D Fermi Gases

In this chapter, we discuss the experimental observations on spin imbalanced quasi-two dimensional Fermi gases, where we rely upon our knowledge of the experimental layout, together with high resolution, rapid dual imaging, and radio-frequency sweep techniques discussed in Chapter 4 to produce and image a gas. Further, we illustrate how the analytic methods developed in the first half of Chapter 5 and Appendix C are applied to study column density profiles, cloud radii, and central densities of spin-imbalanced gases.

Column density difference profiles reveal a dome-shaped profile for low interaction strengths. At higher interaction strengths, a flat centre accompanied by two peaks at the edges are consistent with a balanced-core feature. However, the observed minority and majority radii at various magnetic fields, corresponding to different values of interaction strength, $q = E_F/E_b$, are reasonably well fit by the polaron model of the free energy described earlier in this thesis, with E_F the ideal gas Fermi energy at the trap center and E_b the 2D dimer binding energy. The ratio of the central 2D densities for the two spin species is extracted from our images based on a

Thomas-Fermi model, and separately with inverse Abel transform techniques. Not predicted by the polaron model is an observed transition from a spin-imbalanced normal fluid phase to a spin-balanced central core above a critical imbalance. We develop a balanced core model for the two-dimensional density, and obtain from the model a column density to explain the observed phase separation.

6.1 Preparing a spin-imbalanced quasi 2D Fermi gas

In the experiments described in this chapter, a 50-50 mixture of the two lowest hyperfine states of ^{6}Li, denoted 1 and 2, is confined in a 50-Watt single beam carbon dioxide laser trap and cooled by forced evaporation near the Feshbach resonance at 832 G. During this process, the trapping laser intensity is gradually reduced while a retro-reflected trapping laser beam is smoothly turned on by raising a mechanical chopper. The interference of the incoming and retro-reflected beams results in a standing wave at low beam intensity. To achieve spin-imbalance, the bias magnetic field is swept in 0.8 seconds to 1200 G, where the cloud is weakly-interacting. Then, a frequency-swept radio-frequency pulse is applied to deplete atoms in state 2. The pulse is resonant with a transition from state 2 to a higher lying hyperfine state 3. By varying the amplitude of the ramp, the population imbalance between states 1 and 2 can be controlled. To minimize heating effects and subsequent trap losses due to three-body inelastic collisions, atoms in state 3 are removed with an optical pulse of approximately 5 μs duration, chosen to be on a time scale fast compared to the three-body recombination rate.

The magnetic field is then swept to the field of interest, which sets the dimer binding energy and thus the interaction strength $q = E_F/E_b$. The standing wave trap is further lowered to cool the gas to an energy near the ground state. With our method of forming imbalanced mixtures, the number of atoms in the majority state $N_1 \cong 800$ is held approximately constant as N_2 is varied. Moreover, the ratio N_2/N_1

is nearly the same for each trap site, as the initial 50-50 mixture is trapped in the standing wave before the radio-frequency pulse is applied. As discussed in Chapter 2, the temperature of the samples was determined by fits to quasi-2D Fermi gas profiles to be $T/T_F < 0.21$. Both atom number and imbalance fraction were found to be stable over all magnetic fields employed. All experiments are conducted with the same trap frequencies, so the transverse Fermi energy of the majority component is nominally the same for all experiments.

6.2 Trap Characterization

The trap frequencies were determined by parametric excitation. As discussed in Chapter 4, the trap used was modulated at a frequency approximately twice that of the resonant frequency in this technique. The radial cloud size is monitored as a function of modulation frequency. Due to tight confinement along the axial direction, the amplitude of the excitation is reduced accordingly to maintain a constant atom number while still observing a 10 percent increase in cloud size. With this method, we determine the axial frequency $\omega_z = 2\pi \times 9.0$ kHz along the axial direction and $\omega_\perp = 2\pi \times 407$ Hz in the transverse direction, leading to a trap aspect ratio of approximately 1:22. Using the measured $\omega_\perp$ yields an ideal gas Thomas-Fermi radius R_{TF1} that is larger than the measured majority radius R_1 for $N_2/N_1 \to 0$. As $R_{TF1} \propto N_1^{1/4}/\omega_\perp^{1/2}$, the Thomas-Fermi radius calculated using the measured trap frequency can be over-approximated by neglecting the population of higher axial states, which was estimated in Chapter 2 to contain up to 20 percent of the majority population for our typical ideal gas Fermi energies. Trap anharmonicity also lowers the measured resonance frequency, increasing the estimated R_{TF1}. For our data analysis, we find that a single axial state polaron model yields good agreement with all measured radii of imbalanced gases, as shown in Figures 6.5, 6.6, and 6.7, if we increase

the transverse frequency to $\omega_z = 2\pi \times 440$ Hz so that the measured majority radius R_1 approaches R_{TF1} as $N_2/N_1 \to 0$. Without further adjustment, this frequency is used to compute the Thomas-Fermi radius and 2D density scale $n_0 \propto N_1^{1/2}\omega_\perp$ for all reported measurements, including the spin-balanced pressure data shown in Figure 5.8.

6.3 Energy scales of samples

In the experiments, typical scales are the following: trap potential depth $U_0 = 3.3\,\mu K$, ideal gas Fermi energy $E_{F1} = 0.85\,\mu K$, Thomas-Fermi radius $R_{TF1} = 17.5\,\mu m$, axial level spacing $h\nu_z = 0.43\,\mu K$; $E_b = 1.15\,\mu K$ at 775 G and the transverse energy $m\omega_\perp^2\langle x^2 + y^2\rangle = 0.32\,\mu K$. E_b is determined from equation (3.62) including the small transverse confinement $\omega_\perp/\omega_z = 0.05$, which increases E_b. The effect on the polaron model is small at and below the Feshbach resonance, due to the logarithmic dependence on E_F/E_b. However, for weak binding, at 1200 G, the effect is large, and $E_F/E_b = 116$ for $\omega_\perp/\omega_z = 0.05$, while $E_F/E_b \sim 10^4$ for $\omega_\perp = 0$. For interacting mixtures, dimer pairing decreases the local Fermi energy of both spin components, suppressing the population of higher axial states, which can be included in more complete treatments. The upper limit of the gas temperature for our experiments, obtained from ideal gas column density profile fits to highly spin polarized ($N_2/N_1 \to 0$) mixtures, shown in Figure 2.3a, is estimated to be $k_BT/E_F = 0.21$.

6.4 High-Resolution Rapid Sequential Imaging

The spatial profiles of both spin states 1 and 2 are measured for the same cloud and determined after time-of-flight to minimize effects due to high cloud density by high-resolution absorption imaging with a Pixelfly QE CCD camera, using sequential imaging beam pulses in rapid succession, each resonant with one of the states. In our

CO_2 laser standing wave trap, the transverse profiles are photographed essentially in-situ as we use an expansion time $t_{exp} = 30 - 40\mu s \ll 1/\omega_\perp$. On the contrary, as $t_{exp} \simeq 1/\omega_z$, the individual clouds expand significantly in the tightly confined direction, which lowers the optical density and reduces systematic effects [66]. Imaging pulses are 5 μs long, separated by 5 μs, with intensities just below the saturation intensity. The one-dimensional column density profiles for each image are obtained by averaging over 20 central sites along the direction of tight confinement. The interested reader will find further details on high resolution imaging presented in Chapter 4.

Since absorption imaging of the first spin state inevitably dissociates atom pairs and releases binding energy, thereby affecting the atom number and cloud size represented by the second image, we rescale the amplitude of the second density profile by a maximum of 11 percent to match the peak density for spin-balanced clouds. Maximum rescaling was required for images at the largest E_b. Cut-off radii and central 2D densities are extracted using ideal gas Thomas-Fermi distributions for each image of 20 pancake clouds. We also use the inverse Abel transformation to obtain model-independent values of 2D central densities. These values were subsequently found to be consistent with those obtained from the Thomas-Fermi distributions.

6.5 Column Density Profiles

Direct absorption imaging measures the column density profiles $n_{1D}(x) = \int dy n_{2D}(x, y)$ as a function of E_F/E_b and N_2/N_1. Here, $N_1(N_2)$ is the number of majority (minority) atoms. Figure 6.1 shows the measured column density profiles, and the difference between majority and minority column density profiles at 832 G, corresponding to $E_F/E_b = 6.6$, while Figure 6.2 shows the observed profiles at 775 G, corresponding to $E_F/E_b = 0.75$. In both figures, the green curves show the density distribution of the majority, while the red curves show the density distribution of the minority. The blue-dashed curves result from a direct subtraction of the minority from the majority

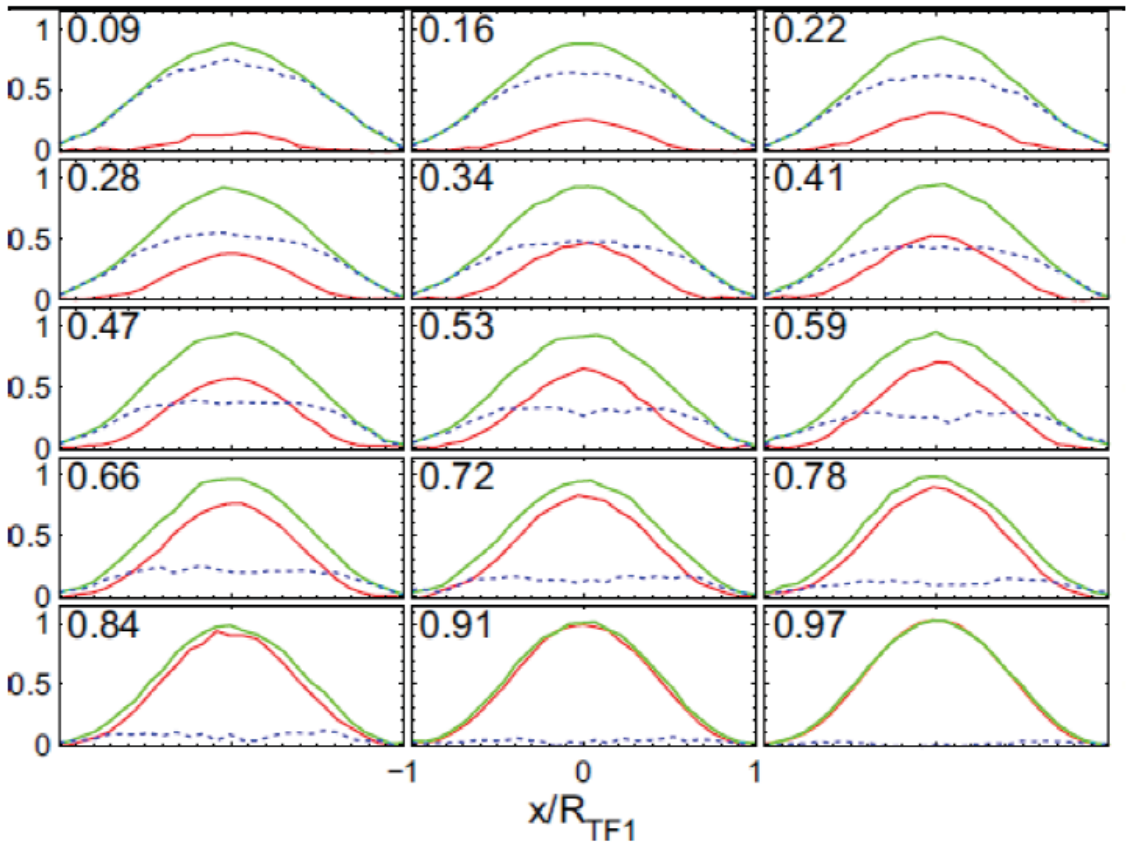

FIGURE 6.1: Measured column density profiles in units of N_1/R_{TF1} at 832 G, for $E_F/E_b = 6.6$ versus N_2/N_1. Green: 1-Majority; Red: 2-Minority. Blue-dashed: Column density difference. Each profile is labelled by its N_2/N_1 range. Notice the difference density profiles are dome-shaped for N_2/N_1 ranging from 0.09 to 0.41. For N_2/N_1 of 0.47 to 0.97, the qualitative features appear consistent with the difference profile of two noninteracting gases; a relatively smooth profile over the radii where the gases overlap, which drops to zero smoothly as the minority vanishes.

distribution. The difference density profiles at 832 G in Figure 6.1 are comparatively dome-shaped and homogeneous in structure, with slight inhomogeneities likely due to shot-to-shot variations; a gradual suppression of the dome-shaped structure to zero is observed with increasing N_2/N_1.

The signatures of phase separation, namely a flat center and two peaks at the edge are evident in the density difference profiles at 775 G. The observed characteristic feature is more prominent for images obtained at high interaction strength

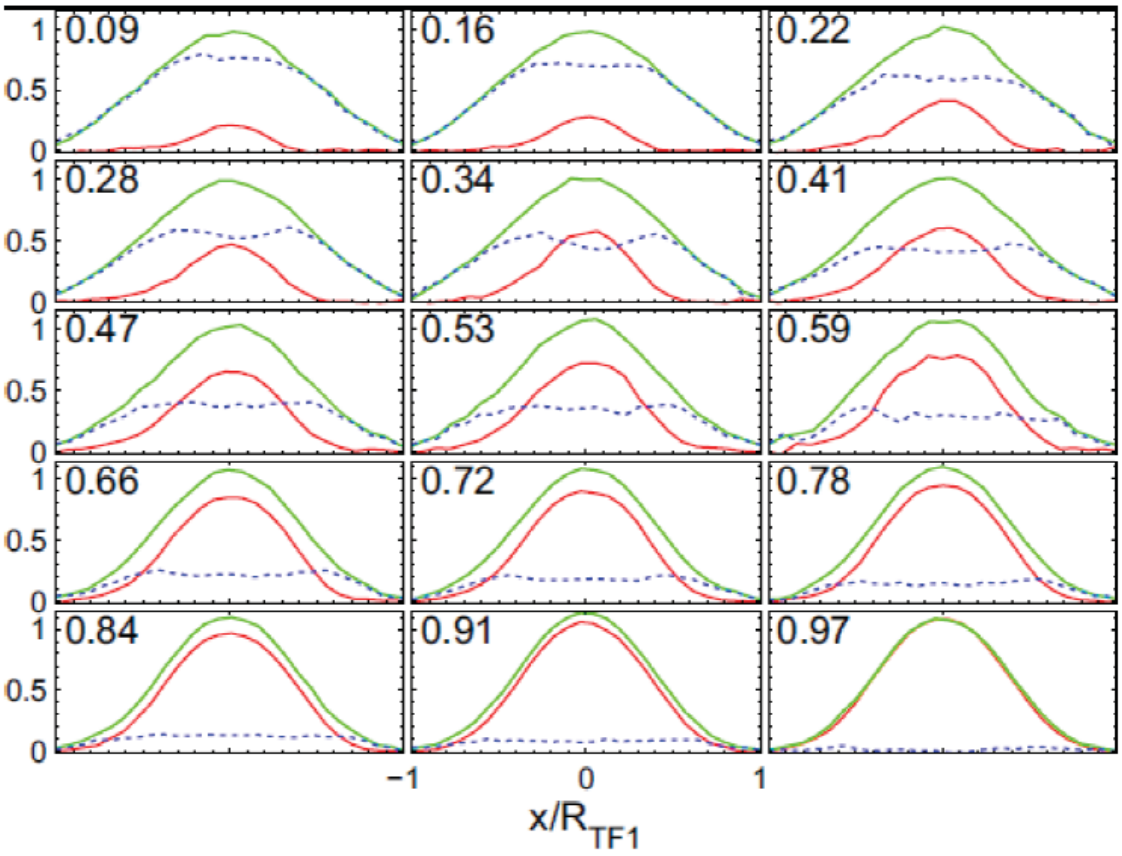

FIGURE 6.2: Measured column density profiles in units of N_1/R_{TF1} at 775 G, for $E_F/E_b = 0.75$ versus N_2/N_1. Green: 1-Majority; Red: 2-Minority. Blue-dashed: Column density difference. Each profile is labelled by its N_2/N_1 range. In contrast to the case for $E_F/E_b = 6.6$ shown in Figure 6.1, a flat center is evident in the density difference for N_2/N_1 from 0.09 to 0.22 for $E_F/E_b = 0.75$. Furthermore, for N_2/N_1 ranging from 0.28 to 0.41, the flat centre and two peaks at the edges are consistent with a fully paired core of the corresponding 2D density profiles. In general, these features are more prominent for profiles of gases with higher interaction strengths.

(or correspondingly low q values). A prominent difference between the profiles in Figures 6.1 and 6.2 is seen for $N_2/N_1 = 0.34$; in Figure 6.2, a suppression in the middle of the cloud is accompanied by two side peaks. This feature is noticeably absent in Figure 6.1. The observed feature in Figure 6.2 is to be expected assuming the LDA for a shell structure with an evenly paired core in a harmonic trap, which we proceed to describe in the next section.

The measured column densities for $N_2/N_1 = 0.5$ are shown in Figure 6.3 as solid red and green curves, with the difference in column densities $n_{c1} - n_{c2}$ shown as the solid blue curve. The dashed curves show the corresponding predictions based on the normalized equations with no adjustable parameters. The predicted profile for the column density difference, as well as for the individual profiles, are in reasonable agreement with the data, both in absolute peak density and width. However, for $E_F/E_b = 0.75$, the data for the difference in the column densities has a flatter profile and sharper edges than the polaron model predictions, consistent with a transition to a balanced core.

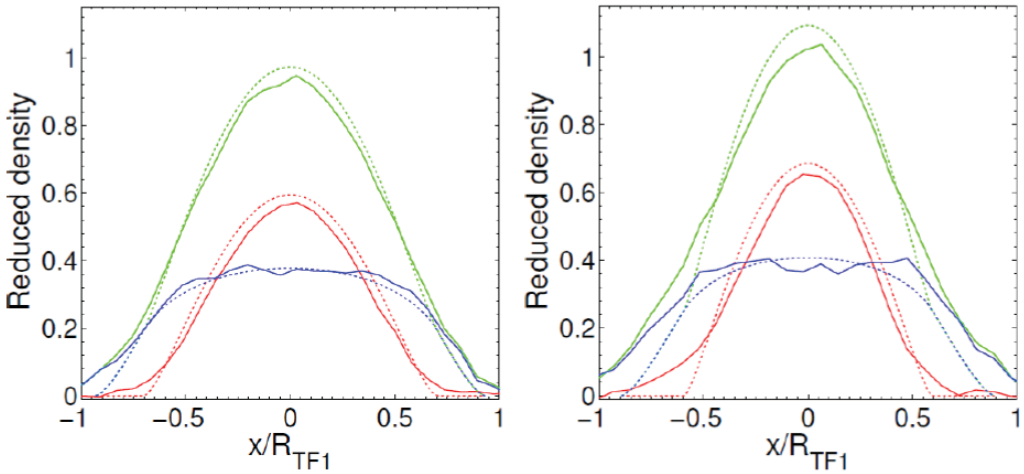

FIGURE 6.3: Column density in units of N_1/R_{TF1} for $N_2/N_1 = 0.5$. Left: $E_F/E_b = 6.1$; Right: $E_F/E_b = 0.75$. Green: 1-Majority; Red: 2-Minority, Blue: Density difference. Solid curves show the data; Dashed curves show the polaron model predictions for the same $\omega_\perp$ used in the fits to the cloud radii and central density data in this chapter.

6.6 2D Balanced Core Model

To further investigate the transition to a balanced core as the fraction N_2/N_1 is increased from zero, we consider a model for a fully balanced 2D core, which is consistent with our observations. We take the radius of the spin-balanced core to

be R_2. Beyond the core, we assume the minority density vanishes and the majority takes the form of a 2D Thomas-Fermi profile. The 2D density profile difference can then be written as $\Delta n_{2D}(\rho) = A\Theta[\rho - R]\Theta[R_1 - \rho](1 - \rho^2/R_2^2)$, where Θ is a Heaviside function. The $\Theta[R_1 - \rho]$ term sets the radius where the majority species drops to zero, and the $(1 - \rho^2/R_2^2)$ determines where the minority vanishes. The corresponding column density difference, $\Delta n_{col} = \int dy \Delta n_{2D}(\sqrt{x^2 + y^2})$, is fit to the data using A and R as free parameters.

An infinitesimal strip of the column density difference for $0 \leqslant R \leqslant R_2$ can be written as

$$\Delta n_{col}^{<}(x) \equiv 2A\Theta[R_2 - x]\Theta[R_1 - x]I^{<}(x), \tag{6.1}$$

where $I^{<}(x) = \int_{\sqrt{R_2^2 - x^2}}^{\sqrt{R_1^2 - x^2}} dy \left(1 - \frac{x^2 + y^2}{R_1^2}\right)$. Similarly, for $R_2 \leqslant \rho \leqslant R_1$, the column density difference is

$$\Delta n_{col}^{>}(x) \equiv 2A\Theta[x - R_2]\Theta[R_1 - x]I^{>}(x) \tag{6.2}$$

with $I^{>}(x) = \int_0^{\sqrt{R_1^2 - x^2}} dy \left(1 - \frac{x^2 + y^2}{R_1^2}\right)$. Evaluating the integrals leads to

$$I^{<}(x) = \frac{2}{3}R_1 \left(1 - \frac{x^2}{R_1^2}\right)^{3/2} - R_2 \left(1 - \frac{x^2}{R_1^2}\right)\left(1 - \frac{x^2}{R_2^2}\right)^{1/2} + \frac{R_2^3}{3R_1^2}\left(1 - \frac{x^2}{R_2^2}\right)^{3/2} \tag{6.3}$$

and

$$I^{>}(x) = \frac{2}{3}R_1 \left(1 - \frac{x^2}{R_1^2}\right)^{3/2}. \tag{6.4}$$

Since the column density difference can be written as

$$\Delta n_{col}(x) = 2A\Theta[R_1 - x]\left\{\Theta[R_2 - x]I^{<}(x) + \Theta[x - R_2]I^{>}(x)\right\}, \tag{6.5}$$

where $\Theta[R_2 - x] + \Theta[x - R_2] = 1$, we see that

$$\Delta n_{col}(x) = 2A\Theta[R_1 - x]\left\{\frac{2}{3}R_1\left(1-\frac{x^2}{R_1^2}\right)^{3/2}\right.$$
$$\left.-\Theta[R_2 - x]\left[R_2\left(1-\frac{x^2}{R_1^2}\right)\left(1-\frac{x^2}{R_2^2}\right)^{1/2} - \frac{R_2^3}{3R_1^2}\left(1-\frac{x^2}{R_2^2}\right)^{3/2}\right]\right\}. \quad (6.6)$$

The results of our fit with a spin balanced core model described in this section for $N_2/N_1 = 0.35$ at $E_F/E_b = 0.75$ are shown in Figure 6.4 as a red solid curve, with data represented by a dashed blue curve. This corresponds to a magnetic field of approximately 775 G. The model fits the flat center and two peaks at the edges well, revealing the consistency of a balanced core theory with measured column densities. However, better imaging statistics and finer models would be required to determine if intermediate phases, such as a three-shell structure might exist in a quasi-two dimensional geometry.

6.7 Cloud radii of imbalanced gases

From the measured column densities for various polarizations at different interaction strengths, the cloud radii for the individual spin species is directly obtainable from fits. The radii at which the individual spins vanish is given by the cut-off radii R_2 and R_1, respectively. The minority species fails to exist beyond the balanced-core radius, while the radius R_1 of the majority species sets the spatial extent of the cloud. Fitting the experimentally obtained column densities using the fit function $n_{1D}(x) = n_{1D}(0)(1 - x^2/R^2)^{3/2}$, i.e., the $y-$ integrated spatial profile of an ideal 2D Fermi gas, gives the cut-off radii R and central 2D densities for each state.

Figures 6.5, 6.6, and 6.7 show the measured radii for the minority R_2 and majority R_1 as a function of N_2/N_1, for $E_F/E_b = 6.6, 2.1$ and 0.75. The blue dots in these figures denote the majority species and the red dots denote the minority. We note

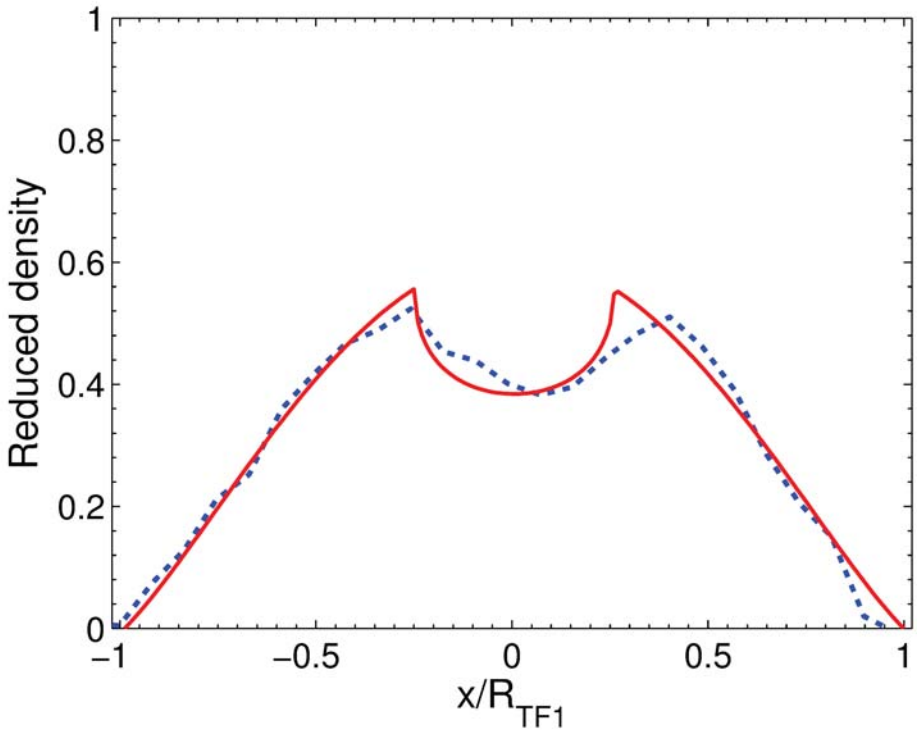

FIGURE 6.4: Measured column density in units of N_1/R_{TF1} for $N_2/N_1 = 0.35$ at $E_F/E_b = 0.75$ shown as a dashed blue curve. Red solid curve shows the balanced core model prediction described in section 6.6.

that the data presented here was obtained by binning; a radiofrequency sweep of arbitrary amplitude generates spin-imbalanced gas samples with a spread of polarisations which is measured in each shot from the measured total numbers N_2 and N_1. Following data acquisition, the column density profiles are averaged and binned over a range of imbalance N_2/N_1 in steps of 0.06. Each profile is labeled by the central value of the corresponding range.

The 2D ideal Fermi gas predictions are denoted by the dotted line and curve; we recall from Chapter 2 that $R_{TF} = (8N)^{1/4}\sqrt{\frac{\hbar}{M\omega_r}}$, implying an explicit dependence only on the atom number and radial trap frequency. Hence, R/R_{TF} for the majority species takes the value of 1 for arbitrary N_2/N_1 while the profile for the minority species takes the shape of $(N_2/N_1)^{1/4}$. The ideal gas result works reasonably well

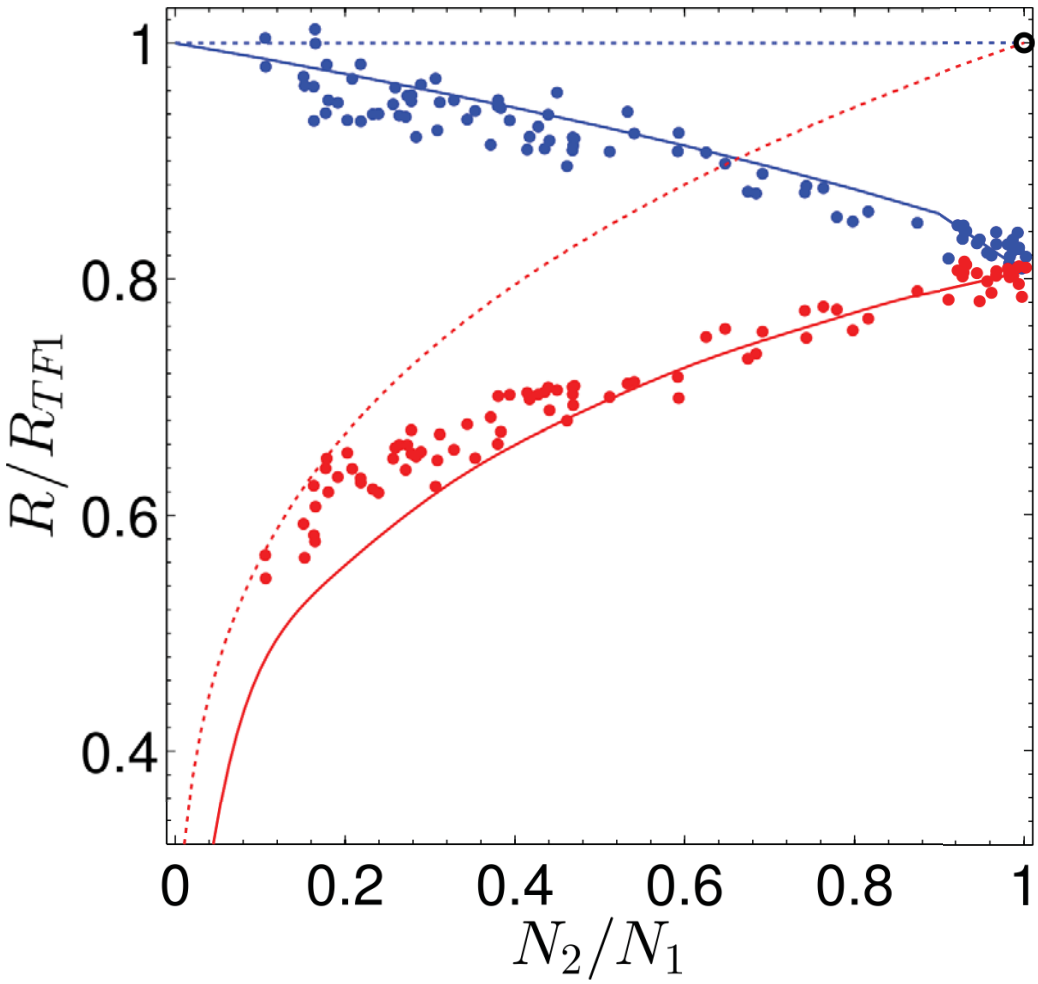

FIGURE 6.5: Majority radii (upper-blue) and minority radii (lower-red) in units of the Thomas-Fermi radius of the majority for $E_F/E_b = 6.6$ (left panel). Dots: Data; Solid curves: 2D polaron model for imbalanced mixture $0 \leqslant N_2/N_1 \leqslant 0.9$; Dashed line and curve: Ideal Fermi gas prediction; Black circle upper right: 2D-BCS theory for a balanced mixture.

for $q = 6.6$ at low N_2, as one might expect. The measured R_1 goes to the ideal gas result for low N_2 in all cases, for our choice of $\omega_\perp$.

The theoretical predictions from a polaron theory, shown as solid curves for N_2/N_1 ranging from 0 to 0.9, for both majority and minority species were calculated with the Mathematica programs in Appendix C, and explained in Chapter 5. In general, we observe that the measured cloud radii deviate from theoretical predictions at low values of N_2/N_1, probably due to inefficient second-stage evaporative cooling

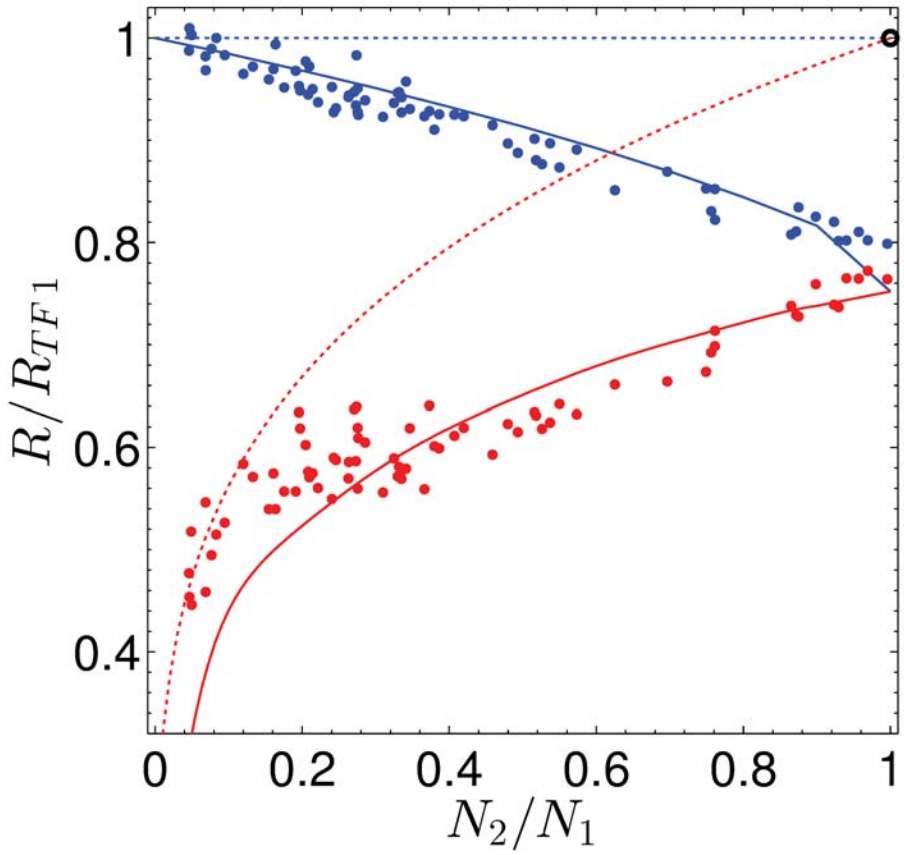

FIGURE 6.6: Majority radii (upper-blue) and minority radii (lower-red) in units of the Thomas-Fermi radius of the majority for $E_F/E_b = 2.1$. Dots: Data; Solid curves: 2D polaron model for imbalanced mixture $0 \leqslant N_2/N_1 \leqslant 0.9$; Dashed line and curve: Ideal Fermi gas prediction; Black circle upper right: 2D-BCS theory for a balanced mixture. The discontinuity between $N_2/N_1 = 0.9$ and $N_2/N_1 = 1$ results from a linear interpolation between these two points.

resulting from the large imbalance in start-state populations. Collisions between unlike particles are therefore inhibited. Moreover, the signal-to-noise ratio in this limit is generally low, a problem which we overcame with the selection of a sufficiently small region of interest in the radial direction (of approximately 5 pixels each way in the radial direction beyond the extent of the clouds).

At the other extreme of spin-balanced mixtures, i.e. when $N_2/N_1 = 1$, we note that the measurements differ from 2D-BCS theory predictions, indicated by black

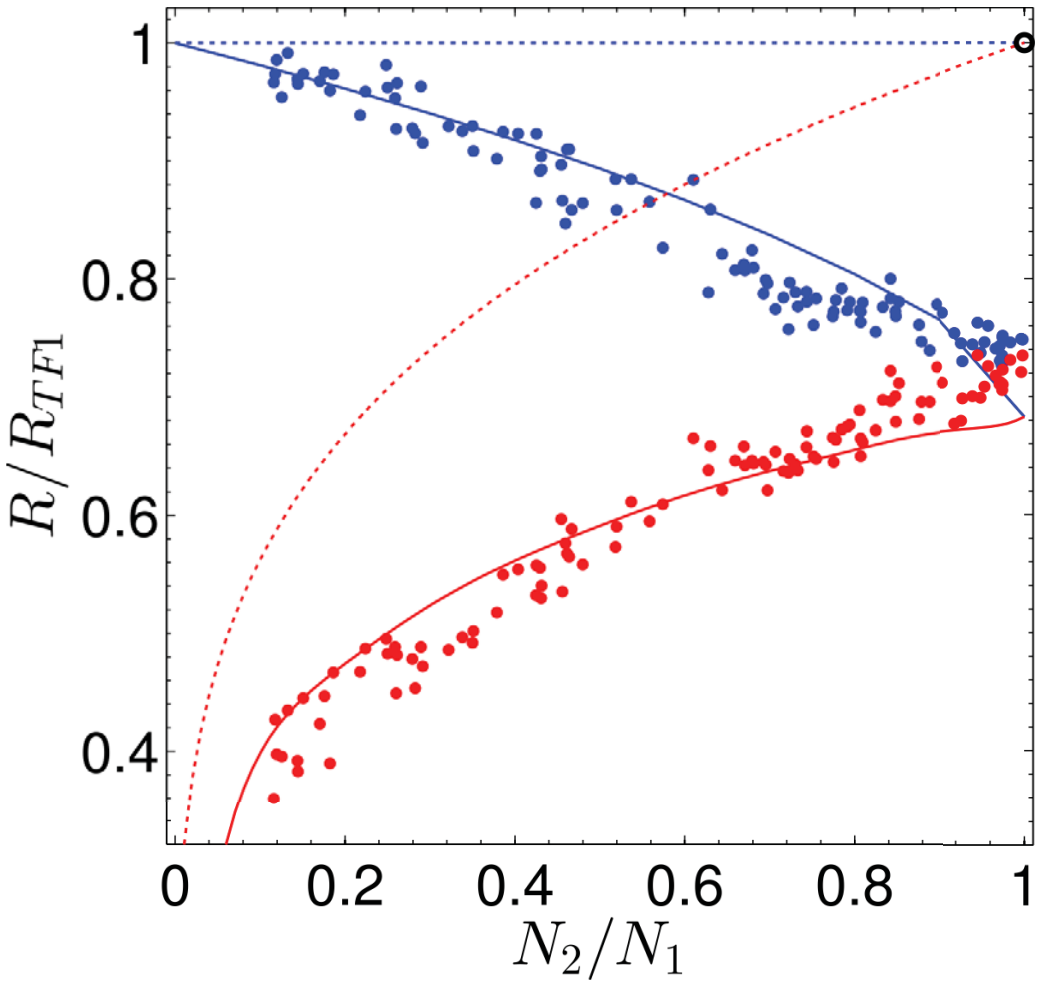

FIGURE 6.7: Majority radii (upper-blue) and minority radii (lower-red) in units of the Thomas-Fermi radius of the majority for $E_F/E_b = 0.75$. Dots: Data; Solid curves: 2D polaron model for imbalanced mixture $0 \leqslant N_2/N_1 \leqslant 0.9$; Dashed curve and line: Ideal Fermi gas prediction; Black circle upper right: 2D-BCS theory for a balanced mixture. The discrepancy between measured and predicted values for the spin balanced samples is accounted for in the text.

circles on the right of each figure. We relegate a further discussion of the predictions of 2D BCS theory and a comparison with the radii to the next section. As the interaction strength varies from $q = E_F/E_b = 6.6$ (Figure 6.5) to 2.1 (Figure 6.6) and then to 0.75 (Figure 6.7), the spin-balanced gas gets substantially smaller. We attribute this to E_b, which we choose with an external magnetic field. As derived in Chapter 2, the majority Fermi energy of the gas is proportional to $\sqrt{N}$ and the

radial trap frequency, $\hbar\omega_\perp$; the majority atom number was measured to be nominally constant at different magnetic fields in our experiments, while the trap frequency was assumed constant. From binding energy predictions in Chapter 3, we saw that a smaller $q = E_F/E_b$ corresponds to a larger binding energy, giving rise to more tightly bound dimers which condense.

The deviation from polaron theory theory predictions for the spin-balanced gas is particularly prominent at $q = 0.75$. The astute reader might note that a comparison against Figure 5.6 for the corresponding data in measurements on spin-balanced gases shows a negligibly small difference in theoretical and measured values of R/R_{TF}, whereas Figure 6.7 shows a discrepancy in R/R_{TF} of 0.08. In obtaining the data for Figure 5.6, a balance in spin populations was first established by imaging each spin species in different time order over several (ten) averages. Subsequently, the first image was used to determine the mean square cloud size and the second image was used to ensure that the atom number was consistent to within 5 percent of the previously measured values for population balanced mixtures.

However, in obtaining the population imbalanced data shown in Figure 6.7, the size and atom number were separately determined for each spin species. While an accurate measurement of the minority population cloud statistics could be obtained through the first image, the second image (of the majority species) necessarily suffers from a lower atom count and enlarged cloud size due to atom acceleration effects arising from the first imaging pulse. We minimized such effects by utilizing short imaging pulse durations, $t < 1/\omega_\perp$, and also by allowing a 30 μs time-of-flight for the first image, and a 40 μs time-of-flight for the second image.

6.7.1 Predictions of BCS Theory for a 2D Fermi Gas

We first compare our data to predictions of BCS theory for a true 2D Fermi gas. The theory shows that the local Fermi energy for a balanced mixture is $\epsilon_{F1} = \mu + E_b/2$,

where $\epsilon_{F1} = \alpha n_1$ and μ is the local chemical potential. Here $n_1 = n_2$ is the local density and $\alpha \equiv 2\pi\hbar^2/m$, with m the atom mass. For a trapping potential $U_{trap}(\rho)$, $\mu = \mu_0 + E_b/2$, the predicted density profile is of the Thomas-Fermi form. For a harmonic trap, $U_{trap}(\rho) = m\omega_\perp^2\rho^2/2$, one obtains $n_1(\rho) = n_1(0)(1 - \rho^2/R_{TF1}^2)$, where $n_1(0) = \epsilon_{F1}(0)/\alpha$. Normalization gives $\epsilon_{F1}(0) \equiv E_F = \hbar\omega_\perp\sqrt{2N_1}$, the Fermi energy of an ideal Fermi gas at the trap center. The radius at which the density vanishes is the corresponding Thomas-Fermi radius $R_{TF1} = \sqrt{2E_F/(m\omega_\perp^2)}$. For the spin-balanced cloud, $N_2/N_1 = 1$, shown as black circles on the top right corner of Figures 6.5, 6.6, and 6.7, the 2D BCS prediction is then identical to that of an ideal gas $R/R_{TF1} = 1$ for both spin states, in disagreement with the measured radii, which are much smaller. We conclude that the BCS mean-field theory (MFT) is, as expected, not adequate for describing our system with intermediate coupling, where interparticle spacing is comparable with pair size. This sets our experiment apart from previously studied nearly 2D systems [36] that produced a good agreement with MFT predictions.

6.7.2 Polaron model for a 2D Fermi Gas

We find instead that the polaron model predictions, shown as the solid curves in Figures 6.5, 6.6, and 6.7, are in good agreement with the measurements. We have extended the predictions for the imbalanced gas from $N_2/N_1 = 0.01$ up to $N_2/N_1 = 0.9$ in steps of 0.05, and separately used the spin-symmetrized free energy density model described in Chapter 5 and Appendix D to calculate the radii for $N_2/N_1 = 1$. The apparent discontinuity that results in the theoretical predictions between $N_2/N_1 = 0.9$ and $N_2/N_1 = 1$ in the figures is an artifact of an interpolation between these two points.

Figures 6.8, 6.9, and 6.10 show the measured ratios R_1/R_2, which are nearly independent of $\omega_\perp$. The value of $\omega_\perp$ was scaled to get $R_1 = R_{TF1}$ for $N_2 = 0$. At this

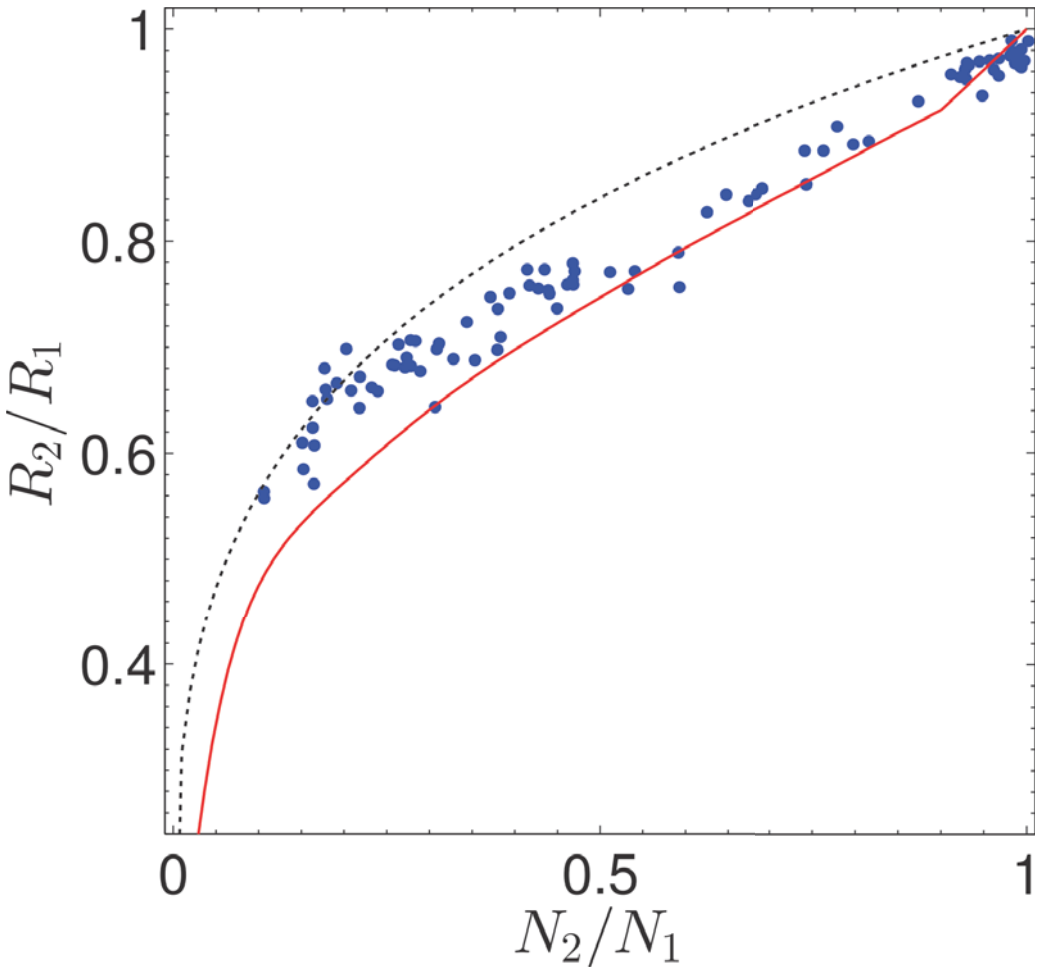

FIGURE 6.8: Ratio of the minority to majority radius versus N_2/N_1 for q of 6.6. Dots: Data; Solid curve: 2D polaron model, Dashed curve: Ideal Fermi gas prediction

point, we recall from chapter 2 that the Fermi energy of an ideal 2D gas, $E_F \propto \sqrt{N}$. Since the Fermi energy is in turn proportional to the square of the cloud size, $E_F \propto R^2$, the predictions for an ideal 2D Fermi gas lead to $(N_2/N_1)^{1/4}$. These are shown as dotted curves. It is however evident that the data is still in reasonable agreement with the predictions of a polaron model, shown as solid curves. At low N_2 for the smallest E_b, the slight deviation from theory is probably due to finite temperature effects. The general agreement reinforces the suggestion that 2D polarons play an important role in determining the cloud profiles for the spin-imbalanced quasi-two-dimensional strongly interacting Fermi gas.

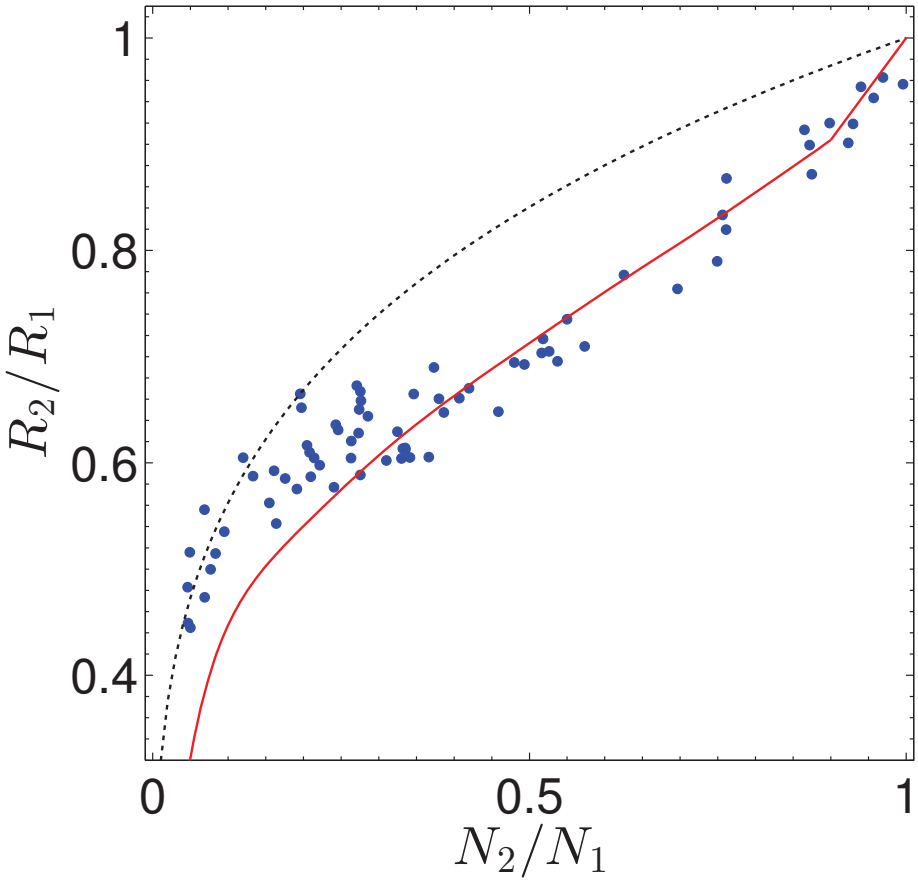

FIGURE 6.9: Ratio of the minority to majority radius versus N_2/N_1 for q of 2.1. Dots: Data; Solid curve: 2D polaron model, Dashed curve: Ideal Fermi gas prediction

We find the single axial state polaron model yields good agreement with all measured radii of the balanced gas, if we increase the transverse frequency from the parametrically determined value of $\omega_\perp = 2\pi \times 407$ Hz to $\omega_\perp = 2\pi \times 440$ Hz, so that the measured majority radius R_1 approaches R_{TF1} as $N_2/N_1 \to 0$. Without further adjustment, this frequency is used to compute the Thomas-Fermi radius and 2D density scale, $n_0 \propto N_1^{1/2}\omega_\perp$ for all measurements reported. We find that reducing N_1 instead of increasing $\omega_\perp$ is inconsistent with the data and is not equivalent: The density n_0 and R_{TF1} scale in the same direction with N_1, while they scale in opposite directions with $\omega_\perp$.

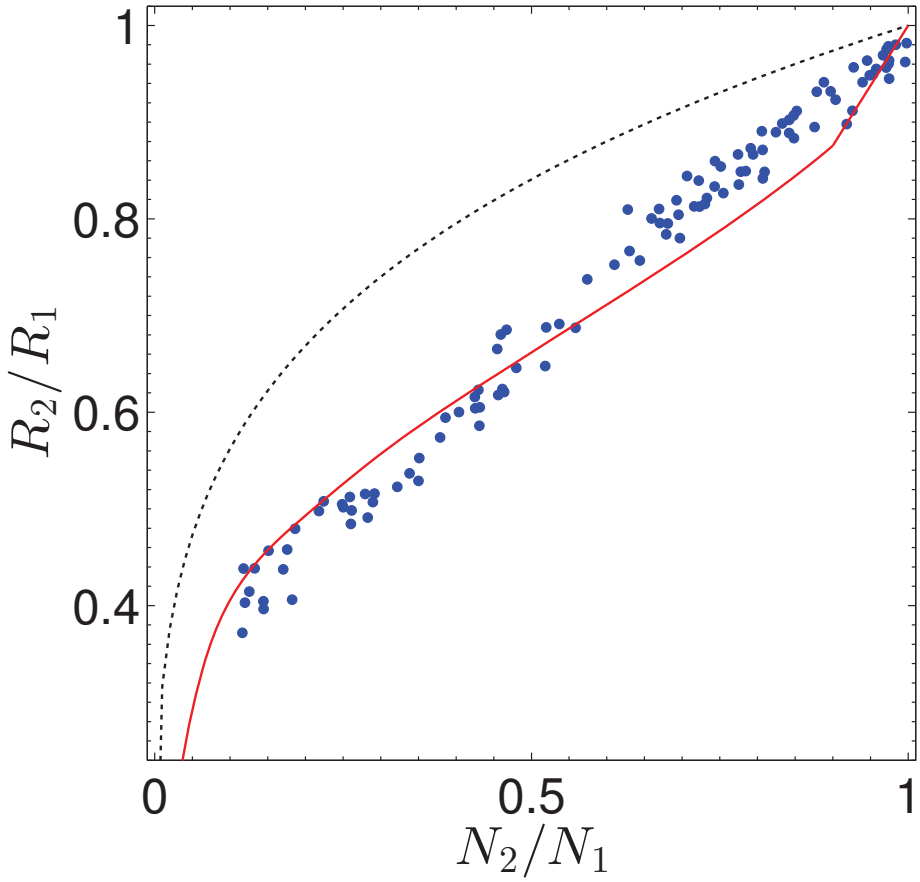

FIGURE 6.10: Ratio of the minority to majority radius versus N_2/N_1 for q of 0.75. Dots: Data; Solid curve: 2D polaron model, Dashed curve: Ideal Fermi gas prediction

6.8 Central densities of imbalanced gases

We have also measured the central two dimensional densities for each species, n_{2D}, and obtained the central density ratio n_2/n_1 of the 2D gas as a function of N_2/N_1 using two methods. This allows us an estimate of the systematic error in measurement. First, we fit a Thomas-Fermi 1D profile to each column density, from which we find the corresponding 2D densities. We recall that the Thomas-Fermi 1D profile is given by $n_{1D}(x) = n_{1D}(0)\left(1 - x^2/R^2\right)^{3/2}$, which is related to the 2D density by $n_{1D}(x) = \int dy n_{2D}(x, y)$. Explicit forms for both densities were given in equations 2.63

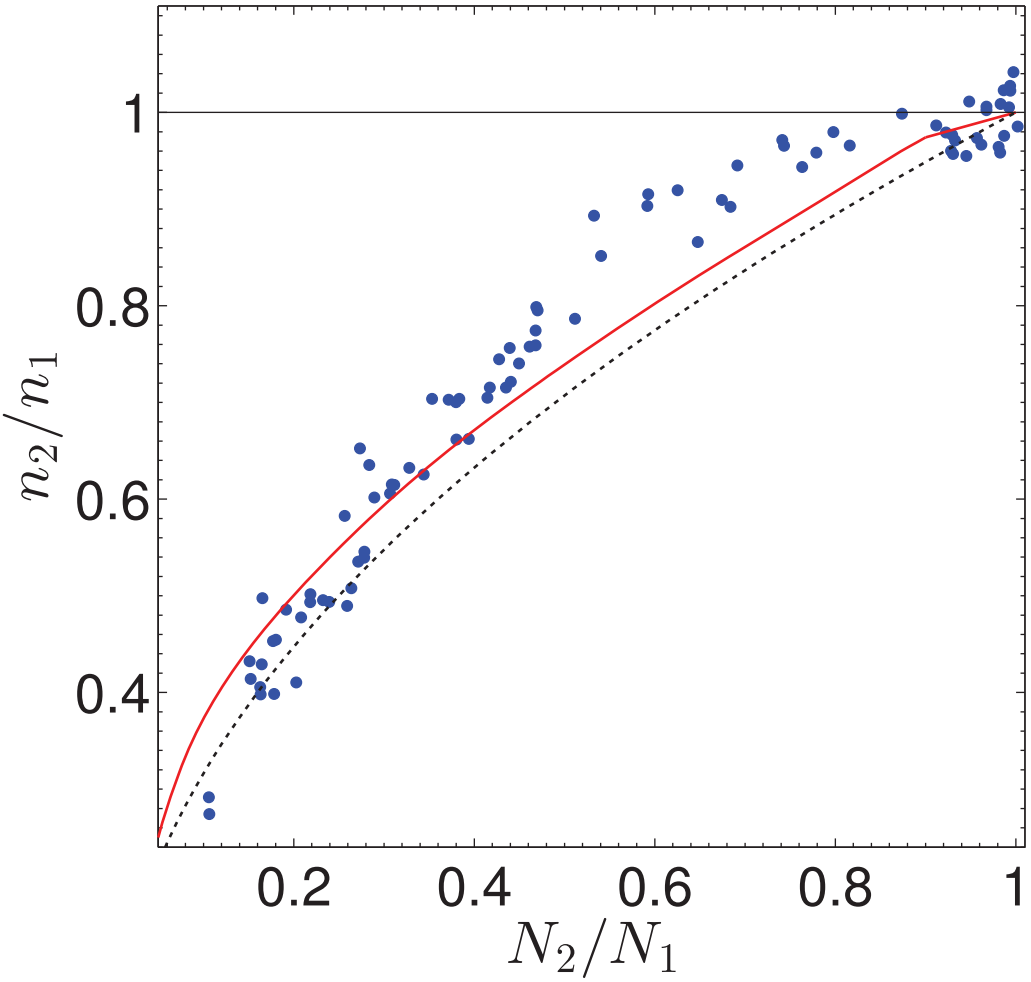

FIGURE 6.11: Ratio of minority to majority 2D central densities for $E_F/E_b = 6.6$. Blue dots: Data; Red solid curve: 2D polaron model; Dashed black curve: Ideal Fermi gas prediction. The polaron model yields a smooth density-ratio variation across the polarisation spectrum at this magnetic field, in reasonable agreement with data obtained from Thomas-Fermi fits to the data.

and 2.66 of this thesis. The density ratios for three interaction strengths obtained this way are shown in Figures 6.11, 6.12, and 6.13.

The agreement with the polaron model is reasonably good at 832 G, where $E_F/E_b = 6.6$. However, as the interaction strength is increased to $E_F/E_b = 0.75$ by increasing the dimer binding energy at 775 G, the 2D central densities abruptly become balanced above a critical ratio N_2/N_1. Furthermore, the core persists for a wider range of polarisation values as the interaction strength increases.

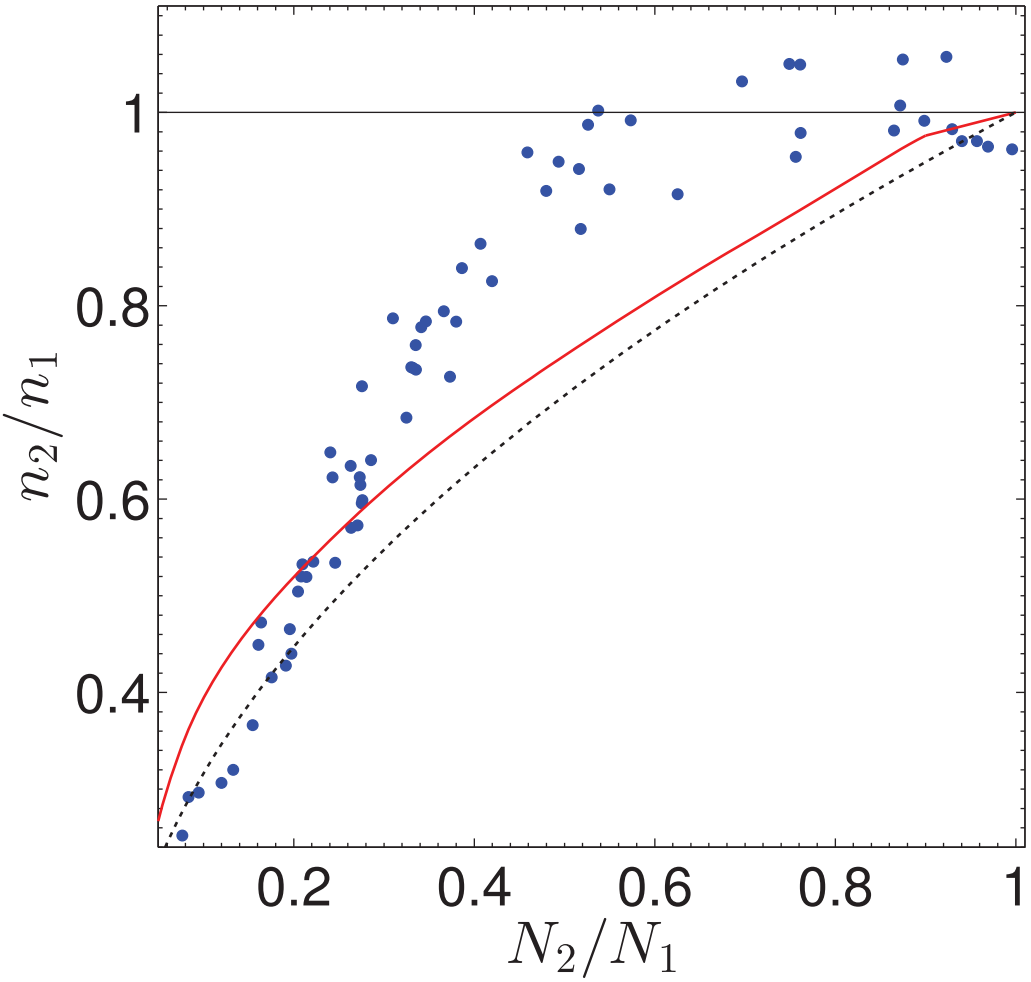

FIGURE 6.12: Ratio of minority to majority 2D central densities for $E_F/E_b = 2.1$ (middle panel). Blue dots: Data; Red solid curve: 2D polaron model; Dashed black curve: Ideal Fermi gas prediction. A spin-balanced core develops over a range of imbalance, in clear disagreement with the polaron model. As with the prior figure, data is extracted from Thomas-Fermi fits.

In a separate study, we found that modelling the two spin species by independent Gaussian profiles yielded a smooth 2D central-density-ratio curve, intermediate between the polaron fit and the phase-separated profile, as a function of polarisation.

We also employed an inverse Abel transformation of the column densities [67] to extract the peak 2D densities. To account for the elliptical geometry of the standing wave trap, we implement a scaling of the form $y \to \tilde{y} \equiv y\omega_y/\omega_x$. The inverse Abel transform is then

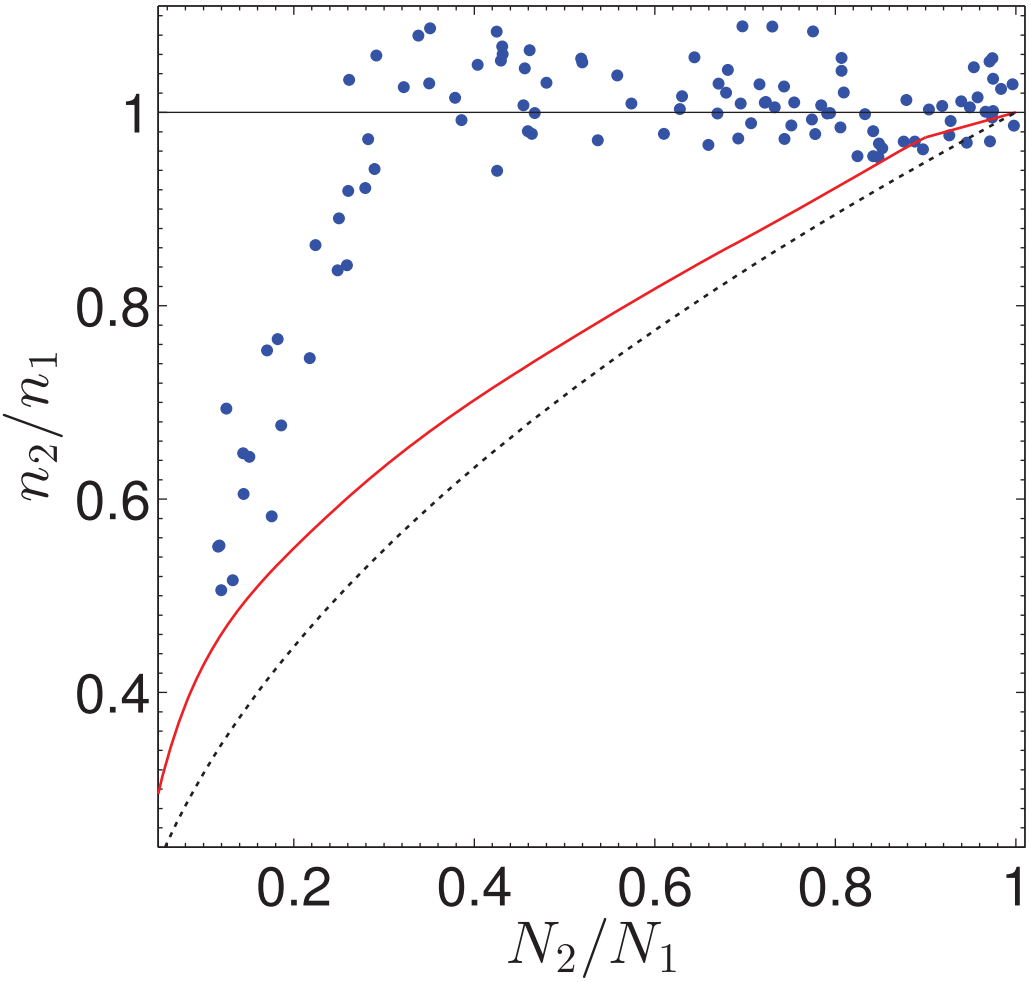

FIGURE 6.13: Ratio of minority to majority 2D central densities for the strongest interactions $E_F/E_b = 0.75$. Blue dots: Data obtained from Thomas-Fermi fits to column densities; Red solid curve: 2D polaron model; Dashed black curve: Ideal Fermi gas prediction. Stronger interactions balance the central densities over an even wider range of imbalance than in Figure 6.12. A steep drop in ratio of central 2D densities develops where N_2/N_1 is approximately 0.3.

$$n_2(\tilde{r}) = -\frac{\omega_y/\omega_x}{\pi}\int_\rho^\infty \frac{dn_1}{dx}\frac{dx}{\sqrt{x^2-\tilde{r}^2}} \tag{6.7}$$

with $\tilde{r} \equiv \sqrt{x^2+\tilde{y}^2}$. The 2D density at the center of the trap is obtained by fitting a parabola to within 70 percent of the apparent Thomas-Fermi radius. While this technique assumes only radial symmetry of the trap and is independent of the validity

of the local density approximation, it suffers from the setback that the data extracted is noisy. Shown in Figure 6.14 is the ratio of 2D densities obtained by transforming the column densities obtained at $q = E_F/E_b = 0.75$.

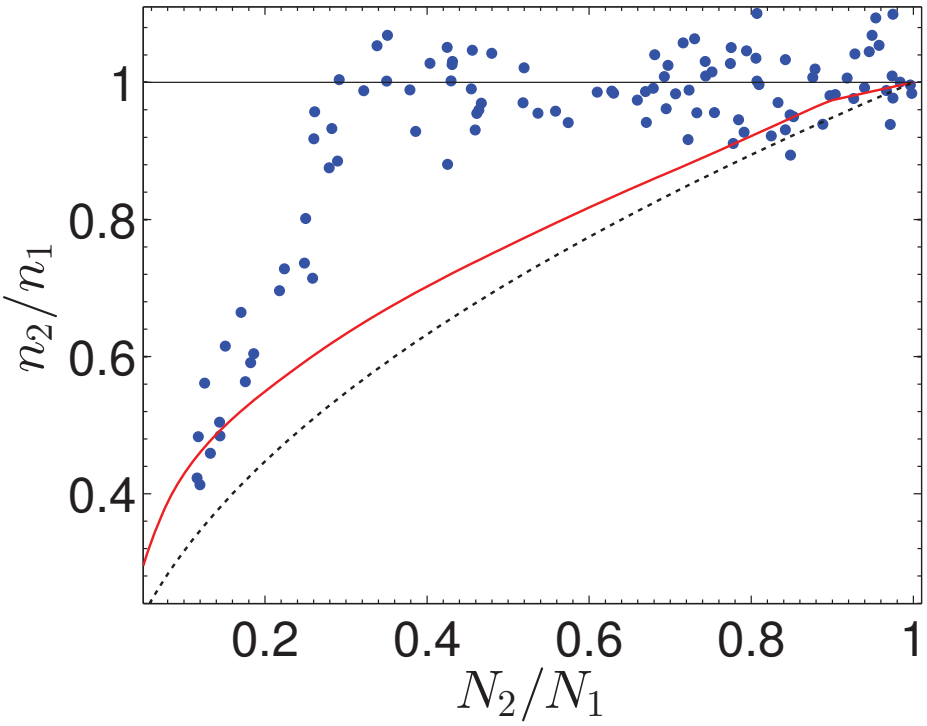

FIGURE 6.14: Ratio of minority to majority 2D central densities for the strongest interactions $E_F/E_b = 0.75$. Blue dots: Data obtained from inverse Abel transform; Red solid curve: 2D polaron model; Black dotted curve: Ideal Fermi gas prediction. The data extracted with this method still reveals a deviation from polaron theory predictions, but shows a wider spread about the spin-balanced density ratio of 1.

Qualitatively, the ratio of 2D central densities obtained by performing an inverse Abel transform of the column densities, reveals a deviation from polaron theory predictions as observed in Figure 6.13 with Thomas-Fermi fits. The roll-off to a linear dependence at low N_2/N_1 is smeared out compared to that observed in Figure 6.13. The spread of values about the density-balanced ratio of $n_2/n_1 = 1$ is larger for data extracted from inverse Abel transform fits than with Thomas-Fermi fits. Quantitatively, we note that both Thomas-Fermi fits and inverse Abel transform

methods yield similar results to within 5 percent.

7

Summary and Conclusions

In conclusion, this thesis describes the first studies on a spin-imbalanced strongly interacting quasi-2D Fermi gas [63]. This work serves as an experimental reference for a large amount of theoretical predictions [68, 53, 69, 40, 70, 71, 72, 52, 41, 26, 73] on imbalanced 2D and quasi-2D Fermi gases, most of which are based on mean-field descriptions. As pointed out in [18, 74, 75, 42], the unique quasi-2D regime is host to a variety of technologically relevant features such as enhanced superfluid temperatures in condensed matter systems. Moreover, our table-top realization serves as a fertile testbed for theories pertinent to geometrically and compositionally similar quantum matter ranging from the recently discovered iron-based superconductors [7] to layered quantum well materials [2].

Indeed, the many-body physics of a quasi-2D system [39, 63] is distinct from that of a true two-dimensional gas. To access the many-body, quasi-2D regime in a standing wave optical dipole trap, the atoms are subject to an external magnetic field where the two-body interaction is varied about a magnetically tunable Feshbach resonance. At unitarity, one obtains the unique interplay and coexistence of reduced dimensionality, many-body physics, and strong interactions, necessitating theoretical

treatment beyond the mean-field level. In contrast, the many-body regime of a true 2D gas [36] is a weakly interacting one, well described by mean-field 2D BCS theory [19]; many-body effects are noticeably absent in the strongly interacting regime of a true 2D gas.

To see how this so, we turn to the energy scales involved, namely the trap-induced two-body binding energy, E_b, the Fermi energy E_F, which is proportional to the square root of the number of particles and radial trap frequency, and energy level spacing in the axial direction, $h\nu_z$, which is the dominant energy scale. For a true (kinematically) 2D gas, the condition $E_F \ll h\nu_z$ restricts motion of constituent particles to the ground axial state. There, the condition for many-body effects, namely $E_b \simeq E_F$ is achieved only in the weakly interacting BCS regime, where $E_b \ll h\nu_z$. A quasi-2D gas is obtained when the Fermi energy is comparable to the axial trap energy spacing. In our trap, the two-body binding energy at unitarity is approximately a quarter that of the axial energy level spacing, and the Fermi energy is approximately six times that of the two-body binding energy, yielding $E_b < h\nu_z \simeq E_F$. Since energy scales inversely with length squared, this corresponds to a picture where the size of trap-induced dimers at unitarity is comparable to the interparticle spacing. At unitarity where the two-body scattering length diverges, particles of unlike spins interact strongly within the dimers, resulting in a strongly interacting many-body scenario.

The measured spatial profiles, cloud radii, and central densities for spin-balanced quasi-2D gases in this thesis were found to be inconsistent with predictions of a microscopic mean-field theory, namely true two-dimensional Bardeen-Cooper-Schrieffer (BCS) theory, for varying values of the two-body binding energy. Furthermore, our prior radiofrequency spectra [39] of spin-balanced mixtures at unitarity in quasi-2D geometries could not be fit to 2D dimer theory. Instead, the spectra were very well fit to theoretical spectra derived from a two-dimensional polaron picture, com-

posed of an impurity immersed in a majority Fermi sea, and its excitations with net zero momenta. Employing an analytic approximation to this model, we derived the two-dimensional density profiles across the spectrum of polarisations at various magnetic fields. We have further presented the polaron thermodynamics of both spin-imbalanced and spin-balanced gases, and applied its predictions in our analysis of column density profiles obtained with high resolution, rapid sequential absorption imaging.

The 2D polaron model captures much of the behavior of the spin-imbalanced normal fluid mixtures, and is particularly effective at predicting measured cloud radii. While this suggests that polarons play an important role, measurements of the column densities and ratio of the 2D central densities reveal a phase transition to a spin-balanced central core, observed above a critical value of minority-to- majority ratio, which is not predicted by the 2D polaron model of the free energy. More precise calculations of the pressures for the balanced and imbalanced components are needed to explain the observed phase separation and critical spin-imbalance. A step in this direction has been taken recently by reference [65]. Quantum Monte Carlo simulations reveal a smooth dependence on energy at intermediate coupling strengths, which the authors have interpreted as evidence for a smooth crossover from a microscopic fermionic polaron to bosonic molecular state with significant mixing between polaron and molecular components. Our measurements should serve as a test for predicted phase diagrams, which will help to reveal the structure of a quasi-2D Fermi gas.

Looking ahead, interesting avenues of research might involve the nature of the observed transitions in spin-imbalanced quasi-2D Fermi gases and their associated macroscopic phenomenologies, the existence and nature of the observed core and shell structure in the presence of spin-imbalance, as well as predictions arising from the polaron model employed in our studies. In the broader scheme of ultracold gases,

this thesis provides an impetus for continued research in emerging subfields ranging from the pursuit of the 2D to 3D crossover as the chemical potential is raised relative to the axial trap spacing, temperature-dependent effects such as the relation of preformed pairs to condensation in quasi-2D Fermi gases, fluctuation thermodynamics of quantum gases [73, 12], and the nature of the Berezinskii-Kosterlitz-Thouless transition in quasi-2D imbalanced gases.

Appendix A

Temperature Calibration of a quasi-2D Fermi Gas

A.1 Temperature Calibration of a quasi-2D Fermi Gas

PROGRAM DESCRIPTION: This Mathematica 9.0 program generates column density profiles for a quasi-2D Fermi gas with a known trap depth and axial trap spacing at arbitrary temperatures for data fitting. The axial population per state is determined in the appropriate section.

```
1.  Trap depth in E_F units
U=3.3/0.85
3.88235

2.  Trap level spacing in E_F units
S=0.43/0.85
0.505882

3.  Assume 3 axial states find \[Mu] as a function of T
j[\[Mu]_,T_]:=4*NIntegrate[\[Rho]*(T*Log[(1+Exp[(\[Mu]-
U*(1-Exp[-\[Rho]^2/U]))/T])/(1+Exp[(\[Mu]-U)/T])]),{\[Rho],0,2}]+
4*NIntegrate[\[Rho]*(T*Log[(1+Exp[((\[Mu]-S)-U*(1-Exp[-\[Rho]^2/U]))/T])
```

```
/(1+Exp[((\[Mu]-S)-U)/T])]),{\[Rho],0,2}]+4*NIntegrate[\[Rho]*
(T*Log[(1+Exp[((\[Mu]-2S)-U*(1-Exp[-\[Rho]^2/U]))/T])/
(1+Exp[((\[Mu]-2S)-U)/T])]),{\[Rho],0,2}];

j1[k_]:=x/.FindRoot[j[x,k]-1==0,{x,0.8}];

FindRoot[j[x,0.21]-1==0,{x,0.8}]
{x->0.75005}

4.  Population per axial state for T/T_F=0.21

4*NIntegrate[\[Rho]*(0.21*Log[(1+Exp[(0.75005-
U*(1-Exp[-\[Rho]^2/U]))/0.21])/(1+Exp[(0.75005-
U)/0.21])]),{\[Rho],0,2}]

0.782164

4*NIntegrate[\[Rho]*(0.21*Log[(1+Exp[((0.75005-S)
-U*(1-Exp[-\[Rho]^2/U]))/0.21])/(1+Exp[((0.75005-S)
-U)/0.21])]),{\[Rho],0,2}]

0.192592

4*NIntegrate[\[Rho]*(0.21*Log[(1+Exp[((0.75005-2S)
-U*(1-Exp[-\[Rho]^2/U]))/0.21])/(1+Exp[((0.75005-2S)
-U)/0.21])]),{\[Rho],0,2}]

0.025245

5.  Plot of \[Mu] as a function of T

ListPlot[Table[{i,j1[i]},{i,0.05,0.6,(0.6-0.05)/100}],
AxesLabel->{T/Subscript[T, F],\[Mu]/Subscript[E, F]}]
```

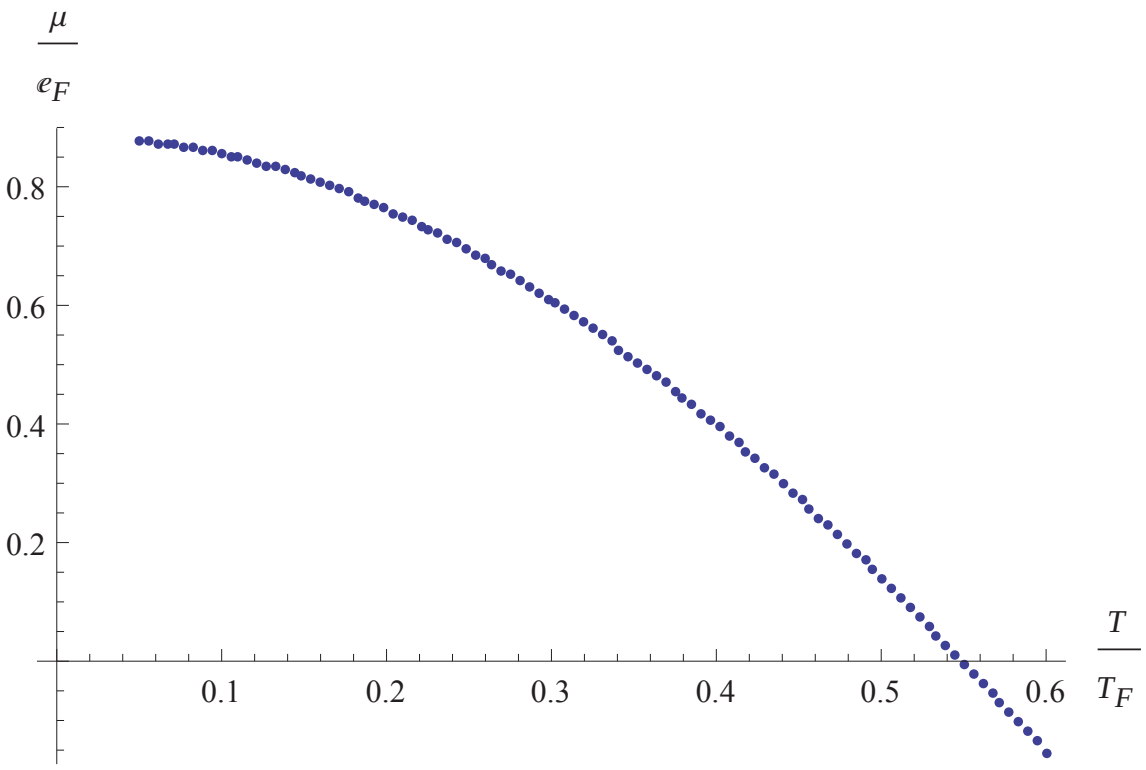

6. Assume 3 axial states and T of 0.21, plot 1D column density

```
n1Dallthree[x_,T_]:=NIntegrate[T*Log[(1+Exp[(j1[T]-
U*(1-Exp[(-x^2-y^2)/U]))/T])/(1+Exp[(j1[T]-U)/T])],{y,0,2}]+
NIntegrate[T*Log[(1+Exp[((j1[T]-S)-U*(1-Exp[(-x^2-y^2)/U]))/T])
/(1+Exp[((j1[T]-S)-U)/T])],{y,0,2}]+NIntegrate[T*Log[(1+Exp[((j1[T]-2S)
-U*(1-Exp[(-x^2-y^2)/U]))/T])/(1+Exp[((j1[T]-2S)-U)/T])],{y,0,2}];

Profilen1Dallthree=ListPlot[Table[{i,n1Dallthree[i,0.21]},{i,0,1.5,
(1.5-0)/500}], AxesLabel->{x/Subscript[R, TF1],Subscript[n, c]}]
```

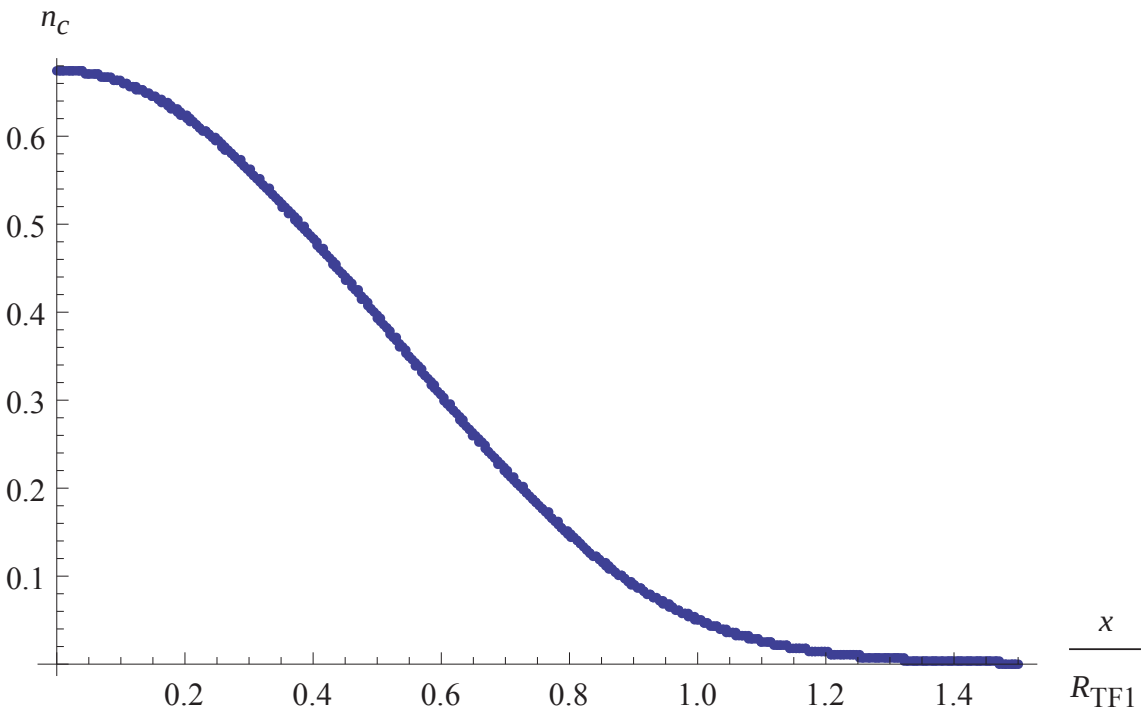

7. Assume 3 axial states and T of 0.18, plot 1D column density

```
Profilen1Dallthree1=ListPlot[Table[{i,n1Dallthree[i,0.18]},{i,0,1.5,
(1.5-0)/500}], AxesLabel->{x/Subscript[R, TF1],Subscript[n, c]}]
```

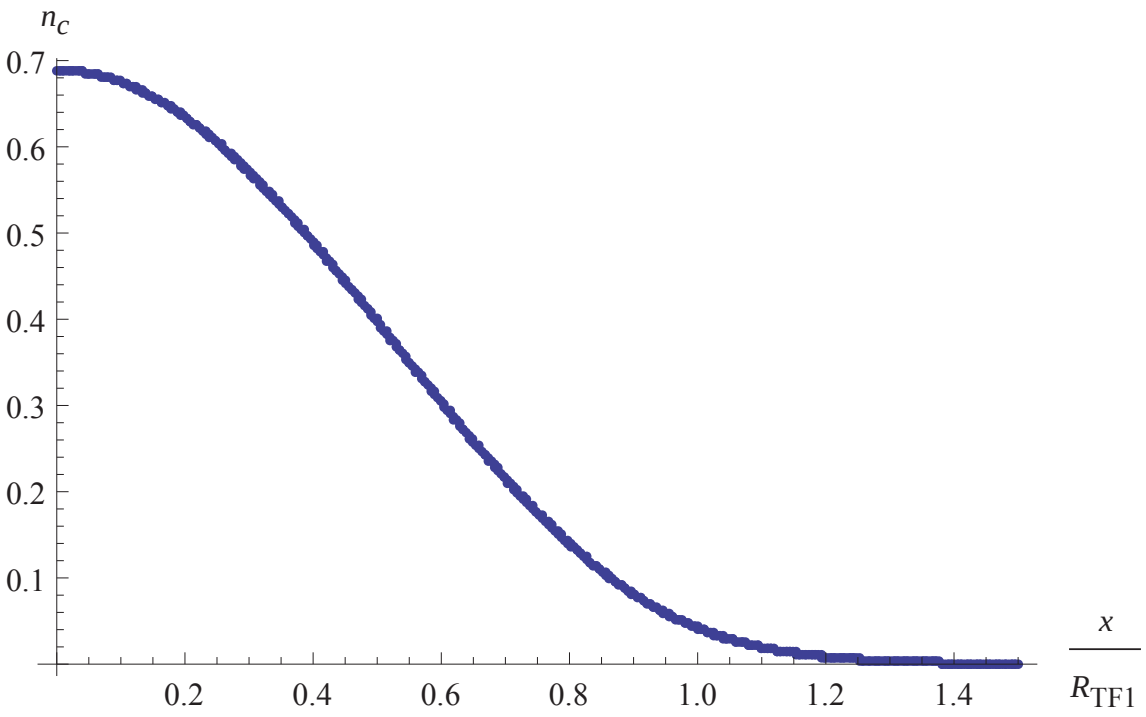

8. Assume 3 axial states and T of 0.14, plot 1D column density

```
Profilen1Dallthree2=ListPlot[Table[{i,n1Dallthree[i,0.14]},{i,0,1.5,
(1.5-0)/500}], AxesLabel->{x/Subscript[R, TF1],Subscript[n, c]}]
```

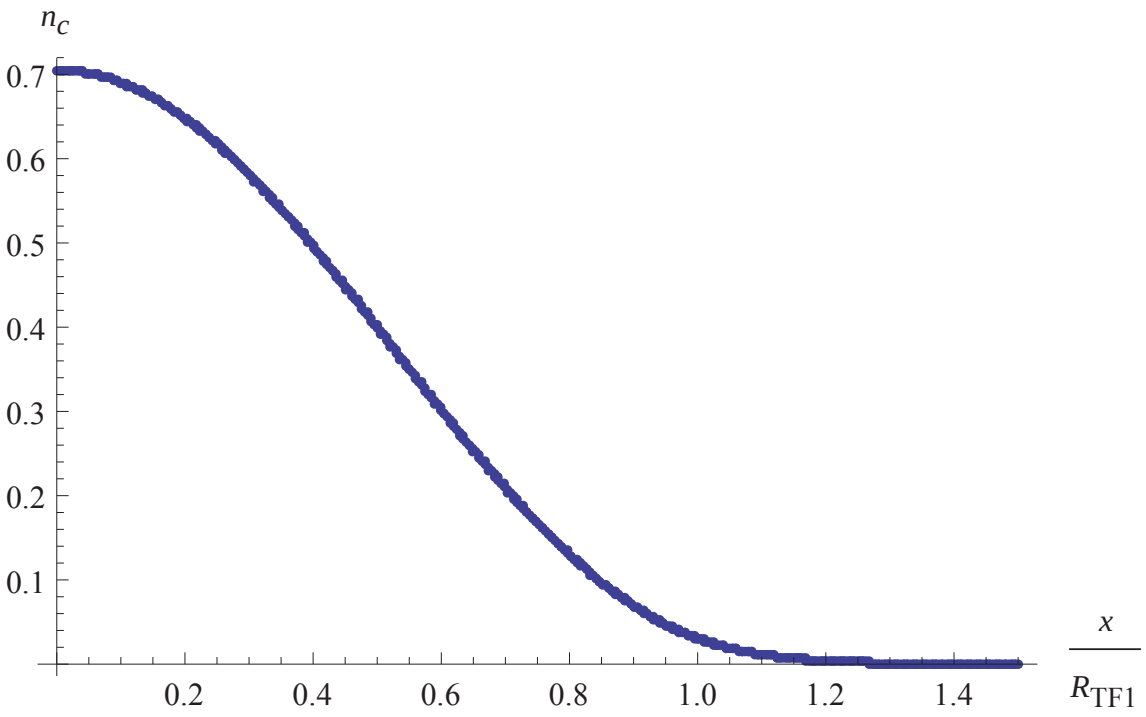

9. Exporting files to Excel

```
Export["C:\\Users\\Willie Ong\\Desktop\\ColumnDensityTp21.xls",
Table[{i,n1Dallthree[i,0.21]},{i,0,2,(2-0)/100}]]
C:\Users\Willie Ong\Desktop\ColumnDensityTp21.xls

Export["C:\\Users\\Willie Ong\\Desktop\\ColumnDensityTp18.xls",
Table[{i,n1Dallthree[i,0.18]},{i,0,1.5,(1.5-0)/500}]]
C:\Users\Willie Ong\Desktop\ColumnDensityTp18.xls

Export["C:\\Users\\Willie Ong\\Desktop\\ColumnDensityTp14.xls",
Table[{i,n1Dallthree[i,0.14]},{i,0,1.5,(1.5-0)/500}]]
C:\Users\Willie Ong\Desktop\ColumnDensityTp14.xls

Export["C:\\Users\\Willie Ong\\Desktop\\ColumnDensityTp21new.xls",
Table[{i,n1Dallthree[i,0.21]},{i,0,2,(2-0)/500}]]
C:\Users\Willie Ong\Desktop\ColumnDensityTp21new.xls
```

Appendix B

FORT Loading and PMT Probing Cycle

B.1 FORT Loading and PMT Probing Cycle

PROGRAM DESCRIPTION: This EXCEL file lists the analog and digital channels activated in loading an optical dipole trap from a MOT and subsequent probing with a photomultiplier tube. It is employed as a diagnostic cycle prior to our experiments.

	step#	1	2	3	4	5	6	7	8	9	10	11	12	13	14
	duration	64950	5000	50	500	2	300	2700	1640	230	130	100	4900	5001	10
AO1	MOT Freq	4.19	4.19	4.19	7.3	7.3	0	4.19	4.19	0	0	8.19	0	0	4.19
AO2	MOT Amp	2.67	2.67	2.67	0.23	0.25	0	0.35	2.67	0	0	2.67	0	0	2.67
AO3	Rep Freq	10.82	10.82	10.82	10.76	0	0	10.82	10.82	0	0	10.9	0	0	10.82
AO4	Lock offset	7.43	7.43	7.43	7.43	7.43	7.43	7.43	7.43	7.43	7.43	7.43	7.43	7.43	7.43
AO5	MOT Mag	2.9	2.9	2.9	2.9	2.9	0	0	0	0	0	0	0	0	2.9
AO6	High Mag	0	0	0	0	0	0	0	0	0	0	0	0	0	0
AO7	chopper	0	0	0	0	0	0	0	0	0	0	0	0	0	0
AO8	CamAo Freq	0	0	0	0	0	0	0	0	0	0	0	0	0	0
D1	Rep Amp	On	On	On	On	Off	Off	On	On	Off	Off	On	Off	Off	On
D2	Mast Shut	On	On	On	On	On	Off	Off	Off	Off	On	On	On	On	On
D3	Rep Shut	On	On	On	On	On	Off	Off	Off	Off	On	On	On	On	On
D4	Slow Shut	On	On	Off	Off	Off	Off	Off	Off	Off	Off	Off	Off	Off	On
D5	Cam AO Freq	Off	Off	Off	Off	Off	Off	Off	Off	Off	Off	Off	Off	Off	Off
D6	Cam AO Amp	Off	Off	Off	Off	Off	Off	Off	Off	Off	Off	Off	Off	Off	Off
D7	Lowering Trig	Off	Off	Off	Off	Off	Off	Off	Off	Off	Off	Off	Off	Off	Off
D8	CO2 state	On	On	On	On	On	On	On	On	On	On	On	On	On	On
D9	probe Shut	Off	Off	Off	Off	Off	Off	Off	Off	Off	Off	Off	Off	Off	Off
D10	Cam1 Trigger	Off	Off	Off	Off	Off	Off	Off	Off	Off	Off	Off	Off	Off	Off
D11	dye unlock	Off	Off	Off	Off	Off	Off	Off	Off	Off	Off	Off	Off	Off	Off
D12	dye f-shift	Off	Off	Off	Off	Off	Off	Off	Off	Off	Off	Off	Off	Off	Off
D13	PMT gate	Off	Off	Off	Off	Off	Off	Off	On	On	On	On	On	Off	Off
D14	RF on	Off	Off	Off	Off	Off	Off	Off	Off	Off	Off	Off	Off	Off	Off
D15	Cam2 Trigger	Off	Off	Off	Off	Off	Off	Off	Off	Off	Off	Off	Off	Off	Off
D16	Flipper Mirror	Off	Off	Off	Off	Off	Off	Off	Off	Off	Off	Off	Off	Off	Off
D17	Par Trigger	Off	Off	Off	Off	Off	Off	Off	Off	Off	Off	Off	Off	Off	Off
D18	n/c	Off	Off	Off	Off	Off	Off	Off	Off	Off	Off	Off	Off	Off	Off
D19	Current Sensor	Off	Off	Off	Off	Off	Off	Off	Off	Off	Off	Off	Off	Off	Off
D20	Spin Balence	Off	Off	Off	Off	Off	Off	Off	Off	Off	Off	Off	Off	Off	Off
D21	DyeFrShiftGel	Off	Off	Off	Off	Off	Off	Off	Off	Off	Off	Off	Off	Off	Off
D22	USB6289 trig	On	Off	Off	Off	Off	Off	Off	Off	Off	Off	Off	Off	Off	Off
D23	chop_move	Off	Off	Off	Off	Off	Off	Off	Off	Off	Off	Off	Off	Off	Off
D24	chop_polar	Off	Off	Off	Off	Off	Off	Off	Off	Off	Off	Off	Off	Off	Off

Appendix C

Quasi-2D Fermi Gas Density Profile Calculator

C.1 Quasi-2D Fermi Gas Density Profile Calculator

PROGRAM DESCRIPTION: This Mathematica 9.0 program generates the density profile of a spin-imbalanced quasi-2D Fermi gas with a polarisation N_2/N_1 of 0.5 at $E_F/Eb = 6.6$. In this appendix, $x = n_{\perp 2}/n_{\perp 1}$, and $u = n_{1\perp}(0)/n_0$.

```
1. Polaron Energy Definition

y[q_]:=-2/Log[1+2*q]
yprime[q_]:=(q*(y[q])^2)/(1+2q)

2. Compute density at trap center

(* For P = 0.5, q = 6.6,take starting xperp to be 0, subsequently
plot u against xperp, with xperp between 0 and 1. xperp=
n2perp/n1perp, u=n1perp(0)/n_{0} *)

FindRoot[(1/2)*(1+0.5)-(1/2)*u^2*(1+0^2+2*0*(y[6.6*u]+
yprime[6.6*u]))==0,{u,1}]
```

```
{u->1.22474}

ListPlot[{{0,1.22474},{0.05,1.25283},{0.1,1.27918},{0.15,1.30331},
{0.2,1.32478},{0.25,1.34314},{0.3,1.35802},{0.35,1.36908},
{0.4,1.37613},{0.45,1.37902},{0.5,1.37775},{0.55,1.37243},
{0.6,1.36325},{0.65,1.35048},{0.7,1.33448},{0.75,1.31562},
{0.8,1.29433},{0.85,1.27102},{0.9,1.24609},{0.95,1.21991},
{1,1.19284}}]
```

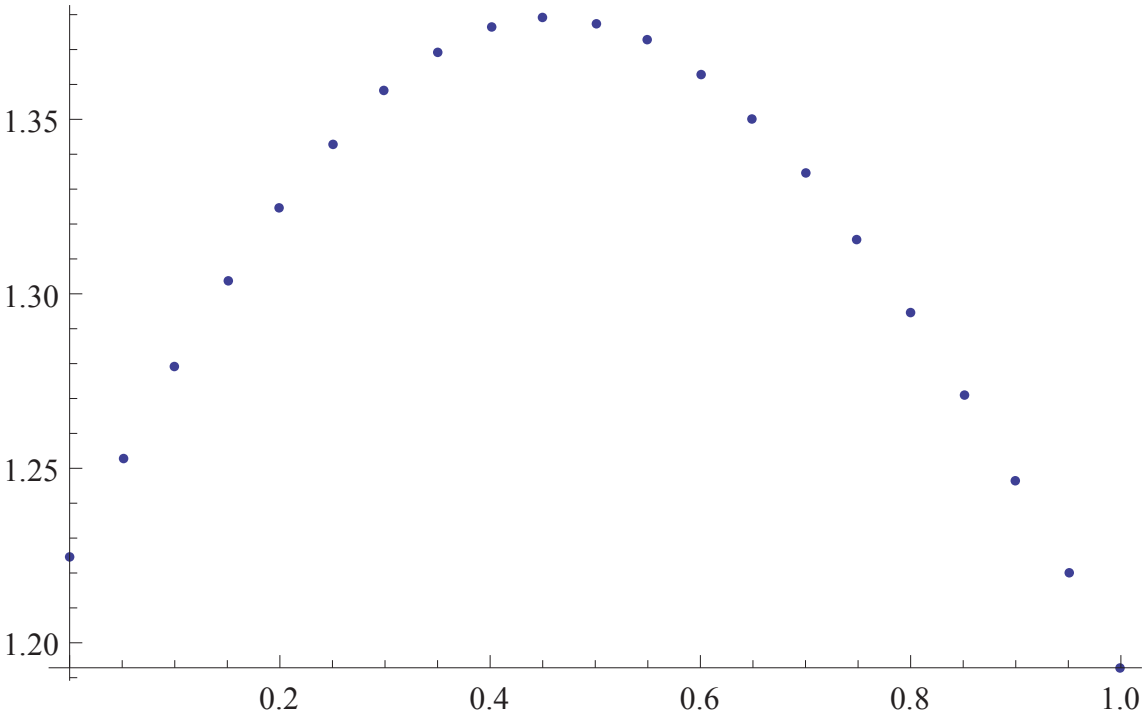


```
f=Interpolation[{{0,1.22474},{0.05,1.25283},{0.1,1.27918},
{0.15,1.30331},{0.2,1.32478},{0.25,1.34314},{0.3,1.35802},
{0.35,1.36908},{0.4,1.37613},{0.45,1.37902},{0.5,1.37775},
{0.55,1.37243},{0.6,1.36325},{0.65,1.35048},{0.7,1.33448},
{0.75,1.31562},{0.8,1.29433},{0.85,1.27102},{0.9,1.24609},
{0.95,1.21991},{1,1.19284}}]

InterpolatingFunction[{{0.,1.}},<>]
```

```
Plot[%[x],{x,0,1}]
```

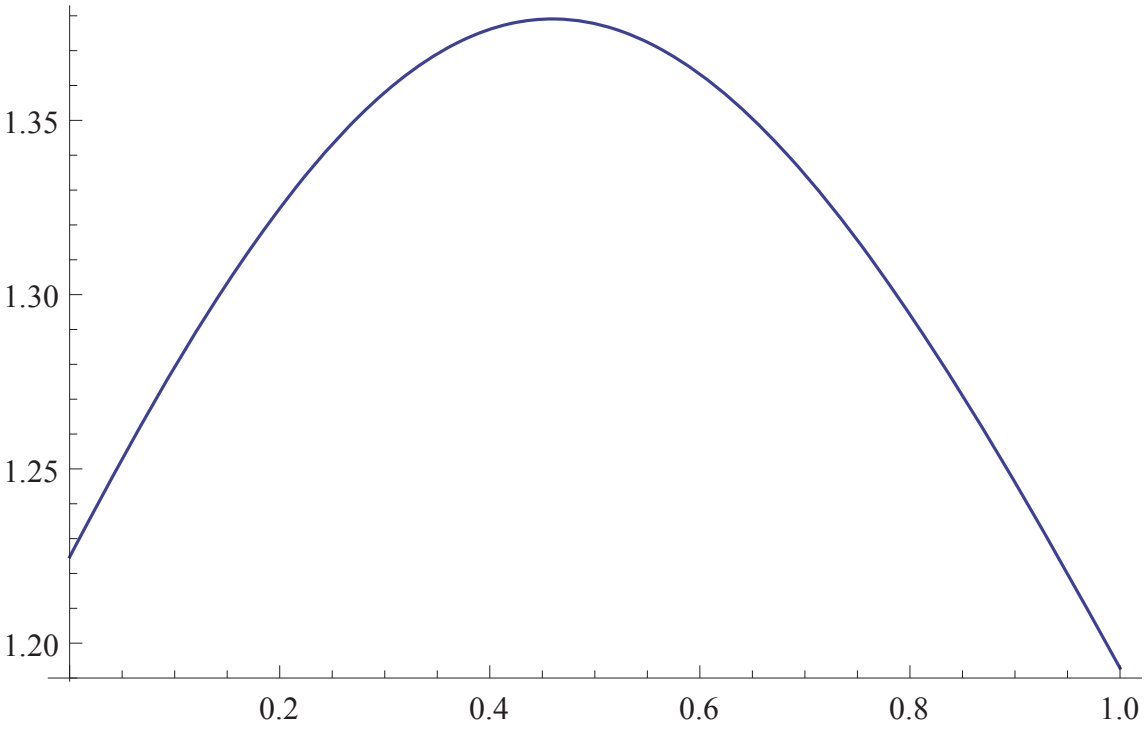


```
(* Just as a check, I try to find the values of interpolating
function at x of 0.53 and 0.82 *)

f[0.53]
1.37503

f[0.82]
1.28523

(* To begin, I compute minority and majority central chemical
potentials with x (denoted by s and t) values of 0.2,0.5 & 0.8 *)

3. Minority (2) Chemical Potential at trap center

mu2[s_]=f[s](s+y[6.6*f[s]]);
```

```
mu2[0.5]
-0.243866

4. Majority (1) Chemical Potential at trap center

mu1[t_]=f[t](1+t(y[6.6*f[t]]+yprime[6.6*f[t]]));

mu1[0.5]
1.06102

5. Majority Radius (R1) Calculation

(* Similarly, compute R1 for values of x of 0.2, 0.5, and 0.8 *)

R1[t_]=Sqrt[mu1[t]];

R1[0.5]
1.03006

6. Minority Radius (R2) Calculation

solspfive=NSolve[Rpf^2==mu2[0.5]-(mu1[0.5]-Rpf^2)*y[6.6*(mu1[0.5]
-Rpf^2)]&&Rpf>0,Rpf,Reals]

{{Rpf->0.599171}}

Rpfive=Rpf/.solspfive[[1]]
0.599171

7. Central Density of majority at R2

n_Rtwop5=mu1[0.5]-Rpfive^2
0.702012

8. Central Density of majority at origin
```

```
Dmajpfive=NSolve[mu1[0.5]-mu2[0.5]*(y[6.6*n]+yprime[6.6*n])==
n*(1+y[6.6*n]*(y[6.6*n]+yprime[6.6*n]))&&n>0,n,Reals]
{{n->1.37775}}

Dmaj_pfive=n/.Dmajpfive[[1]]
1.37775
```

9. Density Profile of Majority Species between R2 and R1

```
data1point5=ListPlot[Table[{i,mu1[0.5]-i^2},{i,Rpfive,R1[0.5],
(R1[0.5]-Rpfive)/50}]]
```

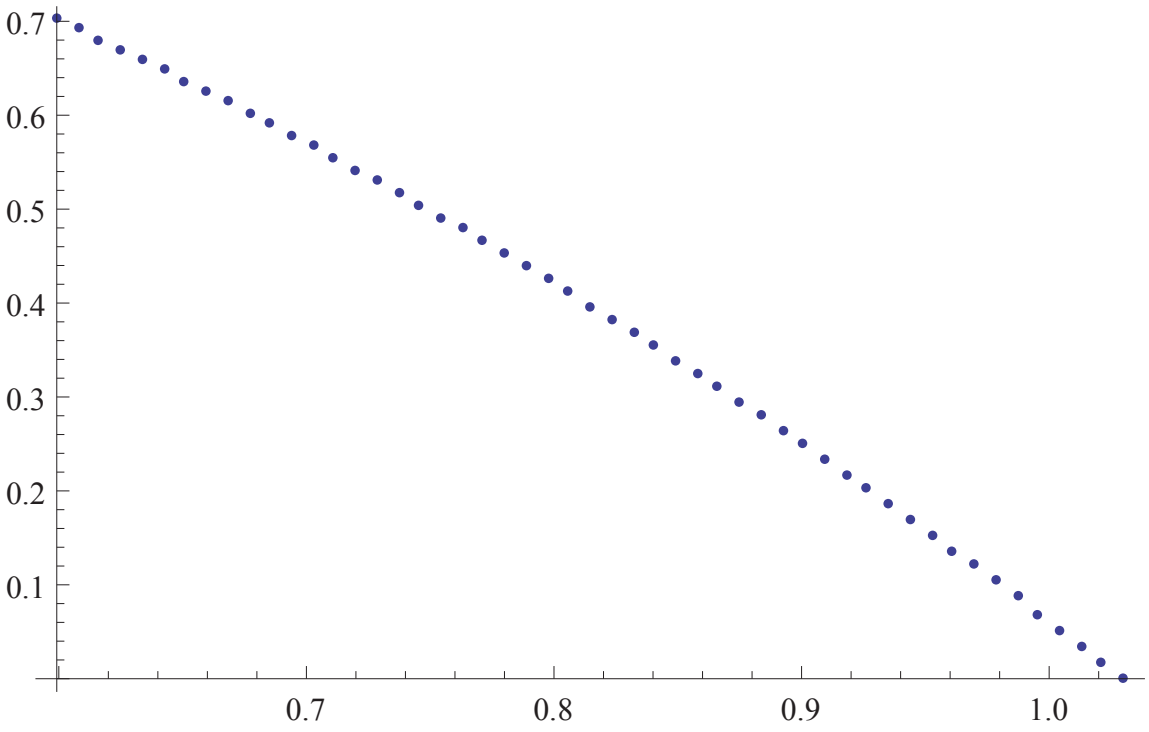


```
Export["C:\\Users\\Willie Ong\\Desktop\\DensityProfileMinp5at6psix.xls",
Table[{i,mu1[0.738106]-i^2},{i,Rpsolsoln,R1[0.738106],
(R1[0.738106]-Rpsolsoln)/50}]]

C:\Users\Willie Ong\Desktop\DensityProfileMinp5at6psix.xls
```

10. Density Profile of Majority Species between 0 and R2 for x of 0.5

```
NSolve[(mu1[0.5]-\[Rho])-(mu2[0.5]-\[Rho])*(y[6.6*n]-yprime[6.6*n])-
n*(1-y[6.6*n]*(y[6.6*n]-yprime[6.6*n]))==0,{\[Rho]}]
```

```
{{\[Rho]->(-1.06102-0.243866 ((26.4 n)/((1. +13.2 n) Log[1. +13.2 n]^2)
-2./Log[1. +13.2 n])+1. n (1. +(2. ((26.4 n)/((1. +13.2 n)
Log[1. +13.2 n]^2)-2./Log[1. +13.2 n]))/Log[1. +13.2 n]))/
(-1.+(26.4 n)/((1. +13.2 n) Log[1. +13.2 n]^2)-2./Log[1. +13.2 n])}}
```

```
\[Rho]twopointfive[n_]:=\[Sqrt](-1.061018-0.24386((26.4 n)/
((1. +13.2n) Log[1. +13.2n]^2)-2./Log[1. +13.2n])+1.n (1. +
(2.((26.4n)/((1.+13.2n) Log[1. +13.2n]^2)-2./Log[1.+13.2n]))/
Log[1.+13.2n]))/(-1.+(26.4n)/((1.+13.2n) Log[1.+13.2n]^2)-2./
Log[1.+13.2n])
```

```
Table[{\[Rho]twopointfive[j],j},{j,0.702012,1.37774,(1.37774-0.702012)
/50}]
```

```
{{0.599171,0.702012},{0.593782,0.715527},{0.588305,0.729041},
{0.582739,0.742556},{0.577083,0.75607},{0.571336,0.769585},
{0.565495,0.783099},{0.559559,0.796614},{0.553525,0.810128},
{0.547391,0.823643},{0.541156,0.837158},{0.534815,0.850672},
{0.528366,0.864187},{0.521807,0.877701},{0.515133,0.891216},
{0.508341,0.90473},{0.501426,0.918245},{0.494385,0.93176},
{0.487213,0.945274},{0.479904,0.958789},{0.472453,0.972303},
{0.464854,0.985818},{0.457099,0.999332},{0.449182,1.01285},
{0.441095,1.02636},{0.432828,1.03988},{0.424372,1.05339},
{0.415715,1.06691},{0.406846,1.08042},{0.397751,1.09393},
{0.388414,1.10745},{0.378819,1.12096},{0.368946,1.13448},
{0.358772,1.14799},{0.348271,1.16151},{0.337414,1.17502},
```

```
{0.326166,1.18854},{0.314485,1.20205},{0.302322,1.21557},
{0.289616,1.22908},{0.276293,1.24259},{0.262261,1.25611},
{0.247398,1.26962},{0.231546,1.28314},{0.214486,1.29665},
{0.195903,1.31017},{0.175315,1.32368},{0.15191,1.3372},
{0.124105,1.35071},{0.0878155,1.36423},{0.00238905,1.37774}}

data2pointfive=ListPlot[Table[{\[Rho]twopointfive[j],j},{j,0.7020
,1.37774,(1.37774-0.702012)/50}]]
```

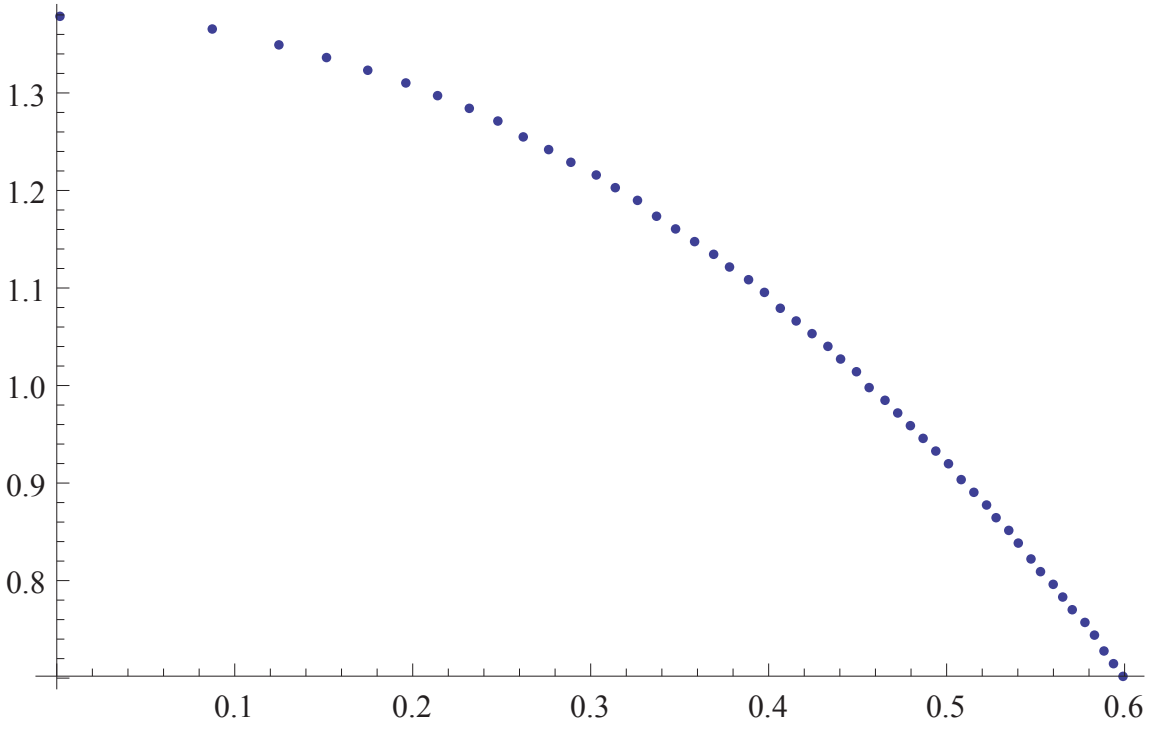


```
Show[data2pointfive, data1point5, PlotRange -> All]
```

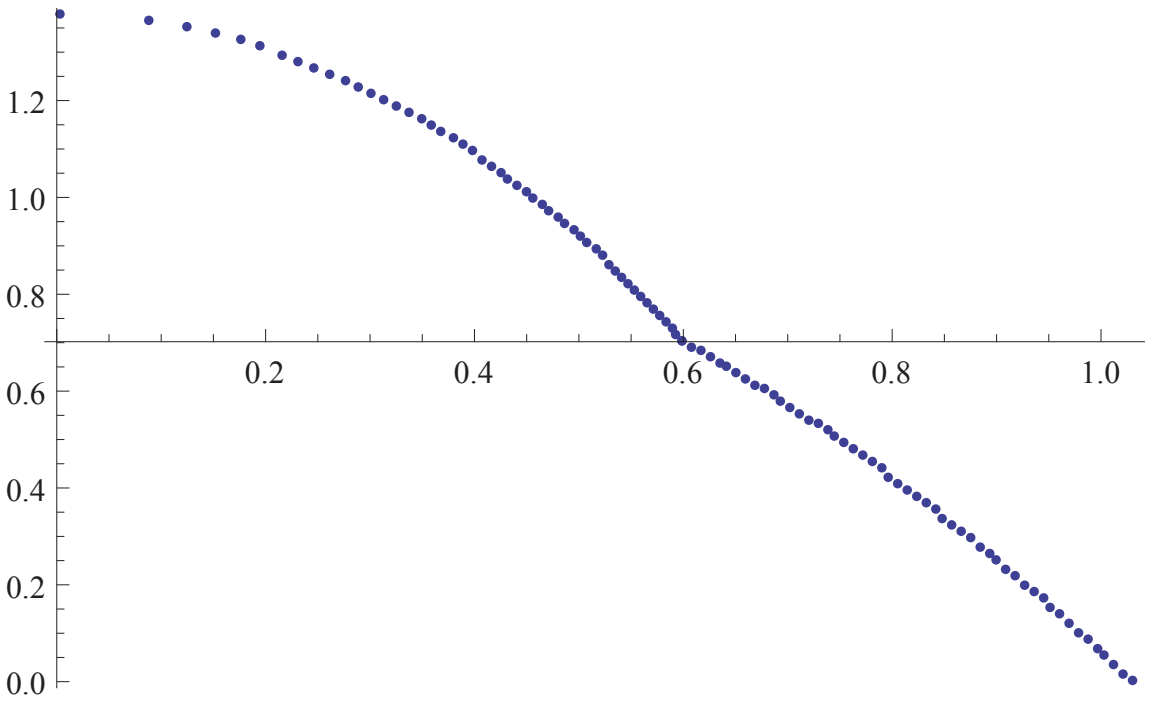


```
pointspointfive={{0.59917,0.70201},{0.59378,0.71552},{0.58830,0.72904},
{0.58274,0.74256},{0.57708,0.75607},{0.57134,0.76958},{0.56549,0.78309},
{0.55955,0.79661},{0.55352,0.81012},{0.54739,0.82364},{0.54115,0.83715},
{0.53481,0.85067},{0.52836,0.86418},{0.52180,0.87770},{0.51513,0.89121},
{0.50834,0.90473},{0.50142,0.91824},{0.49438,0.93175},{0.48721,0.94527},
{0.47990,0.95874},{0.47245,0.97230},{0.46485,0.98581},{0.45709,0.99933},
{0.44918,1.01284},{0.44109,1.02636},{0.43282,1.03987},{0.42437,1.05339},
{0.41571,1.06690},{0.40684,1.08041},{0.39775,1.09393},{0.38841,1.10744},
{0.37881,1.12096},{0.36894,1.13447},{0.35877,1.14799},{0.34827,1.16150},
{0.33741,1.17502},{0.32616,1.18853},{0.31448,1.20205},{0.30232,1.21556},
{0.28961,1.22907},{0.27629,1.24259},{0.26226,1.25610},{0.24739,1.26962},
{0.23154,1.28313},{0.21448,1.29665},{0.19590,1.31016},{0.17531,1.32368},
{0.15191,1.33719},{0.12410,1.35071},{0.08781,1.36422},{0.00238,1.37774}};

ifunpointfive=Interpolation[pointspointfive]

InterpolatingFunction[{{0.00238905,0.599171}},<>]
```

```
Plot[ifunpointfive[k],{k,0,0.599171},Epilog->Map[Point,pointspointfive],
PlotRange->All]
```

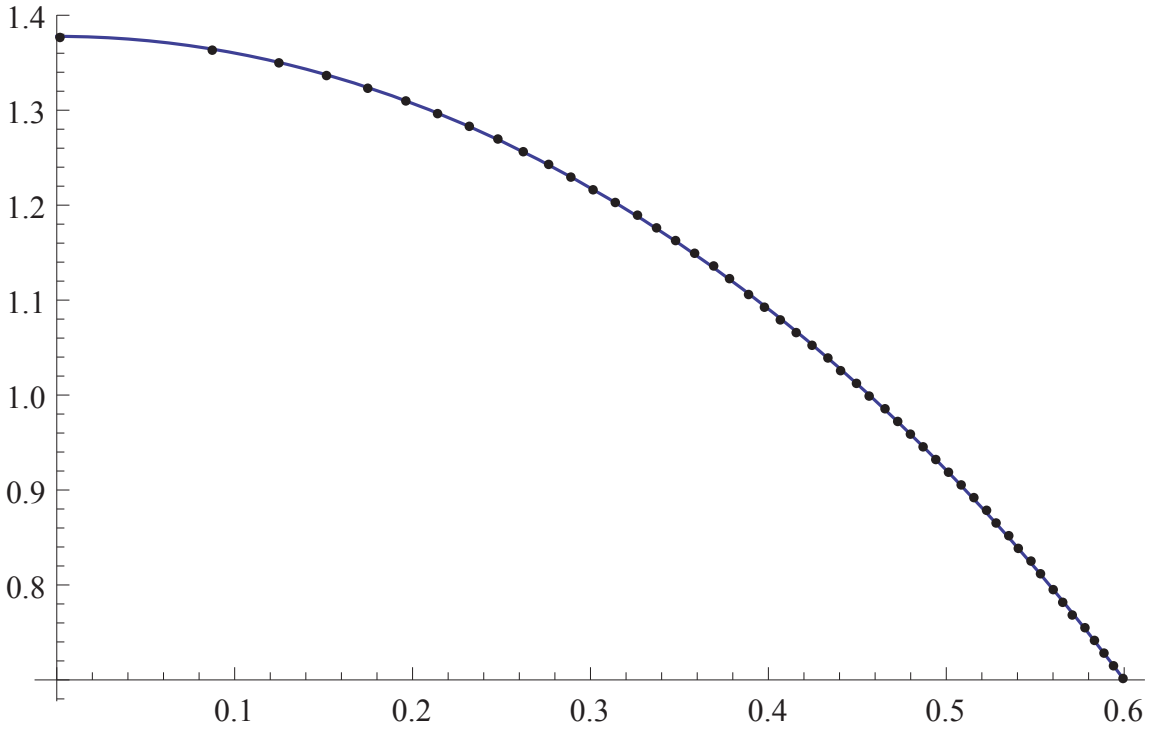


```
Integration of density profile for x=0.5

4*(NIntegrate[x*ifunpointfive[x],{x,0,0.599171}]+NIntegrate[y*(mu1[0.5]
-y^2),

{y,0.599171,1.03006}])

1.24659

(* The appropriate value of x would yield
an integral value of 1. We iterate the steps
above for values of x ranging from 0 to 1 in
steps of 0.1 and interpolate to locate the
```

```
right value of x. *)

ListPlot[{{0.01, 1.4999}, {0.1, 1.4913}, {0.2, 1.46249}, {0.3,
1.42704}, {0.4, 1.33783}, {0.5, 1.24659}, {0.6, 1.14436}, {0.7,
1.03919}, {0.8, 0.938547}, {0.9, 0.848052}, {1, 0.770924}}]
```

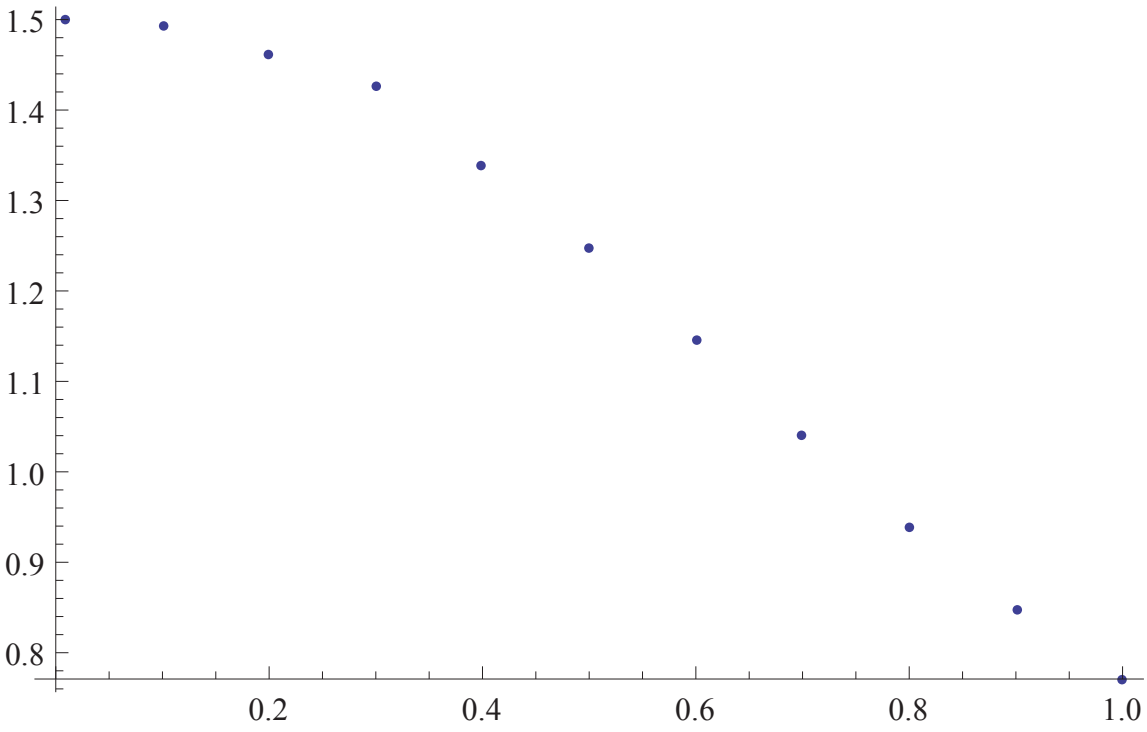


```
f = Interpolation[{{0.01, 1.4999}, {0.1, 1.4913}, {0.2,
1.46249}, {0.3, 1.42704}, {0.4, 1.33783}, {0.5, 1.24659},
{0.6, 1.14436}, {0.7, 1.03919}, {0.8, 0.938547}, {0.9,
0.848052}, {1, 0.770924}}]

InterpolatingFunction[{{0.01,1.}},<>]


FindRoot[f[x] == 1, {x, 0.7}]

{x -> 0.738106}
```

```
(* I now proceed to calculate the minority and majority chemical
potentials at the trap center, minority and majority radii, and
the 2D densities for x = 0.738106 at q of 6.6*)

11. Minority (2) Chemical Potential at trap center

mu2[s_]=f[s](s+y[6.6*f[s]]);

mu2[0.738106]

12. Majority (1) Chemical Potential at trap center

mu1[t_]=f[t](1+t(y[6.6*f[t]]+yprime[6.6*f[t]]));

mu1[0.738106]
0.868542

13. Majority Radius (R1) Calculation

R1[t_]=Sqrt[mu1[t]];

R1[0.738106]
0.931956

14. Minority Radius (R2) Calculation

solsoln=NSolve[Rpf^2==mu2[0.738106]-(mu1[0.738106]-Rpf^2)*
y[6.6*(mu1[0.738106]-Rpf^2)]&&Rpf>0,Rpf,Reals]

{{Rpf->0.700438}}

Rp=Rpf/.solsoln[[1]]
0.700438

15. Central Density of majority at R2

n_Rtwop738106 = mu1[0.738106] - Rpsolsoln^2
```

```
0.377928

16. Central Density of majority at origin

Dmajpsolsoln =
NSolve[mu1[0.738106] - mu2[0.738106]*(y[6.6*n] + yprime[6.6*n])
==n*(1 + y[6.6*n]*(y[6.6*n] + yprime[6.6*n])) && n > 0, n, Reals]

{{n -> 1.32034}}

17. Density Profile of Majority Species between R2 and R1

data1pointsolsoln = ListPlot[Table[{i, mu1[0.738106] - i^2},
{i, Rpsolsoln, R1[0.738106], (R1[0.738106] - Rpsolsoln)/50}]]
```

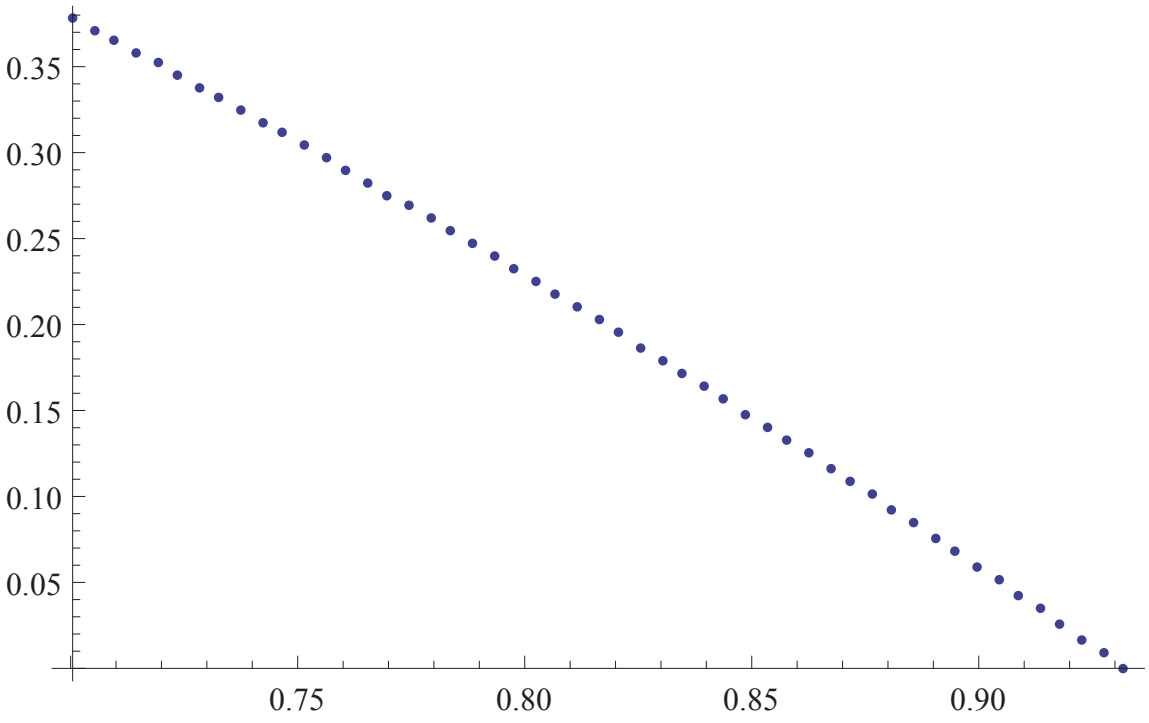

```
Export["C:\\Users\\Willie Ong\\Desktop\\DensityProfileMinp5at6psix.xls",
Table[{i,mu1[0.738106]-i^2},{i,Rpsolsoln,R1[0.738106],
(R1[0.738106]-Rpsolsoln)/50}]]
```

```
C:\Users\Willie Ong\Desktop\DensityProfileMinp5at6psix.xls
```

18.Density Profile of Minority Species between 0 and R2 for x of 0.738106

```
NSolve[(mu1[0.738106] - \[Rho]) - (mu2[0.738106] - \[Rho])*(y[6.6*n] +
yprime[6.6*n]) - n*(1 + y[6.6*n]*(y[6.6*n] + yprime[6.6*n])) == 0,
{\[Rho]}];
```

```
\[Rho]twopointsolsoln[n_] := \[Sqrt]((-0.868541 + 0.068315 ((26.4n)/
((1.+ 13.2n) Log[1.+ 13.2n]^2) - 2./Log[1.+ 13.2n]) + 1.n (1.+ (
2.((26.4n)/((1.+ 13.2n) Log[1.+ 13.2n]^2) - 2./Log[1.+ 13.2n]))/
Log[1.+ 13.2n]))/(-1.+ (26.4n)/((1.+ 13.2n) Log[1.+ 13.2n]^2) - 2./
Log[1.+ 13.2n]))
```

```
Table[{\[Rho]twopointsolsoln[j], j}, {j, 0.377928, 1.32034,
(1.32034 - 0.377928)/50}]
```

```
{{0.700438, 0.377928}, {0.694934, 0.396776}, {0.689259, 0.415624},
{0.683418, 0.434473}, {0.677416, 0.453321}, {0.671254, 0.472169},
{0.664935, 0.491017}, {0.658461, 0.509866}, {0.651832, 0.528714},
{0.645049, 0.547562}, {0.638111, 0.56641}, {0.631017, 0.585259},
{0.623767, 0.604107}, {0.616359, 0.622955}, {0.608789, 0.641803},
{0.601057, 0.660652}, {0.593157, 0.6795}, {0.585086, 0.698348},
{0.576841, 0.717196}, {0.568415, 0.736045}, {0.559804, 0.754893},
{0.551, 0.773741}, {0.541997, 0.792589}, {0.532786, 0.811438},
{0.523359, 0.830286}, {0.513707, 0.849134}, {0.503816, 0.867982},
{0.493676, 0.88683}, {0.483273, 0.905679}, {0.47259, 0.924527},
```

```
{0.461609, 0.943375}, {0.450311, 0.962223}, {0.438673, 0.981072},
{0.426669, 0.99992}, {0.414267, 1.01877}, {0.401432, 1.03762},
{0.388124, 1.05646}, {0.374293, 1.07531}, {0.359881, 1.09416},
{0.344814, 1.11301}, {0.329006, 1.13186}, {0.312345, 1.15071},
{0.294688, 1.16955}, {0.275846, 1.1884}, {0.255556, 1.20725},
{0.233446, 1.2261}, {0.208937, 1.24495}, {0.181062, 1.2638},
{0.147932, 1.28264}, {0.104672, 1.30149}, {0.00126991,1.32034}}

data2pointsolsoln = ListPlot[Table[{\[Rho]twopointsolsoln[j], j},
{j, 0.377928, 1.32034, (1.32034 - 0.377928)/50}]]
```

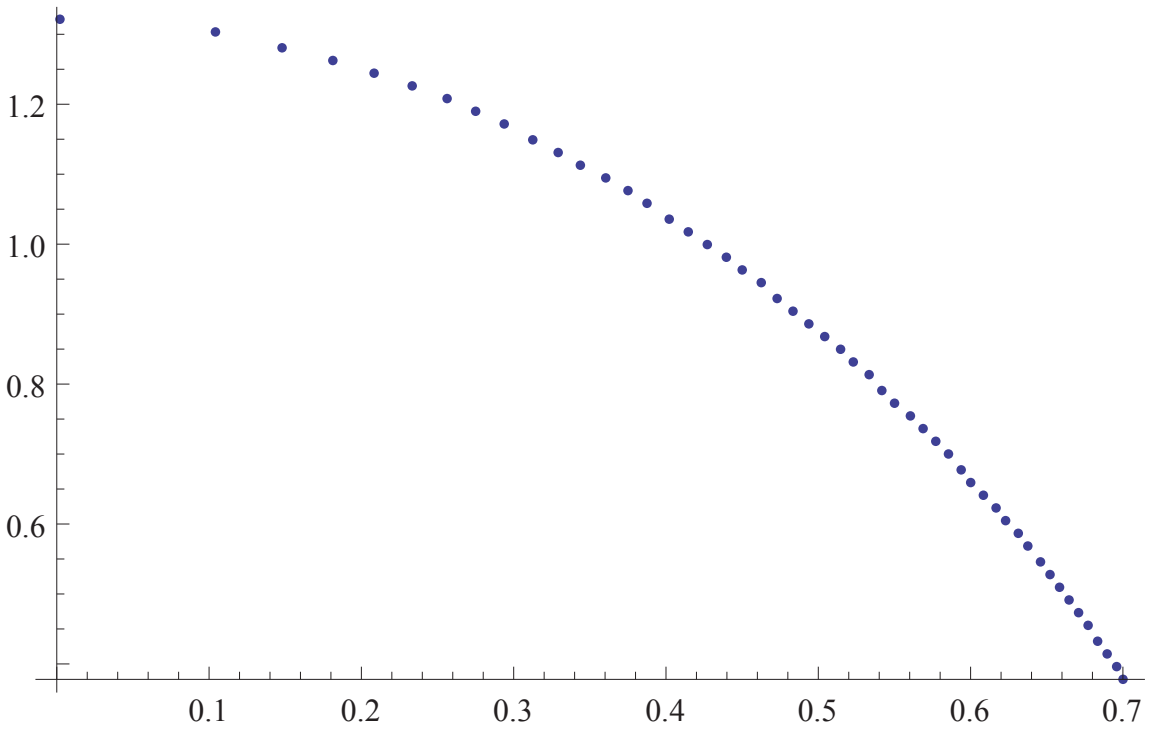


```
Show[data2pointsolsoln, data1pointsolsoln, PlotRange -> All]
```

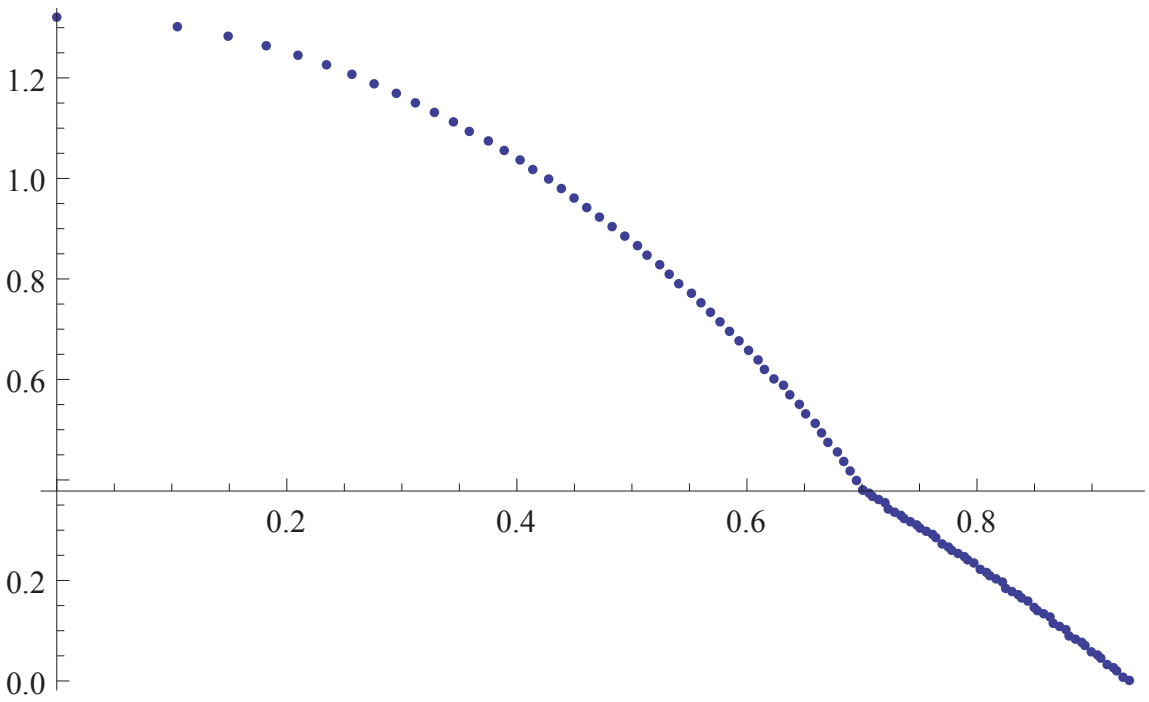

C.2 Density vs Polarisation Iterator for q = 6.6

PROGRAM DESCRIPTION: The following Mathematica 9.0 program provides the x ($n_{\perp 2}/n_{\perp 1}$) values obtained by numerical iterations of Appendix C.1 to evaluate the theoretical density profiles of a spin-imbalanced quasi-2D Fermi gas at $E_F/Eb = 6.6$ for all polarizations. Data tabulated is in the form (x-value,integral-value). The value of x appropriate for the polarization is that which gives an integral value of 1.

```
1. P of 0.1

ListPlot[{{0.01,1.09994},{0.1,1.09367},{0.2,1.07302},
{0.3,1.03587},{0.4,0.982464},{0.5,0.91571},{0.6,0.840598},
{0.7,0.763135},{0.8,0.688944},{0.9,0.62227},{1,0.565613}}]
```

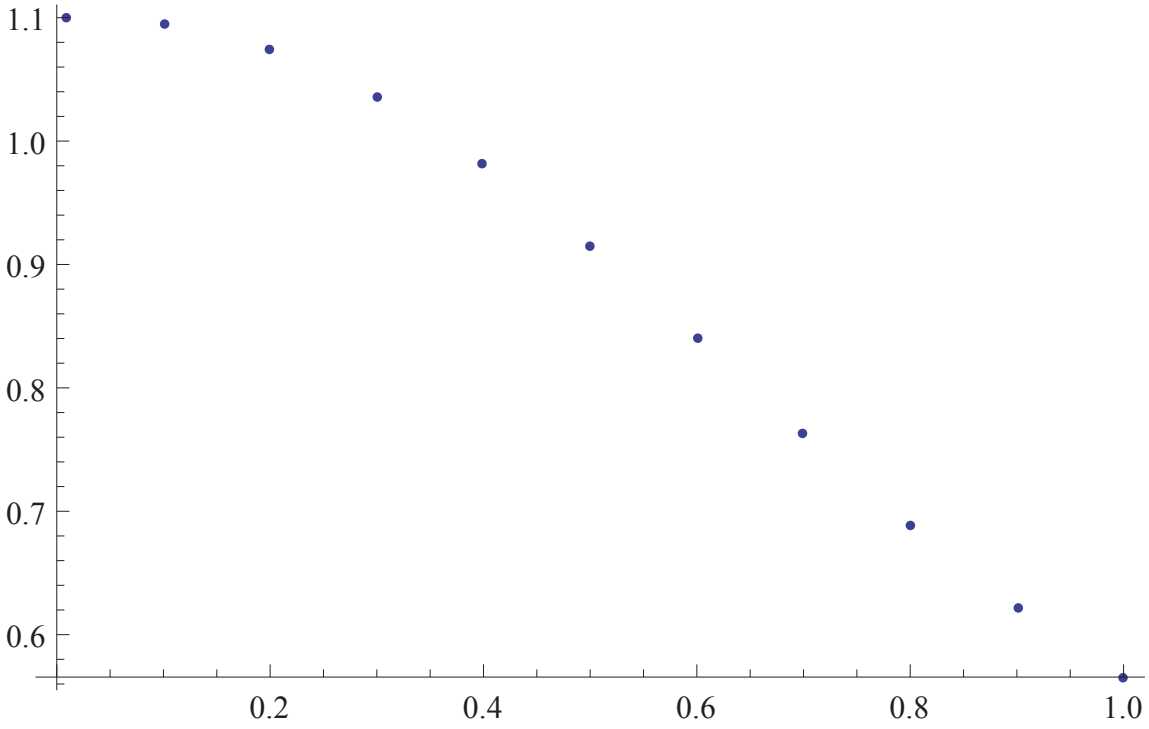


```
f=Interpolation[{{0.01,1.09994},{0.1,1.09367},{0.2,1.07302},
{0.3,1.03587},{0.4,0.982464},{0.5,0.91571},{0.6,0.840598},
{0.7,0.763135},{0.8,0.688944},{0.9,0.62227},{1,0.565613}}];

FindRoot[f[x]==1,{x,0.3}]
{x->0.370035}

f[0.370035]
1.
```

2. P of 0.2

```
ListPlot[{{0.01,1.19994},{0.1,1.19315},{0.2,1.17041},
{0.3,1.12971},{0.4,1.07134},{0.5,0.998464},{0.6,0.916569},
{0.7,0.83217},{0.8,0.751364},{0.9,0.678734},{1,0.616955}}]
```

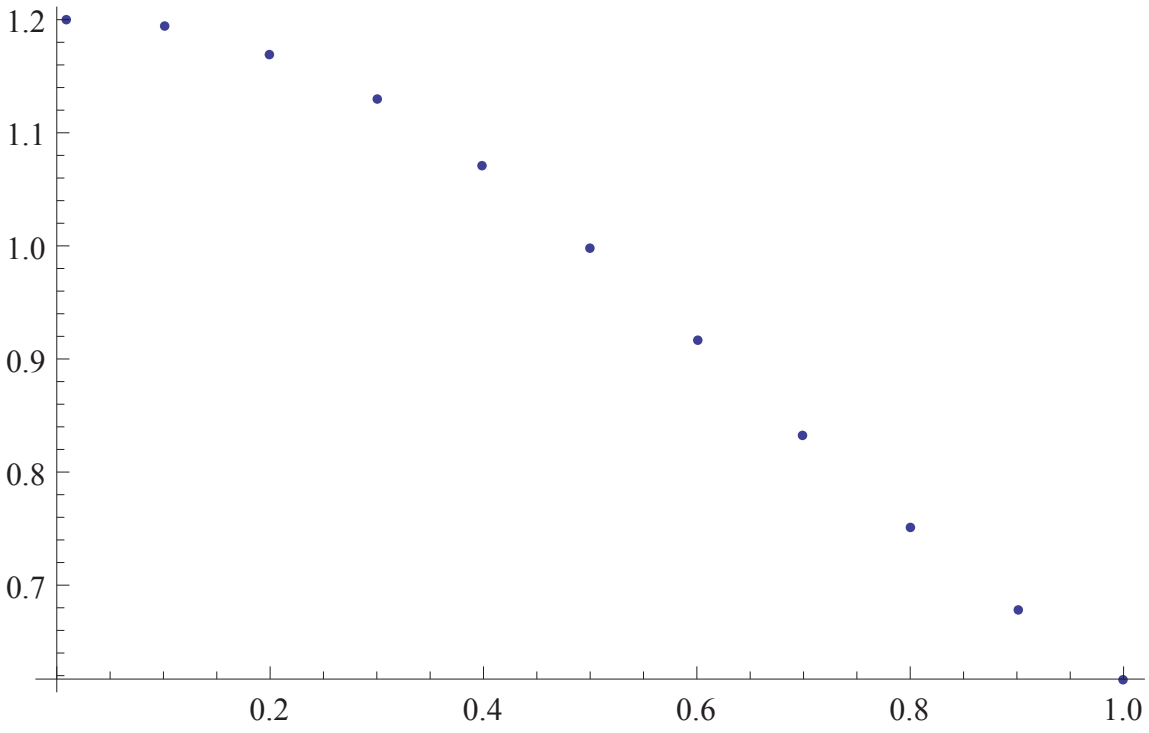


```
f=Interpolation[{{0.01,1.19994},{0.1,1.19315},{0.2,1.17041},
{0.3,1.12971},{0.4,1.07134},{0.5,0.998464},{0.6,0.916569},
{0.7,0.83217},{0.8,0.751364},{0.9,0.678734},{1,0.616955}}]

InterpolatingFunction[{{0.01,1.}},<>]

FindRoot[f[x]==1,{x,0.5}]
{x->0.498036}
```

3. P of 0.3

```
ListPlot[{{0.01,1.29994},{0.1,1.29254},{0.2,1.26778},{0.3,1.22353},
{0.4,1.16019},{0.5,1.0812},{0.6,0.992522},{0.7,0.90119},
{0.8,0.813781},{0.9,0.735177},{1,0.668286}}]
```

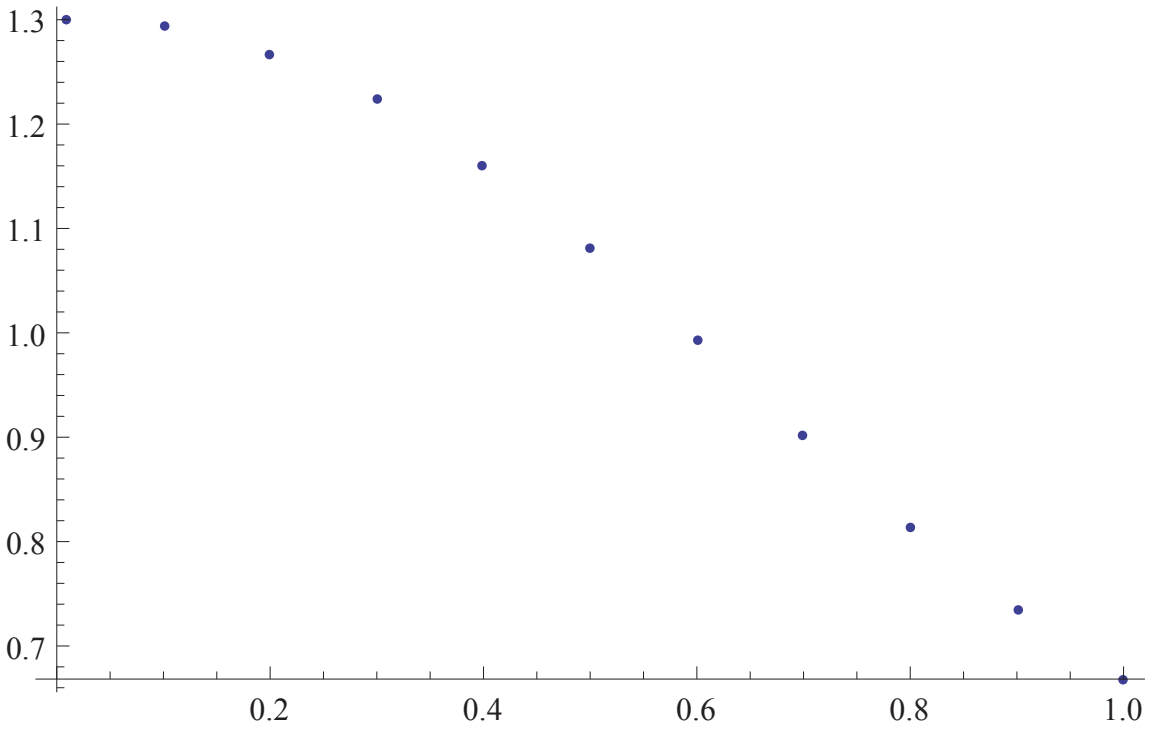


```
f=Interpolation[{{0.01,1.29994},{0.1,1.29254},{0.2,1.26778},
{0.3,1.22353},{0.4,1.16019},{0.5,1.0812},{0.6,0.992522},
{0.7,0.90119},{0.8,0.813781},{0.9,0.735177},{1,0.668286}}]

InterpolatingFunction[{{0.01,1.}},<>]

FindRoot[f[x]==1,{x,0.6}]
{x->0.591788}
```

4. P of 0.4

```
ListPlot[{{0.01,1.39993},{0.1,1.3919},{0.2,1.36515},{0.3,1.31734},
{0.4,1.24901},{0.5,1.16392},{0.6,1.06845},{0.7,0.970193},
{0.8,0.876174},{0.9,0.791615},{1,0.719609}}]
```

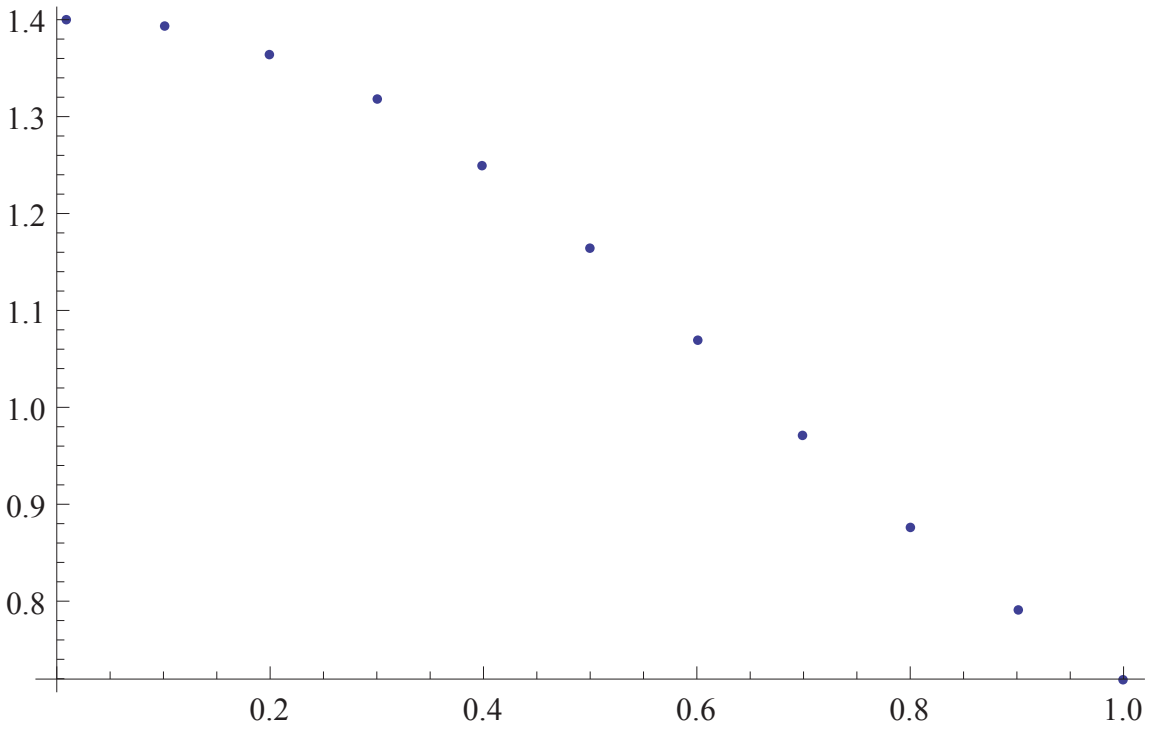


```
f=Interpolation[{{0.01,1.39993},{0.1,1.3919},{0.2,1.36515},
{0.3,1.31734},{0.4,1.24901},{0.5,1.16392},{0.6,1.06845},
{0.7,0.970193},{0.8,0.876174},{0.9,0.791615},{1,0.719609}}]

InterpolatingFunction[{{0.01,1.}},<>]

FindRoot[f[x]==1,{x,0.7}]
{x->0.669537}
```

5. P of 0.5

```
ListPlot[{{0.01,1.4999},{0.1,1.4913},{0.2,1.46249},{0.3,1.42704},
{0.4,1.33783},{0.5,1.24659},{0.6,1.14436},{0.7,1.03919},
{0.8,0.938547},{0.9,0.848052},{1,0.770924}}]
```

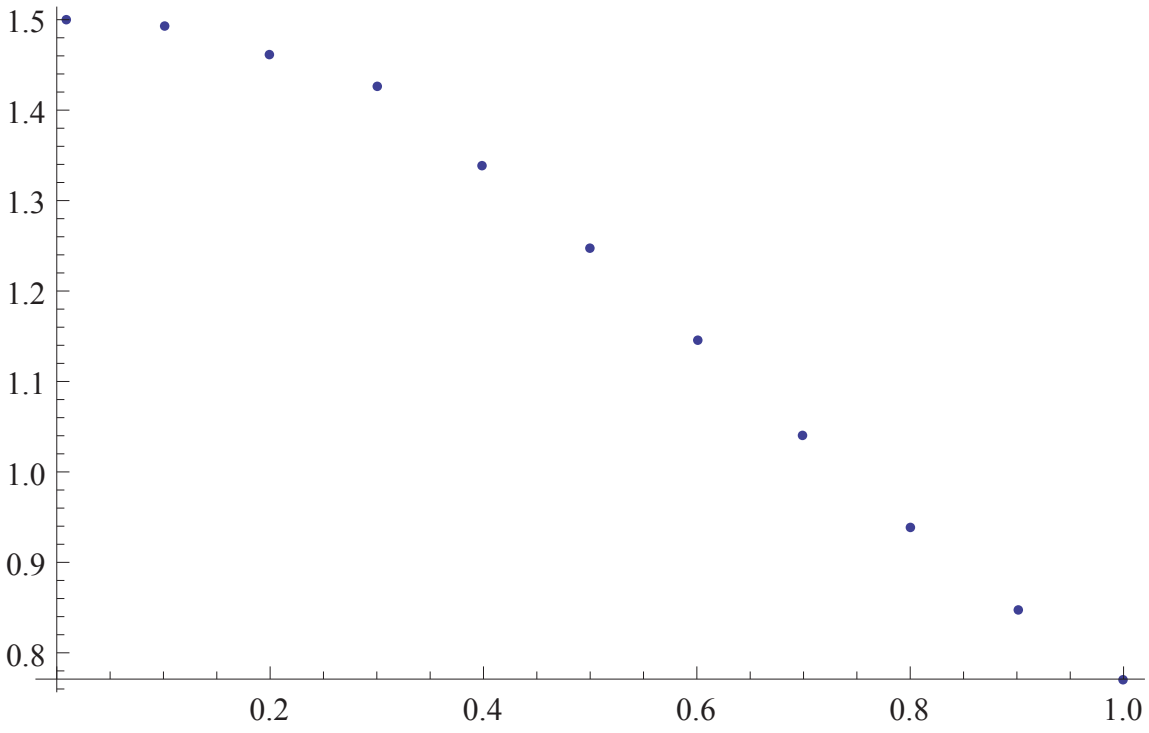


```
f=Interpolation[{{0.01,1.4999},{0.1,1.4913},{0.2,1.46249},
{0.3,1.42704},{0.4,1.33783},{0.5,1.24659},{0.6,1.14436},{0.7,1.03919},
{0.8,0.938547},{0.9,0.848052},{1,0.770924}}]

InterpolatingFunction[{{0.01,1.}},<>]

FindRoot[f[x]==1,{x,0.7}]
{x->0.738106}

6. P of 0.6

ListPlot[{{0.01,1.59991},{0.1,1.59066},{0.2,1.55983},{0.3,1.50491},
{0.4,1.42659},{0.5,1.32925},{0.6,1.22024},{0.7,1.10816},
{0.8,1.00092},{0.9,0.904474},{1,0.822242}}]
```

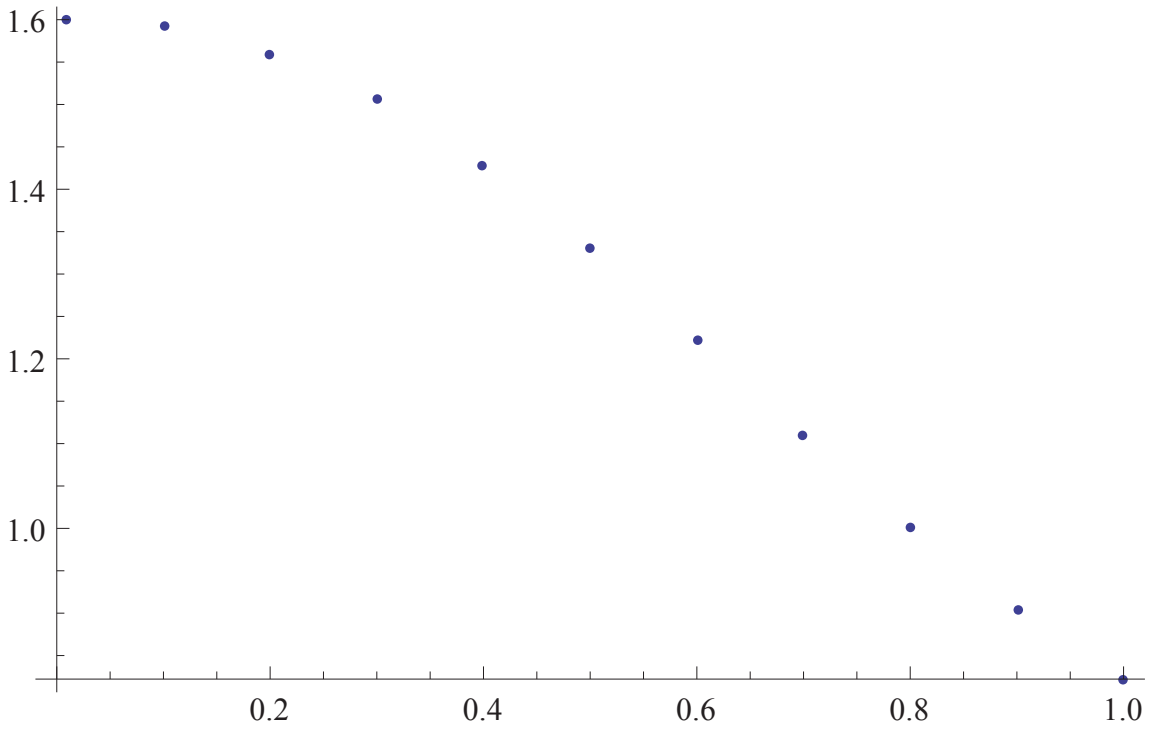


```
f=Interpolation[{{0.01,1.59991},{0.1,1.59066},{0.2,1.55983},
{0.3,1.50491},{0.4,1.42659},{0.5,1.32925},{0.6,1.22024},{0.7,1.10816},
{0.8,1.00092},{0.9,0.904474},{1,0.822242}}]

InterpolatingFunction[{{0.01,1.}},<>]

FindRoot[f[x]==1,{x,0.8}]
{x->0.800899}
```

7. P of 0.7

```
ListPlot[{{0.01,1.69991},{0.1,1.69004},{0.2,1.65715},{0.3,1.59868},
{0.4,1.51535},{0.5,1.41188},{0.6,1.2961},{0.7,1.17711},
{0.8,1.06329},{0.9,0.960889},{1,0.873547}}]
```

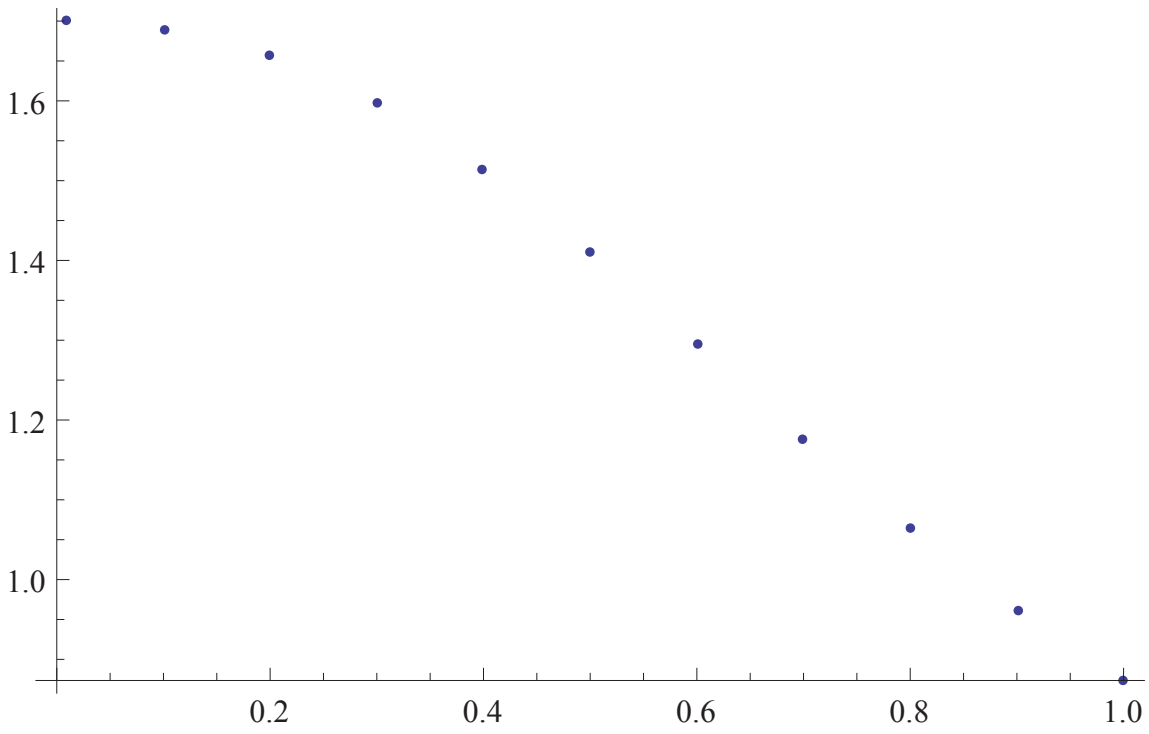


```
f=Interpolation[{{0.01,1.69991},{0.1,1.69004},{0.2,1.65715},
{0.3,1.59868},{0.4,1.51535},{0.5,1.41188},{0.6,1.2961},{0.7,1.17711},
{0.8,1.06329},{0.9,0.960889},{1,0.873547}}]

InterpolatingFunction[{{0.01,1.}},<>]

FindRoot[f[x]==1,{x,0.85}]
{x->0.860243}
```

8. P of 0.8

```
ListPlot[{{0.01,1.7999},{0.1,1.78941},{0.2,1.75448},{0.3,1.69243},
{0.4,1.60409},{0.5,1.4945},{0.6,1.37195},{0.7,1.24605},{0.8,1.12565},
{0.9,1.01728},{1,0.924837}}]
```

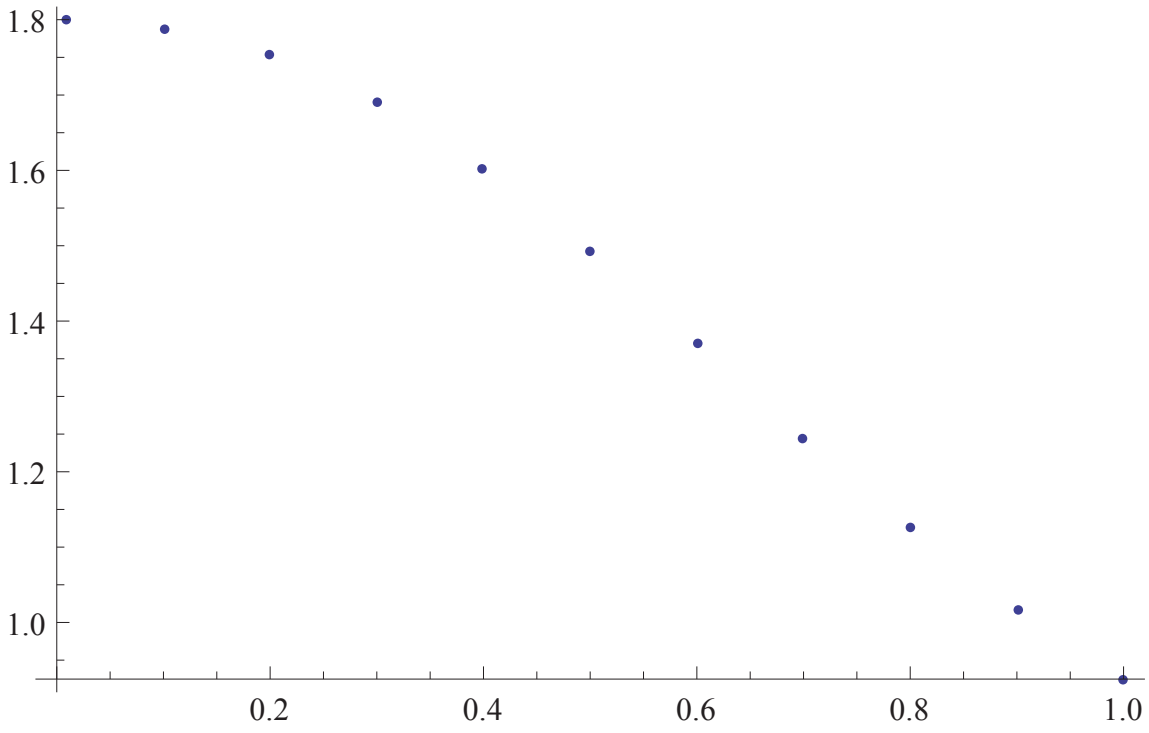


```
f=Interpolation[{{0.01,1.7999},{0.1,1.78941},{0.2,1.75448},{0.3,1.69243},
{0.4,1.60409},{0.5,1.4945},{0.6,1.37195},{0.7,1.24605},{0.8,1.12565},
{0.9,1.01728},{1,0.924837}}]

InterpolatingFunction[{{0.01,1.}},<>]

FindRoot[f[x]==1,{x,0.85}]
{x->0.91734}

9. P of 0.9

ListPlot[{{0.01,1.89989},{0.1,1.88877},{0.2,1.8518},{0.3,1.78615},
{0.4,1.69283},{0.5,1.57711},{0.6,1.44778},{0.7,1.31497},{0.8,1.18798},
{0.9,1.07369},{1,0.97613}}]
```

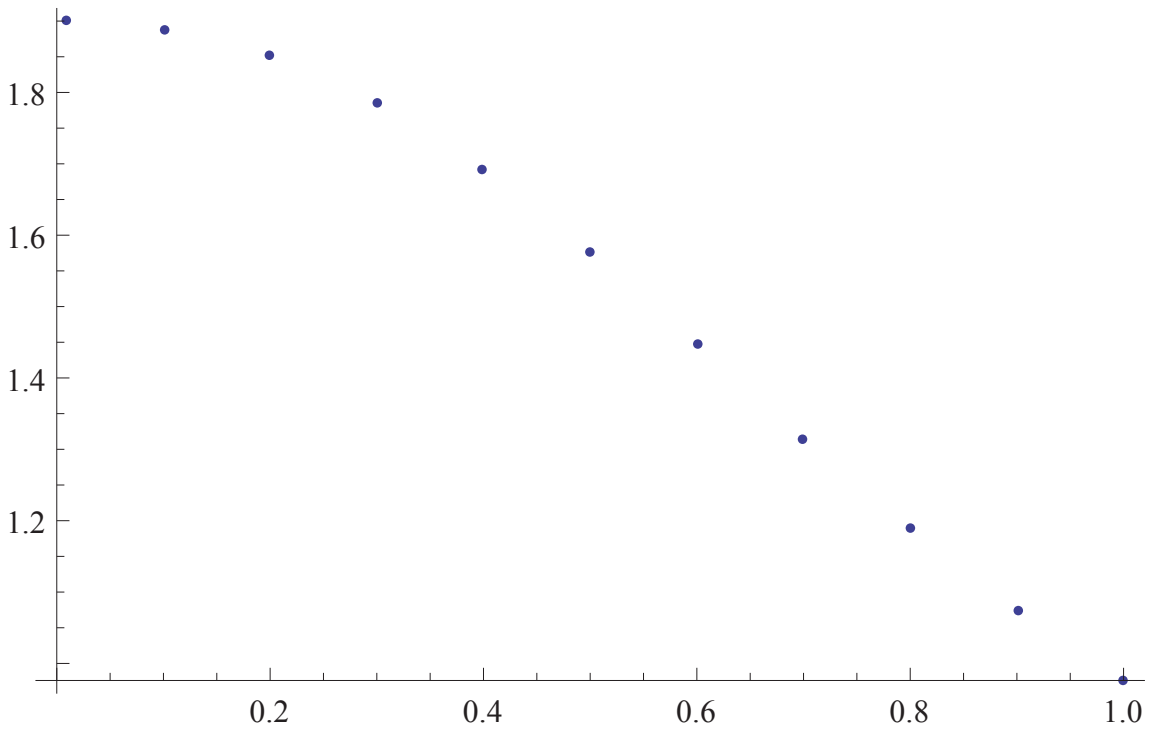


```
f=Interpolation[{{0.01,1.89989},{0.1,1.88877},{0.2,1.8518},{0.3,1.78615},
{0.4,1.69283},{0.5,1.57711},{0.6,1.44778},{0.7,1.31497},{0.8,1.18798},
{0.9,1.07369},{1,0.97613}}]

InterpolatingFunction[{{0.01,1.}},<>]

FindRoot[f[x]==1,{x,0.9}]
{x->0.973636}
```

C.3 Density Ratio Calculator for q = 2.1 and q = 0.73

PROGRAM DESCRIPTION: The following Mathematica 9.0 program provides the x ($n_{\perp 2}/n_{\perp 1}$) values obtained by numerical iterations of Appendix C.1 to evaluate the theoretical density profiles of a spin-imbalanced quasi-2D Fermi gas at $q = E_F/Eb = 2.1$ and $q = E_F/Eb = 0.73$ for all polarizations. Data tabulated is in the form (x-value,integral-value). The value of x appropriate for the polarization is that which gives an integral value of 1. These are the x-values used to calculate the theoretical majority and minority radii and the central density ratios in Chapter 6.

```
1. q=2.1, P of 0.1
f=Interpolation[{{0.01,1.09996},{0.1,1.09514},{0.2,1.07807},
{0.3,1.04561},{0.4,0.996224},{0.5,0.931116},{0.6,0.854694},
{0.7,0.773577},{0.8,0.694894},{0.9,0.624589},{1,0.566354}}];

FindRoot[f[x]==1,{x,0.4}]
{x->0.393367}

2. q=2.1, P of 0.2
f=Interpolation[{{0.01,1.19996},{0.1,1.19463},{0.2,1.17584},
{0.3,1.14019},{0.4,1.08607},{0.5,1.01496},{0.6,0.93164},
{0.7,0.843341},{0.8,0.75778},{0.9,0.681299},{1,0.617875}}]

FindRoot[f[x]==1,{x,0.5}]
{x->0.518811}

3. q = 2.1, P of 0.3
f=Interpolation[{{0.01,1.29995},{0.1,1.2941},{0.2,1.27357},
{0.3,1.23472},{0.4,1.17588},{0.5,1.09874},{0.6,1.00855},
{0.7,0.913089},{0.8,0.820637},{0.9,0.737992},{1,0.669382}}]

FindRoot[f[x]==1,{x,0.6}]
{x->0.609054}

4. q = 2.1, P of 0.4
f=Interpolation[{{0.01,1.39994},{0.1,1.3936},{0.2,1.3713},
{0.3,1.32922},{0.4,1.26565},{0.5,1.18247},{0.6,1.08542},
{0.7,0.982803},{0.8,0.883491},{0.9,0.794685},{1,0.720882}}]

FindRoot[f[x]==1,{x,0.7}]
{x->0.683252}

5. q = 2.1, P of 0.5
f=Interpolation[{{0.01,1.49993},{0.1,1.49307},{0.2,1.46901},
```

```
{0.3,1.4237},{0.4,1.35539},{0.5,1.26618},{0.6,1.16223},
{0.7,1.05248},{0.8,0.946309},{0.9,0.851376},{1,0.772387}}]

FindRoot[f[x]==1,{x,0.7}]
{x->0.748562}

6. q = 2.1, P of 0.6
f=Interpolation[{{0.01,1.59993},{0.1,1.59255},{0.2,1.56671},
{0.3,1.51815},{0.4,1.44508},{0.5,1.34985},{0.6,1.23902},
{0.7,1.12215},{0.8,1.00913},{0.9,0.908047},{1,0.823886}}]

FindRoot[f[x]==1,{x,0.8}]
{x->0.808503}

7. q = 2.1, P of 0.7
f=Interpolation[{{0.01,1.69992},{0.1,1.69202},{0.2,1.6644},
{0.3,1.61257},{0.4,1.53476},{0.5,1.43346},{0.6,1.31578},
{0.7,1.19178},{0.8,1.07193},{0.9,0.964712},{1,0.875393}}]

FindRoot[f[x]==1,{x,0.85}]
{x->0.865449}

8. q = 2.1, P of 0.8
f=Interpolation[{{0.01,1.79991},{0.1,1.79148},{0.2,1.76208},
{0.3,1.70699},{0.4,1.62439},{0.5,1.51706},{0.6,1.39251},
{0.7,1.2614},{0.8,1.13473},{0.9,1.02139},{1,0.926885}}]

FindRoot[f[x]==1,{x,0.85}]
{x->0.920799}

9. q = 2.1, P of 0.9
f=Interpolation[{{0.01,1.8999},{0.1,1.89097},{0.2,1.85974},
{0.3,1.80136},{0.4,1.71399},{0.5,1.60062},{0.6,1.46924},
{0.7,1.331},{0.8,1.1975},{0.9,1.07805},{1,0.978377}}]
```

```
FindRoot[f[x]==1,{x,0.9}]
{x->0.976201}

1. q=0.73, P of 0.1
f=Interpolation[{{0.01,1.09997},{0.1,1.0967},{0.2,1.08428},
{0.3,1.05856},{0.4,1.01575},{0.5,0.954327},{0.6,0.876772},
{0.7,0.789892},{0.8,0.703178},{0.9,0.625861},{1,0.564385}}];

FindRoot[f[x]==1,{x,0.2}]
{x->0.428556}

2. q = 0.73, P of 0.2
f=Interpolation[{{0.01,1.19997},{0.1,1.19633},{0.2,1.18256},
{0.3,1.15414},{0.4,1.10705},{0.5,1.03981},{0.6,0.955219},
{0.7,0.860743},{0.8,0.766629},{0.9,0.682712},{1,0.61584}}]

FindRoot[f[x]==1,{x,0.5}]
{x->0.549077}

3. q=0.73, P of 0.3
f=Interpolation[{{0.01,1.29997},{0.1,1.29595},{0.2,1.28081},
{0.3,1.24965},{0.4,1.19829},{0.5,1.12521},{0.6,1.03359},
{0.7,0.931556},{0.8,0.830052},{0.9,0.739551},{1,0.667293}}]

FindRoot[f[x]==1,{x,0.6}]
{x->0.633526}
```

```
4. q = 0.73, P of 0.4
f=Interpolation[{{0.01,1.39995},{0.1,1.39557},{0.2,1.37903},
{0.3,1.34514},{0.4,1.28946},{0.5,1.21053},{0.6,1.11191},
{0.7,1.00231},{0.8,0.893447},{0.9,0.796385},{1,0.718763}}]

FindRoot[f[x]==1,{x,0.7}]
{x->0.70208}

5. q = 0.73, P of 0.5
f=Interpolation[{{0.01,1.49994},{0.1,1.49518},{0.2,1.47724},
{0.3,1.44059},{0.4,1.38058},{0.5,1.29579},{0.6,1.19014},
{0.7,1.07303},{0.8,0.956831},{0.9,0.853227},{1,0.770235}}]

FindRoot[f[x]==1,{x,0.7}]
{x->0.762118}

6. q=0.73, P of 0.6
f=Interpolation[{{0.01,1.59995},{0.1,1.59479},{0.2,1.57543},
{0.3,1.53601},{0.4,1.47163},{0.5,1.38098},{0.6,1.26833},
{0.7,1.1437},{0.8,1.02018},{0.9,0.910047},{1,0.821702}}]

FindRoot[f[x]==1,{x,0.8}]
{x->0.817243}

7. q = 0.73, P of 0.7
f=Interpolation[{{0.01,1.69994},{0.1,1.69439},{0.2,1.67359},
{0.3,1.63139},{0.4,1.56265},{0.5,1.46611},{0.6,1.34647},
```

```
{0.7,1.21433},{0.8,1.08352},{0.9,0.966883},{1,0.873194}}]

FindRoot[f[x]==1,{x,0.85}]
{x->0.86988}

8. q = 0.73, P of 0.8
f=Interpolation[{{0.01,1.79994},{0.1,1.79399},{0.2,1.77177},
{0.3,1.72672},{0.4,1.65362},{0.5,1.55121},{0.6,1.42455},
{0.7,1.28494},{0.8,1.14684},{0.9,1.02371},{1,0.92467}}]

FindRoot[f[x]==1,{x,0.85}]
{x->0.921567}

9. q = 0.73, P of 0.9
f=Interpolation[{{0.01,1.89993},{0.1,1.89357},{0.2,1.86989},
{0.3,1.82205},{0.4,1.74455},{0.5,1.63623},{0.6,1.50259},
{0.7,1.3555},{0.8,1.21014},{0.9,1.08052},{1,0.976163}}]

FindRoot[f[x]==1,{x,0.9}]
{x->0.974344}
```

Appendix D

2D Density of a Spin-Balanced quasi-2D Fermi Gas

D.1 2D Density of a Spin-Balanced quasi-2D Fermi Gas

PROGRAM DESCRIPTION: This Mathematica 9.0 program generates the 2D density profile for a spin-balanced quasi-2D Fermi gas with an interaction parameter, q, of 2.1.

```
1. Polaron Energy Definition

y[q_]:=-2/Log[1+2*q]

yprime[q_]:=(q*(y[q])^2)/(1+2q)

2. Compute density at trap center q2p1

FindRoot[n== 1/Sqrt[1+y[2.1*n]+yprime[2.1*n]],{n,2}]

{n->1.52091}

3. Chemical Potential at trap center q2p1

mu=1.52091*(1+y[2.1*1.52091]+1/2 yprime[2.1*1.52091])

0.328689

4. Cloud Radius q2p1
```

```
R1=Sqrt[mu+1/(2*2.1)]
0.75285

5. Density Profile q2p1

\[Rho][n_]:=Sqrt[mu-n*(1+y[2.1*n]+1/2 yprime[2.1*n])];

BalProfile2p1=ListPlot[Table[{\[Rho][i],i},{i,0,1.52091,(1.52091-0)/100}]]
```

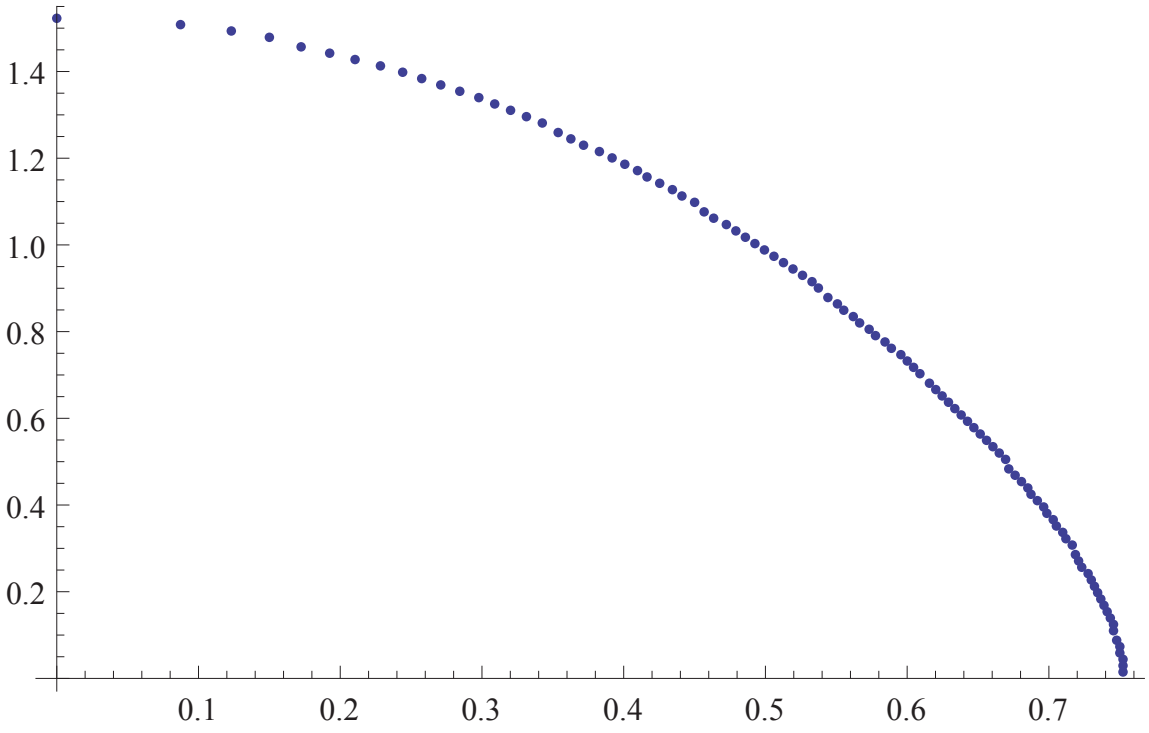

Bibliography

[1] Cheng Chin, Rudolf Grimm, Paul Julienne, and Eite Tiesinga. Feshbach resonances in ultracold gases. *Rev. Mod. Phys.*, 82:1225, 2010.

[2] M. Konig, S. Wiedmann, C. Brune, H. Buhmann A. Roth, L. W Molenkamp, X-L.Qi, and S-C. Zhang. Quantum spin hall insulator state in hgte quantum wells. *Science*, 318:766, 2007.

[3] B. Clancy. *Hydrodynamics of a Rotating Strongly Interacting Fermi gas*. PhD thesis, Duke University, 2008.

[4] L. Luo. *Entropy and Superfluid Critical Parameters of a Strongly Interacting Fermi gas*. PhD thesis, Duke University, 2008.

[5] C. Cao, E. Elliott, J. Joseph, H. Wu, J. Petricka, T. Schaefer, and J. E. Thomas. Universal quantum viscosity in a unitary fermi gas. *Science*, 331:58, 2011.

[6] E. Elliott, J. A. Joseph, and J. E. Thomas. Anomalous minimum in the shear viscosity of a fermi gas. *Phys. Rev. Lett.*, 113:20406, 2014.

[7] H. Takahashi, K. Igawa, K. Arii, Y. Kamihara, M. Hirano, and H. Hosono. Superconductivity at 43 k in an iron-based layered compound la1-x fxfeas. *Nature*, 453:376, 2008.

[8] A. Chubukov, D. V. Efremov, and I. Eremin. Magnetism, superconductivity, and pairing symmetry in iron-based superconductors. *Phys. Rev. B*, 78:134512, 2008.

[9] H. Mayaffre, S. Kramer, M. Horvatic, C. Berthier, K. Miyagawa, K. Kanoda, and V. F. Mitrovic. Evidence of andreev bound states as a hallmark of the fflo phase in k-(bedt-ttf)2cu(ncs)2. *Nat. Phys.*, 10:928, 2014.

[10] F. Piazza, W. Zwerger, and P. Strack. Fflo strange metal and quantum criticality in two dimensions: theory and experimental evidence in organic superconductors. *arXiv*, 1506:08819, 2015.

[11] M. R. Norman. The challenge of unconventional superconductivity. *Science*, 332:196, 2011.

[12] L. He, H. Lu, G. Cao, H. Hu, and X.-J. Liu. Quantum fluctuations in the bcs-bec crossover of two-dimensional fermi gases. *arXiv*, 1506:07156, 2015.

[13] P. C. Hohenberg. Existence of long range order in one and two dimensions. *Phys. Rev.*, 158:383, 1967.

[14] N. D. Mermin and H. Wagner. Absence of ferromagnetism or antiferromagnetism in one- or two-dimensional isotropic heisenberg models. *Phys. Rev. Lett.*, 17:1133, 1966.

[15] Yusuke Nishida, Sergej Moroz, and Dam Thanh Son. Super efimov effect of resonantly interacting fermions in two dimensions. *Phys. Rev. Lett.*, 110:235301, 2013.

[16] L. P. Pitaevskii and A. Rosch. Breathing modes and hidden symmetry of trapped atoms in two dimensions. *Phys. Rev. A*, 55:R853(R), 1997.

[17] G. M. Bruun. Long-lived higgs mode in a two-dimensional confined fermi system. *Phys. Rev. A*, 90:023621, 2014.

[18] M. Baranov, D. Efremov, and M. Yu. Kagan. The enhancement of the superconductive transition temperature in quasi-2d materials in a parallel magnetic field. *Physica C: Superconductivity*, 218:75, 1993.

[19] M. Randeria, J.-M. Duan, and L.-Y. Shieh. Bound states, cooper pairing, and bose condensation in two dimensions. *Phys. Rev. Lett.*, 62(1):981, 1989.

[20] S. Schmitt-Rink, C. M. Varma, and A. E. Ruckenstein. Pairing in two dimensions. *Phys. Rev. Lett.*, 63:445, 1989.

[21] J. P. Martikainen and P. Torma. Quasi-two-dimensional superfluid fermionic gases. *Phys. Rev. Lett.*, 95:170407, 2005.

[22] S. S. Botelho and C. A. R. Sa de Melo. Vortex-antivortex lattice in ultracold fermionic gases. *Phys. Rev. Lett.*, 96:040404, 2006.

[23] W. Zhang, G. D. Lin, and L. M. Duan. Berezinskii-kosterlitz-thouless transition in a trapped quasi-two-dimensional fermi gas near a feshbach resonance. *Phys. Rev. A*, 78:043617, 2008.

[24] J. Tempere, S. N. Klimin, and J. T. Devreese. Effect of population imbalance on the berezinskii-kosterlitz-thouless phase transition in a superfluid fermi gas. *Phys. Rev. A*, 79:053637, 2009.

[25] G. Bertaina and S. Giorgini. Bcs-bec crossover in a two-dimensional fermi gas. *Phys. Rev. Lett.*, 106:110403, 2011.

[26] Daniel E. Sheehy. Fulde-ferrell-larkin-ovchinnikov state of two-dimensional imbalanced fermi gases. *arXiv*, v1:1407.8021, 2014.

[27] M. W. Zwierlein, A. Schirotzek, C. H. Schunck, and W. Ketterle. Fermion superfluidity with imbalanced spin populations. *Science*, 311:492, 2006.

[28] G. B. Partridge, W. Li, R. I Kamar, Y. a. Liao, and R. G. Hulet. Pairing and phase separation in a polarized fermi gas. *Science*, 311:503, 2006.

[29] D. E. Sheehy and L. Radzihovsky. Bec-bcs crossover, phase transitions and phase separation in polarized resonantly-paired superfluids. *Ann. Phys.*, 322:1790, 2007.

[30] F. Chevy. Swimming in the fermi sea. *Physics Viewpoint*, 2:48, 2009.

[31] A. Schirotzek, C. H. Wu, A. Sommer, and M. Zwierlein. Observation of fermi polarons in a tunable fermi liquid of ultracold atoms. *Phys. Rev. Lett.*, 105:030404, 2010.

[32] Y. A. Liao, A. S. C. Rittner, T. Paprotta, W. Li, G. B. Partridge, R. G. Hulet, S. K. Baur, and E. J. Mueller. Spin-imbalance in a one-dimensional fermi gas. *Nature*, 467:567, 2010.

[33] P. Fulde and R. A Ferrell. Superconductivity in a strong spin-exchange field. *Phys. Rev.*, 135:A550, 1964.

[34] A. I. Larkin and Yu.N. Ovchinnikov. Inhomogeneous state of superconductors. *Zh. Eksp. Teor. Fiz.*, 47:1136, 1964.

[35] M. Feld, B. Frohlich, E. Vogt, M. Koschorreck, and M. Kohl. Observation of a pairing pseudogap in a two-dimensional fermi gas. *Nature*, 480:75, 2011.

[36] A. T. Sommer, L. W. Cheuk, M. J. H. Ku, W. S. Bakr, and M. W. Zwierlein. Evolution of fermion pairing from three to two dimensions. *Phys. Rev. Lett.*, 480:045302, 2011.

[37] M. G. Ries, A. N. Wenz, G. Zurn, L. Bayha, I. Boettcher, D. Kedar, P. A. Murthy, M. Neidig, T. Lompe, and S. Jochim. Observation of pair condensation in the quasi-2d bec-bcs crossover. *arXiv*, 1409:5373, 2014.

[38] S. Zollner, G. M. Bruun, and C. J. Pethick. Polarons and molecules in a two-dimensional fermi gas. *Phys. Rev. A*, 83:021603(R), 2011.

[39] Y. Zhang, W. Ong, I. Arakelyan, and J. E. Thomas. Polaron-to-polaron transitions in the radio-frequency spectrum of a quasi-two-dimensional fermi gas. *Phys. Rev. Lett.*, 108:235302, 2012.

[40] H. Caldas, A. L. Mota, R. L. S. Farias, and L. A. Souza. Superfluidity in two-dimensional imbalanced fermi gases. *J. Stat. Mech.*, page 10019, 2012.

[41] S. Yin, J. P. Martikainen, and P. Torma. Fulde-ferrell states and berezinskii-kosterlitz-thouless phase transition in two-dimensional imbalanced fermi gases. *Phys. Rev. B*, 89:014507, 2014.

[42] A. M. Fischer and M. M. Parish. Quasi-two-dimensional fermi gases at finite temperature. *Phys. Rev. B*, 90:214503, 2014.

[43] V. L. Berezinskii. Destruction of long-range order in one-dimensional and two-dimensional systems having a continuous symmetry group ii. quantum systems. *Sov. Phys. JETP*, 34:610, 1972.

[44] J. M. Kosterlitz and D. J. Thouless. Ordering, metastability and phase transitions in two-dimensional systems. *J. Phys. C*, 6:1181, 1973.

[45] E. Tiesinga, B. J. Verhaar, and H. T. C. Stoof. Threshold and resonance phenomena in ultacold ground-state collisions. *Phys. Rev. A*, 47:4114, 1993.

[46] G. Zurn, T. Lompe, A. N. Wenz, S. Jochim, P. S. Julienne, and J. M. Hutson. Precise characterization of ^{6}li feshbach resonances using trap-sideband resolved rf spectroscopy of weakly bound molecules. *Phys. Rev. Lett.*, 110:135301, 2013.

[47] M. Bartenstein, A. Altmeyer, S. Riedl, R. Geursen, S. Jochim, C. Chin, J. H. Denschlag, R. Grimm, A. Simoni, E. Tiesinga, C. J. Williams, and P. S. Julienne. Precise determination of ^{6}li cold collision parameters by radio-frequency spectroscopy on weakly bound molecules. *Phys. Rev. Lett.*, 94:103201, 2005.

[48] X. Du, L. Luo, B. Clancy, and J. E. Thomas. Observation of anomalous spin segregation in a trapped fermi gas. *Phys. Rev. Lett.*, 101:150401, 2008.

[49] D. A. Butts and D. S. Rokhsar. Trapped fermi gases. *Phys. Rev. A*, 101:150401, 1997.

[50] J. Kinast, A. Turlapov, J. E. Thomas, Q. Chen, J. Stajic, and K. Levin. Heat capacity of a strongly interacting fermi gas. *Science*, 307:1296, 2005.

[51] Jesper Levinsen and Meera M. Parish. Strongly interacting two-dimensional fermi gases. *arXiv*, v1:1408.2737, 2014.

[52] M. M. Parish and J. Levinsen. Highly polarized fermi gases in two dimensions. *Phys. Rev. A*, 87:033616, 2013.

[53] L. He and P. Zhuang. Phase diagram of a cold polarized fermi gas in two dimensions. *Phys. Rev. A*, 78:033613, 2008.

[54] F. Chevy. Universal phase diagram of a strongly interacting fermi gas. *Phys. Rev. A*, 74:063628, 2006.

[55] M. Klawunn and A. Recati. Fermi polaron in two dimensions: Importance of the two-body bound state. *Phys. Rev. A*, 84:033607, 2011.

[56] Sadhan K. Adhikari. Quantum scattering in two dimensions. *Am. J. Phys.*, 54:4, 1989.

[57] D. S. Petrov and G. V. Shlyapnikov. Interatomic collisions in a tightly confined bose gas. *Phys. Rev. A*, 64:012706, 2001.

[58] I. Bloch, J. Dalibard, and W. Zwerger. Many-body physics with ultracold gases. *Rev. Mod. Phys.*, 80:885, 2008.

[59] Y. Zhang. *Radio Frequency Spectroscopy of a Quasi-Two-Dimensional Fermi Gas*. PhD thesis, Duke University, 2013.

[60] Kerson Huang. *Statistical Mechanics*. John Wiley and Sons, 2001.

[61] M. Houbiers, R. Ferwerda, H. T. C. Stoof, W. I. McAlexander, C. A. Sackett, and R. G. Hulet. Superfluid state of atomic ^{6}li in a magnetic trap. *Phys. Rev. A*, 56:4864, 1997.

[62] J. Kinast. *Thermodynamics and Superfluidity of a Strongly Interacting Fermi gas*. PhD thesis, Duke University, 2008.

[63] W. Ong, Chingyun Cheng, I. Arakelyan, and J. E. Thomas. Spin-imbalanced quasi-two-dimensional fermi gases. *Phys. Rev. Lett.*, 114:110403, 2015.

[64] Y. i. Shin. Determination of the equation of state of a polarized fermi gas at unitarity. *Phys. Rev. A*, 77:041603, 2008.

[65] Shahin Bour, Dean Lee, H.-W. Hammer, and Ulf-G. Meibner. Ab initio lattice results for fermi polarons in two and three dimensions. *arXiv*, v2:1412.8175, 2014.

[66] Kirill Martiyanov, Vasiliy Makhalov, and Andrey Turlapov. Observation of a two-dimensional fermi gas of atoms. *Phys. Rev. Lett.*, 105:030404, 2010.

[67] Vasiliy Makhalov, Kirill Martiyanov, and Andrey Turlapov. Ground-state pressure of quasi-2d fermi and bose gases. *Phys. Rev. Lett.*, 112:045301, 2014.

[68] G. J. Conduit, P. H. Conlon, and B. D. Simons. Superfluidity at the bec-bcs crossover in two-dimensional fermi gases with population and mass imbalance. *Phys. Rev. A*, 77:053617, 2008.

[69] J. Tempere, S. N. Klimin, and J. T. Devreese. The effect of population imbalance on the berezinskii-kosterlitz-thouless phase transition in a superfluid fermi gas. *Phys. Rev. A*, 79:053637, 2009.

[70] M. A. Resende, A. L. Mota, R. L. S. Farias, and H. Caldas. Finite temperature phase diagram of quasi-two-dimensional imbalanced fermi gases beyond mean-field. *Phys. Rev. A*, 86:033603, 2012.

[71] S. N. Klimin, J. Tempere, and J. T. Devreese. Pseudogap and preformed pairs in the imbalanced fermi gas in two dimensions. *New J. Phys.*, 14:103044, 2012.

[72] M. J. Wolak, B. Gremaud, R. T. Scalettar, and G. G. Batrouni. Pairing in a two-dimensional fermi gas with population imbalance. *Phys. Rev. A*, 86:023630, 2012.

[73] P. Strack and P. Jakubczyk. Fluctuations of imbalanced fermionic superfluids in two dimensions induce continuous quantum phase transitions and non-fermi-liquid behavior. *Phys. Rev. X*, 4:021012, 2014.

[74] Vudtiwat Ngampruetikorn, Jesper Levinsen, and Meera M. Parish. Pair correlations in the two-dimensional fermi gas. *Phys. Rev. Lett.*, 111:265301, 2013.

[75] M. Bauer, M. M. Parish, and T. Enss. Universal equation of state and pseudogap in the two-dimensional fermi gas. *Phys. Rev. Lett.*, 112:135302, 2014.

Biography

Willie Chuin Hong Ong was born in Singapore on the 17th of June 1982. He earned his Bachelor's of Science in Physics from the University of Illinois at Urbana-Champaign in 2006. Following a one-year stint in the data storage industry and serving on the academic committee of the International Physics Olympiad, his interests in the intersections of light and quantum materials led him to pursue a PhD at Duke University in the Fall of 2007. He joined the AMO Physics laboratories of Dr. John Thomas in Spring 2009. Following the labs' relocation to North Carolina State University in the Spring of 2012, he co-built a laboratory (with post-doctoral research associate Ilya Arakelyan) now affectionately known as Riddick 212. There, he pioneered high-resolution atom imaging capabilities and conducted the first density profile studies on spin-imbalanced quasi-2D Fermi gases. Some of his work along this direction is the subject of this thesis.

In addition to his investigations in the lab, he was the Research Editor of the Physical Sciences and Mathematics Division of the Journal of Young Investigators (www.jyi.org), and an educator for pre-Med Physics courses at Duke. His efforts in the classroom were multiply recognised with AAPT Outstanding Teaching Assistant Awards and the Mary Creason Memorial Award.

Publications

1. W. Ong, C. Cheng, I. Arakelyan, and J. E. Thomas, "Spin-Imbalanced Quasi-Two-Dimensional Fermi Gases", *Physical Review Letters*, **114**, 110403 (2015).

2. Y. Zhang, W. Ong, I. Arakelyan, and J. E. Thomas, "Polaron-to-Polaron Transitions in the Radio-Frequency Spectrum of a Quasi-Two-Dimensional Fermi Gas ", *Physical Review Letters*, **108**, 235302 (2012).